HIGH-RESOLUTION CHARACTERISATION OF STRESS CORROSION CRACKING

Martina Meisnar

The Queen's College

University of Oxford

A thesis submitted for the degree of Doctor of Philosophy

Department of Materials

Trinity Term 2015

The image of stress corrosion I see
Is that of a huge unwanted tree
Against whose trunk we chop and chop,
But which outgrows the chips that drop;
And from each gash made in its bark
A new branch grows to make more dark
The shade of ignorance around its base,
Where scientists toil with puzzled face.
(S P Rideout, 1967)

Abstract

The degradation of reactor grade stainless steels and their susceptibility to stress corrosion cracking (SCC) when exposed to the pressurised water reactor (PWR) primary water environment has been a topic of intense research for many decades. Nevertheless, our understanding of the underlying mechanisms of SCC remains incomplete to date. It has been generally accepted that only high-resolution (electron) microscopy techniques are capable of revealing the yet unidentified processes involved in SCC crack propagation. For this reason, one of the main objectives of this project was to make new techniques with improved spatial resolution accessible to SCC research. While low-keV energy dispersive X-ray spectroscopy (EDX) was used for the preliminary analysis of SCC cracks, transmission Kikuchi diffraction (TKD) and atom probe tomography (APT) were used for high-resolution studies of the microstructure and chemistry near the crack tip. In particular, TKD proved very beneficial for revealing the extent of the strain concentration around the crack tip. For the application of APT to SCC research, a novel method for preparing APT needles containing entire SCC crack tips was developed. The method was then used for acquiring very localised compositional measurements of the crack tip and GB oxide chemistry with extraordinary accuracy.

The second objective of this thesis was to understand the impact of the SCC test temperature on the crack growth rate (CGR) in SUS316 stainless steel. It was found that after steady growth with increasing temperature, a peak in the CGR occurred at ~ 320°C, followed by a substantial drop towards higher temperatures. The inhibition of the CGR with increasing temperature between 320° and 360°C and its impact on the microstructure were studied via analytical transmission electron microscopy (TEM) and TKD. Furthermore, the potential impact of thermally activated diffusion and mechanical response-based mechanisms was investigated. It appears that higher dislocation density and strain concentrations around the crack tips at lower temperature (i.e. 320°C) lead to possibly enhanced brittle-like fracture at the crack tip. An enhanced model for the ongoing processes involved in SCC crack propagation based on the experimental results is presented at the end of this work.

Preface

This thesis comprises the work carried out by the author in the Department of Materials, University of Oxford, under the supervision of Prof. Sergio Lozano-Perez and Prof. Michael Moody.

No part of this thesis has previously been submitted for a degree at this or any other university. The work of other authors used in this thesis is acknowledged accordingly; a list of references is provided at the end of the text.

Some of the work presented in this thesis has already been published by the author or presented at conferences.

Journal publications

M Meisnar, M Moody, S Lozano-Perez. *Atom probe tomography of stress corrosion crack tips in SUS316 stainless steels*, Corros.Sci. 98 (2015) 661-671

M Meisnar, A Vilalta-Clemente, A Gholinia, M Moody, AJ Wilkinson, N Huin, et al. *Using transmission Kikuchi diffraction to study intergranular stress corrosion cracking in type 316 stainless steels*, Micron. 75 (2015) 1-10.

M Meisnar, S Lozano-Perez, M Moody, J Holland. *Low-energy EDX - A novel approach to study stress corrosion cracking in SUS304 stainless steel via scanning electron microscopy*, Micron. 66 (2014) 16-22.

S Lozano-Perez, J Dohr, **M Meisnar**, K Kruska. *SCC in PWRs: Learning from a Bottom-Up Approach*, Metallurgical and Materials Transactions E. 1 (2014) 194-210.

Conference publications

M Meisnar, S Lozano-Perez, M Moody, J Holland. Novel SEM characterization of SCC through low-keV EDX, *Proceedings of the 16th International Conference on Environmental Degradation of Materials in Nuclear Power Systems - Water Reactors* (August 2013, Asheville, NC, USA).

S Lozano-Perez, **M Meisnar**, J Dohr, K Kruska, Reviewing the internal oxidation mechanism as a plausible explanation for SCC in PWR primary water, *Proceedings of the 16th International Conference on Environmental Degradation of Materials in Nuclear Power Systems - Water Reactors* (August 2013, Asheville, NC, USA).

Conference presentations

M Meisnar, M Moody, S Lozano-Perez. High-resolution characterization of the temperature dependence of stress corrosion crack propagation in grade 316 stainless steel, ***Proceedings of the 17th International Conference on Environmental Degradation of Materials in Nuclear Power Systems - Water Reactors*** (August 2015, Ottawa, CAN) - in print

M Meisnar, A Vilalta-Clemente, A J Wilkinson, M Moody, S Lozano-Perez. Transmission Kikuchi diffraction characterization of intergranular stress corrosion cracking in grade 316 stainless steel, ***Proceedings of the 17th International Conference on Environmental Degradation of Materials in Nuclear Power Systems - Water Reactors*** (August 2015, Ottawa, CAN) - in print

M Meisnar, S Lozano-Perez, M Moody. High-resolution analytical TEM to study stress corrosion cracking in stainless steels, ***International Microscopy Congress*** (September 2014, Prague, CZ).

M Meisnar, S Lozano-Perez, M Moody. Using high-resolution analytical TEM to study stress corrosion cracking in stainless steels, ***Microscopy of Oxidation 9*** (April 2014, Nottingham, UK).

M Meisnar, S Lozano-Perez, M Moody, J Holland. Novel SEM characterization of SCC via low-keV EDX, ***Proceedings of the 16th International Conference on Environmental Degradation of Materials in Nuclear Power Systems - Water Reactors*** (August 2013, Asheville, NC, USA).

Funding

This project was funded by AREVA, France, through the Florey Areva scholarship in cooperation with The Queen's College, Oxford. Further funding was received in the form of travel grants from The Worshipful Company of Armourers and Brasiers, The Worshipful Company of Founders, the European Microscopy Society, the Institute of Materials and The Queen's College.

Acknowledgements

First and foremost, I would like to thank my advisor, Prof. Sergio Lozano-Perez, for his exceptional support. He generously provided guidance, encouragement and, most importantly, his time for discussions whenever needed. Sergio, I am particularly thankful for everything I learned from you about electron microscopy and consider myself very fortunate to have been your student!

Secondly, I would also like to address many thanks to Prof. Michael Moody and Dr. Tomas Martin, who introduced me to atom probe tomography. Without their help, I would not have been able to achieve such successful atom probe results.

I am also very grateful for all the training and help I received from the EM support team at Oxford Materials throughout the years. Special thanks shall go to Dr. Gareth Hughes, Gabriella Chapman and, although already deservedly retired, Steve Lett.

In addition, I would like to thank all of my colleagues from the Nanoanalysis Group for their support throughout my time here, in particular Dr. Arantxa Vilalta-Clemente who contributed so much to the TKD research. Likewise, I would like to thank Dr. Karen Kruska, from whom I inherited this project and who passed on many important notes and useful advice. Furthermore, although located on the other side of the world, I would like to express my gratitude to Prof. Koji Arioka from INSS (Japan) for providing samples and for valuable discussions and guidance.

Last, but not least, I would like to thank my family for their constant support. Without them it would not have been possible to achieve all of my goals. So kann es nicht weiter gehen...!

Glossary

ADF	Annular dark field
AES	Auger electron spectroscopy
AISM	Adsorption-induced slip mechanism
AIDE	Adsorption-induced dislocation emission
APT	Atom probe tomography
ASTM	American Society for Testing and Materials
ATEM	Analytical transmission electron microscope/microscopy
BF	Bright field
BWR	Boiling water reactor
CCP	Cubic closest packed
CGR	Crack growth rate
CL	Constant load
CT	Compact tension/Crack tip depending on context
CTOD	Crack tip opening displacement
CW	Cold work
DB	Deformation band
DF	Dark field
EAC	Environmentally assisted cracking
EBSD	Electron backscatter diffraction
EDX	Energy dispersive X-ray spectroscopy
EELS	Electron energy loss spectroscopy
EM	Electron microscope/microscopy
FCC	Face-centred cubic
FEG	Field emission gun
FIB	Focussed ion beam
FICM	Film-induced cleavage model
FRM	Film-rupture model
FWHM	Full width half maximum
GB	Grain boundary
GIF	Gatan image filter
HAADF	High-angle annular dark field
HAC	Hydrogen assisted cracking

HE	Hydrogen embrittlement
HELP	Hydrogen-enhanced local plasticity
HT	High tension
IG	Intergranular
IGSCC	Intergranular stress corrosion cracking
IPF	Inverse pole figure
IQ	Image quality
LEAP	Local-electrode atom probe
LWR	Light water reactor
MO	Misorientation
MSA	Multivariate statistical analysis
OI	Oxford Instruments
PWR	Pressurised water reactor
PZ	Plastic zone
ROI	Region of interest
SCC	Stress corrosion cracking
SE	Secondary electron
SFE	Stacking fault energy
SHE	Standard hydrogen electrode
SMM	Surface mobility model
SPF	Stress projection factor
SS	Stainless steel
STEM	Scanning transmission electron microscopy
TG	Transgranular
TKD	Transmission Kikuchi diffraction
ZLP	Zero loss peak

Table of Contents

1. Introduction

According to a recent World Nuclear Association report, 11.5% of the world's electricity is currently produced by nuclear reactors.[1] The production of nuclear energy is carbon emission free and hence this energy source is once again growing in prominence. This is demonstrated by the number of recent nuclear new-build projects in both developing and developed countries. In the UK alone, 16 nuclear reactors are currently in operation with a cumulative capacity of 10 gigawatts of electricity, producing 18% of the country's electricity.[2] While all but one of these reactors is to be phased out by 2023, the government has already given the green light for a new generation of nuclear reactors in the UK.

The average lifetime of a nuclear reactor is 30-40 years, but in many cases this operational period has been extended by several additional decades. For this reason, predicting the long-term performance of nuclear reactors and maximising their lifetime has long been one of the major goals of the nuclear industry. During operation, nuclear reactor components are subjected to a corrosive environment, high temperature and pressure as well as radiation. Under these conditions, even purpose-designed nuclear materials are susceptible to certain forms of degradation, which may ultimately lead to the failure of entire reactor components.

Stress corrosion cracking (SCC) is a common form of degradation of the structural materials used within nuclear reactors (e.g. stainless steels and nickel alloys). This cracking occurs, not exclusively, in the primary circuit of pressurised water reactors

[1] World Nuclear Association (July 2015), http://www.world-nuclear.org/info/Facts-and-Figures
[2] World Nuclear Association (Sept 2015), http://www.world-nuclear.org/info/Country-Profiles

(PWRs). These microscopic cracks develop due to a combination of the corrosive PWR primary water environment and the pre-existence or residual stresses within the material and serve to significantly limit the lifespan of the reactor as a whole. Although SCC was first discovered many decades ago, the exact mechanisms underlying the initiation and propagation of this cracking are still not well understood. Research in this area is increasingly reliant on a combination of high-resolution microscopy techniques and materials modelling to provide new insights and, in turn, provide the nuclear industry with reliable predictions of the lifetime of reactor components.

This thesis introduces the phenomenon of intergranular stress corrosion cracking (IGSCC) and presents the current state-of-the-art of SCC research, achieved by previous research efforts. Next, new research to improve the resolution limits of conventional microscopy techniques and make novel high-resolution methods accessible to SCC research are presented. Finally, the application of these methods to characterise the temperature dependence of IGSCC in SUS316 stainless steels is demonstrated and the results are discussed in detail.

1.1 Materials challenges in pressurised water reactors (PWRs)

The successful long-term performance of structural materials in nuclear power systems is the key to their safe and economic operation over many decades. Of the currently 438 existing nuclear reactors worldwide 277 are PWRs, some of which have been in

operation since the 1950s.[3] During their lifetime, nuclear reactor components are subjected to a highly adverse environment of high temperature and pressure, corrosion and radiation [1].

In a PWR, the energy produced by nuclear fission heats up the highly pressurised primary cooling water, which is then pumped to the steam generator where the produced steam drives a turbine, generating electricity. The PWR primary circuit consists of the reactor pressure vessel (RPV), holding the reactor core and the coolant (water), the pressuriser, the steam generator, the coolant pump and pipes running between those components to transport the pressurised water. While the fuel (uranium oxide) is clad with zirconium alloys, the majority of components in the primary loop consist of stainless steels (e.g. SUS304 and SUS316), high strength alloys (e.g. INCONEL alloy X750) and nickel alloys (e.g. Alloy 600 and Alloy 690). Carbon steels are mainly used in the secondary circuit for piping [2]. This thesis will focus entirely on stainless steels SUS304 and SUS316 that are utilised within the primary side of PWRs.

Due to the exposure of these materials to the aggressive fission reactor environment, certain structural and microstructural faults may develop. Material degradation manifests itself for instance in the form of irradiation-induced hardening, hydrogen embrittlement (HE) or stress corrosion cracking (SCC), all of which can cause the failure of entire components with catastrophic consequences. Recent operational experience, such as the Davis-Besse Nuclear Power Plant event [3], shows that SCC can have a significant impact on the plant safety [4]. During a safety inspection of the Davis-Besse nuclear power station in 2002, the regulatory authority found a football-sized

[3] IAEA PRIS database, www.iaea.org/pris

hole, caused by corrosion, in the RPV head. As a consequence, the regulatory authority imposed a large fine (over $ 5 million) and shut down the power station for almost 2 years for further inspection.

In order to ensure the safe and efficient operation of nuclear reactors, phenomena like SCC require extensive characterisation with the ultimate goal of providing accurate lifetime and performance predictions [1]. In a report from 2011, the International Atomic Energy Agency (IAEA) remarks: "Stress corrosion cracking (SCC) is one of the significant ageing degradations for major components of both pressurised water reactors (PWRs) and boiling water reactors (BWRs) and is still an important technical issue [...] As a result, significant research and development efforts have been made to determine the factors affecting [Primary Water Stress Corrosion Cracking] PWSCC" [4].

1.2 Intergranular stress corrosion cracking in PWR primary water

1.2.1 Corrosion principles

In general, metals do not occur naturally in their metallic form, but are usually processed from their ores at the expense of energy [5]. Therefore, if exposed to an environment such as air, metals tend to degrade back to their naturally occurring ore-form. As an example, pure iron exposed to air develops a film of iron oxide on the surface, also known as rust, while being transformed back into iron ore.

Corrosion is the electrochemical process, illustrated in Figure 1, in which the metal is attacked by chemically aggressive ions present in the environment through simultaneous transfer of electrons within the metal. In the case of Fe, firstly, a positively charged Fe^{n+} ion is created by the release of electrons from an area on the surface of the

metal, which is acting as an anode. This process is known as oxidation. Simultaneously, a process called reduction occurs on another part of the surface, acting as a cathode. Through the transfer of electrons within the metal, a negatively charged species is created in the solution, in this case hydroxide molecules (OH^-). The positive Fe^{n+} ion on the anodic surface of the metal can then bond with negatively charged hydroxide molecules, emitting from the cathode.

Oxidation: $Fe \rightarrow Fe^{n+} + n$ electrons

Reduction: $O_2 + 2H_2O + 4e^- \rightarrow 4OH^-$

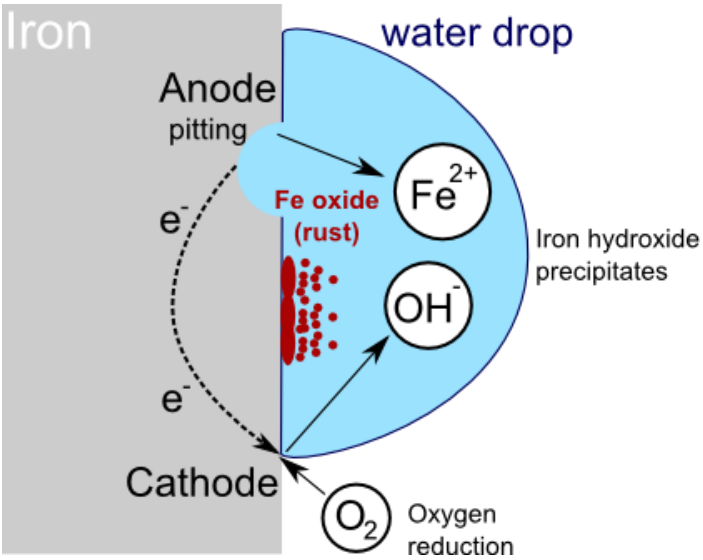

Figure 1. Illustration of the corrosion process: Oxidation at anode, reduction at cathode; Iron hydroxide precipitates and rust forms at the material surface

As long as the material is in contact with the corrosive environment, it will continue to degrade [6]. Some metals or alloys are more stable against corrosion than others, depending on their corrosion potential and the reducing power of the respective

environment. Each material reacts differently to various environments and may corrode in one but not necessarily in another [5].

The galvanic series, shown in Figure 2, is a table, which lists metals and alloys in order of their relative electrical potential (i.e. their tendency to corrode). It shows that stainless steels SUS304 and SUS316 as well as noble metals such as silver are very corrosion-resistant, whereas less noble metals or alloys such as zinc are more susceptible to corrosion. It should be emphasised that, according to the galvanic series, nickel is a much nobler metal than pure iron (not shown in Figure 2), a fact that is significant for this work.

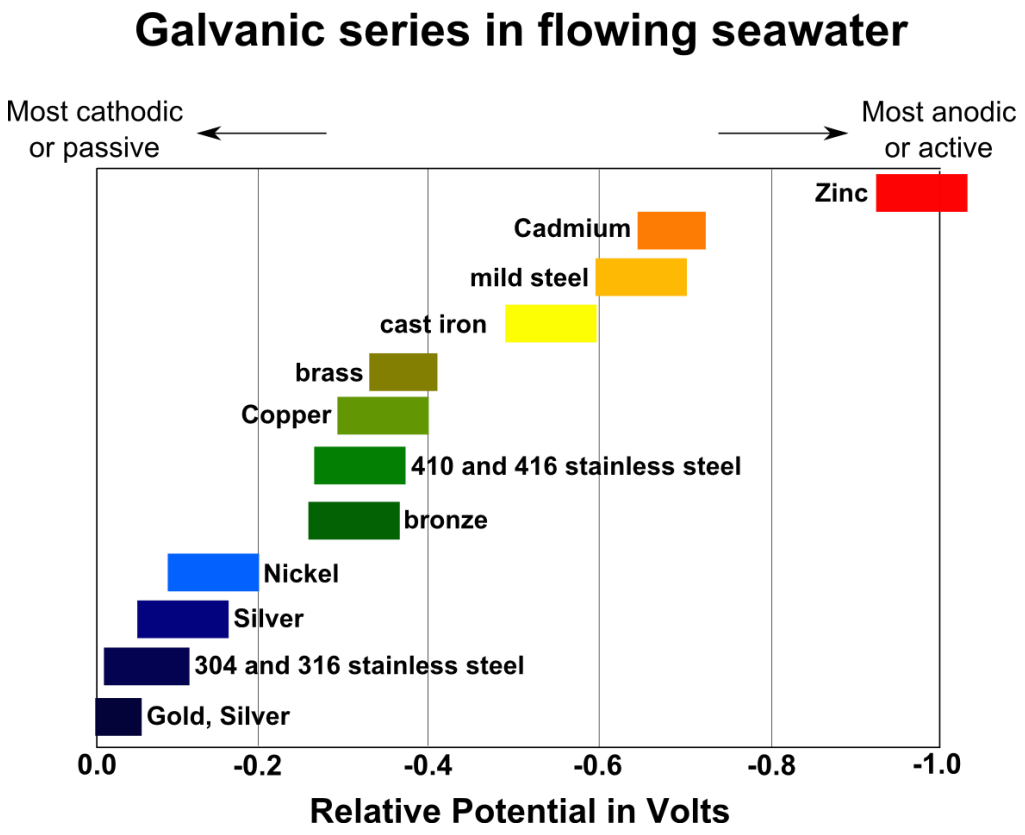

Figure 2. Galvanic series in flowing seawater, illustrating the nobility of certain metals and alloys: Zinc, cast iron and Copper are less noble than Nickel and will therefore corrode more easily; SUS304 and SUS316 are highly corrosion resistant; vertical axis: arbitrary values

Another factor influencing the corrosion susceptibility of an alloy is the pH, the power of hydrogen, which is effectively measured as the negative logarithm of the hydrogen ion concentration within a solution. The stable phases of metals or alloys in aqueous electrochemical solutions are described by the Pourbaix diagram, also known as E-pH diagram [7,8]. Similar to the well-known phase diagram, it maps out the equilibrium phases of the oxidation products as specific areas, separating the different existing oxide types via lines. Figure 3 shows the Pourbaix diagram of a typical austenitic stainless steel such as SUS304 and SUS316. The vertical axis represents E_H, the oxidation-reduction potential in Volts with reference to the standard hydrogen electrode (SHE), and the horizontal axis represents the pH. The domains of stability, as a function of potential and pH, represent the different corrosion products of the alloy (e.g. Fe_2O_3 and Cr_2FeO_4) at a given point in E_H-pH space. Pourbaix diagrams are based on corrosion thermodynamics and calculated via specific computer programs [9].

The Pourbaix diagram offers a degree of predictability for electrochemical systems as it describes the nature of the reactions on the surface of a given alloy under certain environmental conditions. Historically, in the search for the perfect PWR primary water conditions, the pH value varied between 6.9 - 7.4. At this near-neutral pH value, the only possible corrosion products, according to Figure 3, are hematite (Fe_2O_3), chromite (Cr_2FeO_4) and the spinel-type oxide Fe_2NiO_4. However, this is only one example of a Pourbaix diagram for austenitic stainless steel. The formation of certain oxide types can vary significantly depending on the alloy composition and the environment.

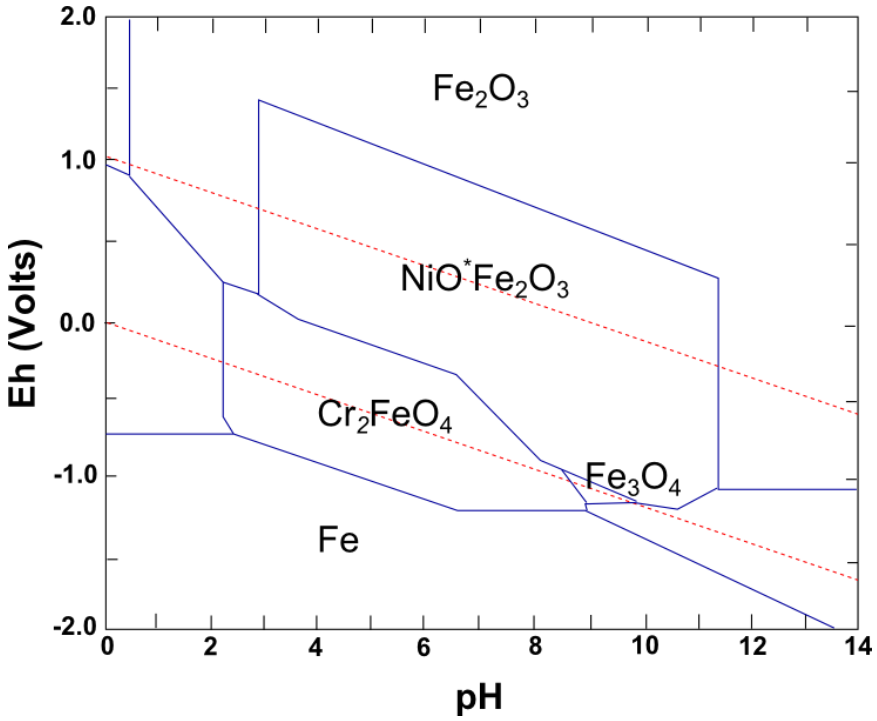

Figure 3. Pourbaix diagram of austenitic stainless steel at 300 °C: corrosion products depending on the pH separated by blue lines (almost neutral in PWR primary water) and the electrochemical potential (with reference to the standard hydrogen electrode); red lines: equilibrium potential of H_2O

1.2.2 SCC in PWR primary water

During operation, structural materials are usually exposed to at least some level of tensile, compressive or residual stress. In combination with these stresses and a specific environment, normally corrosion-resistant materials such as stainless steels are susceptible to SCC.

The failure of structural materials was first thought to be connected to the overload of ductile materials with regard to their ultimate tensile stress (UTS), the maximum stress a material can withstand before failing. Later, it was realised that repeated loading < 50% UTS can also cause failure, the so-called fatigue failure, a

process that can be accelerated by corrosion, i.e. corrosion fatigue. Finally, constant load in a corrosive environment was revealed as a source of SCC. During the following years of research, an increasing number of cases, i.e. material-environment combinations, were discovered, where SCC occurred at successively smaller loads and less aggressive environments [10].

The process of SCC in PWR primary water is generally divided into an initiation followed by a propagation phase, as described in Chapter 1.4. It strongly depends on the incidence of a susceptible alloy microstructure under tensile stress within an aqueous environment (a chemical solution in which the solvent is water, e.g. PWR primary water). The term environment includes the solution chemistry as well as other variables such as temperature and electrochemical potential [11]. All of these variables and their interdependencies combine to make SCC very difficult to understand and predict [10].

SCC generally manifests as one of two types of cracking morphology: intergranular (IGSCC) or transgranular. However, mixed modes are also possible, depending on the alloy-environment combination. In reactor grade stainless steels SUS304 and SUS316, IGSCC is the dominant fracture mode, which shall be addressed further in this thesis [12].

1.2.3 SCC in stainless steels

Stainless steel (SS) is the umbrella term for steel alloys with a minimum amount of 12 wt.% chromium (Cr). The major element of SS is iron (Fe) but it also contains other elements such as nickel (Ni) and carbon. When exposed to oxygen, a passive film of chromium oxide (Cr_2O_3) forms spontaneously on the SS surface. Due to this protective,

self-repairing oxide layer, usually no rust or 'stains' develop on the material's surface in ambient or aqueous environments [13,14]. Chromium is the main element facilitating the formation of this passive film and therefore, the higher the Cr content, the stronger the oxide and its ability to restore itself after damage. The Ni content is known to have a beneficial effect on the mechanical performance of SS, as it stabilises the austenitic phase and makes it tough and ductile. Similar to Cr, the element molybdenum (Mo) reinforces the passive oxide film and improves the resistance to localised corrosion (e.g. pitting and SCC). One of the few distinctions between the respective compositions of SUS304 and SUS316, as listed in Table 1, is the addition of Mo to SUS316, giving slightly better corrosion-properties than its SUS304 counterpart. Although the addition of carbon is known to increase the material's strength and hardness, it is often treated as unwelcome impurity in SS [15]. The formation of carbides sensitises SS and makes it susceptible to corrosion attack, especially IGSCC. Therefore, it is desirable to control the carbon content whilst in production [16].

Although the SS surface is generally protected by passivation, the Cr oxide can breakdown locally due to heterogeneities in the material, e.g. grain boundaries, inclusions, etc., or by the segregation of aggressive species to certain locations at the material surface, i.e. localised corrosion. However, in addition to the corrosive environment, a certain level of tensile stress, which can be below the macroscopic yield stress, is necessary for SCC to develop [15]. The three pre-requisites for SCC are illustrated in Figure 4.

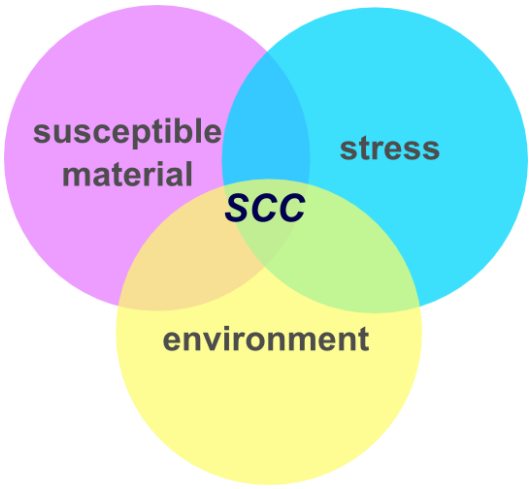

Figure 4. Necessary conditions for SCC: 1) Susceptible material such as stainless steel; 2) Stress: tensile or compressive; 3) Environment such as PWR primary water

Stainless steel undergoes SCC in a number of corrosive environments. This work mainly focuses on SCC in high-temperature, high-pressure aqueous environments such as those experienced within PWR or BWR primary water. Dissolved oxygen (in BWRs) or hydrogen (in PWRs) in high purity water facilitates the oxidation of austenitic stainless steels. It also increases the electrochemical potential, making the material more susceptible to SCC [17]. Additional cold-working of austenitic stainless steel enhances the dislocation density within the material and results in dislocation entanglement [18,19]. This increases the material's susceptibility to sensitisation and intergranular corrosion. Figure 5 illustrates some of the ongoing processes of SCC in stainless steels.

When the SS surface is exposed to an aqueous solution such as PWR primary water, a protective Cr oxide film develops, covering the unprotected areas of the material. Any applied tensile stress causes the material to locally deform, inducing dislocations as well as deformation bands. The protective oxide film can break locally due to slip or impurities such as a dislocation-rich grain boundary (or deformation band)

intersecting the material's surface. Subsequently, local metal dissolution takes place and the metal is attacked on an increasingly larger (cleavage-like) surface area.

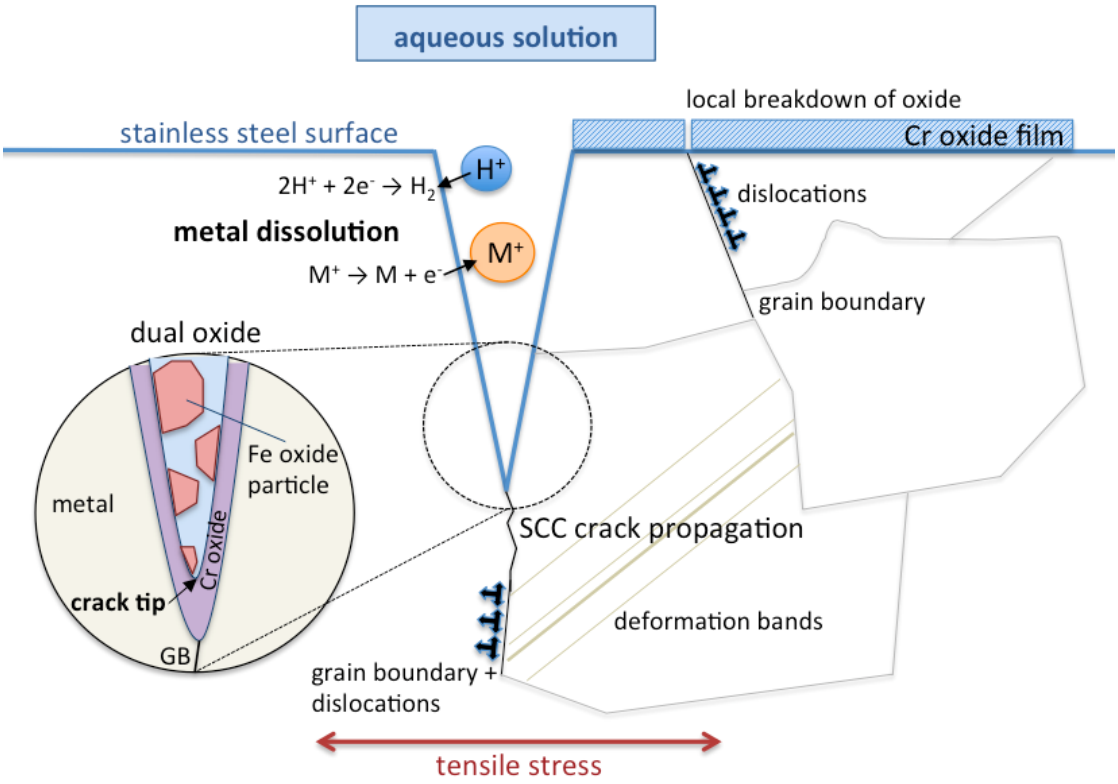

Figure 5. Illustration of SCC in stainless steels: the material is submerged in an aqueous solution; a protective oxide film of certain thickness forms on the surface; due to external stress, deformation occurs in the microstructure and the oxide film can break locally; at the crack tip, a dual oxide layer forms; dislocations accumulate at the GBs

The mechanisms underlying SCC are central to this thesis and will be discussed in detail later. However, it has been established that while metal dissolution occurs along attacked grain boundaries in SS, a dual oxide layer forms on all exposed surfaces. Dislocations and impurities along the attacked grain boundary promote the propagation of the stress corrosion crack. More details on the crack propagation process will follow in later chapters.

1.3 SCC testing

It has been established in the previous sections that some PWR components might fail after many years in operation due to SCC and other forms of degradation. As it is generally not feasible to wait for several decades to observe SCC in actual in-service reactor components, other methods for the simulation of this failure mode in a laboratory environment were developed. The general approach is to expose the stressed material to a corrosive environment over a reasonable time period and extrapolate the results to predict the long-term structural performance [20]. A multitude of standardised SCC tests have been developed and recorded by the American Society for Testing and Materials (ASTM), the International Organization for Standardization (ISO) and the National Association of Corrosion Engineers (NACE) [21-24].

In a publication from 1992, Turnbull discusses different SCC testing methods. He remarks that the relative brevity of laboratory tests compared to usual service lifetimes has to be compensated by acceleration of the test via the application of more severe mechanical stressing or more severe environments. However, the test must remain representative of the failure occurring during service [25]. Depending on the testing conditions that are to be simulated, pre-cracked or smooth (i.e. non-pre-cracked) specimens can be used for the SCC test. A smooth sample represents an initially flawless material, whereas a pre-cracked specimen simulates already existing flaws in the material [26]. For this work, only static load tests of notched, pre-cracked specimen are relevant and hence these will now be discussed in further detail.

Stress corrosion testing with pre-cracked specimens involves subjecting a fatigue pre-cracked specimen to a constant load or displacement, such as tensile stress or

bending, under simultaneous exposure to a chemical environment. In addition to initiating SCC, the objective of the test is also to investigate the conditions under which a SCC crack propagates, i.e. the crack growth rate (CGR) and the threshold stress intensity K_{ISCC} at which SCC begins to develop. Specimens in which the stress intensity factor increases with increasing crack length can be used to determine K_{ISCC}, whereas specimens, in which the stress intensity factor is independent of the crack length, can be used for studying the underlying stress corrosion mechanisms [25]. The crack growth, a key parameter for calculating the stress intensity factor, is usually measured in terms of the average crack length across the thickness of the specimen via electrical resistance using a comparator technique, also known as potential drop method, which is described in more detail in [27-29]. Further details about SCC testing of pre-cracked specimens under constant load can be retrieved from the according standardised procedures (ASTM E 1681-03, BS 6980, ISO 7539-6:2003) but will be discussed further in this text.

1.4 SCC crack initiation and crack growth

The time evolution of SCC is an important factor in the prediction of the lifetime of nuclear reactor components. The common practice is to distinguish between "initiation" and "propagation" period in the SCC process [30].

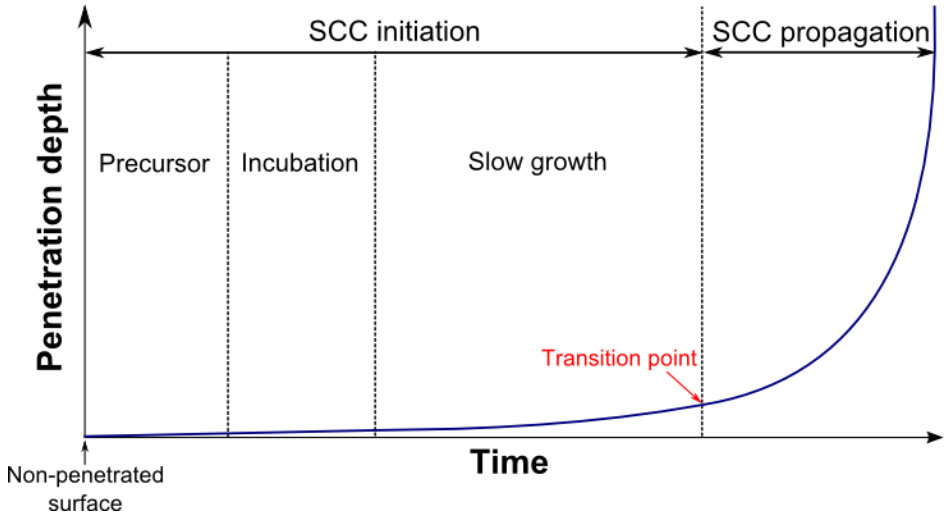

Figure 6. Definition of initiation and propagation period; SCC initiation: precursors (no SCC visible yet), incubation (first SCC segments develop), slow growth; transition: sudden rise of penetration depth; SCC propagation: IGSCC develops at certain rate

Figure 6 depicts the time-dependent SCC penetration depth of a material, divided into the initiation and propagation period of the stress corrosion crack. As time evolves, from a non-penetrated surface at time zero, the conditions for SCC are set by the precursor period in which no SCC is visible yet. In the incubation period, the first SCC segments develop, but are not visible yet. During the slow-growth phase, SCC propagates at a very low rate. A sudden rise of the penetration depth indicates the start of the SCC propagation phase in which microscopic intergranular cracks develop at a certain rate [30].

Recent work of Arioka *et al* focuses on the requirements for the transition from the incubation stage to steady SCC growth in SUS316 stainless steel. The experiments showed that slight deformation at the tip of a 50 μm pre-crack caused local stress to develop. When the local stress attained a certain critical stress, SCC growth, which is not necessarily intergranular, from the pre-crack tip to grain boundaries began [31]. The formation of cavities at the final stages of the initiation period could be the first indicator for SCC crack propagation. Initiation could be accelerated with cold work or elevated temperature leading to faster SCC growth. These interdependencies are established and discussed in more detail in further publications by Arioka *et al* [32-34].

Furthermore, Terachi *et al* studied the CGR of SUS304 and SUS316 stainless steel samples in different water chemistries and at different pre-existing stress levels. While there is no observable difference in the CGR due to the different material compositions, there seem to be significant changes in the CGR due to temperature, cold work level and mechanical properties such as yield strength and stress intensity. For example, the CGR of cold worked specimens appears to increase with increasing stress intensity or yield strength [35]. While the CGR increases with increasing temperature at lower temperatures, it exhibits a peak at ~ 320°C and decreases thereafter for higher temperatures [36-38]. The influence of the testing temperature on the CGR will be further discussed in Chapter 5.

1.5 Proposed models for SCC

First observed and discussed in the 1940s [39], SCC was soon identified as a major problem for the nuclear industry. Therefore, it has been the focus of many research groups around the world and studied extensively for many decades. Despite these efforts, there is still no theoretical model or general consensus on the governing mechanisms within the scientific community. Through experimental investigation it has been established that SCC is influenced by parameters such as alloy composition, electrochemical potential, stress, temperature, solution chemistry and pH. The fact that these parameters are not independent further exacerbates the development of a universal SCC model that quantitatively describes the underlying SCC mechanisms and provides predictions for crack propagation. A number of SCC CGR-limiting processes have also been identified: thermally activated diffusion of metallic species and oxygen, electrochemical reactions on the material surface in contact with the solution and internal response of the material to external strain (e.g. slip).

A number of models have been suggested by previous research in the literature dating back to the 1950s, most of which isolate one process treating it independently from the others. Although this approach does not consider the interactions of all processes, there is still significant insight to be gained from the developed models. This chapter will discuss the most recognised models for intergranular SCC established to date, some of which representing a potential basis for future models.

1.5.1 Film-rupture model

One of the earliest studies investigating the film-rupture model (FRM) was conducted by Logan in the 1950s [40]. He placed the model within what was called the "generalised theory of stress corrosion" at that time [39]. It describes stress corrosion as an electrochemical process along localised paths that behave anodic to the surrounding material. Logan states that the presence of additional mechanical stresses may cause the material, protected by a passive film, to tear apart locally, exposing an unprotected layer of metal. Until a new passive film forms, a small portion of the metal surface can dissolve. This concept is associated with the mechanism previously postulated by Mears *et al* in which protective films on metal surfaces are ruptured [41]. In addition, Logan describes crack bifurcations and branching as a result of crystallographic obstacles, such as non-metallic inclusion, lattice discontinuity, etc., in the anodic path. In his publication, Logan recognises the demand of data necessary to establish the validity of the film-rupture model (FRM) in the "Generalised Theory of SCC". Therefore, a number of experiments were conducted comparing the electrochemical potential of protected and unprotected metal surfaces that were known to be susceptible to SCC. It was concluded, that electrolytic action could indeed be caused by sufficiently high stresses in a corrosive environment between film-free (anodic) and filmed (cathodic) areas [40].

Later, in a publication from 1975, Scully scrutinises the understanding of crack propagation at that time. On the basis of the earlier works of Mears, Logan and others, Scully describes the sequence of events occurring at the tip of a propagating stress corrosion crack based on the FRM [42].

Figure 7 illustrates the film-rupture mechanism for SCC [42,43]. The process of crack propagation commences at a crack tip covered with a protective oxide film extending over the entire crack surface. A slip plane, located ahead of the crack tip, undergoes shear, induced by internal or external stress, and a new, unprotected surface is created. While repassivation begins at the outer edge of the new surface, the exposed metal dissolves slowly under corrosion attack. The crack propagation process depends on the rates of corrosion and repassivation. Stress corrosion cracks can only propagate if the rate of corrosion is higher than the rate of repassivation. The corrosion damage, further growth of the crack into the material, is determined by the constant charge that passes until the protective film is renewed. After that, the process reiterates [42].

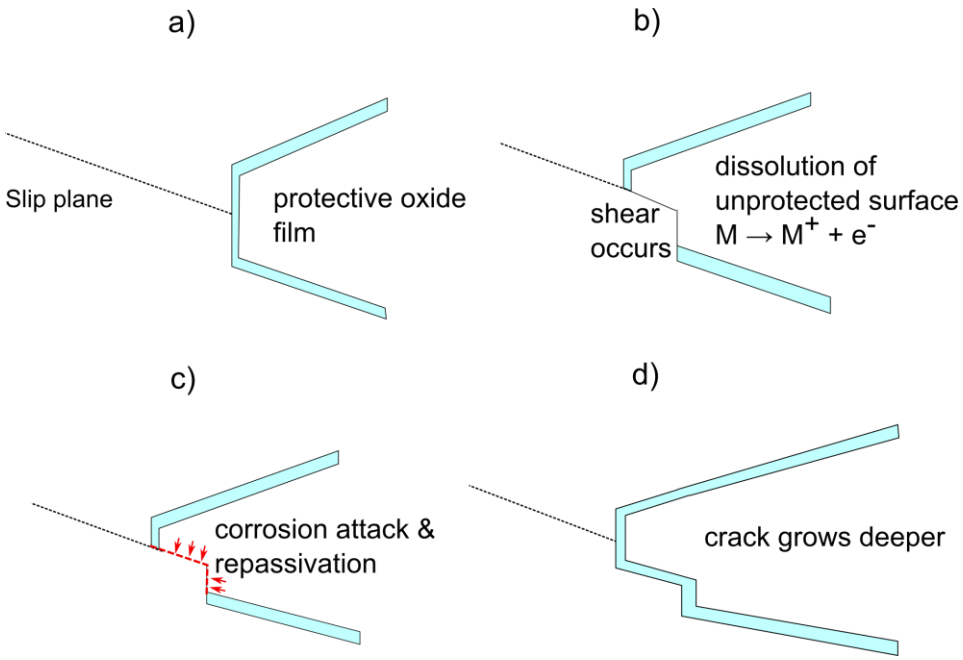

Figure 7. Schematic explaining the film-rupture model: a) The surface of a crack tip is covered with a protective oxide film; b) The slip plane undergoes shear and a new, unprotected, reactive surface is created; c) Corrosion attack occurs on the reactive surface while repassivation begins on the outer edge; d) The crack flank repassivates after the corrosion attack. Anodic dissolution and plastic deformation caused the crack to grow deeper into the material

Scully's description of the FRM is partly based on Vermilyea's previous findings, whereby strain and corrosion are considered as "mutually stimulating". While strain accelerates corrosion by periodically causing film rupture, corrosion continuously removes the most severely strain hardened material in the immediate vicinity of the crack tip [44]. This model was shown to yield good results for SUS304. Andresen and Ford confirmed this result in a publication from 1988, reviewing the quantitative formulation of the FRM [45]. By modelling environmental cracking of SUS304, the authors statistically validated the FRM for this and other materials under light water reactor (LWR) conditions.

In recent years however, the FRM has been reviewed more critically by members of the SCC community. In particular, the strain rate at the crack tip and the CGR have come under scrutiny [46-51]. While there seems to be agreement that the FRM only applies to intergranular SCC [52], two opposing approaches towards the FRM exist [50]: "continuous" (Vermilyea) and "discontinuous" (Ford, Andresen and Shoji). The discrepancy of treating the electrochemical process in discrete steps (film rupture, dissolution, repassivation) while simultaneously applying continuum mechanics to calculate strain rates by Vermilyea [44] is now considered highly controversial. Critics of this method argue that relatively large depths of corrosion are necessary to explain the plastic strain distributions ahead of the crack tip [50]. Subsequently, other researchers have made attempts to adapt the FRM and introduce new parameters, e.g. Hall introduced a variable stress intensity factor [53].

In summary, the FRM is a solid model to explain the fundamentals of SCC, especially for reactor grade SS in PWR environments. It postulates that plastic strain at

the crack tip fractures a brittle oxide film, allowing a burst of metal dissolution prior to re-establishment of the film. Nevertheless, under closer inspection utilising modern modelling techniques, significant discrepancies between the calculations and experimental results are apparent [46-48,50,51]. In his 2007 publication, Gutman concludes that experimental and analytical data so far acquired, indicate that there may be more than one mechanism involved in stress corrosion crack propagation as opposed to the FRM alone [46].

1.5.2 Surface mobility model

Probably the most controversial model for SCC is the surface mobility model (SMM). It was introduced in 1987 by Galvele [54], who disregarded both the FRM and the film-induced cleavage model, which is mainly concerned with transgranular cracking and therefore not included in this thesis. Galvele's SMM has been subject to severe criticism [55-57].

Galvele proposed a model that is based upon the idea that vacancies, moving along the crack flank towards the crack tip, allow the crack to open further (Figure 8). The model strongly depends on the surface diffusion coefficient (D_s) which itself, in aqueous environments, is a function of the surface contamination (oxides produced by the electrochemical process on the metal surface). If D_s is high enough, an atom at the crack tip can be replaced by a vacancy lowering the local stress which results in the relaxation of the lattice. Although Galvele claims an "outstanding accuracy of experimental results with the surface mobility model" [58], the study concludes with the

remark that "surface mobility remains rather vague and the application of the SCC mechanism based on it would require better definition".

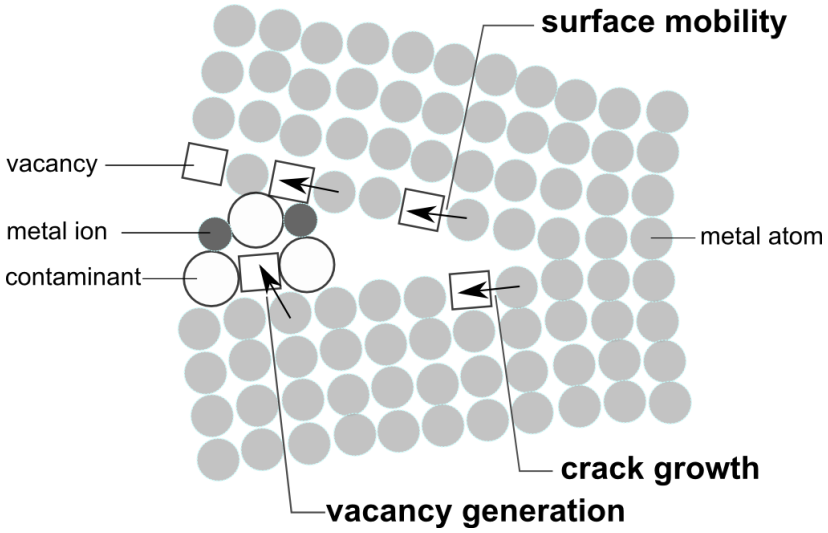

Figure 8. Crack propagation via surface mobility: every time the stressed lattice at the crack tip captures a vacancy, the crack propagates an atomic distance. The diffusion rate of the vacancies is the controlling parameter in this process. The corrosive environment increases the surface mobility by inserting contaminants that support the formation of vacancies on the metal surface.

Galvele's work was critically reviewed by Sieradzki and Friedersdorf [55], based on consideration of the thermodynamics of stressed alloys to elucidate serious errors in the SMM. They claim that the model overestimates SCC velocities in ductile fcc metals by about 14 orders of magnitude. After highlighting the errors of Galvele's original establishment of the SMM and reformulating the mechanism, Sieradzki and Friedersdorf conclude that SCC crack propagation via surface mobility can in principle occur, however, other modes of cracking (e.g. anodic dissolution, film-induced cleavage) are usually more dominant [55]. Ten years later, Gutman declared that the SMM "contains inner contradictions and mutually excluding statements" [56]. He promotes the approach

of dividing the stress corrosion process into separate phenomena acting at the crack tip, hence determining the underlying SCC mechanisms.

1.5.3 Hydrogen adsorption

First described in 1875, hydrogen embrittlement remains a wide-ranging phenomenon that causes metals to become brittle and facture. Hydrogen embrittlement (HE) is caused by the unintentional introduction of hydrogen into the metal, either in solution or in a gaseous state, which can lead to hydrogen assisted cracking (HAC). Studied intensely by Troiano in the 1960s [59] and Beachem [60] in the 1970s, it was found that HE is observed to increase at higher temperatures and slower strain rates.

In 1988, Lynch proposed the adsorption-induced slip mechanism (AISM), which was later termed adsorption-induced dislocation emission (AIDE). The author proposes that environmentally assisted cracking (EAC), including SCC, is caused by the fact that adsorption of hydrogen facilitates the injection of dislocations at the crack tip, promoting the coalescence of cracks with voids ahead of cracks [61]. In this model, hydrogen atoms are adsorbed near the crack surfaces after dissociation of gaseous or liquid hydrogen molecules (e.g. water) due to electrochemical reactions in the environment. As a result, weaker inter-atomic bonds cause dislocations and high strains (shear movement) to form in the crack tip region. Finally, the crack propagates (cleavage-like) by the growing and coalescing of micro-voids at the crack tip (Figure 9).

a)

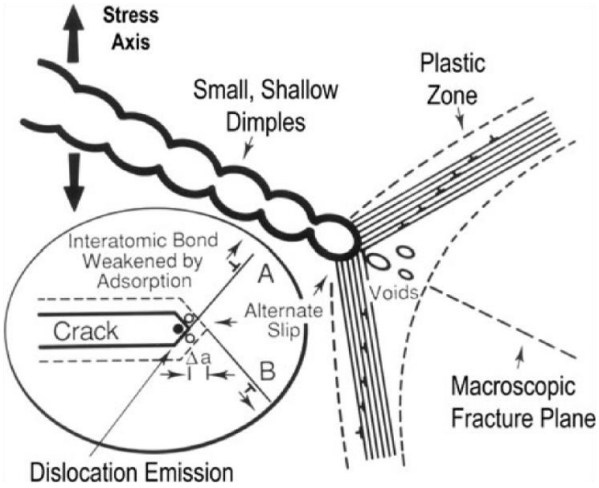

b)

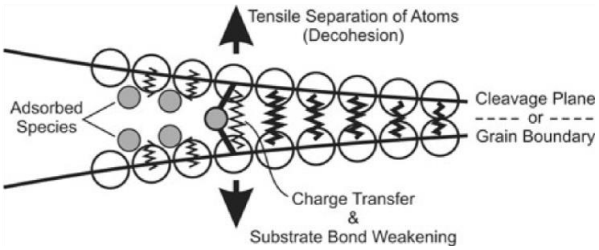

Figure 9. Schematic diagram illustrating crack propagation by hydrogen adsorption [62]: a) adsorption-induced dislocation emission due to the weakening of atomic bonds; b) the adsorbed species (hydrogen) weakens the interatomic bonds at the crack tip, leading to dislocation emission. Micro-voids nucleate and coalesce ahead of the crack tip until the crack opens up further; *Reprinted from Metallic Material Trans A Phys Metall Mat Sci, Vol. 44, Lynch et al, Mechanisms and kinetics of environmentally assisted cracking: Current status, issues, and suggestions for further work, pp. 1209-1229, Copyright (2013), with permission from Elsevier*

Lynch bases his hypothesis merely on the study of fracture planes and directions, the detailed fracture-surface appearance and the distribution of slip around crack tips. He also notes that in some systems adsorption is not responsible for HAC or SCC in which case he supports the FRM [61].

Important work on hydrogen embrittlement, the effects of hydrogen on specific materials and the interaction of hydrogen with dislocations was conducted by Birnbaum *et al* in the 1980s and 1990s [63-70]. In 1994, the researchers review the mechanisms of hydrogen-related fracture and evaluate the stress-induced hydride formation, decohesion and hydrogen-enhanced local plasticity (HELP) [68]. They conclude their study of HELP, which is based on the idea that hydrogen reduces the misfit energy and therefore the resistance to shear slip with the result of enhanced deformations of the crack tip, pointing out that the evidence for HELP is strong but not entirely conclusive.

In 2008 Liu proposed a similar mechanism based on HELP, aiming to introduce "A unified model of environment-induced cracking" [71]. Lynch criticises this model [72] on the basis that Liu did not acknowledge his previous work properly. In his most recent publication [62], Lynch discusses current EAC mechanisms, SCC and HE amongst others, and remarks that evidence to date suggests that adsorption-based mechanisms, involving weakening of substrate interatomic bonds so that dislocation emission or decohesion is facilitated, accounts for embrittlement in many systems.

In conclusion, it appears that the proposed adsorption-based mechanisms are not universal and other mechanisms based on dissolution may also be present. The mechanisms of hydrogen-assisted cracking are undoubtedly different for different fracture modes, depending on material properties and testing conditions. It is also evident that rate-controlling mechanisms for EAC, specifically SCC, are not well established yet. Lynch remarks in his most recent publication that in some systems adsorption kinetics is probably rate-controlling, while in other systems, depending on the fracture mode, anodic or cathodic reactions might be the rate-controlling processes [62].

1.5.4 Internal oxidation

The concept of internal oxidation as a possible cause of SCC was first published by Scott and Le Calvar in 1993 [73], trying to establish an alternative hypothesis for SCC in the nickel-based Alloy 600. In this publication, internal oxidation is defined as the corrosion/oxidation of the less noble minor alloying element(s) in the material, while the main solvent remains untouched. This phenomenon is particularly relevant for Alloy 600 (with high Ni and low Fe and Cr content) because internal oxidation is highly favoured in the case that the major element does not oxidise significantly. Scott and Le Calvar concluded that their model explains all the known thermodynamic and kinetic trends of stress corrosion crack propagation and the crack propagation rate in nickel-based alloys, especially for high temperatures (300 - 400°C). These results were validated by Rebak in 1996 [74].

Subsequent works in this area appear to expand upon this initial concept of internal oxidation to the point that there is no general consensus of its scope today. Some scientists define grain boundary oxidation in SS, including the formation of Fe and Cr oxides as major alloying elements in the material, within the framework of internal oxidation [75], a concept other researchers disagree with [76,77]. While the concept of internal oxidation as a source of SCC is indeed valid, its scope and the effects on specific materials need to be re-established.

1.5.5 Summary

Over the last 60 years, a variety of SCC mechanisms have been proposed, explaining SCC crack propagation based on electrochemistry (anodic dissolution, film formation at crack tips), diffusion (transport of vacancies at the material's surface), hydrogen adsorption or internal oxidation. However, no single mechanism has been accepted as the "universal mechanism of SCC". In contrast, most scientists currently working on SCC believe that a number of different mechanisms are involved in the overall process of crack propagation [42,46,62]. It is now widely accepted that the development of SCC depends on the material's properties, some of which can be identified by the crack (tip) morphology and fracture geometry. Others can only be determined by studying the crack tip chemistry and plastic deformation around the crack tip. A number of material-environment combinations susceptible to SCC have been investigated and recorded [78,79].

In conclusion, further investigations need to be undertaken for selected materials, taking into account all possibly involved mechanisms, in order to explain SCC for specific systems. High-resolution microscopy techniques, e.g. transmission electron microscopy (TEM) and atom probe tomography (APT), enable studies of the crack tip on an atomic or nanoscale, providing novel information about its chemistry and elemental composition. Evidently, continued progress of these microscopy techniques is the foundation for current and future SCC studies. This thesis describes such efforts of the author to improve the accessibility of high-resolution techniques for SCC research and presents a study of the temperature dependence of the SCC crack growth rate.

1.6 SCC research - state of the art

Our understanding of SCC has developed significantly throughout the past decades. Constant improvement of (electron) microscopy techniques as well as computer modelling appears to be the key to the continued progress in SCC research. Enormous research efforts over many years have led to important insights into the distinct features involved with SCC and its underlying mechanisms. The current "state of the art" will be discussed in this section, referencing many previous studies in this area undertaken by different authors. As the focus of this section is upon features that will be discussed later in this thesis with regard to its original research, no claim of completeness is made.

1.6.1 Crack morphology

During a constant load stress corrosion test using a fatigue pre-cracked compact tension (CT) specimen, a crack develops originating in the vicinity of the pre-crack tip. In samples rolled in T-S direction, the SCC crack usually bifurcates in close proximity to the pre-crack, splitting into two paths that are at an angle of ~ 120° [35], also shown in Figure 21. In addition, in the case of intergranular SCC, bifurcations can be observed when the crack encounters multiple grain boundaries, which it could potentially propagate along. As a result, the crack may split into multiple paths or just propagate along one of the grain boundaries. The reason, why SCC cracks propagate along certain grain boundaries rather than others has not been established yet. One possible answer could lie within the crystallographic misorientation between two adjacent grains, also known as grain boundary misorientation (discussed further in Chapter 4.2.2). It has been observed that there may be a connection between specific grain boundary (GB)

parameters (e.g. Schmid and Taylor factor) and the SCC susceptibility of certain GBs [80]. For instance, it was suggested that increasing GB inclination and decreasing Schmid factor (explained in Chapter 2.2.3) lead to the highest normal stress on the GB, making it more susceptible to cracking. In addition, data suggest that cracking is more likely along GBs, which exhibit discontinuous slip. The influence of slip transfer and GB misorientation on SCC will be discussed in detail in Chapter 4.2.

A primary, dominant or active crack is known to grow throughout the entire length of the SCC test as a result of the applied stress and the corrosive environment. The tip of such a crack was exposed to high stresses throughout the test and the open volume near the crack tip did not have enough time to fill with Fe-rich oxide (in the case of SUS316 and SUS304) before the SCC test was stopped. Therefore, only limited oxidation could develop at the crack tip. In contrast, a secondary crack might have been dominant at some point during the test but its advance was arrested before the end of the SCC test. Exposed to lower stresses and the corrosive environment for a longer period of time, secondary cracks are often found near triple points and filled with oxide [81].

Fracture mechanics distinguishes between three modes of cracking: Mode I (opening ↔ cleavage), Mode II (sliding ↔ slip) and Mode III (tearing ↔ torsion) [82]. While Mode I corresponds to cleavage-like crack propagation, Mode II resembles crack propagation due to the activation of certain slip systems within the crystal. During intergranular SCC crack propagation under constant load one or a combination of Mode I and Mode II are involved. A key objective of the SCC characterisation described in this work is the identification of the mode of cracking, which will be discussed further in detail in Chapter 5.3.1.

1.6.2 Oxide chemistry

The process of SCC in SS is inherently accompanied by the formation of oxides at the crack tip, crack flanks and, in some cases, grain boundary (GB) oxidation ahead of the crack tip. Many studies of the formation of these oxide structures have been previously conducted. These mainly concern the location, oxide chemistry and the orientation relationship between oxide and surrounding matrix.

It has been established that a typical stress corrosion crack, growing in reactor grade SS, such as SUS316 and SUS304, tested under PWR primary water conditions, appears as shown in Figure 10 [81,83-91].

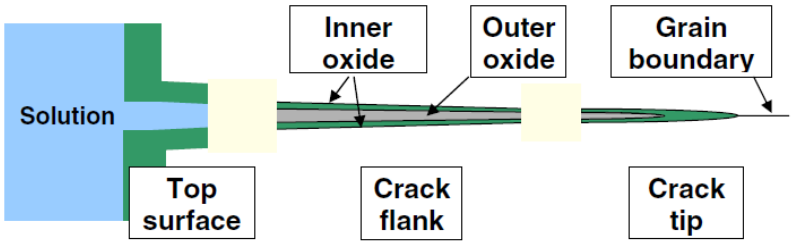

Figure 10. Basic schematic of the oxide chemistry of a stress corrosion crack in reactor grade stainless steel; *Reprinted from Journal of Nuclear Materials, Vol. 374, Lozano-Perez et al, High-resolution imaging of complex crack chemistry in reactor steels by NanoSIMS, pp. 61-68, Copyright (2008), with permission from Elsevier*

As the solution is in contact with the surface of the material, a layer of protective surface oxide forms on all exposed parts of the metal. Further down the open crack, a dual oxide layer is present. It consists of an outer oxide layer (in contact with the solution), which has been established to be either crystalline Fe oxide (Fe_3O_4 - magnetite) or a Fe-rich spinel-type oxide, $(Fe_2M)O_4$ (where M is Cr or Ni). An inner oxide layer has been observed at the oxide-metal interface and determined as a Cr-rich,

Fe-depleted spinel oxide. Although it is often defined in the literature as $(FeCr_2)O_4$, measurements indicate that the exact composition of many inner oxides deviates slightly from this stoichiometry. This is also the case for some of the results highlighted in this thesis and will be discussed further in Chapter 5.3.2. The surface oxide has a similar dual-layer structure and its thickness increases with increasing test temperature [92-94]. The growth of oxide layers in simulated PWR environments remained a controversial topic until Stellwag published a comprehensive study, including methods such as SEM, TEM, AES and Mößbauer spectroscopy, asserting that the outer layer forms due to the precipitation of metal ions released from the metal surface or the solution. In contrast, the inner Cr-rich spinel oxide seems to grow as a result of the passivation reaction in the corrosive environment and significantly increases the corrosion resistance of the alloy [95,96].

X-ray diffraction profiles of a stress corrosion crack in a SUS316 stainless steel sample, acquired by Terachi *et al*, show a dual oxide that consists of an outer layer of Fe_3O_4 (magnetite) and an inner layer of $(FeCr_2)O_4$, the thermodynamically most stable corrosion products for SUS316 in PWR primary water [85]. Cross-sectional TEM analysis was also applied in the same study and confirmed the double layer structure for both surface oxides and oxides formed inside SCC cracks (Figure 11). The authors found that the outer layer consists of single-crystal particles, whereas the inner Cr-rich spinel oxide contains many fine polycrystalline grains, as illustrated in Figure 11a.

The results published by Terachi *et al* are in agreement with the findings of other authors [81,88,91,97-100]. Figure 12 shows the efforts of Lozano-Perez *et al* to

characterise the oxides formed in an open SCC crack via NanoSIMS. Both outer crystalline Fe-rich particles and an inner Cr-rich spinel-type oxide were identified [90].

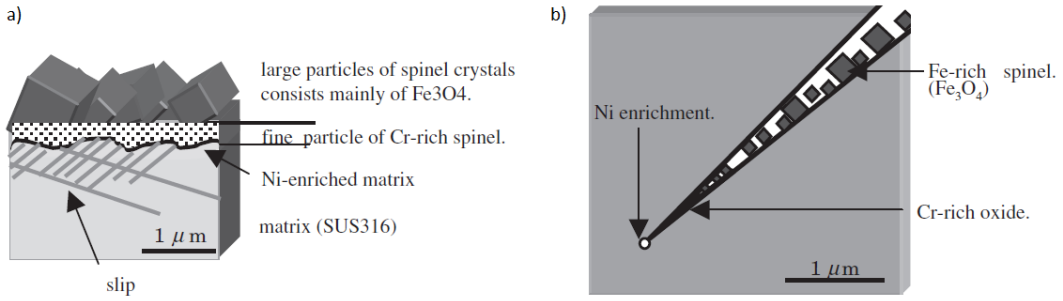

Figure 11. a) Schematic of dual oxide layer formed on the surface of an SUS316 stainless steel specimen exposed to simulated PWR primary water; b) Schematic of SCC crack tip and the oxide layers formed on the surface of the open crack; Ni enrichment is pointed out ahead of the crack tip [85]; *Reprinted from Journal of Nuclear Science and Technology, Vol. 42, Terachi et al, Microstructural characterization of SCC crack tip and oxide film for SUS 316 stainless steel in simulated PWR primary water at 320°C, pp. 225-232, Copyright (2005), with permission from Elsevier*

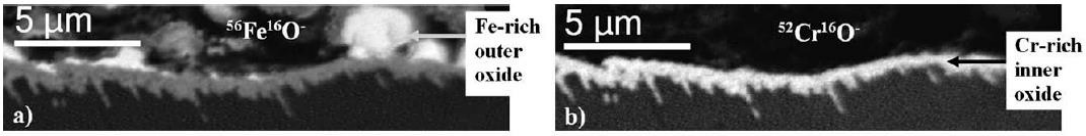

Figure 12. NanoSIMS maps showing the dual oxide in a SUS304 stainless steel sample [90]: a) coarse grained outer Fe-oxide layer; b) fine grained inner Cr-oxide layer; *Reprinted from Acta Materialia, Vol. 57, Lozano-Perez et al, Multi-scale characterization of stress corrosion cracking of cold-worked stainless steels and the influence of Cr content, pp. 5361-5381, Copyright (2009), with permission from Elsevier*

In the course of their atom probe characterisation of surface oxides and grain boundary oxidation, Kruska *et al* found that a stoichiometric spinel oxide such as the outer Fe-rich spinel, $(M_yFe_{1-y})_3O_4$ with y ~ 0.7, and the inner Cr-rich spinel, $(Fe_xCr_{1-x})_3O_4$ with x ~ 2/3, usually consists of 57.1% oxygen and 42.9% metal. In addition, these

researchers discuss in the same publication that due to their high dislocation density, GBs appear to be fast-diffusion paths for a number of metallic and non-metallic species and therefore show enhanced oxidation. This concept of internal oxidation has already been discussed in Chapter 1.5.4. Some researchers believe that the internal oxidation of GBs may be one of the most plausible proposals in the search for the underlying SCC mechanisms [73,101]. However, the complex geometry and small dimensions of grain boundaries have so far impeded the exact establishment of the grain boundary oxide chemistry [100].

Intergranular corrosion, i.e. GB oxidation, in SS has been reported to appear mainly in connection with the sensitisation of grain boundaries. The term sensitisation refers to the depletion of Cr at grain boundaries, making them weaker and therefore more susceptible to intergranular attack. While some austenitic SS alloys have been reported to show intergranular attack [102], reactor grade stainless steels SUS304 and SUS316 have a high enough Cr content (16-18% Cr) to withstand sensitisation and hence intergranular corrosion [103]. In general, GB oxidation has not been observed for these two alloys in the absence of external stresses or deformation. Nevertheless, first hints towards grain boundary oxidation, in the form of weakly linked oxide structures located at grain boundaries, in cold-worked SUS304 were found in regions of high defect density via atom probe tomography (APT) and electron-energy loss spectroscopy (EELS) by Kruska *et al* [100]. The results suggest that the stoichiometry of the GB oxide spinel is similar to $Fe_{1-x}Ni_xCr_2O_4$ with $x\sim1/3$. As weak regions, such as oxidised GBs, enhance the SCC susceptibility of the alloy, more information on their structure and chemistry is necessary. Within the framework of this thesis, GB oxidation

immediately ahead of the SCC crack tip has been investigated, revealing new insights into the oxide chemistry in this region. For more details see Chapter 4.3.

1.6.3 Crack tip chemistry

Historically, it has been a challenge to precisely determine the crack tip chemistry due to its very small dimensions, often in the range of a few nanometres. In the last decade, with the advent of analytical TEM and the ongoing improvement in achievable spatial resolution, first studies of the crack tip chemistry have been made possible. However, due to the 2D nature of the technique, the TEM results actually represent projections of a 3D volume over the entire sample thickness and are therefore slightly obscured. Only with the relatively recent establishment of atom probe tomography (APT) in this field the true aspect and nature of oxidation at the crack tip began to be revealed. In particular, the quantification of very small oxide structures is only reliable via APT (for more details see Chapter 4.3).

In Terachi's TEM study of the oxide chemistry in SCC cracks, substantial Ni enrichment was observed ahead of the crack tip [85]. This phenomenon has subsequently been detected by other research groups as well [35,88,100]. Nickel is the noblest element under PWR conditions in comparison with the other main matrix constituents of SUS304 and SUS316: Cr and Fe. Nickel typically remains metallic when not directly exposed to the corrosive environment and diffuses through the crystal away from any newly oxidised regions. As a result, Ni enrichment is often observed behind the oxide-metal interface of SCC cracks or ahead of the oxidation front of SCC crack tips.

In a comprehensive study of a SCC crack tip in an SUS304 stainless steel sample, tested under simulated PWR primary water conditions, Lozano-Perez *et al* compared EELS elemental maps of O, Fe, Cr and Ni, respectively, in order to understand the crack tip chemistry (Figure 13).

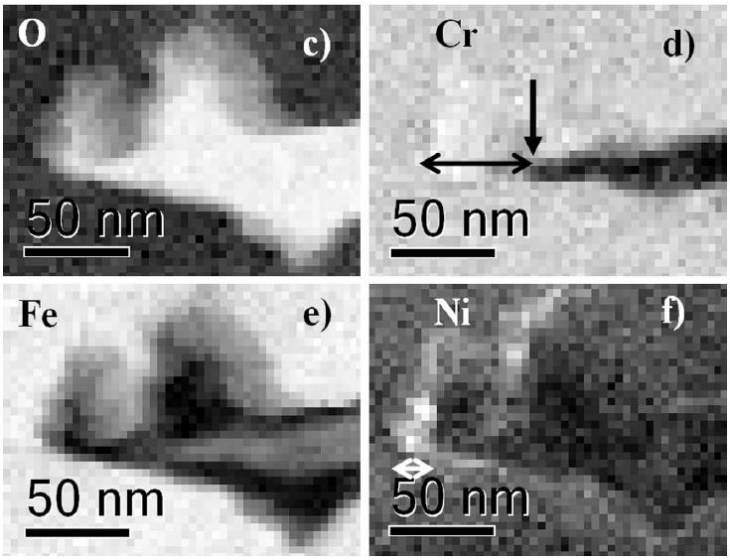

Figure 13. EELS elemental maps of crack tip region [90]: c) O map; d) Cr map: vertical arrow indicates crack tip, horizontal arrow indicates width of Cr oxide; e) Fe map; f) Ni map: Ni enrichment indicated with white arrow (~ 10 nm); *Reprinted from Acta Materialia, Vol. 57, Lozano-Perez et al, Multi-scale characterization of stress corrosion cracking of cold-worked stainless steels and the influence of Cr content, pp. 5361-5381, Copyright (2009), with permission from Elsevier*

While the O map shows the extent of the oxidised region near the crack tip (Figure 13c), the Cr map (Figure 13d) shows the actual location of the crack tip (indicated with the black arrow). Neither Cr enrichment nor Cr depletion inside the crack tip oxide were observed in this work (although it is known that usually inner oxides in regions of higher stresses/deformation tend to also be richer in Cr, indicating Cr diffusion towards higher stress gradients). The Fe map (Figure 13e) indicates an outer

Fe-rich (probably spinel-type) oxide and Fe depletion of the inner Cr spinel-type oxide. The elemental Ni map (Figure 13f) shows Ni enrichment ahead of the oxidation front (indicated with white arrows, width ~ 10 nm) [90].

The hypothesis of Ni enrichment being a result of the selective oxidation of certain metallic species has been established based on the findings of Terachi *et al* and other research groups [36,37,76,81,85,90]. While Fe and Cr oxides form easily on free surfaces, Ni tends to reject the oxide. In addition, there seems to be a difference in the diffusion rates of the three matrix elements, with Ni exhibiting the slowest (substitutional) diffusion rate. This could be another reason for the accumulation of Ni at the metal-oxide interface or ahead of oxidised crack tips [85].

On multiple occasions, the origin of the Fe surplus in the outer oxide as well as the Ni surplus at crack flanks and the crack tip has been discussed. While the diffusion of metallic species in the matured crack seems to occur mainly through the metal-oxide interface, it has been established that the main diffusion path for O and all matrix elements at the crack tip is the GB (as discussed further in Chapter 4.3.3). This may lead to enhanced GB oxidation, as explained before, and also to diffusion of metallic species through the GB. Both Fe and Cr have been observed to diffuse from the matrix towards the crack tip, whereas Ni tends to move into the other direction away from forming oxide structures. The authors' own observations of this phenomenon will be shown in Chapters 5.3.2 and 5.3.3.

1.6.4 Plastic deformation near the crack tip

External stresses imposed on ductile materials such as austenitic stainless steels are clearly visible in the microstructure as slip, twinning or deformation bands (for details see Chapter 2.2). Under increasing stress, the material deforms first elastically and then plastically for as long as dislocation mobility allows for slip and other deformation modes to occur. In an SCC specimen, the plastic strain is usually concentrated around the crack tips in the sample enabling further crack propagation. Nevertheless, there may be also other regions in the sample with high stress concentration. It has been suggested, that the rate of crack propagation might be dependent on the level and extent of the so-called "plastic zone" around the crack tip [104]. However, the measurement of the plastic zone has proven to be very difficult and a mere "fracture mechanics approach" based on the crack tip opening displacement (CTOD) is insufficient. The attempt to use a novel technique to measure the plastic zone and quantify plastic deformation around crack tip is a core topic of this thesis and will be discussed further in Chapter 4.2.

1.6.5 Influence of cold work

Cold working or work hardening is the process of strengthening a material by deliberately introducing changes in the microstructure through the application of external stresses. During this process, a high number of dislocations are generated within the material (e.g. point defects as well as slip and deformation bands), eventually preventing new dislocations from nucleating and plastic deformation from occurring; hence the material has become harder.

Researchers discovered that cold working of SS results in changes in the grain shape as well as the grain orientation [90]. There are many ways to cold work a material but SCC samples to be tested under simulated PWR primary water conditions are usually rolled to a reduction in thickness at room temperature (hence the term cold work). Cold-rolling to a 20% reduction in thickness, for example, is called 20% cold work. Although it is well known that cold work modifies the mechanical properties of materials and many investigations on this topic have been published, the exact impact on crack growth and SCC susceptibility is not fully established yet [83,85,90,105,106]. However, it was recently discovered that remarkable differences in the crack growth rate exist between the T-S and T-L rolling direction. Crack growth parallel to rolling direction (T-L) seemed accelerated compared to IGSCC perpendicular to rolling direction (T-S) [107].

The influence of cold work on the microstructure of SS is well documented. In the 1980s, cold work was found to be beneficial for long-term corrosion resistance in SUS304 [108,109]. Langevoort *et al* established that cold work does not alter the oxidation mechanisms or oxide compositions but affects the diffusion rates through the oxide and the metal. Due to the increased dislocation density, the oxidation rates seemed enhanced. In addition, researchers found that due to the increasing proportion of high-angle sub-boundaries and the development of faster diffusion paths, cold work changes the GB diffusion rates of the alloy constituents [90,105,110]. In support of this theory, Arioka *et al* found that cold working slightly increases the thickness of surface oxides under PWR primary water conditions [111]. In addition, Kruska *et al* established that the depth of oxidation also depends on the cold work level and external stresses applied. It

was found that the deepest oxidation depths occur for materials under heavy load and 20% cold work (the highest in this study) [106,112]. Furthermore, an increase in the CGR with increasing cold work level has been observed and reported for SS under PWR conditions in various publications [35,111,113-115].

1.6.6 Oxidised deformation bands

It has been established, that during cold working prior to the SCC test, dislocations are introduced into the material. As dislocations move through the crystal they may pile up at different glide planes, which can lead to the nucleation of deformation bands (DBs) on sub-boundaries in the grains (with up to 20° misorientation); further explained in Chapter 2.2.5. According to recent studies, rising levels of cold work entail an increased density of DBs [90]. Etching of the sample cross-section with colloidal silica suspension after the polishing process increases the contrast of microstructural features in the microscope. As a result, features such as slip and deformation bands can be observed [81]. Lozano-Perez *et al* examined oxidised DBs via NanoSIMS and TEM and found that a Cr-rich oxide can form along these deformation bands. Detailed characterisation via micro-diffraction revealed that the oxides formed at the attacked DBs match the common $FeCr_2O_4$ spinel structure [90]. Furthermore, Lozano-Perez *et al* report that DBs parallel to the applied stress direction and perpendicular to the open crack appear to oxidise preferentially.

1.6.7 Influence of water chemistry

Boiling water reactors (BWRs) and pressurised water reactors (PWRs) differ in the chemical composition of their primary water, i.e. the concentration of dissolved hydrogen. Studies of increased Cr content in both oxygenated (BWR) and hydrogenated (PWR) water by Arioka *et al* showed increasing thickness of the Cr oxide layer only for the PWR environment. Therefore, it was concluded that the oxidation mechanism was indeed affected by the water chemistry [83]. In a study conducted by Terachi *et al*, the oxidation of SUS316 in hydrogenated water and the influence of small variations (e.g. boric acid additions) in the water chemistry were examined. This research found that changes in the water chemistry did not affect the structure of the double-layered oxide film but did affect its thickness. The film thickness appeared to increase with increasing amounts of dissolved hydrogen and decreasing boric acid [84]. This is consistent with the basic corrosion theory predicting increased iron release with rising levels of dissolved hydrogen [90].

1.6.8 Influence of Cr content

In a different study, Arioka *et al* showed that the Cr concentration also influences the CGR in austenitic SS under PWR primary water conditions. In particular, increasing Cr content seems to lead to decreasing IGSCC crack growth rates [107]. In order to reveal the influence of the Cr concentration on the oxide formation and IGSCC, Lozano-Perez *et al* investigated the difference between SUS304 (18.2 wt.% Cr) and a modified SUS304-like (15 wt.% Cr) SS sample [90]. The results showed that the oxidised portion of the GB ahead of the crack tip is longer in the 15% Cr sample. Nickel enrichment at

the GB extended to a length of 100 nm in the 15% Cr sample compared to 20 nm in the SUS304 alloy. Similar observations were made by analysing several crack tip regions in comparable orientation with respect to the straining direction and depth within the sample. Lozano-Perez *et al* suggest that the different behaviour between the alloys might be due to the lower Cr availability in the 15% Cr sample, delaying the formation of a protective Cr oxide layer and therefore leading to more extensive corrosion attack. Furthermore, the observations did not show any obvious effects of the Cr content on the deformed microstructure in terms of grain size, shape and density of deformation bands [90].

2. Material

2.1 SUS316 and SUS304-12Cr

The material studied in this thesis is austenitic stainless steel. Firstly, type SUS316, commonly found in the primary circuit of PWRs, was used for the study of the temperature dependence of the crack growth rate presented in Chapter 5. It was also used for the development and application of transmission Kikuchi diffraction (TKD) and atom probe tomography (APT) techniques in Chapters 4.2 and 4.3, respectively. Secondly, a SUS304-like sample with low Cr content of 12% was the focus of the low-energy SEM-EDX study in Chapter 4.1. Due to the lower Cr content, the oxidation rates were enhanced in this sample, which was ideal for the study of crack flank and crack tip oxides as well as oxidised deformation bands via low-keV SEM-EDX.

The SUS316 samples, provided by INSS (Japan), as well as the SUS304-12Cr sample were tested under PWR primary water conditions until SCC occurred. The material compositions are listed in Table 1.

Alloy	Fe	Cr	Ni	C	Si	Mo	Mn	P	S
316INSS	Bal.	16.54	10.00	0.047	0.045	2.07	1.42	0.024	0.001
304-12Cr	Bal.	12.00	10.00	0.06	0.5	-	1.5	<0.025	<0.001

Table 1. Chemical content of 316INSS and SUS304-12Cr with lower Cr content (wt.%)

Four SCC specimens (SUS316 INSS - 316INSS), tested at temperatures of 320°C, 340°C, 350°C and 360°C, respectively, by the Institute of Nuclear Safety System

(INSS) in Japan, have been the focus of a study investigating the temperature dependence of SCC in SS (Chapter 5); SCC test details are given in Table 2. Comparing key features, i.e. crack path and morphology, elemental distribution, crack tip chemistry, plastic deformation, in these specimens via a variety of electron microscopy methods, has offered some insight into the CGR changes at higher temperatures. Furthermore, the same samples were used for the transmission Kikuchi diffraction (Chapter 4.2) and atom probe tomography (Chapter 4.3) studies presented in this thesis. Prior to autoclave testing, the specimens underwent solution treatment followed by water quenching and uni-directional cold-rolling to a thickness reduction of 20%. The SCC test was performed at the INSS laboratories using a pre-cracked ½ CT specimen in the T-S direction in an autoclave under constant load (30 MPa $m^{1/2}$). The four samples were exposed to a testing environment of simulated PWR primary water chemistry (hydrogenated water: 500 ppm B + 2 ppm Li, + 30 cm^3-STP/kg-H_2O DH_2) for 720.5 hours at 340°C, 350°C and 360°C and 1003.9 hours at 320°C. All samples exhibited SCC by the time the test was concluded. More information about the standard methods for SCC testing can be found in Chapter 1.3 and on the ASTM website (www.astm.org).

Name	**Cold work [%]**	**Test temperature [°C]**	**Test duration [h]**	**Stress intensity factor (start) [MPa√m]**	**Yield strength [N/mm²]**
SUS316-O	20	360	720.5	30.2	570
SUS316-N	20	350	720.5	29.8	571
SUS316-M	20	340	720.5	30	572
SUS316-G	20	320	1003.9	30.3	575

Table 2. SCC test data of SUS316 samples given by INSS

The SUS304-12Cr sample with an artificially lower Cr content of 12 wt.% (Table 1) was selected for the low-energy EDX study presented in Chapter 4.1. Due to its lower Cr content it suffers more pronounced preferential oxidation along grain boundaries and DBs and is very suitable to simulate the behaviour of low-Cr grain boundaries or other regions of lower Cr content in the sample. The material underwent a 100 min solution treatment at 1060°C followed by water quenching and uni-directional cold-rolling to a thickness reduction of 20%. The SCC test was performed using a pre-cracked ½ CT specimen in an autoclave under constant load (30 MPa $m^{1/2}$) in a testing environment of simulated PWR primary water chemistry (500 ppm B + 2 ppm Li, + 30 cm^3-STP/kg-H_20 DH_2) for 666 h at 320°C.

2.2 Deformation in stainless steels

The primary phase of SUS316 and SUS304 is austenite, which has a face-centered cubic (fcc) crystal structure. The alloy composition of austenitic SS determines the grade: grade 316 (SUS316) consists of 16-18% Cr, 10-14% Ni and 2-3% Mo, which also increases the alloy's corrosion resistance, and balance - Fe. The fcc crystal structure is a sub-group of the cubic closest packed (ccp) crystal structures. Figure 14a illustrates the fcc unit cell with the lattice parameter a (a = 3.59 Å for SUS316), consisting of atoms at each corner of the cell as well as an atom in the centre of each face. The closest packed plane in austenitic SS is the {111} plane (Figure 14b).

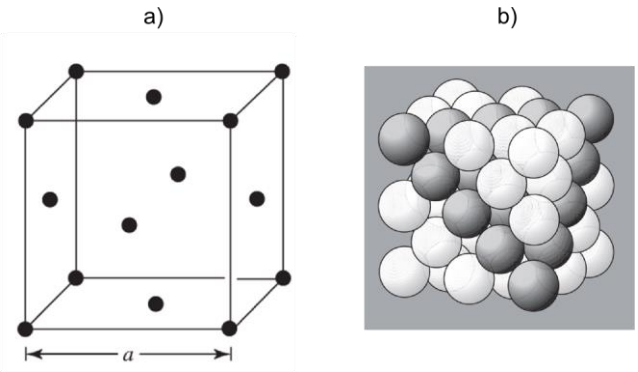

Figure 14. a) face-centered cubic unit cell with lattice parameter a; b) {111} plane in fcc lattice, denoted by dark spheres, is the closest packed plane

The unperturbed SUS316 lattice exhibits point defects as well as planar defects such as twin and grain boundaries. In case the material is exposed to external stresses, i.e. cold work, a number of additional defects develop in the microstructure. These defects, created by externally applied forces, will be explained in Chapters 2.2.1-2.2.7.

2.2.1 Stacking faults

A stacking fault is the interruption of the stacking sequence between the layers of the crystal lattice. The fcc lattice has the stacking sequence ABCABC, as illustrated in Figure 15. This sequence can be interrupted intrinsically by the planar accumulation of vacancies, e.g. ABCABABC as in Figure 15a, or extrinsically by agglomeration of interstitials, e.g. ABCABAC as in Figure 15b, in one of the layers.

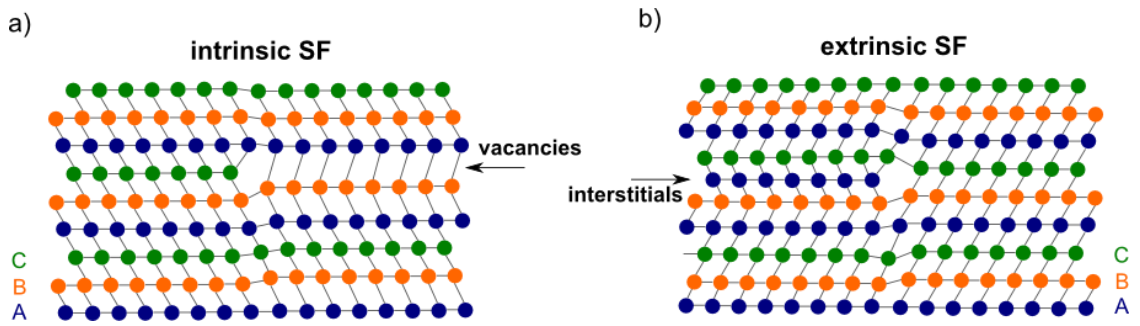

Figure 15. Stacking faults (SFs) in the fcc lattice: a) intrinsic SF, vacancy agglomeration; b) extrinsic SF, interstitial agglomeration

These deviations of the crystal lattice from its regular configuration can be represented in the form of energy, the stacking fault energy (SFE), which is a material constant. Early work on the compositional dependence of the SFE of fcc Cu-Al alloys was conducted by Swann *et al* in the 1960s [116-118].

The SFE is a material property and its magnitude controls the ease of cross-slip and therefore the stress-strain response in fcc materials [119]. The SFE of SS (SUS316: SFE = 42 mJ/m^2) is lower than that of Ni alloys (pure Ni: SFE = 75 mJ/m^2) and strongly depends on the alloy composition and temperature. The addition of elements such as Ni, Cu, Mo and possibly Cr, C and N increases the SFE of SS and therefore improves their

resistance to SCC [120-122]. For example, type SUS304 has a SFE of ~ 20 mJ/m^2, but the addition of Mo yields type SUS316, which has a higher SFE of 42 mJ/m^2.

The material's susceptibility to undergo slip is closely related to its SFE. This is important because slip on the material surface or at the crack tip can cause the protective oxide film to break, enhancing SCC initiation. The lower the SFE, the wider the stacking faults that appear within the material, increasing the probability for planar slip to occur. Therefore, low-SFE materials are more prone to SCC [122,123]. In addition, the SFE also controls the mechanisms of microstructural deformation under stress [120].

2.2.2 Slip

From an external perspective, it is not always directly detectable that slip has occurred, as it does not manifest obviously in the microstructure. Figure 16 shows a schematic of slip in an fcc crystal. Two portions of the crystal, separated by the slip plane, move in opposite directions due to an external force and come to rest in an equilibrium position [124]. After the occurrence of a slip event, the microstructure looks identical to before, because all atoms are in the correct lattice positions. Since {111} planes in fcc crystals are the closest packed planes (Figure 14), slip preferentially happens along these planes. The easiest slip directions in an fcc crystal lie in the {111} plane and are directions of the <110> family. Altogether, there are 12 slip systems present in fcc: 4 {111} planes with 3 <110> directions, respectively.

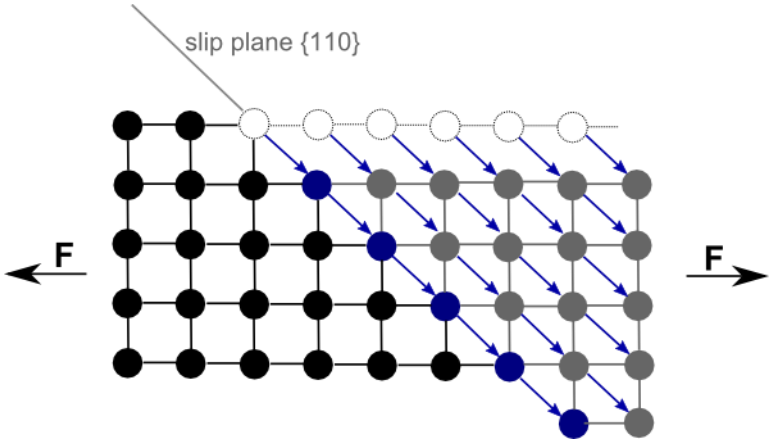

Figure 16. Schematic of slip in an fcc crystal after the application of load F; after moving one atomic distance, all atoms reside in equilibrium positions; therefore, slip may not be visible in the microstructure, but possibly on the edges or the surface of the material

2.2.3 Schmid factor

While the {111} planes are the preferred slip planes in an fcc crystal such as SUS316 stainless steel, other slip systems can be provoked if no more {111} planes can be activated. The external stresses are distributed amongst all of the planes and the stress acting on each plane can be calculated with so-called stress projection factors (SPF). The most commonly used SPF is the Schmid factor, which is most applicable to fcc lattices [125]. The primary slip system, e.g. {111} in SUS316, is identified by the highest Schmid factor. Schmid's law can be written as

$$\tau_c = \sigma_y \cos\varphi \cos\lambda \qquad \text{(Equation 1)}$$

where $\boldsymbol{\cos\varphi \cos\lambda}$ is the **Schmid factor** and σ_y is the yield stress (λ ... angle between slip direction and the direction of the externally applied force; φ ... angle between slip plane normal and direction of external force). It was experimentally determined that slip

occurs by dislocation motion and is triggered by a certain critical resolved shear stress τ_c on the plane with the greatest Schmid factor. Once slip has occurred on this plane, slip on other slip planes, with a smaller Schmid factor, can occur [125].

2.2.4 Deformation twinning

As discussed above, twinning and slip are the most dominant deformation modes in SUS316. Deformation twinning is the movement of planes of atoms along a certain crystallographic twin plane. The movement of each individual atom is only a fraction of the lattice parameter, which leads to a local change in the lattice structure and causes an interruption of the fcc stacking sequence (Figure 17) [124].

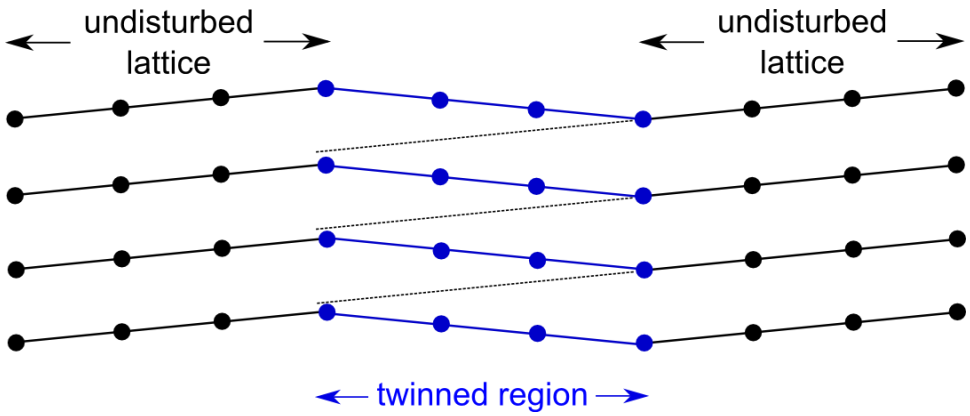

Figure 17. Schematic of deformation twinning: each atom in the twinned region only moves a fraction of the lattice parameter and the lattice is mirrored along the twin plane

The twin plane separates two regions of the crystal from each other, which are mirrored along the twin plane. The twinned region can be observed microscopically as thick band in the microstructure (Figure 18). During the application of external stress, deformation of the crystal lattice occurs mainly in the twinned region.

Deformation twinning in the [111] and [001] orientations has been observed, via TEM, to be the primary deformation mode in the early stages of externally triggered deformation in austenitic SS. At higher stress levels, twin-slip interaction leads to elevated strain hardening because the twins can block the propagation of secondary twins and slip. At high strain rates, after twinning reaches a certain volume fraction, slip takes over as the main deformation mechanism [119,126].

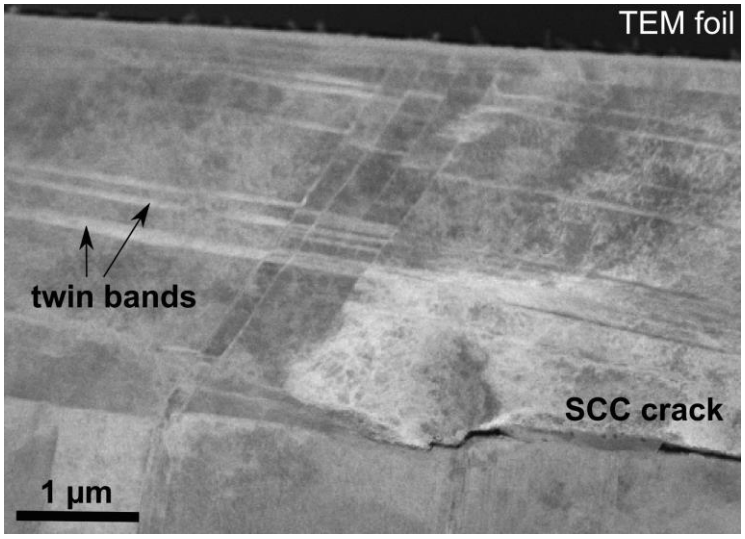

Figure 18. Twin bands in SUS316 SCC sample: the crystal lattice is mirrored along the twin plane, which appears as thick bands in the microstructure

2.2.5 Deformation bands (DBs)

The distinction between deformation twins and DBs is not straightforward and the two terms are often used in the literature to describe the same object. Deformation band is the general term for an accumulation of dislocations in the crystal lattice along a certain crystallographic plane. Similar to deformation twins, they appear as thin (~ 5 - 50 nm) bands on the surface of the material (Figure 19). These dislocations can be any form of

voids or interstitials, as opposed to the mere lateral displacement of atoms in the case of deformation twinning and slip. DBs result from the exposure of the material to external stress and can nucleate at slip bands or deformation twins.

Due to the high dislocation density close to DBs, they can act as fast diffusion paths for oxygen and other elements involved in the oxidation process. Therefore, the rate of oxidation is enhanced in close vicinity to DBs [127]. Furthermore, it has been suggested that oxide formation itself can hinder dislocation glide, therefore locally increasing the stress even further and enhancing the mobility of oxygen.

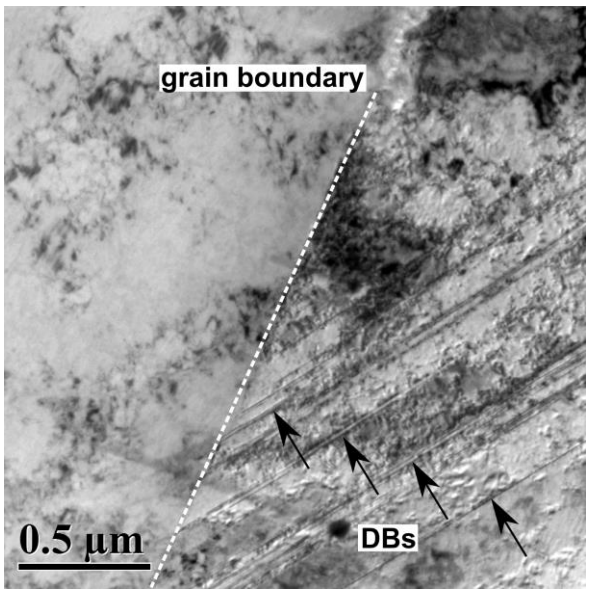

Figure 19. Deformations bands near crack tip in SUS316 SCC sample; they usually occur along {111} planes in SUS316

In SUS316, DBs have been observed to form almost exclusively in {111} planes [104,127]. It has also been established that the existence (or appearance) of DBs depends on the crystallographic orientation of each individual grain with regard to the external stress direction. It should also be noted, that some DBs may not be visible in cross-

section due to the unfavourable orientation of the DB with regard to the surface of the material, e.g. DBs parallel to the surface are not observable.

2.2.6 Martensitic transformation

Stainless steels exist in three main crystallographic formations: austenitic, ferritic and martensitic. In general, the matrix composition and temperature determine the SS phase. However, the austenite phase (fcc) can locally transform into martensite (bcc) under the influence of high external strain [128,129]. The austenite-martensite phase transformation involves coordinated shear and is usually associated with large lattice distortions due to volume change [130]. Within the external stress levels observed in this study, which are small compared to the stresses necessary to form martensite, no austenite-martensite phase transformation was detected.

2.2.7 The role of hydrogen on the deformation of stainless steels

The influence of hydrogen on the deformation of stainless steels was studied as early as the 1980s. Within his studies of the effects of hydrogen on various materials, Birnbaum *et al* also published an article on the influence of hydrogen on the SFE in austenitic stainless steels [131]. Singh et al investigated the effects of hydrogen concentration on the slow crack growth in stainless steels [132]. More studies were conducted in the late 1980s by Perng *et al* on the effects of hydrogen on austenitic stainless steels as well as the influence of plastic deformation on their hydrogen permeability [133-135].

Later, it was proposed by Hatano *et al* that hydrogen adsorption decreases the SFE of SUS304 and SUS316 and therefore enables hydrogen embrittlement (HE). This

may lead to higher numbers of strain-induced vacancies and the increased formation of stacking faults. As a result, planar lattice defects such as twins, slip and deformation bands can lead to higher strain-localisation and faster degradation of the material [136]. As hydrogen is extremely difficult to unambiguously characterise using the microscopy methods used within this study, no conclusions could be made with regard to the influence of hydrogen on the underlying SCC mechanism.

2.3 Microstructure of SUS316

Prior to the SCC investigation, TEM specimens were prepared from regions in SUS316 N and SUS316 M far away from the SCC crack in order to study the baseline microstructure of the samples. Figure 20 shows TEM BF images from a region in SUS316 N and TKD band contrast and average MO maps of a selected area in SUS316 M. The techniques used will be explained in Chapters 3 and 4.2, as this is merely an illustration of the material microstructure that has been exposed to cold working and tensile stress. It could be established that there is a high number of deformation twins and DBs present in all regions of the sample, as exemplified in Figure 20. Some of these DBs are travelling unperturbed through the GB, while others terminate at the GB. The TKD maps indicate that there may be locally enhanced strain concentration where DBs intersect the GB, especially in case of termination of the DB. Based on EBSD maps acquired from the bulk specimens, the average grain size in the samples was determined as 75 μm.

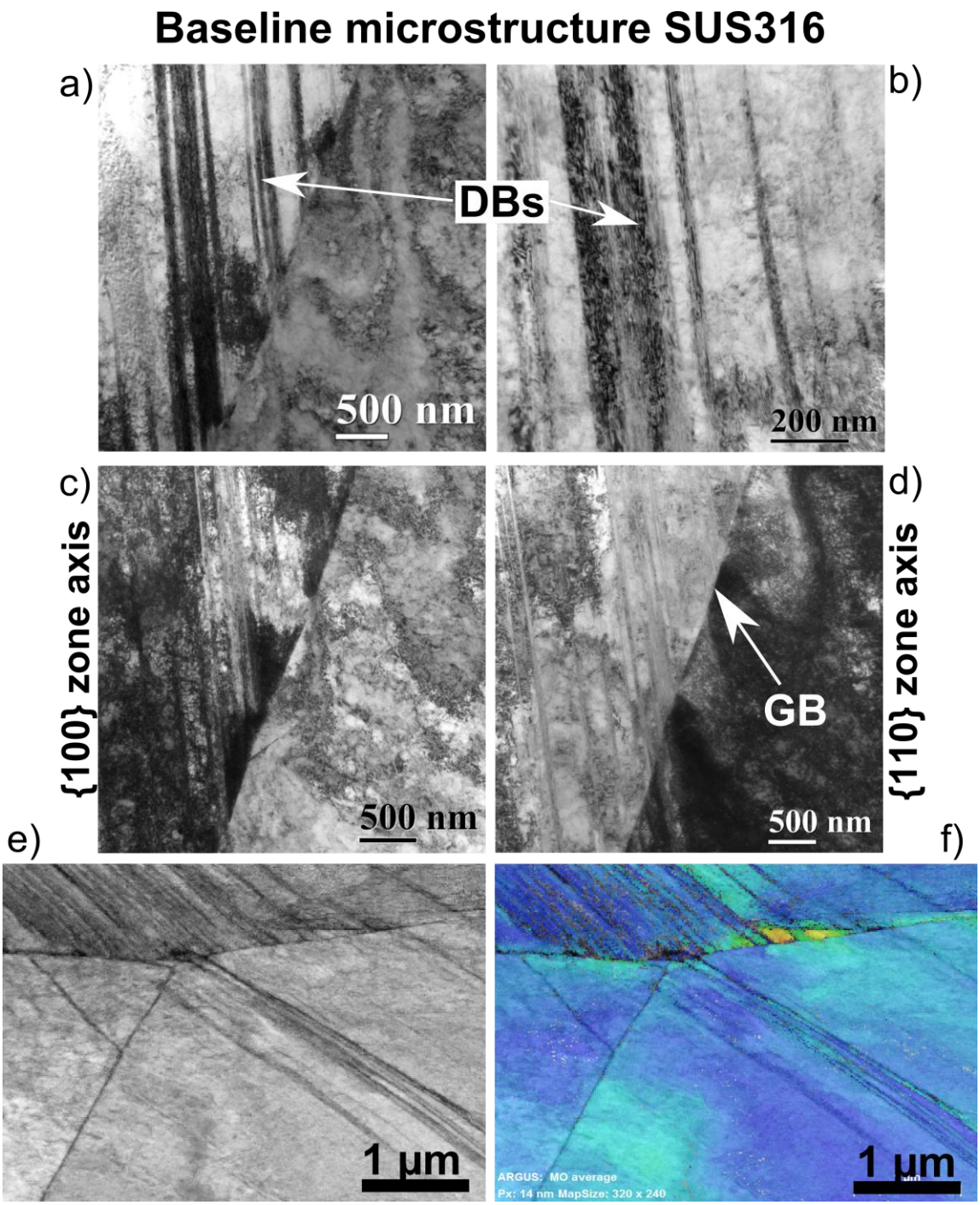

Figure 20. Baseline microstructure of SUS316, observed at far distance from SCC crack: a) TEM BF image including a GB and DBs; b) close-up view of DBs (TEM BF); c) left grain tilted into {100} zone axis, diffraction contrast (TEM BF); d) right grain tilted into {110} zone axis; GB indicated (TEM BF); e) TKD band contrast image of different region in the sample, including GBs and DBs; f) TKD average MO map showing localised strain near the DBs

3. Experimental techniques

In Chapter 1.2.3, it has been highlighted that SCC in stainless steels is a diverse phenomenon that occurs in various material-environment combinations and under a variety of external mechanical conditions. Furthermore, it is influenced by a large number of parameters. While SCC sometimes appears as macroscopic cracks in the material, it is usually not visible without the aid of magnifying instruments. Therefore, thorough SCC characterisation requires the investigation of the crack area in the sample across many length scales - from millimetres to Angstroms. A multi-scale approach and therefore a variety of complementary microscopy techniques have been applied in this thesis. This chapter introduces each (electron) microscopy technique, and the associated sample preparation methodologies, utilised in this thesis. It explains their relative strengths and limitations as well as previous contributions to SCC research.

3.1 Bulk sample preparation

The stainless steel samples (316INSS and 304-12Cr), described in Chapter 2, were received as bulk specimen (15 mm x 15 mm x 1.0 mm) with a rough, oxidised surface. Since the investigation of the SCC crack via any microscopy method requires an evenly polished surface, the cross-sectioned surface of each sample was repeatedly ground with SiC paper (with decreasing grain size) and subsequently polished with 1-µm diamond suspension. Finally, mirror-finish was achieved by treatment with colloidal silica for ~ 15 minutes.

3.2 Visual examination and optical microscopy

The common approach to any SCC investigation is to first examine the crack region in the sample visually and via optical microscopy [35,81,90]. The purpose of this approach is to acquire a good knowledge of the material and its characteristics, as well as defining interesting microstructural features to be studied further with more advanced characterisation techniques. In this specific instance, the crack was not visible to the naked eye and therefore, initial observations had to be made via optical microscopy.

Despite its limited resolution due the restriction of the wavelength of visible light, optical microscopes are still heavily used across many disciplines, especially in the life sciences. Even as material scientists strive for higher and higher spatial resolution, essential information about grain size, orientation and distribution as well as macroscopic features such as cracks, dendrites and other forms of deformation can be gained optically. In a well-polished SCC cross-section, finished with an etching solution, such as colloidal silica, the optical microscope can reveal the crack path, differently oriented grains and in some cases even existing deformations, i.e. deformation bands.

Figure 21 shows the optical micrograph of SCC in a polished 316INSS specimen acquired at slightly under-focussed conditions. Both the location of the pre-crack and the stress corrosion crack are indicated. Due to the application of colloidal silica, etching of the sample surface has taken place, revealing the microstructure including grains, GBs and DBs.

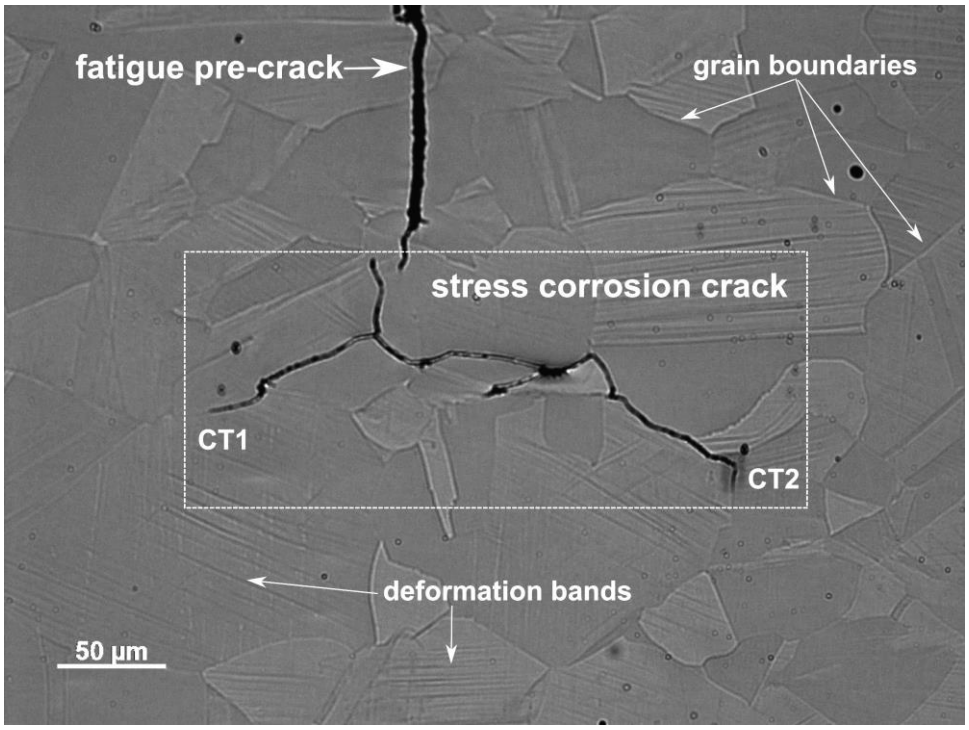

Figure 21. Optical micrograph (under-focus) of stress corrosion crack in polished 316INSS (bulk) specimen: the location of the fatigue pre-crack and the stress corrosion crack, including two crack tips CT1 and CT2, are indicated as well as DBs and GBs

3.3 Scanning electron microscopy (SEM)

The scanning electron microscope (SEM) uses a highly focused electron beam (usually with an accelerating voltage of 20 - 30 kV) to raster the surface of a specimen. An image is created from the signal of the interaction products, such as secondary electrons produced from the interaction of the incident electron beam with the sample, X-rays or backscattered electrons [137,138]. For the application of SEM, the sample surface merely has to be polished to mirror-finish, as for optical microscopy. Due to the ease in SEM sample preparation as well as execution of the technique and its data analysis, SEM is the preferred technique for acquiring an overview of the specimen texture and its

features, such as crack progression, direction, exact location of crack tips, oxide presence, etc. The main advantage of SEM is its capability to map large areas of the sample in short time with significantly improved spatial resolution relative to optical microscopy. Despite the development of SEM, improving the instrument's capabilities significantly in recent years, its spatial resolution is restricted by the resulting interaction volume of the electron beam incident upon the bulk sample [138]. It can therefore not match high-resolution techniques, such as transmission electron microscopy (TEM), which, due to their nature, deal with much smaller interaction volumes (more details in Chapter 3.5).

During the interaction of the electron beam with the bulk specimen, a number of interaction products are created (Figure 22a), each with its individual set of information if extracted and analysed. An SEM creates images using the secondary electrons produced within the interaction volume (Figure 22b). However, X-rays and backscattered electrons also carry valuable information. The analytical techniques used in the framework of this project shall be discussed in the following chapters.

3.3.1 Energy-dispersive X-ray spectroscopy (EDX)

X-rays are generated in SEM during the interaction of the electron beam with the sample, which consists of certain matrix elements with specific atomic structure. Due to the excitation of the atoms in the sample, X-rays with certain energy are produced, enabling the deduction of the elemental composition of the analysed material. The X-rays emitted from the specimen surface are collected by an X-ray detector and displayed as a spectrum. The fundamental principle of this technique is the uniqueness of each

atomic peak in the X-ray spectrum, which determines the elemental composition of the sample [138]. With this information, elemental maps can be extracted that show the existence and local distribution of a single element in the analysed region (Figure 22c).

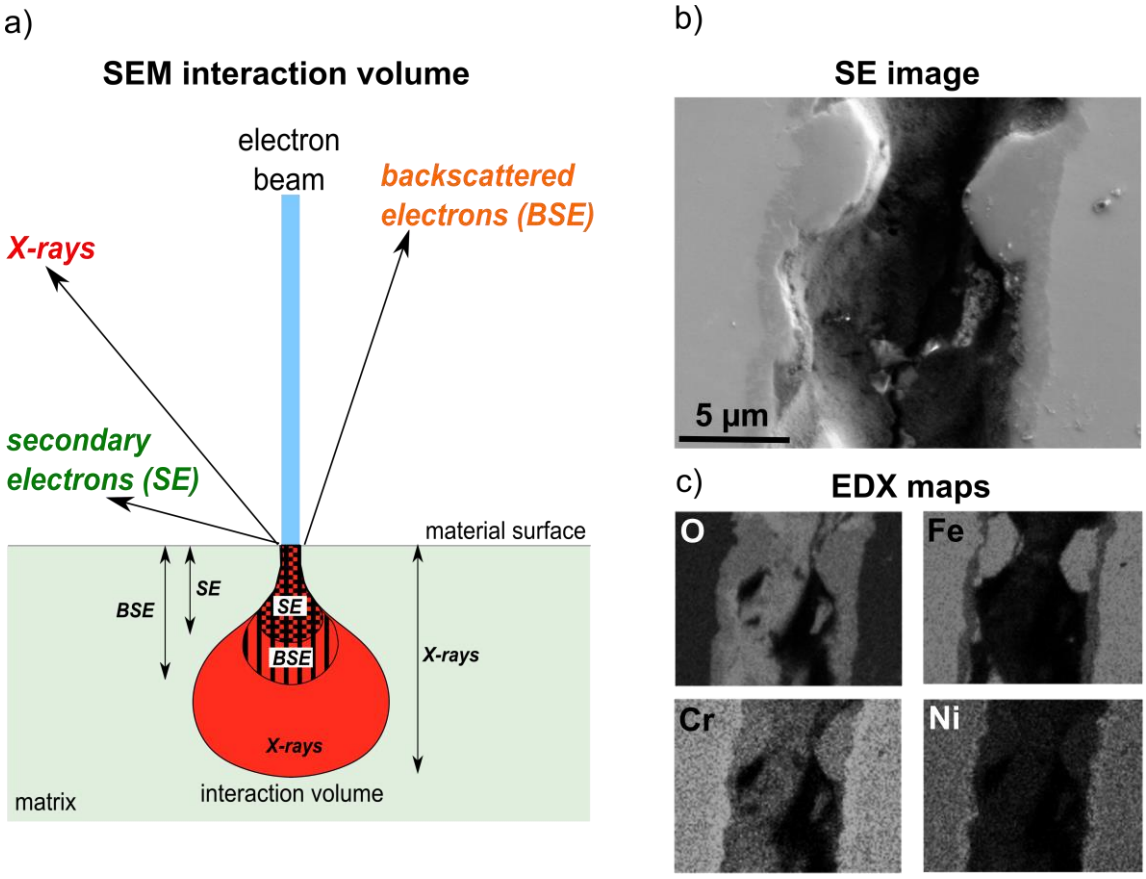

Figure 22. a) SEM interaction volume: origin of secondary electrons (SE), X-rays and backscattered electrons (BSE) within the sample volume; b) SE image of fatigue pre-crack; c) EDX elemental maps of fatigue pre-crack: O K line and Fe, Cr and Ni L lines

X-rays are generated in a relatively large interaction volume (compared to BSE and SE, Figure 22a), its size depending on the energy of the electrons in the incident beam. Lowering the accelerating voltage decreases the interaction volume and hence increases the spatial resolution of the technique.

3.3.2 Low-energy EDX

Usually, the analysis of nanoscale SCC features, for example Ni enrichment ahead of crack tips and at crack flanks, involves the use of high-resolution microscopy methods, which require significant efforts with regards to site-specific sample preparation for TEM and APT, described in Chapters 3.4.1 and 3.4.2, respectively. For this purpose, the successful selection of the most significant regions of interest within the sample, e.g. dominant and active cracks, is crucial. This could potentially be achieved with SEM-EDX, which allows the quick mapping of the entire crack region, including oxide structures and composition, DBs and crack tips, in the specimen. However, this approach is typically at the cost of spatial resolution.

The adjustable accelerating voltage of the SEM determines the energy of the electron beam and hence also defines which X-rays are excited during the interaction with the material. In general, SEMs use accelerating voltages of ~ 20 - 30 kV in order to excite the well-known K lines in the atomic spectra. At the same time, L lines are also excited at these energies, but the information gained from the low-energy part of the atomic spectra is frequently neglected. Energies of at least 12 kV are necessary to excite the K lines, however, the use of higher electron beam energies results in deeper penetration of the electron beam into the sample and therefore a larger interaction volume. As a consequence, the spatial resolution of EDX can be increased with decreasing electron energy [139-141].

Due to the lack of sensitivity of commercial EDX detectors for low-energy X-rays, low-energy EDX has always been a challenge. However, Oxford Instruments (OI) recently produced a novel optimised detector that increases the sensitivity and count rate

of low-energy X-rays. This X-ray detector, which is still in experimental development, was built without a protective window, usually protecting the detector from contamination, in order to increase the amount of low-energy X-rays captured. With this new technology, the utilisation of low accelerating voltages and therefore acquisition of L line spectra, Figure 23 (especially below the O K and Cr L line), is now possible, resulting in better spatial resolution of SEM mapping [142].

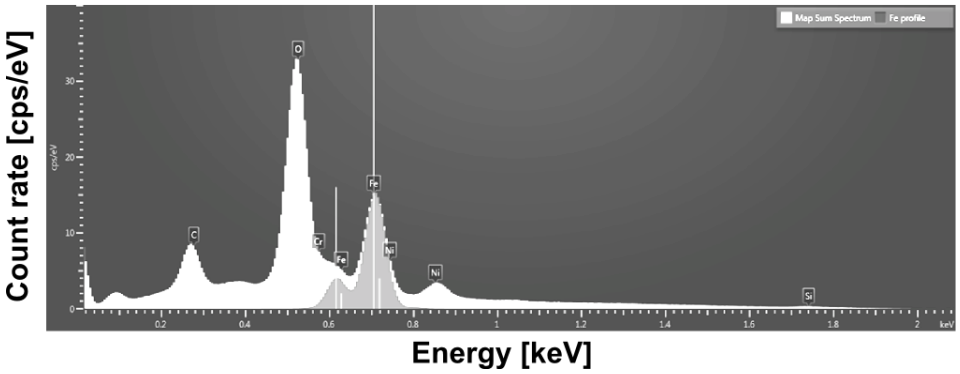

Figure 23. Low-energy EDX spectrum of oxidised region in SCC stainless steel sample (range 0 to 2 keV): O (K line) peak (at ~ 0.5 keV) indicates oxidised region in Fe-Cr-Ni matrix (Fe, Cr and Ni L lines); Fe profile shown in the sum spectrum in grey (spectrum acquired at Oxford Instruments Nanoanalysis laboratory)

In order to test OI's new EDX detector system for nanoscale EDX and simultaneously explore the possibilities to conduct initial SCC analysis via SEM with enhanced resolution, SCC samples were analysed via low-energy EDX in the framework of this thesis. The SEM characterisation was conducted with a Hitachi SU-70 Field Emission SEM at two different accelerating voltages (3 kV and 12 kV), chosen to observe different X-ray lines in the resulting spectra and compare the capabilities of low-energy (3 kV) and high-energy (12 kV) EDX with regard to spatial resolution, count rate and signal-to-noise ratio. Beam currents were intentionally kept similar between the

two voltages. An OI large area silicon drift detector (SDD) with an area of 80 mm^2 (X-Max 80) was used for the EDX acquisitions. The EDX elemental maps and background data were recorded and displayed with AZtec 2.0™, with the option of extracting X-ray elemental map data via two different algorithms for processing X-ray spectral map data, "TruMap™" and Window integrals or "Win int". While the "Win int" method simply integrates over a peak area within a window of certain width, the "TruMap™" deconvolution mapping algorithm removes the background using a top hat filter and deconvolutes the peaks by filtered least squares (FLS) fitting [143]. In order to achieve high-quality data, drift correction was applied to ensure correct spatial registration of all X-rays. Line profiles were extracted and analysed using Gatan Digital Micrograph™ software. To estimate the interaction volume of the electron beam with the material, a Monte Carlo simulation was applied via Casino2x™ software [144].

This study has been conducted in collaboration with Oxford Instruments and its results are discussed in [145] and Chapter 4.1.

3.3.3 Electron backscatter diffraction (EBSD)

The term "backscattered electron" refers to incident electrons that exit the sample surface at high angle and are practically "scattered back" into the direction of the incident beam. These electrons carry valuable information about the microstructure and crystallography of the sample. In contrast to X-rays, backscattered electrons are generated in a small volume very close to the surface of the sample (Figure 22a). However, the interaction volume still affects the resolution limit for techniques using backscattered electrons.

In electron backscatter diffraction (EBSD) a phosphor screen, positioned close to the sample surface at an angle of 70°, is used for recording the resulting EBSD pattern, also known as Kikuchi pattern. Depending on the Bragg condition, related to the atomic lattice spacing, some high-angle scattered electrons might diffract and escape the material. These electrons trigger fluorescence on the screen and form the Kikuchi pattern, which is then used by the EBSD software for indexing [146]. Via mathematical functions such as the Hough transform, the software detects bands in the Kikuchi pattern, which are then used to determine the crystallographic orientation in the current interaction volume of the incident beam with the sample. By scanning the sample surface, orientation maps of the chosen region can be created (Figure 24b). It should be noted, that knowledge of the crystallographic phase of the material being investigated, for example austenite for the stainless steels used in this thesis, is essential.

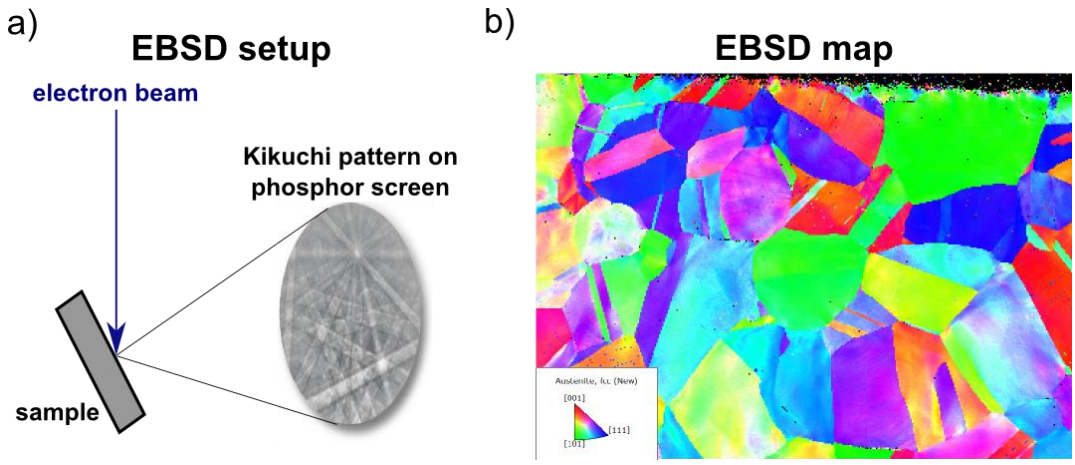

Figure 24. a) EBSD setup: sample tilted 70° toward the detector (phosphor screen); b) EBSD orientation map: inverse pole figures in x-direction (IPFX), colour legend in bottom left corner indicates crystallographic orientation of each grain

Materials scientists have been using EBSD for the gathering of crystallographic data for many decades [146,147]. Similar to many other techniques, recent progress in nano-science has required orientation mapping to improve in terms of spatial resolution. However, reports suggest that EBSD appears to have reached its threshold at around 50 nm, depending on the analysed material [148-150]. This is mainly due to the EBSD geometry and the large interaction volume resulting from the sample thickness. As illustrated in Figure 24a, in EBSD, the sample is tilted 70° with respect to the horizontal towards the phosphor screen (incident beam vertical) and therefore the cone of the incident electron beam is increased. This setup results in an increased interaction volume and therefore limited spatial resolution, as shown via Monte Carlo simulations in [148]. However, the spatial resolution of orientation mapping can be improved using a new method called Transmission Kikuchi diffraction, which is described in the next section.

3.3.4 Transmission Kikuchi diffraction (TKD)

In 2012, Keller *et al* first reported of a new orientation mapping technique closely related to conventional EBSD and initially called transmission electron backscatter diffraction (t-EBSD) but later also known as transmission Kikuchi diffraction (TKD). It uses the SEM equipped with a standard EBSD detector to perform orientation mapping on electron transparent TEM foils [148]. For TKD, the exact same hardware as for EBSD is used, but the geometry of the TKD setup is slightly altered with regard to the specimen position. In systems where TKD is an option, the EBSD software accounts for the geometry modification by adapting the pattern recognition algorithm. The TKD

geometry is derived from the basic EBSD setup (Figure 24a) with the main difference being the specimen position and its orientation with respect to the SEM column.

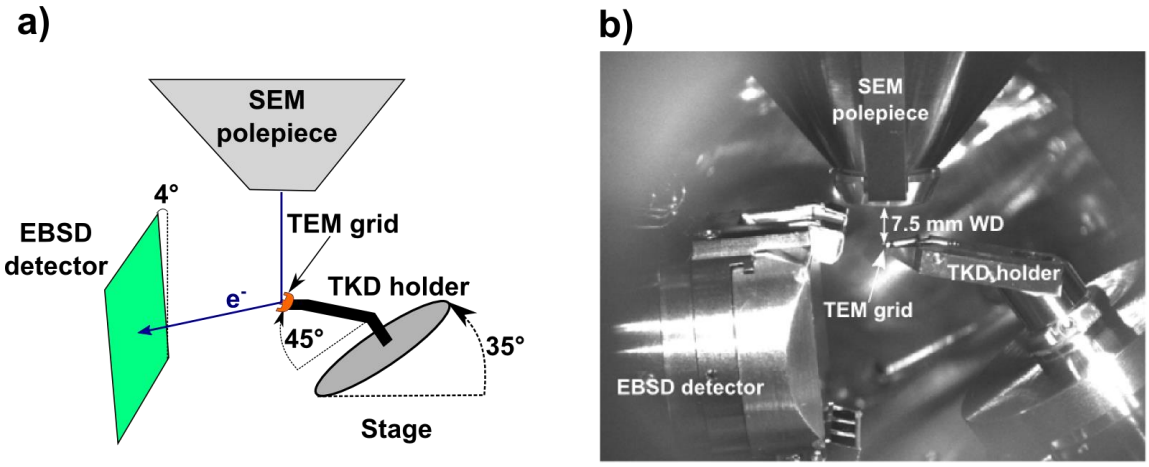

Figure 25. TKD setup in SEM chamber: a) schematic of setup; b) image of SEM chamber; EBSD detector inserted from left (4° upwards tilt); TKD holder mounted on stage (right) holding TEM grid; SEM pole-piece (top)

As displayed in Figure 25, the TEM foil is mounted on a special Bruker TKD sample holder with an intrinsic specimen tilt of 45°. The stage has been tilted in the opposite direction to 35° in order to achieve a net tilt of 10° with respect to the incident electron beam. The working distance is 7.5 mm. Facing upwards slightly (~ 4°), the EBSD detector is inserted from the left-hand side to collect the incoming electrons exiting the bottom sample surface. The detector distance to the specimen is 12 mm.

Due to this setup and the reduced thickness of TEM foil compared to the bulk specimen, the interaction volume of the electron beam with the sample is minimised in TKD. Therefore, the lateral resolution is significantly improved [149]. There seems to be a general consensus amongst the researchers using TKD that this technique offers a significant improvement in spatial resolution, < 10 nm step size are possible as opposed

to ~ 50 nm in EBSD, and that the resulting advantages outweigh the increased effort of preparing electron transparent TEM foils [148,149,151-155]. Therefore, TKD has been applied to SCC research in the framework of this thesis and more details and the results can be viewed in [156] and Chapters 4.2 and 5.3.5.

All TKD maps shown in this thesis were collected with a Zeiss Merlin FEG-SEM and an eFlashHR Bruker EBSD detector system. The TKD maps were acquired at an accelerating voltage of 30 kV and a probe current of 3.5 nA. Different magnifications and step sizes were explored at a constant TKD pattern resolution of 160x120 pixels. Finally, the gathered data were analysed with Esprit 1.9.4, the Bruker orientation mapping software. Uncertainty estimation is provided for all misorientation (MO) profiles. As the TEM lamellae vary slightly in thickness across the entire area and due to heavy deformation in the sample, noise and statistical errors may arise during the acquisition, particularly visible in the MO profiles. Therefore, standard deviation was calculated for every profile around the plateau area, based on the average fluctuation around the extracted plateau value.

3.4 Focused ion beam (FIB)

The preparation of samples appropriate for electron microscopy analysis is very technique-specific. While surface techniques such as SEM only require a mirror finish, high-resolution techniques such as transmission electron microscopy (TEM) and atom probe tomography (APT) require very specific and, in most cases, time-consuming sample preparation. Furthermore, capturing site-specific regions in these types of specimens is particularly difficult and various techniques have been developed by a

number of research groups [91,157-166]. The focused ion beam (FIB) works very similar to an SEM, but instead of electrons scanning the surface of the specimen, the sputtering effect of a Ga^+ ion beam is used to micro-machine site-specific regions in the sample. In addition to an SEM-like imaging function, the ion beam also has a sputtering effect, gradually removing the surface atoms from the imaged region of the sample. Therefore, it is possible to systematically produce trenches and undercuts around a selected region in the specimen in order to extract a certain feature from the bulk sample [91,159,164,166,167].

For the purpose of this study, a FEI FIB200 (single-beam) fitted with a static in-situ micromanipulator and a Pt gas injection system (GIS) was used for the lift-out. A Zeiss NVision 40 (dual-column) FIB was subsequently used for the final stages of the sample preparation process.

3.4.1 TEM specimen preparation using FIB

Due to the nature of the technique (explained in Chapter 3.5), TEM specimens are required to be sufficiently thin so that an adequate number of electrons of the incident beam can travel through and exit the sample.

The TEM sample preparation process via FIB is described in detail in [164] and starts with the selection of an interesting area in the sample and isolating it from the bulk via sputtering in selected rectangular patterns (trenches and undercuts, similar to Figure 27a). The selected volume is then extracted via an in-situ micromanipulator, a thin tungsten needle attached to the microscope enabling in-situ lift-outs. Finally, the extracted volume is attached to a TEM copper grid for final polishing.

It should be noted that FIB-ed TEM specimens are commonly produced in two out of three possible orientations, depending on what feature the investigation focuses on. Plan-view TEM specimens as well as atom probe specimens, illustrated in Figure 26 and Figure 27a, are extracted with their face parallel to the sample surface, e.g. for the study of cracks and crack tips in the sample [157], whereas cross-sectional TEM specimen are extracted perpendicular to the sample surface, e.g. for the study of surface oxides [158].

For the process of final thinning, the plan-view lift-out has to be rotated 90° so that the crack tip cross-section is perpendicular to the Ga^+ beam. In this position, the TEM sample is thinned from both sides to 50 - 100 nm thickness. Langford *et al* mention in their publication that residual stresses in the specimen could lead to mechanical tearing or buckling of the thin TEM foils produced. Usually, this can be counteracted by maintaining a thicker frame around the foil during the final thinning process [157].

3.4.2 Atom probe specimen preparation

The standard sample volume characterised by APT is very small, typically ~ 80 nm x 80 nm x 200 nm. Before the introduction of FIB-based techniques, electro-polishing was used for preparing atom probe needles [168,169]. Due to the small sample volume, site-specific analysis was very challenging and unreliable with specimens prepared by this technique. However, due to advances in FIB instrumentation and methodologies, an abundance of new applications have become accessible to APT [170,171]. Since this time, many techniques have been developed utilising the dual-beam FIB for the re-

sharpening of blunt electro-polished needles and for in-situ lift-out from the bulk as well as for the construction of atom probe needles from thin sheets, ribbons or powder particles [159-163,167,171-176].

The first attempts to prepare atom probe needles containing SCC crack tips were limited by the fact that only single-beam FIB instruments were used [164]. Researchers reported that it was often found that the welding to the supporting tip was insufficient, the location of the grain boundary while milling was uncertain and there was no control over the final location of the crack tip with respect to the apex of the sample. In recent years, the advent of dual-beam FIB instruments has significantly improved the capability for site-specific sample preparation. Within the framework of this thesis, a new procedure for the preparation of atom probe needles containing SCC crack tips has been developed, underpinning novel atom probe characterisation of a stress corrosion crack including open crack, crack tip and the oxidised grain boundary directly ahead of the crack tip. While the results of these efforts will be discussed in Chapter 4.3, the developed specimen preparation technique will be presented on the following pages.

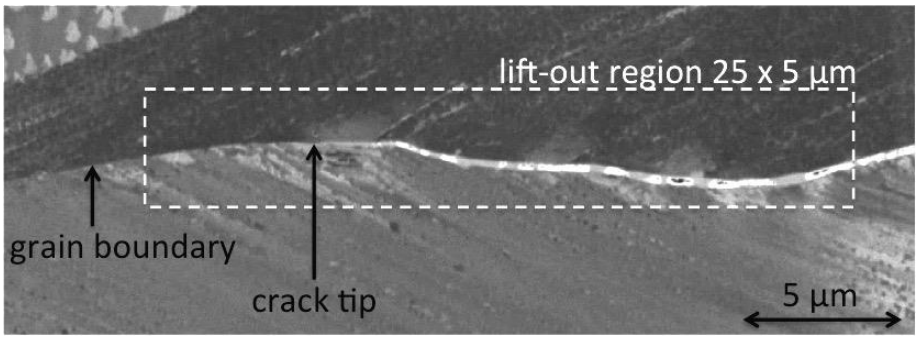

Figure 26 - FIB image (FEI FIB200) of intergranular stress corrosion crack in stainless steel specimen: a region of 25 µm x 5 µm has been selected for lift-out; both crack tip and grain boundary are indicated; *Reprinted from Corrosion Science, Vol. 98, Meisnar et al, Atom probe tomography of stress corrosion crack tips in SUS316 stainless steel, pp. 661-671, Copyright (2015), with permission from Elsevier*

In the first step of the atom probe needle sample preparation process, a 25 µm x 5 µm region of interest (ROI) was selected, as indicated by the dashed white line in Figure 26. The crack tip of the intergranular stress corrosion crack, indicated by the black arrow in Figure 26, was extracted from the bulk via the FIB. Within the highlighted ROI, the crack tip has to be located vertically central and horizontally ~ 5 µm from the left end of the lift-out region.

To protect the crack region from damage during the ion-beam milling or re-deposition of matrix material in the open crack, in the first step, Pt was deposited on top of the ROI. As shown in Figure 27a, trenches were then milled below, on top and on the side facing the crack tip (left side here, as opposed to the side with the open crack on the right) and eventually the volume was separated from the bulk via under-cuts. In the next step, the volume containing the crack tip was lifted out via in-situ micromanipulator using the same procedure as for TEM. Further details can be found in [164]. Finally, the lift-out is welded onto a blunt (~ 30 µm diameter), needle-shaped Cu tomography holder as presented in Figure 27b, which is applicable for both TEM and APT investigation of the needle. The last step is essential for the complementary analysis via TEM, which allows the determination of the location of the crack tip within the needle and to locate distinguishing features for later correlation with the atom probe data.

An essential difference of this method to other techniques is the orientation of the stress corrosion crack within the atom probe needle. Many authors report of preparing only portions of the crack tip or the GB ahead, not knowing the exact distance of their atom probe needle from the crack tip [177]. Others prepare a wedge containing these

features but repeatedly cut off pieces and weld them onto Si post arrays, again raising the issue of uncertainty in the exact location, for details see [159,163,175].

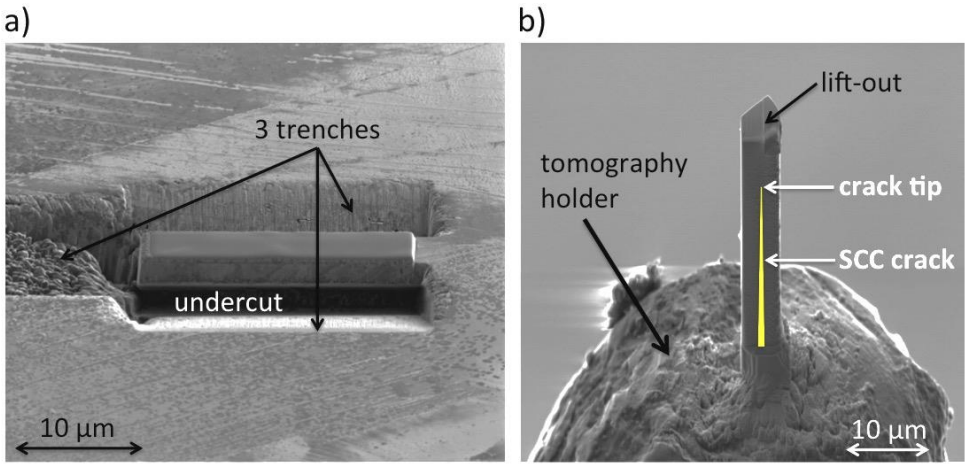

Figure 27 - Details of lift-out technique: a) lift-out method according to [164]; b) lift-out attached to Cu tomography holder for TEM via Pt welding; the approximate location of SCC crack inside the volume is indicated in yellow; *Reprinted from Corrosion Science, Vol. 98, Meisnar et al, Atom probe tomography of stress corrosion crack tips in SUS316 stainless steel, pp. 661-671, Copyright (2015), with permission from Elsevier*

In contrast to these established techniques, the approach developed in this study involves preparing the atom probe needle so that it contains the entire crack in longitudinal orientation through the length of the specimen. The needle should include a portion of the GB ahead of the crack tip, but only a short distance of less than 5 µm. For the final needle sharpening process, the tomography holder containing the lift-out is transferred to the Zeiss NVision dual-beam FIB, which allows high-precision work due its function of simultaneous milling and imaging. During this process, the Cu tomography holder and lift-out specimen need to be parallel to the FIB beam. The sharpening process is fundamental for the overall success of this technique and involves the following steps (SEM and FIB images taken throughout this procedure are shown in Figure 28):

1. Removal of the protective Pt layer in order to expose the open crack and to determine the exact crack tip location within the lift-out (1.5 nA, 700 pA and 300 nA for final cross-section)
2. Thinning of the sample from all four sides to a final cross-section of ~ 500 nm x 1 µm (milling depth ~ 15 µm) while keeping the crack tip and grain boundary centred (700 nA - 300 pA)
3. Annular milling with decreasing probe current (150 pA - 40 pA) and mask diameter
4. Final low-energy cleaning (2 kV, 40 pA) for 500 s

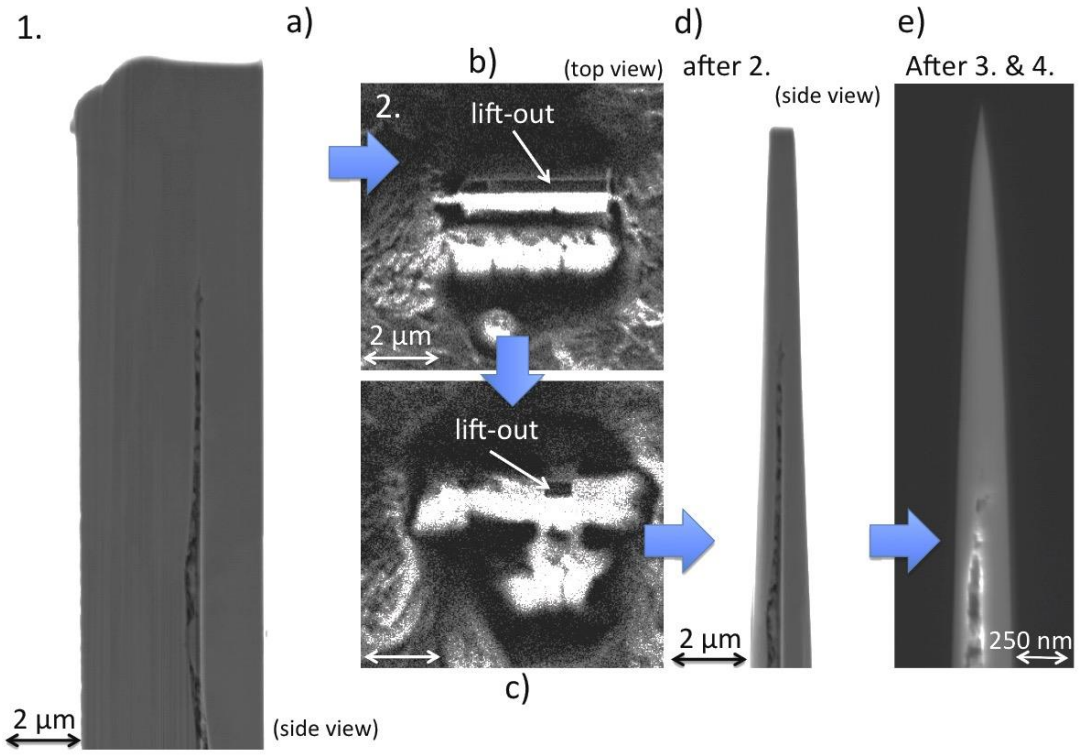

Figure 28 - Steps in the APT needle sharpening procedure: a) SEM SE image after protective Pt layer was removed; b) FIB SE image (top-view) after thinning from top and bottom side and c) after thinning from left and right side; d) SEM SE image of needle in side-view after step 2 and before annular milling; e) SEM InLens image after annular milling and low-energy cleaning; *Reprinted from Corrosion Science, Vol. 98, Meisnar et al, Atom probe tomography of stress corrosion crack tips in SUS316 stainless steel, pp. 661-671, Copyright (2015), with permission from Elsevier*

It was found, that after the annular milling and low-energy cleaning, both contrast and resolution in the FIB are not sufficient to determine the exact location of the crack tip. However, TEM has been used subsequent to the sample preparation process in order to confirm the success of the technique. The successive TEM and APT investigation will be discussed in detail in Chapter 4.3.

3.5 Transmission electron microscopy (TEM)

While the SEM, depending on the type of instrument, reaches its resolution limit between 10 and 50 nm, transmission electron microscopy (TEM) is considered a high-resolution technique with a spatial resolution down to several Ångströms (Å). An electron beam is accelerated to high energies (~ 200 kV) and directed onto a very thin (<100 nm) specimen. A detector, positioned below the sample, captures the electrons passing through the sample, which carry important information about its microstructure, composition and crystallography [178].

Early studies of SCC via TEM were conducted by various research groups starting in the early 1960s [117]. However, sometimes the region of interest was not accessible to TEM, due to the small sample volume and insufficient site-specific specimen preparation techniques [83,88]. When site-specific sample preparation became available in the early 1990s, Nisbet *et al* were one of the first research groups to report on a study of SCC in stainless steels via TEM [179]. Following their lead, other research groups gradually applied this high-resolution electron microscopy method for studying the microstructure of SCC specimens [85-87,180]. The researchers claim that detailed TEM studies of the inner oxide layer, for example, are necessary for a deeper

understanding of the SCC mechanisms and crack initiation. Likewise, the preparation of cross-sectional TEM samples has become a state-of-the-art approach for the observation of surface oxides in SCC samples [85,180-182]. TEM imaging of samples in plan-view orientation provides information on the morphology of the crack tip as well as the oxide and crack tip chemistry [88].

In this study, initial TEM imaging was performed with a JEOL 2100 LaB_6 TEM operated at 200 kV. Further analytical analysis (EELS and EDX) was carried out with a JEOL ARM200F (cold-FEG) TEM at 200kV equipped with a Gatan GIF spectrometer and a JEOL Centurio 100mm^2 EDX detector. This thesis encompasses thorough TEM characterisation of a range of TEM foils containing SCC crack tips, including imaging, electron diffraction, scanning TEM (bright field and dark field) and analytical techniques such as EELS and EDX. These techniques are described in the following chapters and the results will be shown and discussed in Chapters 4.2, 4.3 and 5.

3.5.1 Imaging and electron diffraction

The information that can be acquired via TEM is manifold. While images can be created from the transmitted electrons, the same electrons also carry crystallographic or analytic information. By adjusting the magnetic lenses of the microscope (switching from the image plane to the back focal plane), electron diffraction patterns (DP) can be acquired. In the back focal plane, all electrons scattered from the same crystallographic plane in the sample are collected within a single point, creating a DP. Therefore, each spot in the DP identifies a set of atomic planes in the crystalline material. If the material is

polycrystalline or amorphous, the spots in the DP will appear smeared, forming full or disrupted concentric circles.

Electron diffraction via TEM can be very useful for SCC research, especially in terms of identification of the crystallographic directions in the matrix around the crack as well as the examination of crystalline and amorphous oxides. Figure 29 demonstrates the gathering of crystallographic information via electron diffraction in the TEM. Diffraction patterns were acquired from different regions in the TEM foil containing a stress corrosion crack. The CCD image (Figure 29a) shows the open SCC crack, the crack tip and the GB ahead of it. DPs in grain 1 (Figure 29b) and grain 2 (Figure 29d) determine the crystallographic directions of the [111] and [001] planes based on the spots in the DP. As the oxide inside the open crack (Figure 29c) is polycrystalline, the DP smears into an interrupted ring-shaped form. This is because the oxide consists of many small crystals as opposed to the entirely crystalline grains 1 and 2. In contrast, a completely amorphous structure such as the deposited protective Pt layer on top of the sample results in a DP with distinct concentric fringes (Figure 29e).

The importance of electron diffraction for SCC research has been shown in Terachi's 2005 publication on the characterisation of different surface oxide layers [85]. Diffraction patterns were taken from both outer (Fe oxide) and inner oxide layer (Fe-Cr spinel). It was found that, while the outer oxide DP shows a spot image indicating a crystalline structure, the inner DP consists of fringes, which point towards a polycrystalline structure. This confirmed Terachi's theory that the inner oxide layer consists of a fine-grained spinel oxide, mentioned in Chapter 1.6.2.

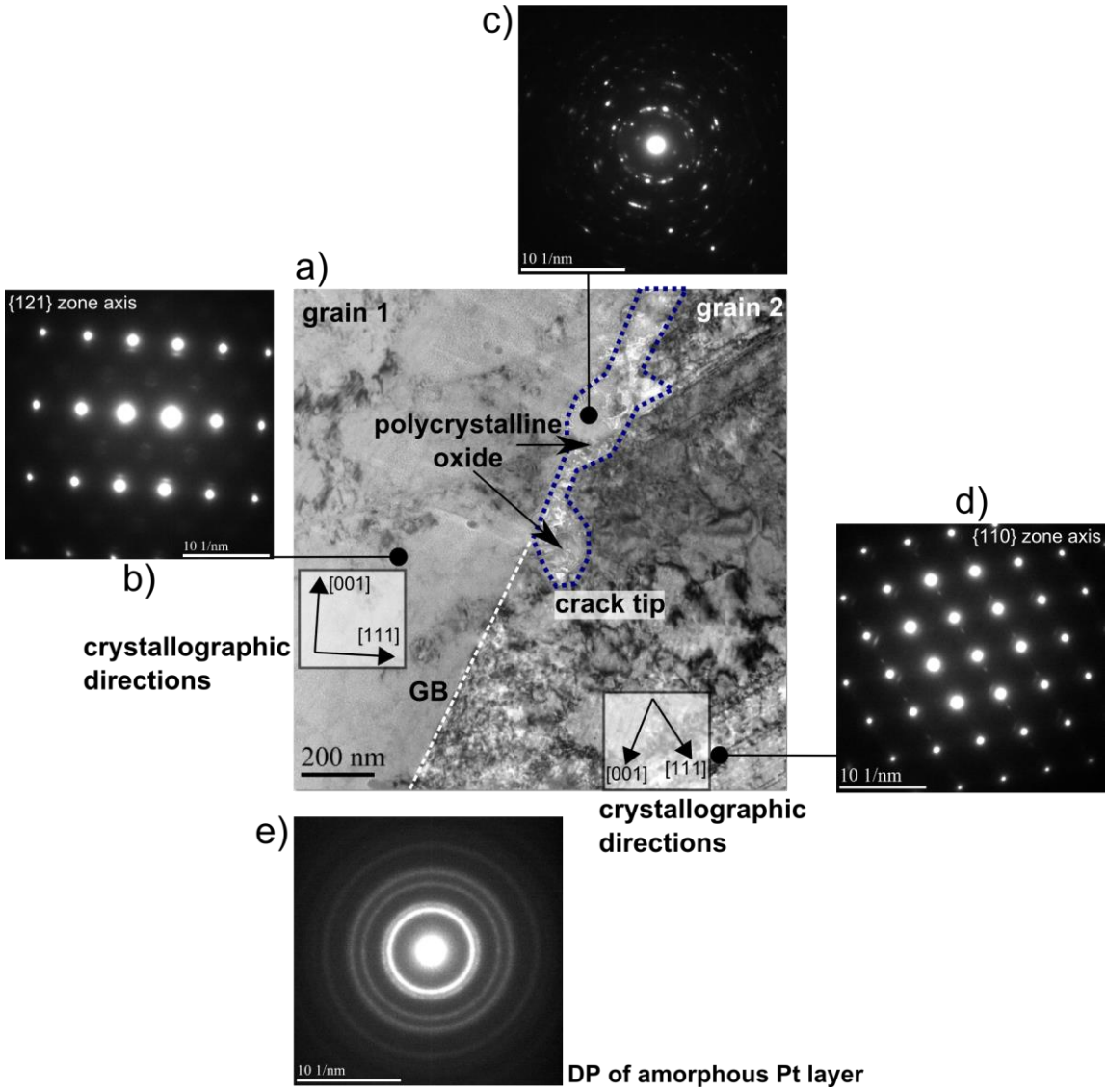

Figure 29. Electron diffraction via TEM: a) bright-field image indicating GB between grain 1 and grain 2, the crack flanks (blue dashed line) and the crack tip; b) diffraction pattern (DP) of grain 1 determines crystallographic directions (grain tilted into {121} zone axis); c) DP of oxide inside open crack: polycrystalline, very small oxide crystals; d) DP of grain 2; crystallographic directions indicated ({110} zone axis); e) example of ring-shaped DP acquired from amorphous Pt layer (not shown in a))

Finally, it should be noted that imaging itself is a very powerful tool for discovering oxide structures. Imaging in under-focused or over-focused conditions allows the localisation and analysis of polycrystalline oxides. In addition, diffraction

contrast reveals irregularities on the surface of the TEM foil, as shown in Figure 30a, and can help to discern between different grains and discover features such as GBs and DBs.

3.5.2 Scanning TEM (STEM)

Besides imaging and diffraction, where the electron beam resides at a certain location, the TEM can also operate in scanning mode where it scans the highly focused beam over the sample surface in a raster. Due to the beam becoming a highly focused spot on the sample surface, analytical characterisation in very specific regions of the sample is possible (EDX and EELS, explained in Chapter 3.5.2.2). The resolution of STEM is restricted by the spot size of the electron beam. Currently, the highest resolutions are achieved by field emission gun (FEG) TEMs due to the high inherent beam currents.

3.5.2.1 High-angle annular dark-field (HAADF)

High-angle annular dark-field (HAADF) imaging requires a special detector in order to collect incoherently diffracted electrons. The HAADF detector masks the main beam, only allowing scattered electrons to be detected. The number of these incoherent scattering events is largely dependent on the size of the atomic nucleus in the current beam spot. Therefore, the HAADF contrast is proportional to the average atomic number, assuming constant thickness and density, resulting in Z-contrast images (e.g. oxides appear darker than the matrix, see Figure 30b) [178].

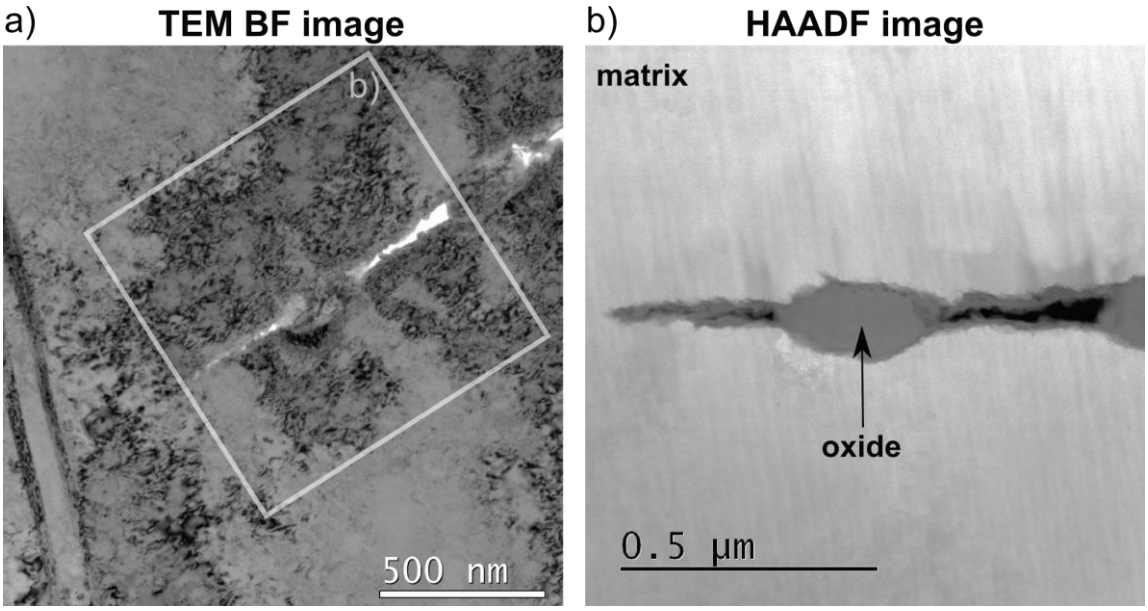

Figure 30. Comparison between TEM bright field (BF) image and STEM HAADF image: a) fringes in TEM image show diffraction contrast; b) Z-contrast in HAADF image: oxides (lower Z) appear darker than matrix (higher Z)

3.5.2.2 Electron energy loss spectroscopy (EELS)

The electrons passing through the thin TEM specimen also carry important analytical information. Electron energy loss spectroscopy (EELS) makes use of the characteristic energy loss of the electrons passing through the sample by recording the energy loss spectrum in each location. In order to avoid multiple scattering events or sample damage due to high beam energies, the TEM specimen has to have a certain thickness, which can be calculated from the mean free path of the electron in the material. For the TEM specimens used in this study, a sample thickness of 40 - 70 nm has proven to be successful.

While most electrons are scattered elastically without the loss of energy (zero loss), some electrons are scattered inelastically and can therefore be used for chemical

analysis. The zero-loss-peak in the EELS spectrum was used for alignment of the spectrum as well as for measuring the sample thickness. The loss of energy in the inelastic scattering process is characteristic for each element and the typical energies for the main constituents of stainless steel and oxygen are listed in Table 3.

Element	Z	Absorption edge	Energy (eV)
O	8	K	532
Cr	24	$L_{2,3}$	575
Mn	25	$L_{2,3}$	640
Fe	26	$L_{2,3}$	708
Ni	28	$L_{2,3}$	855

Table 3. EELS energies for O, Cr, Mn, Fe and Ni

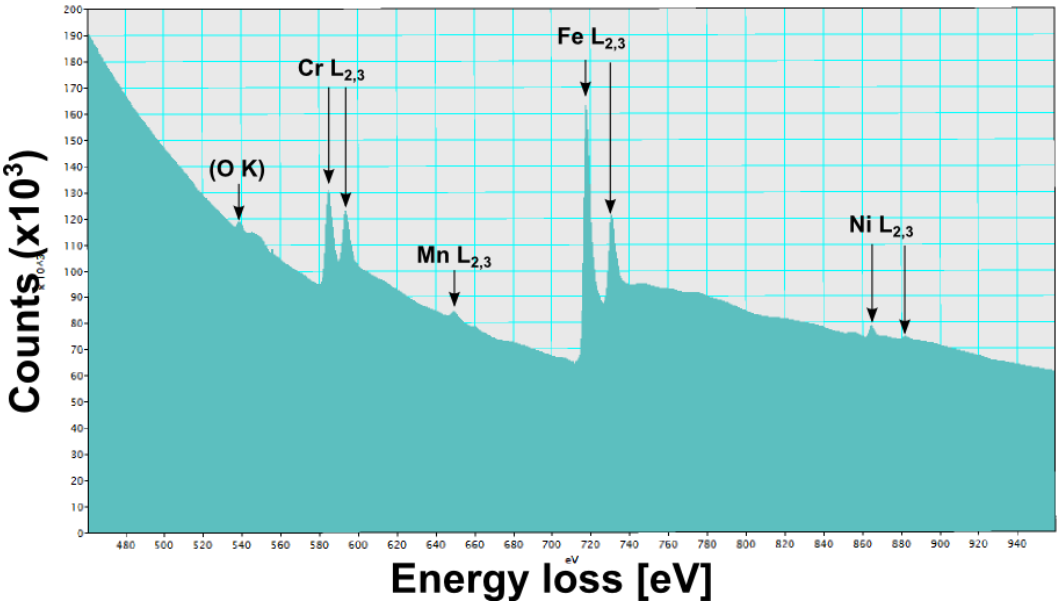

Figure 31. EELS core-loss spectrum of stainless steel matrix: mainly Cr, Mn, Fe and Ni $L_{2,3}$ absorption edges visible, location of O K absorption edge indicated

The core-loss region of the EELS spectrum extracted from the stainless steel matrix is shown in Figure 31. Besides other inelastic scattering interactions, e.g. Phonon and Plasmon excitations, band transitions and Cherenkov radiation, inner-shell ionisations, to be found at higher energies, are responsible for the information gained in the core-loss EELS spectrum.

EELS was carried out with a JEOL ARM200F (cold-FEG) TEM at 200 kV equipped with a Gatan GIF spectrometer and a JEOL Centurio 100mm^2 EDX detector. The convergence angles were 20 and 30 mrad and the collection angle was 40 mrad. The EELS data were acquired with an energy resolution of ~ 0.4 eV. Gatan Digital Micrograph was used to quantify the EELS spectra and extract individual maps for each selected element. After drift-compensation, the acquired EELS data were corrected for statistical errors or noise via multivariate statistical analysis (MSA) software (Hyperspy 0.8, open source). The algorithm includes principal component analysis (PCA) and factorial analysis of correspondence. The mathematical principles of MSA are described in [183,184]. In general, an EELS spectrum is acquired in each pixel and stacked horizontally, so that the data become a "3D data cube". In MSA, a symmetric variance-covariance matrix is created and the eigenvalues, eigenvectors and eigenimages are calculated and extracted. Sorted after relevance, the eigenvectors carrying relevant information can be determined; this method is called the "Scree test". The remaining irrelevant eigenvectors are associated with noise. Finally, the original spectra are reconstructed only using the relevant data, filtering noise and other artefacts [185]. Some EELS results acquired during this project are displayed in Chapters 4.2, 4.3 and 5. The compositional measurements via EELS, all in wt.%, are subject to an experimental error

arising from a number of different sources, not including the generally known uncertainty of the compositional changes throughout the depth of the sample. However, while the relative error of the EELS compositions mainly results from the theoretical cross-sections, the experimental error is minimised via MSA. Therefore, the standard error for all EELS compositional measurements was estimated to be ~ 10%. All acquired EELS maps are shown in the Appendix.

EDX has also been used in combination with TEM in this thesis, however, to a lesser amount than EELS. The technique is very similar to EDX used with SEM and shall not be discussed further here.

3.6 Atom probe tomography (APT)

Direct observation and identification of individual atoms has always been one of the ultimate goals of modern microscopy. Indirect, scattering-based techniques fail on many levels, specifically in terms of spatial resolution and deconvolution of signal and noise. The necessity to capture highly specific regions of interest within the specimen (e.g. a SCC crack tip) was a major reason for applying mainly indirect and beam-based methods to the investigation of SCC in the past. Therefore, until recently, atom probe tomography (APT), a high-resolution technique with excellent chemical sensitivity and a resolution demonstrated to reach the sub-nanometre-level both in-depth and laterally [186], was not accessible for SCC research [187]. However, with the advent of new sample preparation techniques, i.e. dual-beam FIB, enabling the site-specific preparation of atom probe needles (Chapter 3.4.2), the use of APT for SCC characterisation has become more and more accessible. In addition, the introduction of laser-pulsed atom

probe instruments allows the analysis of specimens containing oxides that previously would not have been feasible in voltage pulsing mode [188].

APT is a destructive 3D atomic scale microscopy technique. The specimen, shaped as a thin needle with ~ 50 - 100 nm tip radius, is subjected to an intense standing electric field, on to which either a very sharp pulsed electric field or pulsed laser is superimposed in order to trigger the highly controlled field evaporation of individual ions from the surface of the needle and onto a position-sensitive detector. Based on the time-of-flight of each evaporated ion its mass-to-charge-state ratio, and thus chemical identity, can be determined. A simple back-projection algorithm uses the incident position at which each ion hit the detector to determine the original location of the ion within the specimen. The result is an atomic-scale 3D reconstruction of the field evaporated sample volume, incorporating position and chemical identity of each atom [189].

It is evident that APT offers a unique combination of spatial resolution and chemical sensitivity, with the potential of enabling SCC research to leap forward. Since stress corrosion cracks are 3D features they should also ideally be analysed with a 3D technique to discover the underlying mechanisms of SCC. Although the study of surface oxides [190], oxidised grain boundaries [100] and stress corrosion cracks via APT is a very desirable goal, the technique also has disadvantages. First of all, the preparation of site-specific atom probe samples is still very difficult and time-consuming. This combined with the fact that atom probe needles, containing SCC related microstructure, can often fracture due to brittle oxide structures subject to intense electric fields during the experiment [100,191,192]. In addition, the implantation of Ga^+ ions during the

specimen preparation can cause additional lattice defects, which make the needle even more brittle and prone to fracture. However, this problem can be limited by low-energy cleaning [193].

Within the framework of this thesis, APT was carried out using a LEAP 3000 HR local electrode atom probe instrument in laser-pulse mode [191,194]. Based on previous atom probe analyses of stainless steel samples containing oxide structures, such as surface oxides [100], the chosen experiment conditions were: 0.4 nJ laser energy, 160 kHz pulse rate, 0.15% evaporation rate, 55 K experiment temperature. The experiments were stopped either in case of fracture or when the DC voltage applied to the specimen reached 10 kV. IVAS 3.6.6 software was used for atom probe data reconstruction and data analysis. Compositional measurements for APT, all in at.%, were conducted by creating a sphere-shaped volume of interest and extracting the average mass spectrum from it. This information was used to calculate the bulk composition from within the volume in at.%. The standard error of these compositional measurements was determined via the number of ions in the sphere (3 nm x 3 nm x 3nm) as 2.9%.

This thesis details the development of a new technique for the preparation of atom probe needles (Chapter 3.4.2) and the novel atom probe characterisation of an entire SCC crack including crack tip oxides and the adjacent section of the GB directly ahead. While the initial characterisation of the atom probe needles was conducted via analytical TEM, Ni enrichment and intergranular oxidation ahead of the crack tip have been studied with APT in 3D and with near-atomic resolution. This procedure allows a complementary analysis via TEM and APT, as it first accurately locates features with

TEM that can then be correlated with the reconstructed APT data. The results of this study are shown and discussed further in Chapter 4.3 and [195].

4. Novel techniques to improve high-resolution SCC research

It has been established in the previous chapters that currently, novel insights into the underlying mechanisms of SCC rely heavily on high-resolution (electron) microscopy methods. Steady development of these techniques is closely related to a constant improvement of our understanding of the processes involved in SCC initiation and propagation. Within the framework of this thesis, three novel approaches towards SCC research were applied and evaluated. The results of this endeavour are demonstrated and discussed in the following chapters.

4.1 Low-energy EDX for preliminary SCC characterisation

Intergranular stress corrosion cracking in SUS304-12Cr stainless steel (as described in detail in Chapter 2), tested under PWR primary water conditions, was characterised with unprecedented spatial resolution using novel low-energy (~ 3 kV) EDX with the SEM. The main objective was to perform preliminary SCC analysis with improved spatial resolution and to compare high-kV to low-kV EDX. The relatively low effort required in sample preparation, experiment and data analysis makes SEM the ideal tool for preliminary characterisation and selection of the most important SCC features such as dominant cracks and interesting crack tips, to be studied subsequently by TEM and APT.

EDX maps were used to analyse the Fe, Cr, Ni and O content at crack flanks and crack tips in the sample and examine some of the SCC features mentioned in Chapter 1.6. Special attention was paid to measuring the spatial resolution at both energies and locating active crack tips. The results were used to determine the capability of the new

EDX detector built by Oxford Instruments to capture enough low-energy X-rays for using the L lines of the atomic spectra for elemental mapping (the description of the technique can be found in Chapter 3.3.2). In addition, results from maps acquired via "TruMap" and "Win int" algorithm were compared.

4.1.1 3kV vs 12 kV

Monte Carlo simulations in Figure 32 show computationally that the interaction volume indeed depends on the beam energy of the incident electron beam. They clearly yield a smaller interaction volume of 56 nm x 41 nm for 3 kV (Figure 32a) as opposed to that of 520 nm x 400 nm for 12 kV (Figure 32b).

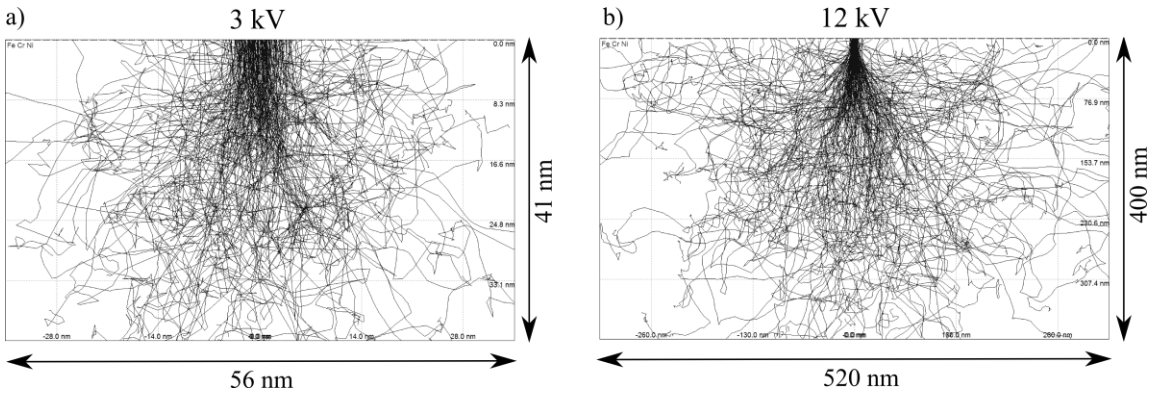

Figure 32. Monte Carlo simulation of interaction volume via Casino2x™ software [144]; calculation for 78 wt.% Fe, 12 wt.% Cr and 10 wt.% Ni; simulated beam with 200 e^- and 10 nm beam radius; a) 3 kV beam energy: interaction volume ~ 56 nm x 41 nm; b) 12 kV beam energy: interaction volume ~ 520 nm x 400 nm.

In order to compare the spatial resolution between high- and low-energy EDX, oxidised deformation bands emanating from an open crack were studied (Figure 33). While in the O maps the DBs appear as very distinct lines for an accelerating voltage of

3 kV (Figure 33a), the same DBs recorded at 12 kV are more blurred (Figure 33b). In order to confirm this initial observation, a line profile was extracted from the same DB in both the 3 kV and the 12 kV map at the same location, indicated by the white box in Figure 33a and b. The width of the line profiles is 10 pixels (equivalent to ~ 100 nm) in order to minimise statistical errors. Figure 33c and Figure 33d illustrate both line profiles, the vertical axis representing the O counts normalised for 10 pixels wide lines (Gatan Digital Micrograph^{TM} averages over 10 adjoining counts) and the horizontal axis indicating the distance in µm. By measuring the full width half maximum (FWHM), the width of the DB and therefore spatial resolution were determined for both energies. The FWHM measurements are based on the data from the line profiles, which exhibit a distinctive peak in elemental O composition at the position of the oxidised DB. After subtraction of the background noise, the net height of the peak is determined, which is then used to measure the FWHM (the width of the peak at half its net height). The standard error calculation in this measurement is based on the assumption of a normal distribution and determined by dividing the mean by the root of the number of data points.

With this technique, it was ascertained that the spatial resolution of low-kV EDX (3 kV: FWHM = 62.5 ± 4.5 nm, Figure 33c) is approximately 30% better than that of high-kV EDX (12 kV: FWHM = 88 ± 6.4 nm, Figure 33d). Furthermore, the images can be considered directly comparable, as the time per pixel for both acquisitions are similar (3 kV: 5 ms, 12 kV: 6 ms). Therefore, both signal-to-noise ratios (SNRs) could be determined using Poisson statistics, which yielded a (173.5 %) better result for 3 kV than for 12 kV (3kV: SNR 2.88, 12kV: SNR 1.66).

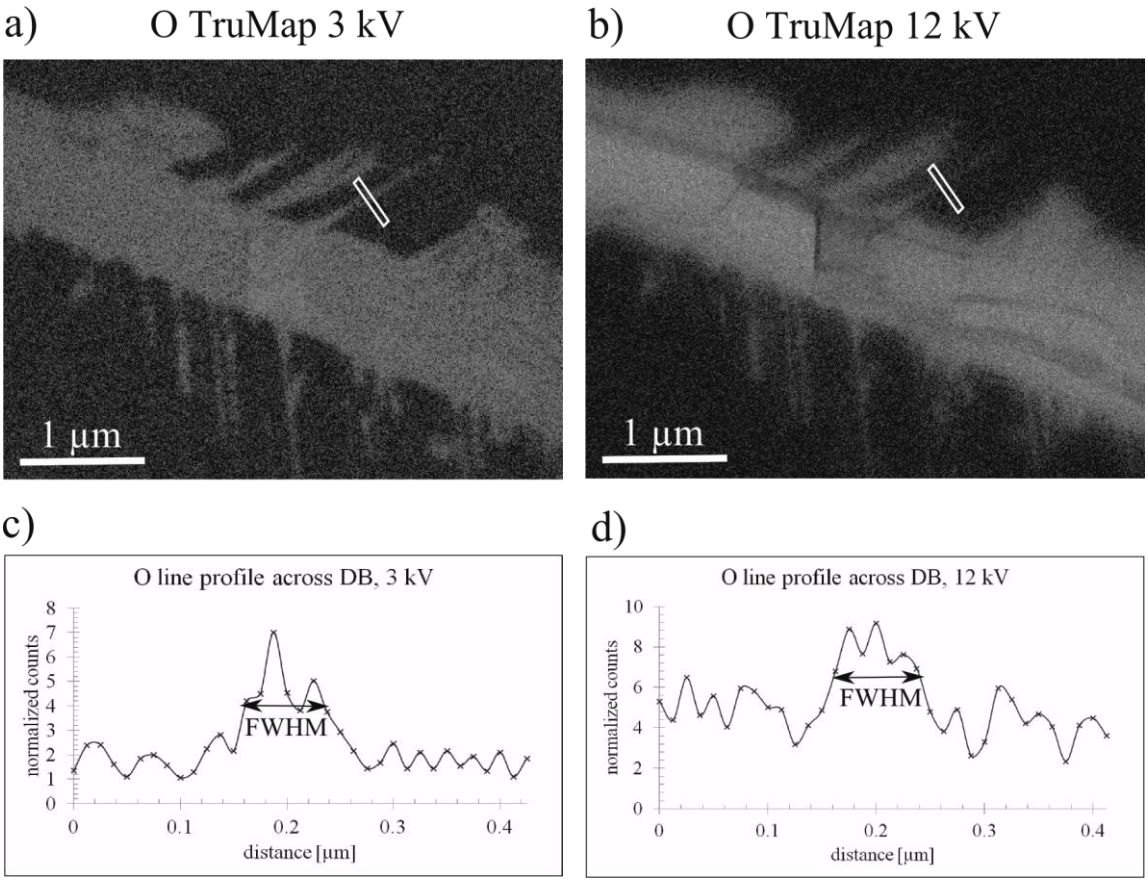

Figure 33. EDX maps of oxidised DBs and line profiles: a) O map at 3 kV accelerating voltage, white box indicates location of line profile (width ~ 100 nm); b) O map at 12 kV accelerating voltage; c) line profile for 3 kV: FWHM = 62.5 ± 4.5 nm, SNR = 2.88; d) line profile for 12 kV: FWHM = 88 ± 6.4 nm, SNR = 1.66

In the next step, the elemental distribution and oxide chemistry at a crack flank in the SUS304-12Cr sample were studied. The observed crack flank section was located at an oxide-filled crack that exhibits Ni enrichment at the matrix-oxide interface. Figure 34 shows the Ni elemental maps at both accelerating voltages (3 and 12 kV) generated via the "TruMap^{TM}" deconvolution algorithm. Again, the Ni enriched region appears more distinct in Figure 34a (3 kV) than in Figure 34b (12 kV).

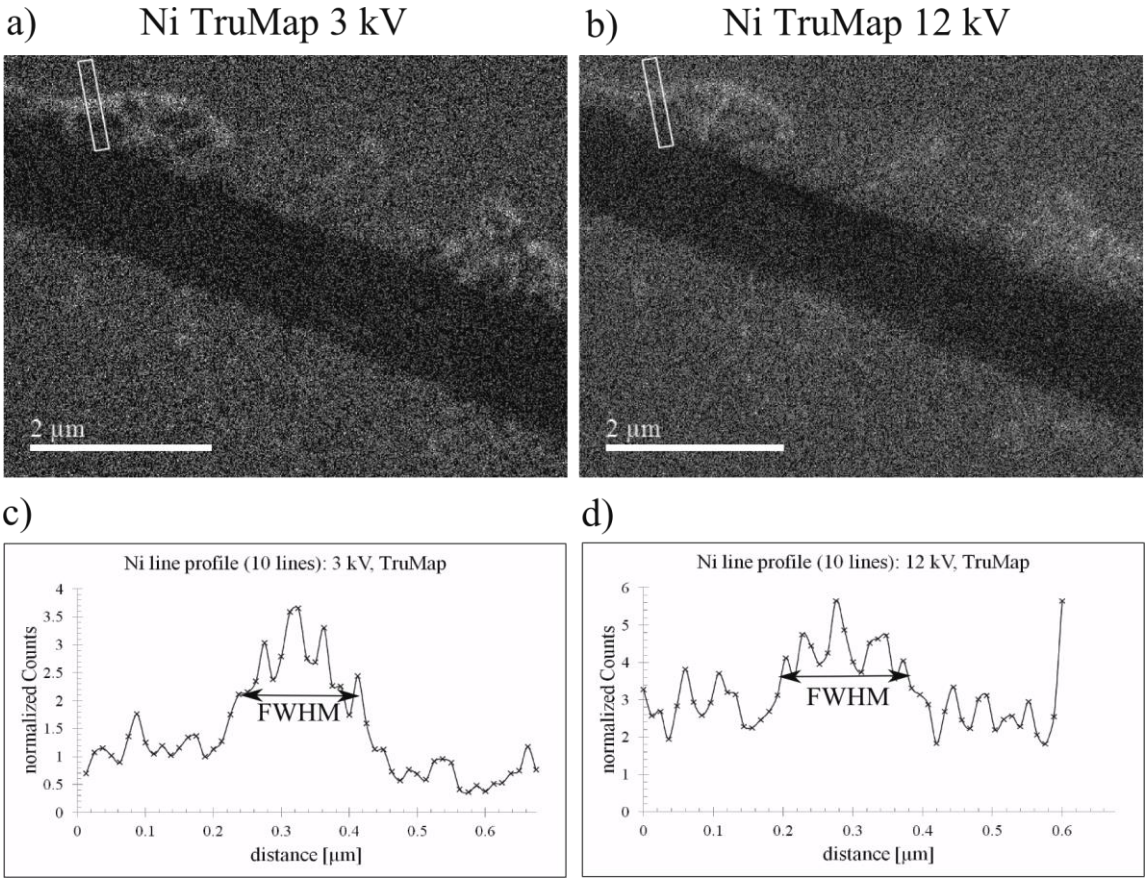

Figure 34. Elemental EDX maps of crack flank and line profiles: a) Ni L line map recorded at accelerating voltage of 3 kV, location of line profile indicated via white box (width ~ 150 nm); b) Ni L line map recorded at 12 kV; c) line profile at 3 kV: FWHM = 150 ± 8.7 nm, SNR = 2.77; d) line profile at 12 kV: FWHM = 172 ± 9.9 nm, SNR = 2.15

Supporting this initial impression, the FWHM measurements revealed a width of the Ni enrichment of 150 ± 8.7 nm for 3 kV (Figure 34c), and 172 ± 9.9 nm for 12 kV (Figure 34d). Based on these results, it can be confirmed that the spatial resolution achieved with the Ni L map at low energies is (~ 15%) better than at high energies. In addition, the SNR also yielded a better result for 3 kV (SNR = 2.77) than for 12 kV (SNR = 2.15).

4.1.2 TruMap™ vs Win Int

In order to compare the results of the "TruMap™" peak deconvolution algorithm and the window-integral (Win Int) method (further explained in Chapter 3.3.2), identical line profiles, at the locations indicated in Figure 34a and b, were extracted from the "Win Int" data for accelerating voltages of 3 kV and 12 kV. At 3 kV, the FWHM measurement based on the "Win Int" data yielded 170 ± 7.2 nm for the width of the Ni enrichment and the SNR was determined to be 2.38. For the 12 kV "Win Int" measurement, the FWHM was determined as 182 ± 10.4 nm and the SNR 1.25.

Evidently, the 3 kV "TruMap™" measurements yield the best spatial resolution and SNR, followed by the 3 kV "Win Int" measurements. Both 12 kV measurements resulted in broader features and worse SNRs than at low energy, whereby it is apparent that the "TruMap™" algorithm performs slightly better than the "Win Int" method.

4.1.3 Crack tip chemistry

In the next step, the local chemistry of two crack tips in the same sample was studied. Figure 35a and Figure 36a show the secondary electron images of two crack tips recorded via SEM at 3 kV. Oxidised DBs are clearly visible for both crack tip 1 (Figure 35a, black arrows) and crack tip 2 (Figure 36a, black arrows). Both crack tips are very different in terms of their oxidation states. While crack tip 1 appears to be filled with larger Fe-oxide particles, according to the line profile in Figure 35b, crack tip 2 does not exhibit such oxide particles near the crack tip (although an oxide plateau appears in the line profile in Figure 36b). This might indicate that crack tip 1 was inactive for some time before the end of the SCC test and therefore, the open crack was filled with Fe-rich

oxide. In contrast, the absence of Fe-rich oxide particles inside crack tip 2 indicates that it may have been active until the SCC test was aborted.

In order to study the elemental distribution in the crack tip region, line profiles were extracted at the locations indicated in Figure 35a and Figure 36a for Fe, Cr, Ni and O. Figure 35b shows the Fe, Cr, Ni and O line profiles at crack tip 1. The steep increase of O concentration between 0.8 and 1 µm indicates the location of the crack tip. The Ni line profile exhibits a peak at ~ 0.4 µm, which is located quite far away from the actual crack tip. In fact, this distance is too far according to previous studies into Ni enrichment ahead of crack tips. Therefore, it is more likely that the Ni peak results from a region where a DB intersects the line profile. This suggests that the Ni enriched region is probably caused by the oxidation of the DB and is not directly connected with the crack tip. Qualitatively, the line profile for crack tip 1 also confirms that the crack is filled with Fe oxide, although its exact stoichiometry (magnetite or spinel type) could not be established conclusively with this technique.

Figure 36b shows the Fe, Cr, Ni and O line profiles for crack tip 2. The decrease in O concentration at ~ 1.5 µm indicates the location of the crack tip. Ahead of the crack tip, the Ni line profile exhibits a plateau, but no distinctive Ni peak. Therefore, no Ni enrichment could be found ahead of crack tip 2 either. In contrast to crack tip 1, the open crack does not exhibit the existence of larger oxide particles near the crack tip. The Fe profile shows a slight decrease of the Fe concentration near the crack tip. In conclusion, these observations suggest that the crack was active when the SCC test was concluded.

Finally, the oxidised DBs located at the bottom crack flank of crack tip 2 in Figure 36b were examined. As some of the DBs are very fine features of less than 100

nm, this region was used to test the resolution limit of the technique. The FWHM of one of the oxidised DBs under observation was determined as 54 ± 3.3 nm, which also appears to be the smallest feature resolvable with this method.

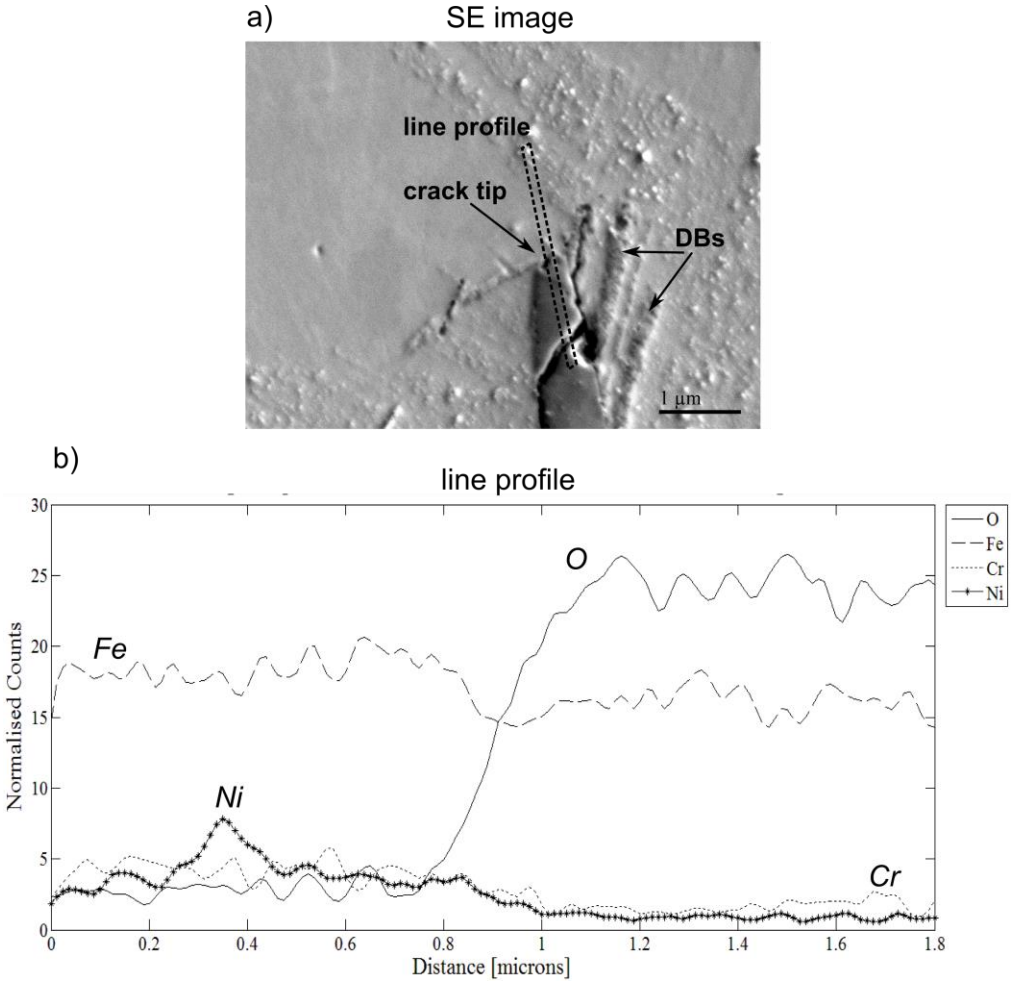

Figure 35. SE image and line profile of crack tip 1: a) SE image of crack tip 1: crack tip location and DBs indicated with black arrows, location of line profile indicated with black dashed box; b) Fe, Cr, Ni and O line profiles at crack tip

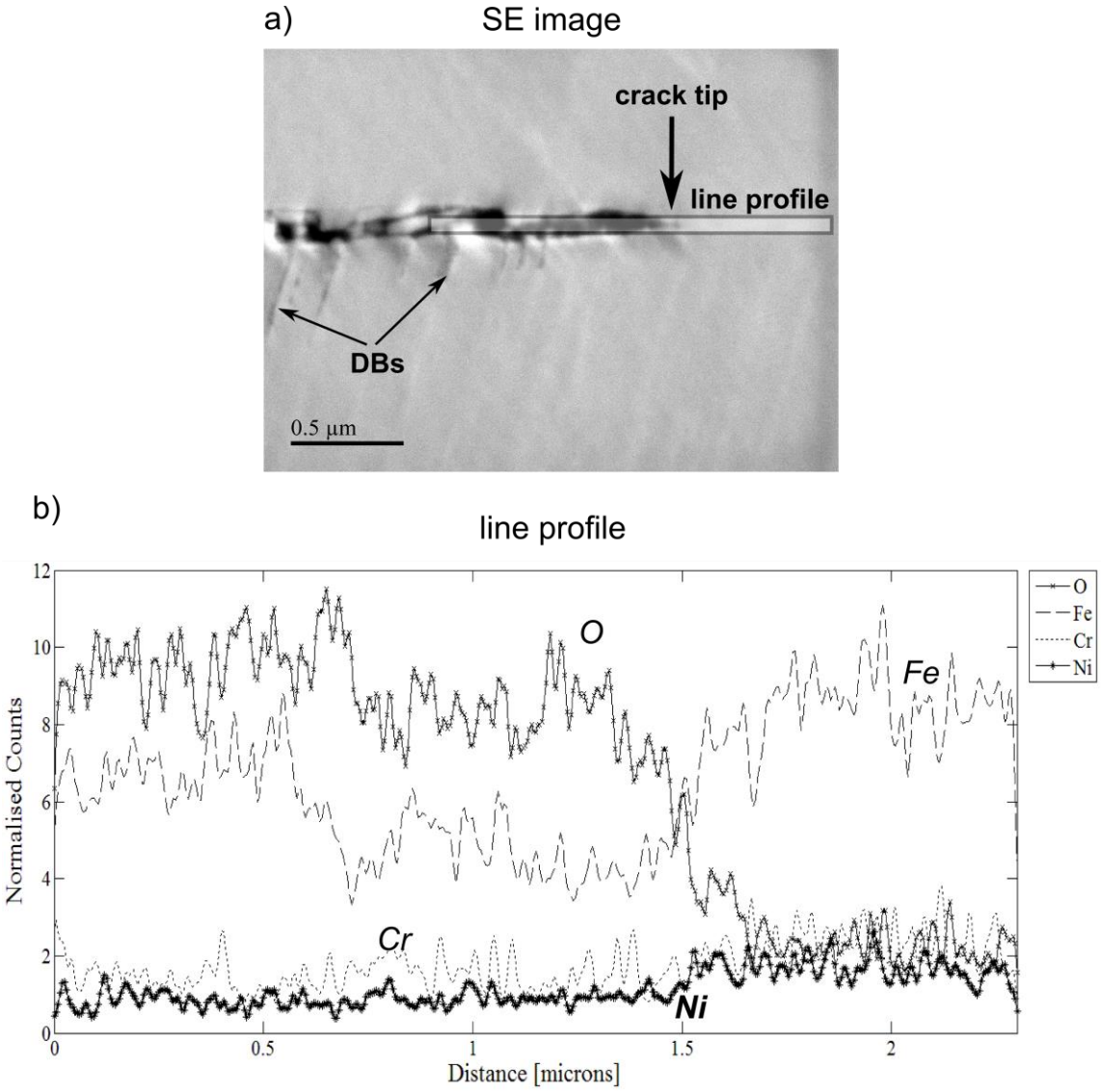

Figure 36. SE image and line profile of crack tip 2: a) SE image of crack tip 2: crack tip location and DBs indicated with black arrows, location of line profile (width ~ 50 nm) indicated with semi-transparent box; b) Fe, Cr, Ni and O line profiles at crack tip (Gauss filter applied for smoothness of profiles); the O curve suggests that the crack tip is located at ~ 1.5 µm

4.1.4 Conclusions

A newly developed windowless large area EDX detector was used to characterise SCC via SEM. This detector, which is still under development, was purposely designed to be windowless in order to increase the count rate for low-energy X-rays, facilitating the

possibility of using the L-lines of transition elements such as Fe, Cr and Ni. One of the drawbacks of this technique is potential contamination from the microscope environment during operation. Therefore, the detector requires protection or sensor warm-up during sample exchange, which makes its operation less routine than currently available SDD detectors. However, the results of this study suggest that the count rate of low-energy X-rays is indeed increased, enabling SCC characterisation at the nanoscale. In addition, the measured width of an oxidised DB was compared for two different accelerating voltages (high: 12 kV, low: 3 kV) in order to demonstrate the relative difference in spatial resolution. It was determined that low-energy EDX is capable of resolving smaller features than high-energy EDX. As a result, it was concluded that the main features of SCC such as the existence and location of oxides, the crack tip chemistry as well as oxidised DBs and Ni enrichment ahead of crack tips can be studied with increased spatial resolution via SEM prior to the application of more challenging techniques (i.e. TEM, APT). Furthermore, it could also be determined which crack tip was active at the end of the SCC test and that the assigning of the spectral data to specific elements via "TruMap^{TM}" yields better spatial resolution and higher SNR.

This demonstrates that SEM in combination with low-energy EDX is an ideal tool for preliminary SCC crack tip analysis in order to provide initial information for further investigations. Low effort in sample preparation due to SEM and relatively high resolution due to the novel detector technology make it possible to study SCC and its most important features in a quick and straightforward way.

4.2 Transmission Kikuchi diffraction for high-resolution orientation mapping

As demonstrated in Chapter 1.6, the crack tip chemistry and oxide composition near SCC crack tips have been studied via high-resolution methods for over a decade and therefore, sufficient analytical data exist to expand our understanding of the underlying SCC mechanisms. However, there is limited information on the relationship between SCC crack propagation, crystallographic features and the existing defects in the sample. This includes the misorientation of the grains on either side of the crack, the plastic deformation before, around and ahead of the crack tip as well as the existence and influence of deformation structures such as slip and deformation bands. Comparing these features in different types of SCC specimen may provide significant new insights with respect to the propagation of SCC.

In the framework of this project, a new method of high-resolution orientation mapping initially called transmission electron backscatter diffraction (t-EBSD), but now more commonly known as transmission Kikuchi diffraction (TKD), was applied to the analysis of SCC crack tips. Conventional EBSD has been conducted for comparative purposes, but was found to lack the spatial resolution for the studied nanoscale features. The results of this work will be demonstrated in the following chapters. It will be shown that with this novel technique, the experimental details of which are described in Chapter 3.3.4, high-resolution crystallographic data can be easily acquired and may contribute to solving some remaining questions about the SCC crack propagation process, such as the impact of plastic deformation around the crack tip, as demonstrated later in Chapter 5.

4.2.1 High-resolution orientation mapping via TKD

This chapter provides a short introduction into the basic functionalities and results of TKD. Complementary TEM analysis was conducted for comparison. Further experimental results and their importance for SCC research will be demonstrated in Chapter 5.

In general, the TKD software, which is usually built into the EBSD system, generates band contrast, grain, inverse pole figure (IPF) and average misorientation maps after the acquisition is stopped.

Figure 37 shows the results of complementary TEM and TKD characterisation of a SCC crack tip in 316INSS (details in Chapter 2), tested at 320°C. For clarity, this crack tip has been named G CT3 and its location within the bulk sample is shown in Figure 57. The HAADF image in Figure 37a shows an IGSCC crack, filled with oxide particles, which appear darker than the surrounding matrix due to Z-contrast in HAADF. A white line ahead of the crack tip indicates the location of the grain boundary. The TKD band contrast image in Figure 37b, also known as image quality map, shows some dark regions with higher deformation density, such as the grain boundary and the open crack. This is because in regions with a high number of dislocations, the index-ability, or the Kikuchi line band contrast, is lower than in regions with fewer defects. Using the TKD band contrast map, the GB, the open crack including larger oxide particles as well as the crack tip can be easily located.

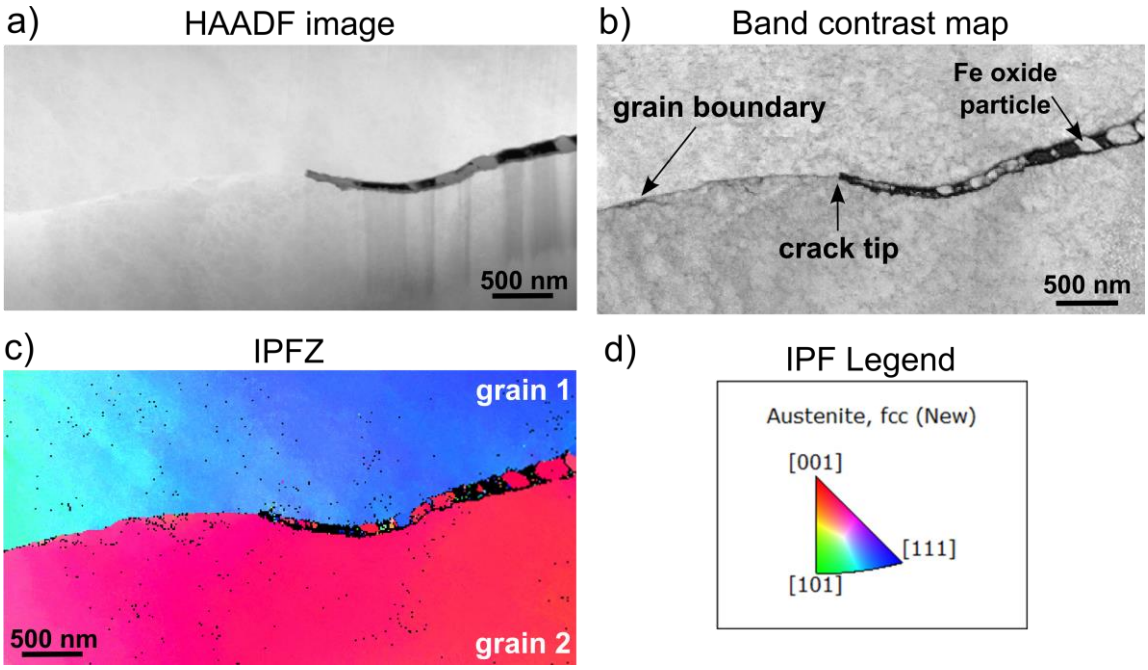

Figure 37. STEM and TKD of SCC crack tip in 316INSS G CT3 sample: a) HAADF image; b) Band contrast (image quality) map: location of GB, crack tip and Fe oxide particle indicated; c) Inverse Pole Figure in z direction (IPFZ), crystallographic orientations of grain 1 and 2 indicated via colour code (see legend); d) IPF legend

Crystallographic information can be gained very easily with TKD. Figure 37c shows the Inverse Pole Figure (IPF) map in z direction. A pole figure is the graphical representation of crystallographic information and illustrates the orientation of the crystal lattice, which is usually demonstrated as stereographic projection. A standard stereographic triangle is used as legend to identify the set of planes existing in the specimen. For instance, the legend in Figure 37d allows the user to determine crystallographic orientations within the sample and explains the meaning of the colour code in relation with the IPFZ map. The top and the bottom grain, grain 1 and 2 respectively, appear to be oriented differently. Grain 1 is oriented towards [111] whereas grain 2 is more in [001] direction, although these are merely estimated values retrieved

from the legend. It could also be established that most of the oxide particles inside the open crack are oriented along grain 2 (pink) and only one oxide particle seems to be oriented along grain 1 (blue). This initial investigation shows, how fast and simple the acquisition of crystallographic data with TKD is.

4.2.2 GB misorientation

Another important factor for IGSCC research that can be measured easily and quickly via TKD, is the grain boundary misorientation (MO). In the current sample, the GB MO has been measured directly ahead of the crack tip. Figure 38a shows a grain map without crystallographic information, indicating the location of the acquired MO profile. The relative MO values are based on the relative matrix rotation of the crystal lattice from one point in the map to another and are a standard output during the post-processing of the data by the software. Here, the line profile represents the relative MO from the point of origin (0) to each point in the line profile, respectively. Therefore, the MO from one point in the map to another can be measured, revealing the grain boundary misorientation.

Figure 38b illustrates the acquired MO profile, which starts at 0 and experiences a sudden increase at the GB to ~ 50 ± 2.4°. Using the MO profile, the thickness of the GB can be estimated as ~ 12 nm. However, this value might be an overestimation, as the GB may not be edge on in the fixed setup of the TKD investigation.

Due to limitations in the TKD software, it was unfortunately not possible to average the profile over a certain width or a number of lines. There is also no option to

extract the raw data from the MO profile and therefore some of the data that will be presented later could not be post-processed.

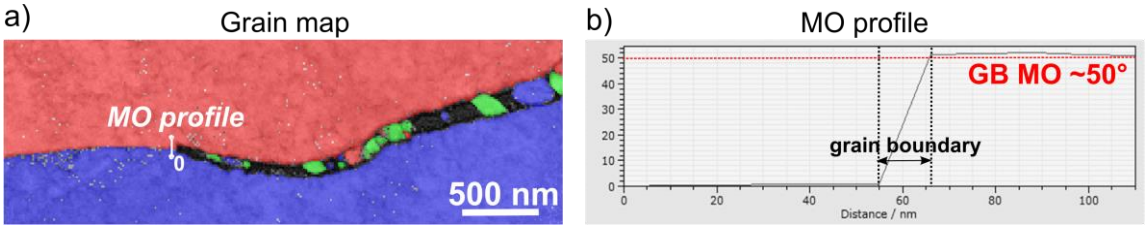

Figure 38. Measurement of grain boundary misorientation (GB MO): a) grain map (no crystallographic information), location of MO profile and origin (0); b) MO profile: ~ 50° ± 2.4° misorientation between top and bottom grain, GB thickness ~ 12 nm (estimation, GB may not be edge on in the TKD measurement)

The relationship between IGSCC crack propagation and the GB MO has already been studied previously within the SCC research community [196-200]. In particular, West *et al* established that there is a connection between slip transfer and other grain boundary parameters and the SCC susceptibility of certain GBs [80]. With TKD, these studies should become much easier in the future, as information on the exact GB MO can be obtained more readily.

4.2.3 GB migration

Under stress or corrosion-enhanced diffusion, it is possible that GBs travel short distances through the crystal resulting in simultaneous growth of one grain at the expense of the other. This phenomenon, known as grain boundary migration, is possibly enhanced in the vicinity of dislocations or lattice deformations and has been discovered close to SCC crack tips several times [201,202].

A crack tip from 316INSS (360°C), named "O CT1", when analysed via TKD, was found to exhibit GB migration. Figure 39 shows the comparison of a STEM bright field image with the local MO map of the crack tip in the sample and elemental EELS SI maps for further comparison. The local MO map (Figure 39b) is based on the MO values in each pixel with reference to an arbitrary reference pixel in grain 1. This is an option in the TKD software which assigns each pixel a "global" MO value with regard to a single chosen reference point within the entire map. Each value within the map represents the MO from the reference point to the respective pixel. Therefore, the map, with the reference point chosen in grain 1, exhibits obvious contrast between the two grains, as the GB MO in O CT1 was determined as 28 ± 1.2°.

Figure 39a shows the boundary between the upper and the lower grain very clearly due to diffraction contrast. The GB extends from the left edge of the image in a straight line, changing its path in close vicinity to the crack tip. Instead of continuing straight towards the crack tip, the GB advances into the bottom grain on a path along the interface of the matrix with the open crack. This is clearly visible in the local MO map (Figure 39b) due to the contrast resulting from the MO between the two grains. In instances, where the diffraction contrast is not as obvious as in the present STEM image, for example due to specimen tilt, TKD is perhaps the most suitable method for studying GB migration ahead of SCC crack tips.

The EELS SI maps taken from the same location in the specimen indicate that the GB migration took place exactly ahead of the oxidation front of the crack tip (Figure 39d, EELS SI map of O K edge). The region through which the GB has passed is enriched in Ni (Figure 39c, EELS SI map of Ni L edge) and both Fe and Cr depleted

(Figure 39e and f, EELS SI maps of Fe and Cr L edge). Evidently, complementary TEM/EELS and TKD analysis is a very useful tool for certain aspects of SCC research.

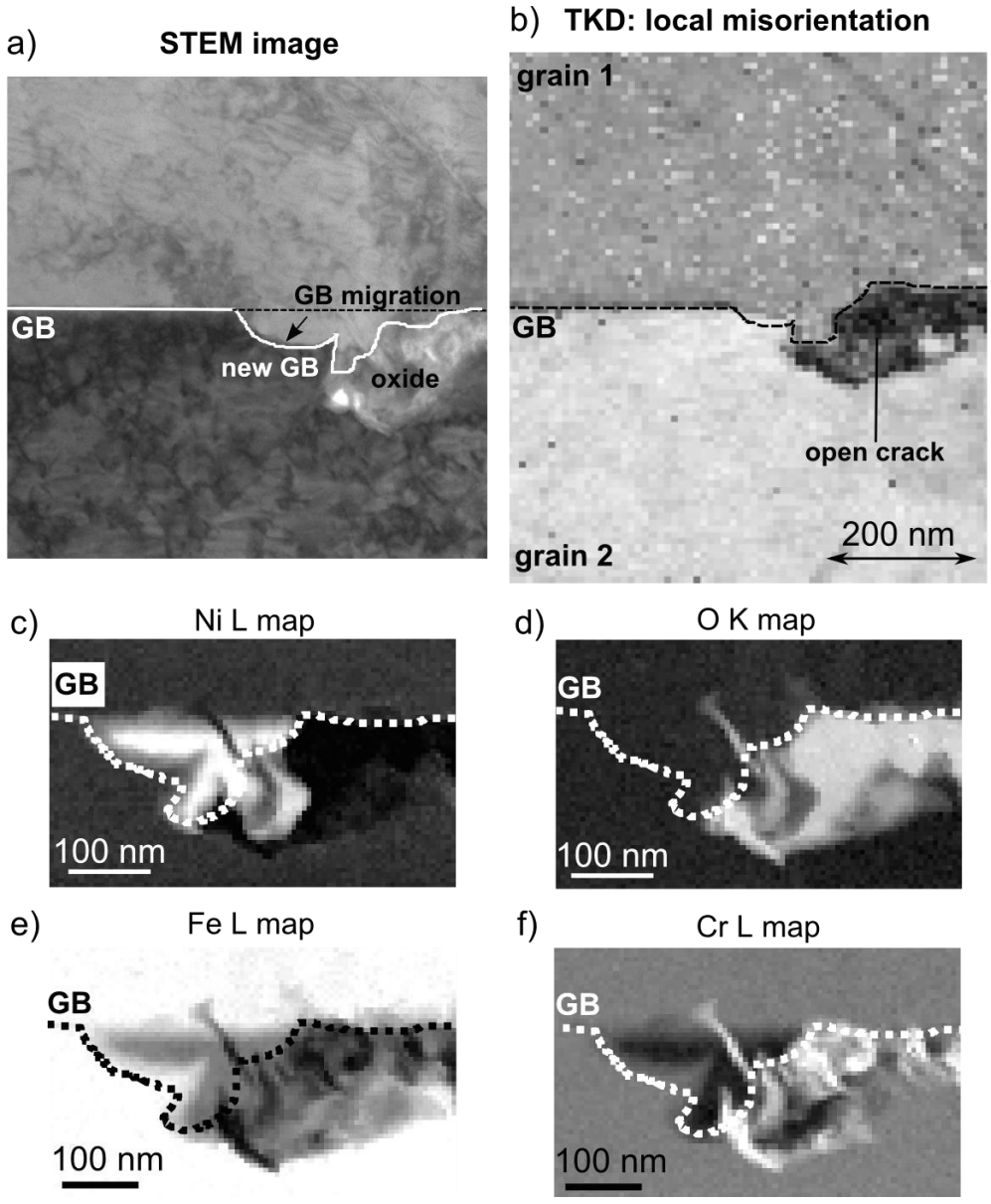

Figure 39. Illustration of GB migration in 316INSS O CT1 sample; a) STEM bright field image acquired with JEOL 2100 at 200 kV; diffraction contrast between the two grains b) local misorientation map recorded via TKD: the contrast between grain 1 and grain 2 results from the different crystallographic orientations of the two grains; c-f) EELS SI maps acquired via JEOL ARM200 at 200 kV (0.7 eV energy resolution, 5 nm pixel size)

4.2.4 Strain distribution and deformation near the crack tip

As previously discussed, insights into the strain distribution and deformed microstructure close to the crack tip is considered highly valuable within the research community. However, to date, limited experimental information has been obtained. Within this study, TKD was identified as a method, never previously utilised for SCC research, which is capable of providing some of this kind of data in an uncomplicated fashion.

Figure 40a shows the STEM HAADF image of another crack tip "N CT2", extracted from 316INSS (350°). The crack tip is here indicated as the end of the oxide, a Cr-rich inner oxide spinel, confirmed via EELS, which has not fractured yet. Via the image quality map in Figure 40b, the GB, crack tip and open crack can be easily located as darker regions in the map. In addition, an average MO map is shown in Figure 40c, illustrating the MO from each pixel to all of its neighbouring pixels as an average MO value. In the average MO map, regions of higher average MO are shown warmer (green, yellow) in the colour-temperature spectrum than regions of lower average MO, shown in shades of blue. It can be observed in Figure 40c, as indicated by the black arrow, that the average MO is higher in the crack tip region than in surrounding areas, indicating a zone of elevated lattice rotation and hence higher dislocation density. This region will henceforth be referred to as the 'plastic zone' (PZ). It should be noted, that the presented results in Figure 40c are merely qualitative and to this point, no quantification of the distribution of plastic deformation in the sample exists.

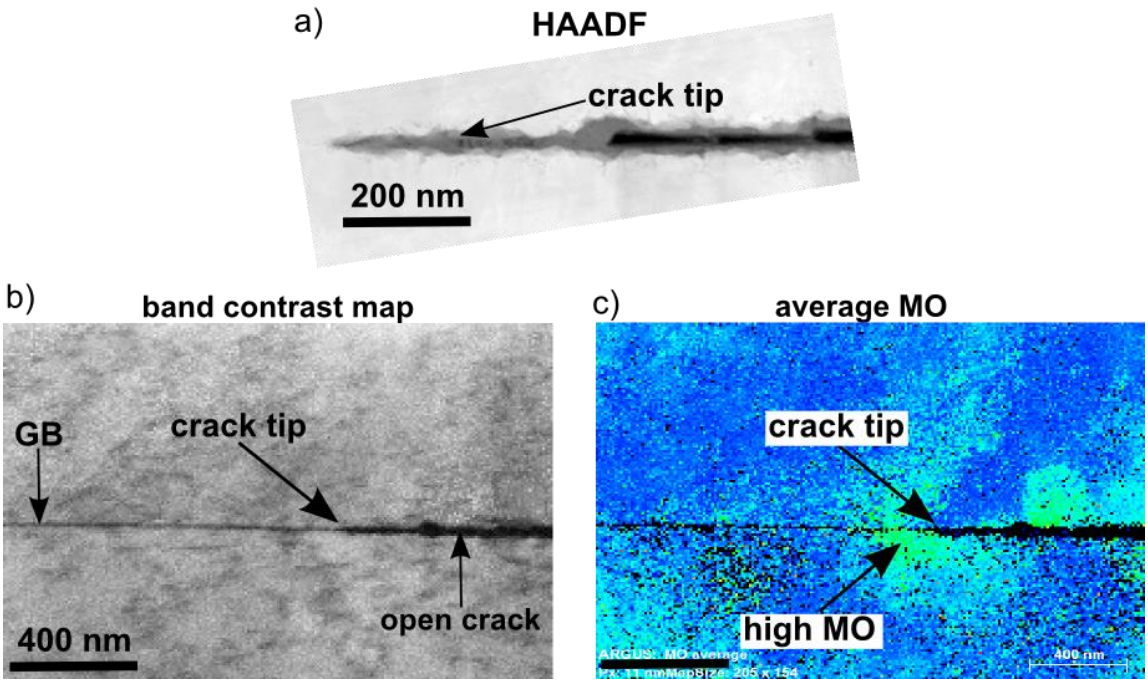

Figure 40. TKD results of SCC crack tip in 316INSS N CT2: a) HAADF image; b) band contrast map: GB, crack tip and open crack indicated; c) average misorientation (MO) map, crack tip location and region of high MO near crack tip indicated, colour-temperature code: warmer colour (green, yellow) indicates higher misorientation than colder colour (blue)

In order to study different types of deformation near the crack tip, another SCC sample (316INSS, 360°C, "O CT2") with similar step-like crack morphology has also been studied via TKD. The results are shown in Figure 41. The HAADF image in Figure 41a clearly shows that the crack propagated in a sequence of distinct steps. Ahead of the crack tip (~ 1.5 μm), the GB exhibits another step, coinciding with a void, presumably formed by the accumulation of lattice vacancies. The GB and void are shown in a close-up view in Figure 41b. Slip bands appear to coincide with the void and each of the steps in the open crack.

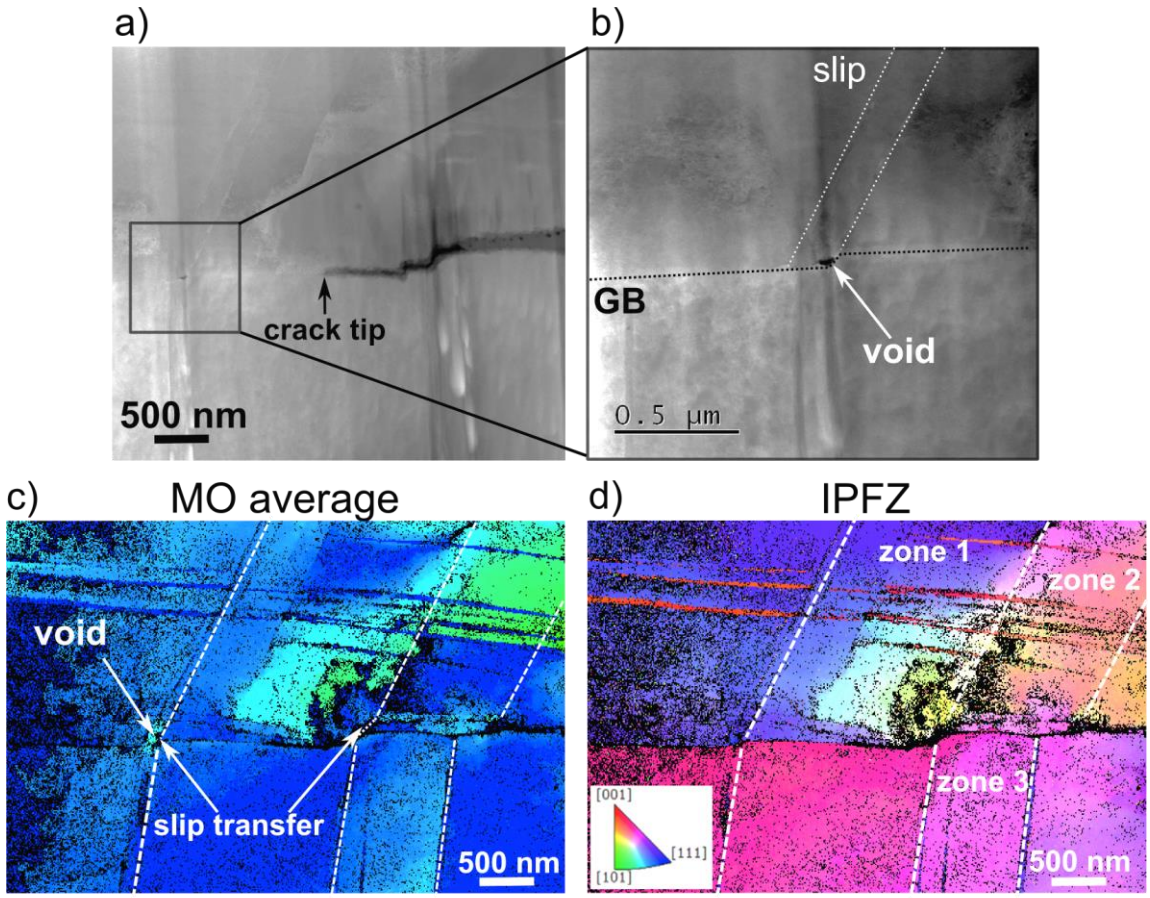

Figure 41. TEM and TKD measurements in SCC crack tip sample O CT2: a) HAADF image; b) close-up HAADF image of void located at GB, slip bands indicated; c) average MO map indicating void and slip (colour temperature spectrum); d) IPFZ map and legend, zones of slightly different crystallographic orientation indicated

The IPFZ map in Figure 41d illustrates how the region between the slip bands, each coinciding with a step in the crack opening or GB, can be divided into zones of slightly different crystallographic orientation due to the colour code. The fact that each of these zones seems to have a slightly different crystallographic orientation could be an indicator that the crack was temporarily arrested before propagating into the next zone. In contrast to the previous specimen "N CT2" (Figure 40), the plastic zone in O CT2 (Figure 41c) seems less pronounced. In O CT2, a zone of higher average MO seems to

be located in the top grain just above the crack tip, where a number of slip bands intersect the open crack.

Furthermore, it can be observed in Figure 41c and d that slip transfer across the GB is present, or in case of the open crack, was present prior to fracture. Slip transfer regions intersecting with GBs have previously been found to be associated with higher plastic deformation [203]. At the location of the void, ~ 1.5 μm ahead of the crack tip, the average MO appears elevated, indicating higher plastic deformation in this zone. Arioka *et al* previously established that vacancies are driven by stress gradients to high stress regions such as crack tips and GBs with high local stresses [37]. The existence of such a void at the GB ahead of the crack tip may also be a significant factor for the crack propagation process. As the GB is known to be a fast-diffusion path for vacancies and interstitials in the material, the void may merge with the crack tip at some point, accelerating the crack propagation process.

4.2.5 Developing a method to quantify plastic deformation

Until now, the indirect relationship between the measured misorientation and relative rotation of the crystal lattice has been used for acquiring MO profiles and MO maps. In fact, the measured misorienation relates to the plastic strain gradients, resulting from lattice curvature and the necessary dislocations to explain it, which often occur near crack tips in constrained volumes [204].

In this chapter, the introduction of a method to quantify plastic deformation around the crack tip using TKD data is presented. However, it should be noted that this

method is an attempt to identify the size and magnitude of the plastic zone around the crack tip and cannot yet deliver absolute quantitative values.

Figure 42 and Figure 43 show the average MO maps of the previously shown SCC crack tips "N CT2" and "O CT2" as well as line profiles extracted from them. Although shown in the average MO maps, with MO values in each pixel depending on its neighbouring pixels, the line profiles represent the relative MO from the point of origin, marked with a white diamond, to each point in the line profile respectively.

It was previously shown, in Figure 40c, that sample 316INSS N CT2 exhibits a region of high MO around the crack tip. With this new method, the extent of this plastic zone was established via MO line profiles and is presented in Figure 42. Figure 42b shows a line profile extracted from the top grain, originating from close vicinity to the crack tip and perpendicular to the GB. The graph indicates, that the MO surges from 0 to a plateau of ~ 2.8 ± 0.8° within the first 50 nm of the crack tip. A similar line profile has also been acquired in the bottom grain, highlighting two distinct plateaus at ~ 2.0 ± 0.6°, reached after 200 nm, and ~ 3.1 ± 0.9°, reached after 600 nm. This suggests that the PZ in the bottom grain stretches further than in the top grain, both reaching plateaus between ~ 2.0° - 3.0°. Similar measurements have been acquired along the crack flanks, ~ 2 μm distance to crack tip, and ~ 4.5 μm ahead of the crack tip. The results are summarised in Table 4.

The data show that the MO plateau value decreases at far distance from the crack tip in both grains at the crack flanks and ahead of the crack tip. At a distance of ~ 4.5 μm ahead of the crack tip in profiles 5 and 6 (locations of which are not visible in the map in Figure 42a), the plateau value decreases to 0.6 ± 0.1° and 0.7 ± 0.1°, respectively.

Similarly, the MO plateau value decreases along the crack flanks away from the crack tip to 1.5 ± 0.4° and 1.2 ± 0.3° in the top and bottom grains at a distance ~ 2.0 µm from crack tip.

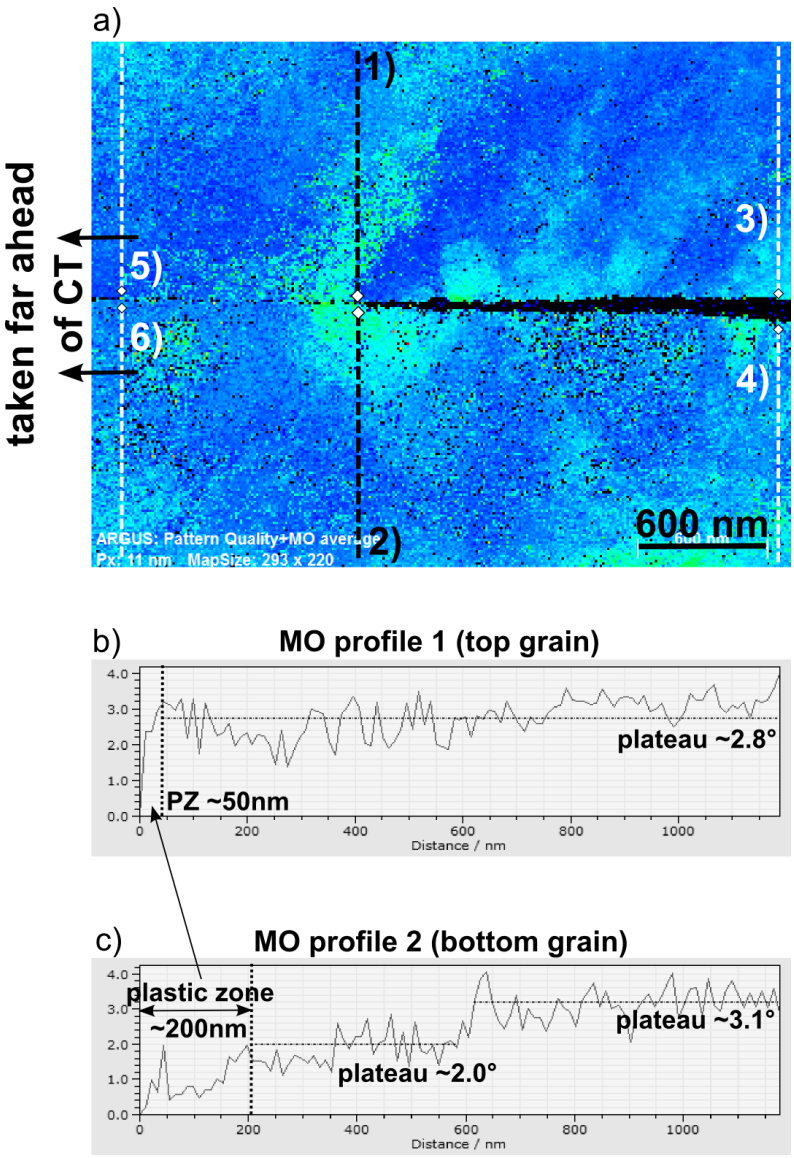

Figure 42. Average MO map and profiles from SCC sample 316INSS N CT2: a) average MO map, indicating the location of MO profiles 1, 2 and 3-6 (origin marked by white diamond); b) MO profile 1 located in top grain commencing at crack tip; c) MO profile 2, located in bottom grain commencing at crack tip; MO profiles indicate height of plateau and extent of plastic zone (PZ)

This analysis confirms that the MO and therefore plastic deformation is indeed concentrated around the crack tip in 316INSS N CT2 and decreases in both grains and directions away from the crack tip. Nevertheless, at some, very localised regions in the sample, such as at the second step in the upper crack flank, there might still be a locally higher level of plastic deformation. Moreover, it can be read from Table 4 that the extent of the PZ is significantly higher in the bottom grain at the crack tip, i.e. profile 2 vs. profile 1, whereas it is higher in the top grain ahead of the crack tip, i.e. profile 5 vs. profile 6.

Grain (profile number)	**Distance from crack tip [µm]**	**Location**	**Plastic zone size [nm]**	**Plateau value [°]**
Top (1)	0.0	Crack tip	50	2.8 ± 0.8
Bottom (2)	0.0	Crack tip	200 600	2.0 ± 0.6 3.1 ± 0.9
Top (3)	2.0	Crack flank	50	1.5 ± 0.4
Bottom (4)	2.0	Crack flank	70	1.2 ± 0.3
Top (5)	4.5	GB	150	0.6 ± 0.1
Bottom (6)	4.5	GB	50	0.7 ± 0.1

Table 4. MO profile values for 316INSS N CT2 in Figure 42a

Another set of MO profiles was extracted at specific locations from sample 316INSS "O CT2" and is presented in Figure 43. Since the top grain appears to be heavily deformed (slip, DBs and cross-slip), line profiles extracted from this region would not be very representative of the PZ around the crack tip. Nevertheless, three line profiles were extracted from the bottom grain to measure the PZ at the void ahead of the crack tip, at the crack tip itself and in zone 3 (Figure 41d), respectively.

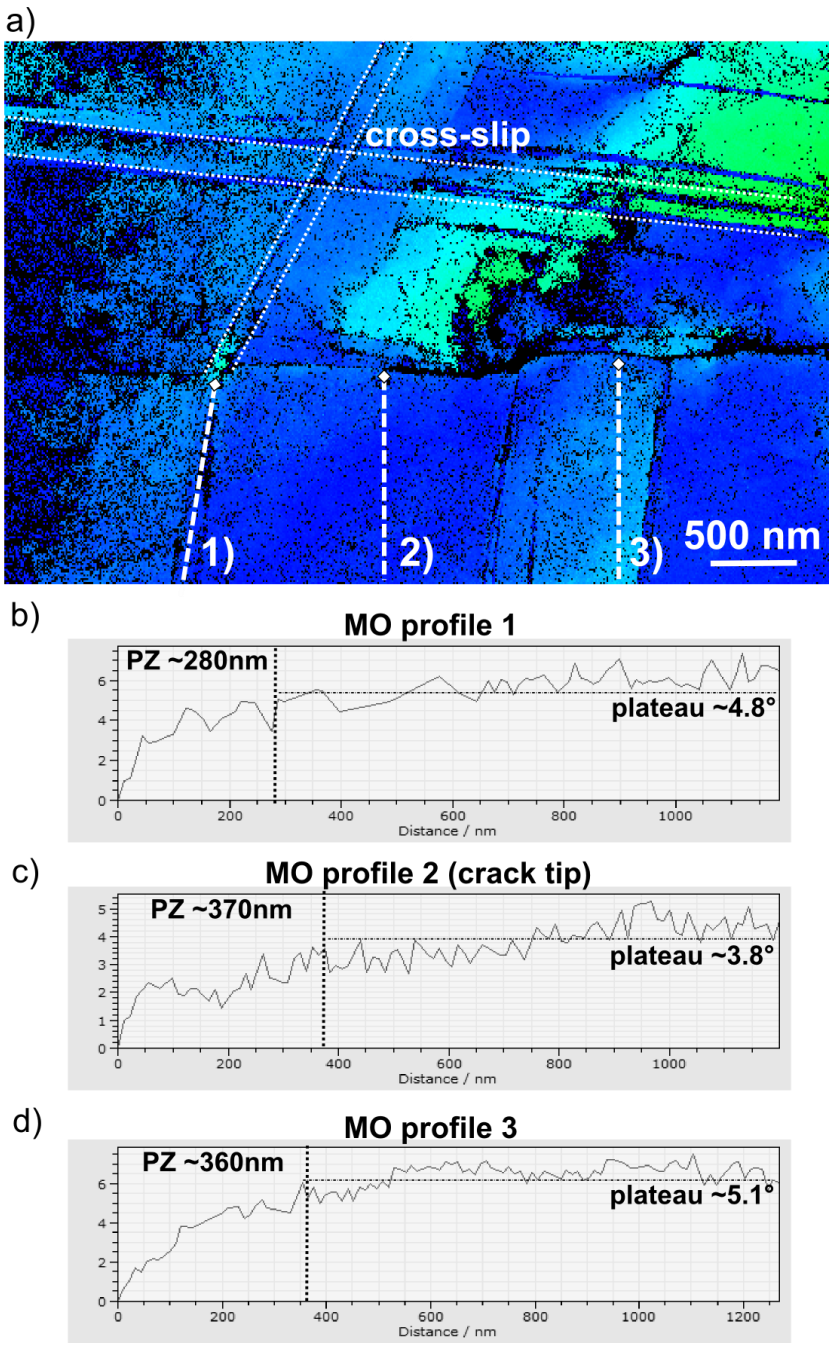

Figure 43. Average MO map and profiles from SCC sample 316INSS O CT2: a) average MO map, indicating the location of MO profiles 1, 2 and 3 (origin marked by white diamond); b) MO profile 1 located in bottom grain at void; c) MO profile 2, located in bottom grain commencing at crack tip; d) MO profile 3, located in bottom grain at crack flank at ~ 1 μm distance from crack tip; MO profiles indicate height of plateau and extent of plastic zone (PZ)

The line profiles are shown in Figure 43b-d. The extent of the PZ at the crack tip is ~ 370 nm, reaching a MO plateau of ~ 3.8 ± 1.0° (Figure 43c). In contrast, the MO plateau at the void and in zone 3 is higher, with 4.8 ± 1.1° and 5.1 ± 1.1°, respectively. Due to their close proximity to slip and DBs, these are areas of high local misorientation and therefore elevated plastic deformation. Compared to sample 316INSS N CT2 in Figure 42, the MO and therefore extent of plastic deformation at the crack tip in 316INSS O CT2 (Figure 43c) appears to be higher. It should be noted, that the colour code in Figure 42 and Figure 43, as well as in all average MO maps generated by the software, is adapted to span only the range of MO values measured in each individual map. Therefore, individual average MO maps are not universally valid and cannot be directly compared in terms of the extent of the PZ. More examples of the application of this method will be shown in Chapter 5.

4.2.6 EBSD vs. TKD and thin-foil effects

It has been mentioned in the literature that the preparation of electron transparent TEM lamellae might entail a certain relaxation of residual stresses in the sample [205]. In addition, the FIB milling could also introduce new dislocations into the specimen due to the interaction with the ion beam. Since TKD is used in this study to establish a gauge for plastic deformation near the crack tip, the influence of such factors could potentially distort the TKD data. Therefore, the final step in this study is the comparison of EBSD and TKD data of the same crack tip, presented in Figure 44. The EBSD data were acquired with a step size of 70 nm for better comparison with TKD (11 nm step size), pushing the resolution limit of the technique.

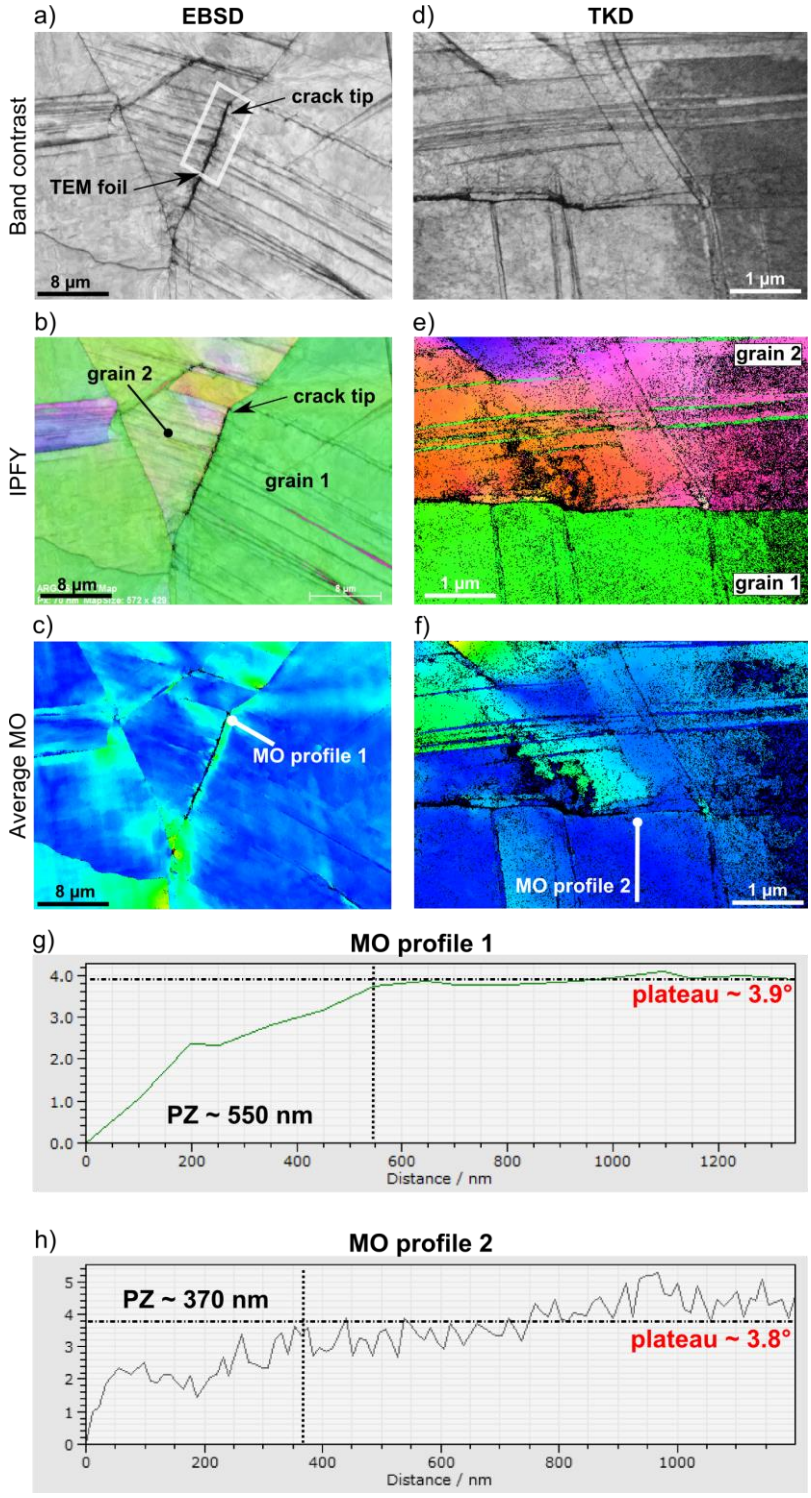

Figure 44. EBSD and TKD maps of 316INSS O CT2: a) EBSD band contrast map, crack tip and location of TEM foil indicated; b) EBSD IPFY map, legend in Figure 37d; c) EBSD average MO map; d) TKD band contrast map; e) TKD IPFY map; f) TKD average MO map; g) MO profile 1 (EBSD); h) MO profile 2 (TKD)

Figure 44a shows the EBSD band contrast map of 316INSS O CT2 and indicates the approximate location of the crack tip. In EBSD, the resolution is too poor to establish this quantity more accurately. The complementary TKD band contrast image is shown in Figure 44d. Furthermore, the inverse pole figure map in y-direction, acquired via EBSD, is illustrated in Figure 44b (legend to be retrieved from Figure 37d). In Figure 44e it can be observed that the crystallographic orientation near the crack tip (grain 1: green, grain 2: pink) in the TKD IPFY map corresponds well to the EBSD IPFY data. Attention should be paid to the fact that the cross-slip in grain 2 can only be observed in the TKD maps, but is not at all visible in grain 2 in the EBSD maps. The reason may be that, due to higher dislocation density and higher stress levels near the crack, cross-slip mainly occurs in close proximity to the open crack and hence could not be picked up via EBSD.

In addition, the average MO at the crack tip in grain 1 in both datasets was compared. Direct visual comparison between Figure 44c and Figure 44f is difficult due to the significant difference in magnitude and the fact that the colour-temperature spectrum is not universally applicable. Therefore, MO profiles were drawn in both grains for each map and the extracted PZ and plateau values were compared (EBSD: Figure 44g, TKD: Figure 44h). The results showed very similar plateau values (EBSD: 3.9° and TKD: 3.8°) and comparable PZ sizes.

Finally, the effect of bending of the thin TEM foil is demonstrated and discussed. Figure 45a shows the average MO map of sample 316INSS G CT3. In general, the level of plastic deformation in this sample is relatively low near the crack tip. Instead of localised plastic deformation at the crack tip, the stresses seem to be concentrated at the

GB ~ 1µm ahead of the crack tip. Furthermore, an elevated level of plastic deformation at the edges of the sample was detected, which indicates that the TEM foil might have bent during the FIB sample preparation process. In order to measure the extent of this bending, a MO profile was acquired in the bottom grain from the left edge to the right edge of the sample (Figure 45b). It shows a MO gradient of ~ 4.5° across the entire length of the sample. In addition, it was also established that no bending in the vertical direction took place. For this reason, the acquisition of the MO profiles from the crack tip outwards in vertical direction should not be affected by the bending of the sample.

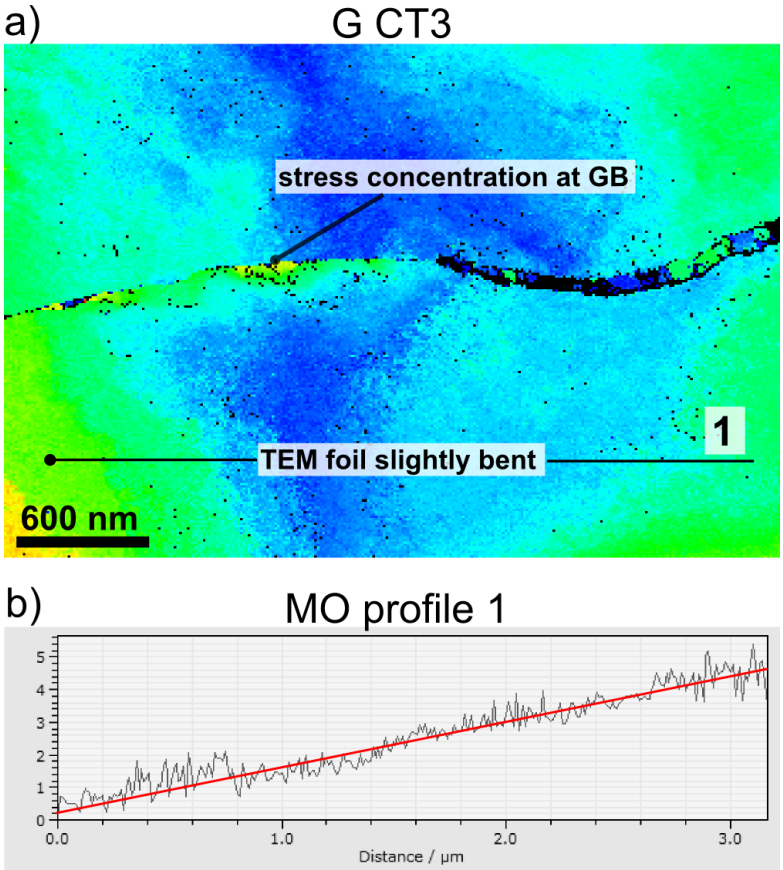

Figure 45. TEM foil bending in sample G CT3: a) average MO map; higher MO at edges due to bending; stress concentration at GB; location of MO profile 1 indicated; b) MO profile 1: ~ 4.5° MO from the left end of the foil to the right end

In conclusion, the comparison of EBSD and TKD confirmed the necessity of high-resolution orientation mapping for SCC research, as nanoscale features cannot be picked up sufficiently via EBSD. It was also concluded that, essentially, the TKD data correlate very well with the EBSD data and no significant influence of the FIB sample preparation process could be detected. The results indicate that it seems reasonable to neglect the relaxation of stresses within the thin foil or the build-up of additional stresses due to FIB sample preparation.

4.3 Making atom probe tomography accessible to SCC research

As stress corrosion cracks are 3D features, it has always been the ultimate goal of the SCC research community to also analyse them with 3D methods. In addition, the need to study SCC features on the nanoscale rules out low-resolution 3D techniques such as 3D FIB slicing. In Chapter 3.6, atom probe tomography (APT) was introduced as a 3D microscopy method with atomic resolution and excellent chemical sensitivity, which has only been applied to limited extent to SCC research. The main reason being, that many nanoscale SCC features, e.g. the oxidised GB ahead of the crack tip, are not easily accessible due to the high sample preparation efforts involved. However, by developing a new method for routinely creating APT needles which incorporate entire SCC crack tips, as described in Chapter 3.4.2, the author successfully applied APT to generate novel data from the crack tip and GB chemistry. It will be shown in this chapter that atom probe data can indeed be used to learn more about the ongoing SCC mechanisms.

4.3.1 Initial TEM investigation

The general sample preparation approach (Chapter 3.4.2), involves efforts that allow an initial investigation of each APT needle via analytical TEM. This enables the correlation of certain features inside the needles with the reconstructed atom probe data in order to provide certainty of the results and a comparative study of the analysed SCC features.

During the process of developing this technique, three APT needles (316INSS) containing SCC crack tips were produced successfully. The specimens were initially analysed with a JEOL 2100 (LaB6 filament, 200 kV), using a TEM tomography holder

(Fischione model 2050: allows for full rotation of the needle around its axis until the grain boundary is edge-on with the electron beam). The results are shown in Figure 46.

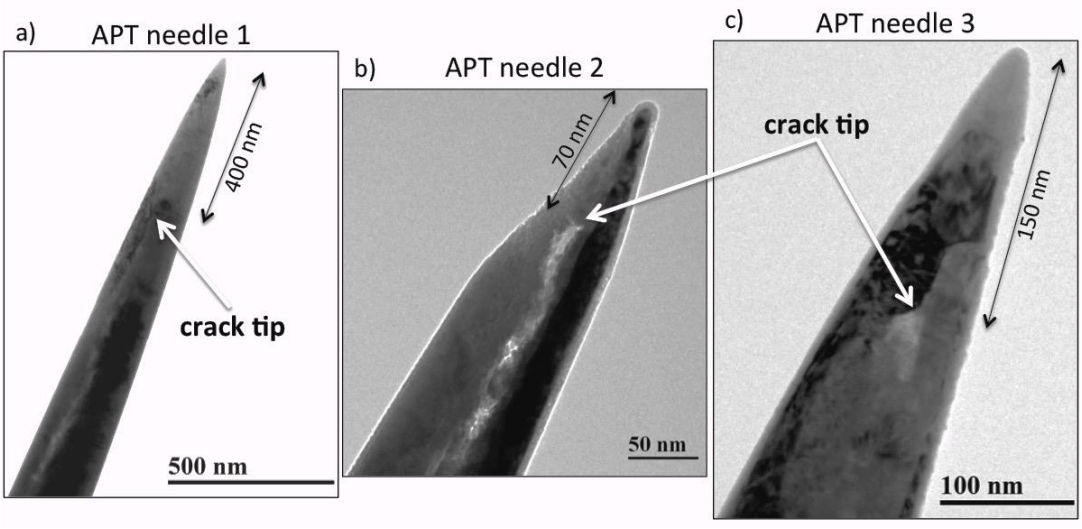

Figure 46 - TEM images of three different atom probe needles prepared, showing the crack tip location and the distance of the crack tip from the apex of the APT needle: a) APT needle 1: 400 nm from apex; b) APT needle 2: 70 nm from apex; c) APT needle 3: 150 nm from apex; *Reprinted from Corrosion Science, Vol. 98, Meisnar et al, Atom probe tomography of stress corrosion crack tips in SUS316 stainless steel, pp. 661-671, Copyright (2015), with permission from Elsevier*

All three APT needles shown in Figure 46 were prepared with the crack tips centrally located, but at different distances from the apex, APT needle 1: 400 nm, APT needle 2: 70 nm and APT needle 3: 150 nm. As will become evident, the distance from the apex is a very important quantity for a successful APT experiment and is hard to control during the sample preparation process.

As discussed in the previous chapter, the term "crack tip" refers to the portion of the open crack or GB oxide, which has fractured last, demonstrated in Figure 47. In APT needles 2 and 3 (Figure 46b and c), the sample is tilted so that the GB is edge-on. Here, the transition from GB to open crack can be observed easily. The open crack is also

filled with oxide, which can be established via analytical TEM. For APT needle 3, high-resolution EELS and EDX data were acquired using a JEOL ARM200F (cold-FEG) TEM at 200 kV. The APT needle was again tilted until the GB appeared edge-on, using the in-built rotation of the tomography holder as well as the stage tilt in the microscope for fine-tuning. The result of the STEM HAADF acquisition is shown in Figure 47, illustrating the tip of the APT needle containing the crack tip and the GB ahead of the crack front. A triple point was discovered ~ 30 nm ahead of the crack tip, highlighted in Figure 47 with the white dashed lines. Figure 48b shows a close-up view of the GB, clearly indicating its path due to diffraction contrast. It could also be established, that the crack tip is located ~ 150 nm from the apex of the atom probe needle.

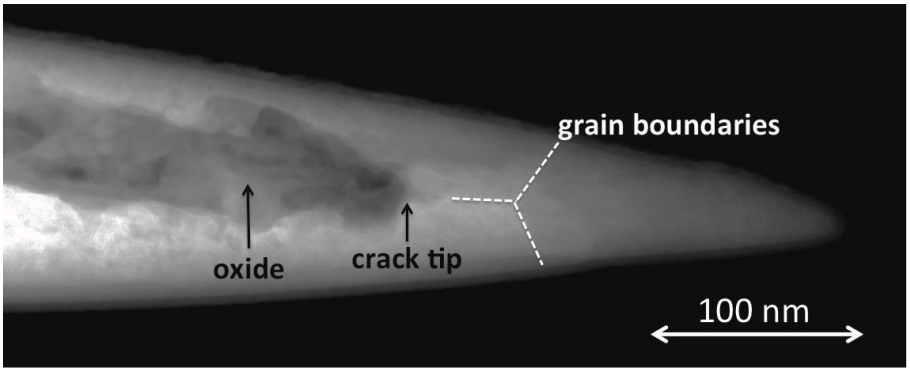

Figure 47 - STEM HAADF image of APT needle 3 indicating the location of crack tip, the oxide inside the crack and the grain boundary ahead of the crack tip (exhibiting a triple point); *Reprinted from Corrosion Science, Vol. 98, Meisnar et al, Atom probe tomography of stress corrosion crack tips in SUS316 stainless steel, pp. 661-671, Copyright (2015), with permission from Elsevier*

The same STEM HAADF image is shown in Figure 48a, indicating the crack tip region from which the close-up image in Figure 48b was taken. The oxide appears darker than the surrounding matrix and a narrow oxide finger (length ~ 15 nm) seems to be protruding into the grain boundary, suggesting GB oxidation ahead of the crack tip.

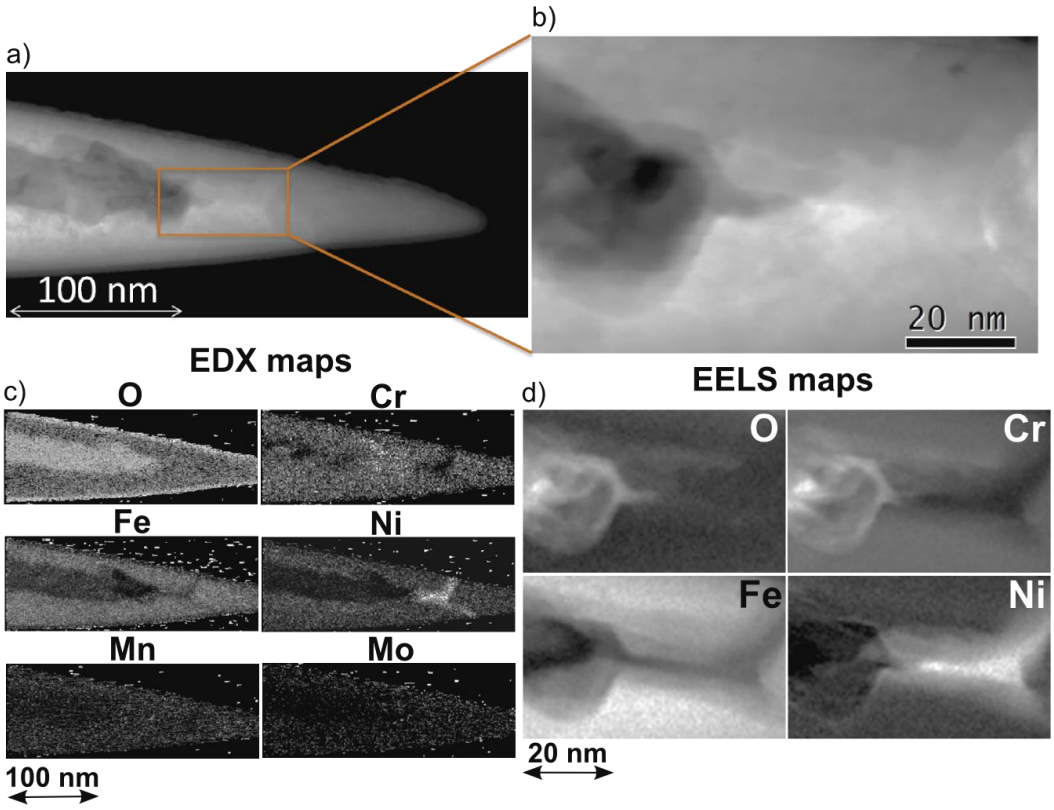

Figure 48 - STEM HAADF, EDX and EELS elemental maps of APT needle 3: a) HAADF image, overview; b) close-up HAADF image; c) EDX elemental maps: O K, Cr K, Fe K, Ni K, Mn K and Mo L lines; d) EELS elemental maps: O K, Cr L, Fe L and Ni L edges; *Reprinted from Corrosion Science, Vol. 98, Meisnar et al, Atom probe tomography of stress corrosion crack tips in SUS316 stainless steel, pp. 661-671, Copyright (2015), with permission from Elsevier*

In order to cover all relevant elements (O, Fe, Cr, Ni, Mn and Mo) in a reasonable acquisition time, both EDX and EELS analysis were conducted. This approach yields first results on the elemental distribution in the crack tip area as well as ahead of it and can be compared to the APT data at a later stage. Some features may be hard to interpret conclusively in the APT data post-processing phase, a situation that might be easily solved with complementary analytical data.

It can be established from the EDX maps in Figure 48c, that both Mo and Mn are present in small quantities and rather evenly distributed throughout the APT needle.

There is a region ahead of the crack tip, which is enriched in Ni and depleted in both Fe and Cr. The EDX O map shows that an oxide layer, a few nanometres thick, has formed on the surface of the atom probe needle and also that oxide fills the open crack.

The EELS elemental maps were acquired at higher magnification (Figure 48d; acquired at ~ 0.4 eV energy resolution, 5 nm step size) and confirm the existence of a Fe-depleted, Cr-rich GB oxide, coinciding with the oxide finger in Figure 48b, ahead of the crack tip. Away from the crack tip along the GB, this region is followed by Ni enrichment, which continues intergranularly beyond the triple point.

In order to measure the composition of the GB oxide, a line profile (4.5 nm width) was extracted from the EELS O, Cr, Fe and Ni maps at the locations indicated in Figure 49a-d. The line profile is shown in Figure 49e and ultimately confirms GB oxidation ahead of the crack tip. The oxidised GB is ~ 5 nm wide (FWHM measurement) and exhibits the following composition: ~ 32.0% O, 29.0% Ni, 24.7% Fe and 14.3% Cr. It should be noted, that this composition was determined via TEM, creating a 2D projection of a 3D volume, not taking into account potential compositional changes throughout the depth of the sample. Therefore, the error of this and all future EELS compositional measurements is rather large and in general hard to determine. However, due to the performed MSA, the experimental error can be minimised and was estimated to be ~ 10% for all EELS compositions. Furthermore, the O concentration within the matrix is potentially higher than expected due to surface oxidation of the APT sample.

The results of the EELS analysis will be compared to the reconstructed atom probe data in the next chapter.

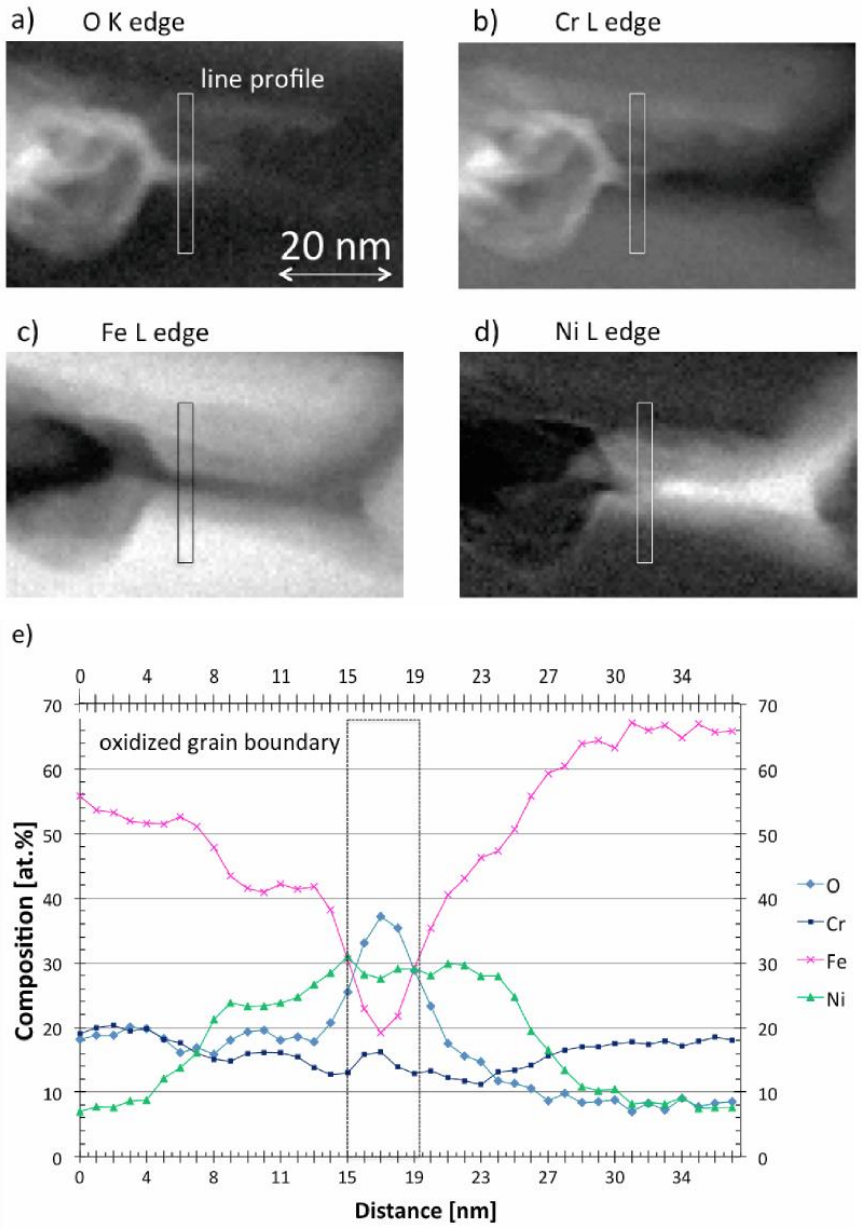

Figure 49 - EELS line profile across oxidised grain boundary: location of line profile in a) O b) Cr c) Fe d) Ni maps; e) EELS line profile, location of oxidised grain boundary indicated; oxidised portion of GB ~ 5 nm wide; composition (averaged over width: 32.0 % O, 29.0 % Ni, 24.7 % Fe, 14.3 % Cr); *Reprinted from Corrosion Science, Vol. 98, Meisnar et al, Atom probe tomography of stress corrosion crack tips in SUS316 stainless steel, pp. 661-671, Copyright (2015), with permission from Elsevier*

After the initial TEM characterisation, APT was performed on all three needles. It should be pointed out, that deformed specimens containing cracks filled with oxides are known to be susceptible to fracture during the atom probe analysis [100,164,191]. Additional lattice defects may be caused by the implantation of Ga^+ ions during the FIB specimen preparation. This makes the needle even more brittle and prone to fracture. However, all atom probe needles underwent final low-energy cleaning at 2 kV and 40 pA for ~ 10 minutes, a method reportedly limiting this problem [193].

4.3.2 Atom probe results

The experimental results were very different for all three needles and yielded useful information for future sample preparation and execution of the technique.

The first sample analysed was APT needle 1 in which the crack tip was located ~ 400 nm from the apex. However, it soon turned out that that 400 nm is too far of a distance under the applied conditions. The end of the experiment, due to high specimen voltage, was reached before any regions close to the crack tip could be evaporated. It was therefore concluded, that the distance of the crack tip to the apex of the needle has to be less than 200 nm.

In contrast, in APT needle 2, the crack tip was located only 70 nm from the needle apex and therefore, the important features were reached very quickly during the acquisition. It is very likely that, before the APT acquisition has reached a stable point after the start-up phase, some parts on the tip of the needle are subject to micro-fractures and therefore evaporate without registration on the detector. If the crack tip is too close to the apex of the needle, it is then possible that important features are missing from the

reconstruction. However, in APT needle 2, evaporated matrix material and oxide structures near the GB up to the very crack tip were found in the dataset. Hence, the reconstructed data indicate that the sample fractured at the point, when the crack tip was reached. As mentioned earlier, fracture events near oxide structures or voids are very common in APT experiments, but there is still valuable data to be extracted from short, involuntarily stopped experiments like this.

The APT run of needle 3 was much more successful than its predecessors and the entire study proved to be the first of its kind, due to complementary high-resolution ATEM analysis. In APT needle 3, the crack tip was located at ~ 150 nm from the needle apex, as shown in Figure 46c. Over 12 million ions from the crack tip region (including the oxidised GB and Ni-enrichment) were collected before the specimen fracture event that resulted in the end of the APT experiment. A volume of roughly 200 nm x 30 nm x 30 nm was reconstructed, as shown in Figure 50. Figure 50a shows the initial TEM image of the needle with the reconstructed volume illustrated as white dashed line. A full rotation of the reconstruction around its z-axis, including Fe, Cr, Ni ions as well as different Cr oxide and Fe oxide ions, is shown in Figure 50b.

In order to study the crack tip region in more detail, this area was reconstructed again separately in Figure 51. The location of the extracted region around the crack tip, including the GB oxide and Ni enrichment, is shown in Figure 51a. The reconstructed data (Figure 51b) show the oxidised portion of the GB directly ahead of the crack tip (red), the Ni-enriched region (green), the triple point as well as the surrounding matrix material (purple). A colour code for the matrix elements and oxide is given as well. For comparison, the EELS maps of Ni and Cr are displayed in Figure 51c and Figure 51d.

The main features appearing in the APT reconstruction, the GB oxide, Ni enrichment along the GB and the triple point, correlate well with the EELS data. However, there may be slight dimensional differences or contortions between the two datasets, possibly resulting from approximations in the 3D reconstruction algorithm in the APT software back-projecting the ion trajectory and calculating the origin of each ion. Nevertheless, with the demonstrated approach, the real dimensions can always be confirmed with the ATEM data. This illustrates again, how beneficial complementary APT and ATEM analysis is.

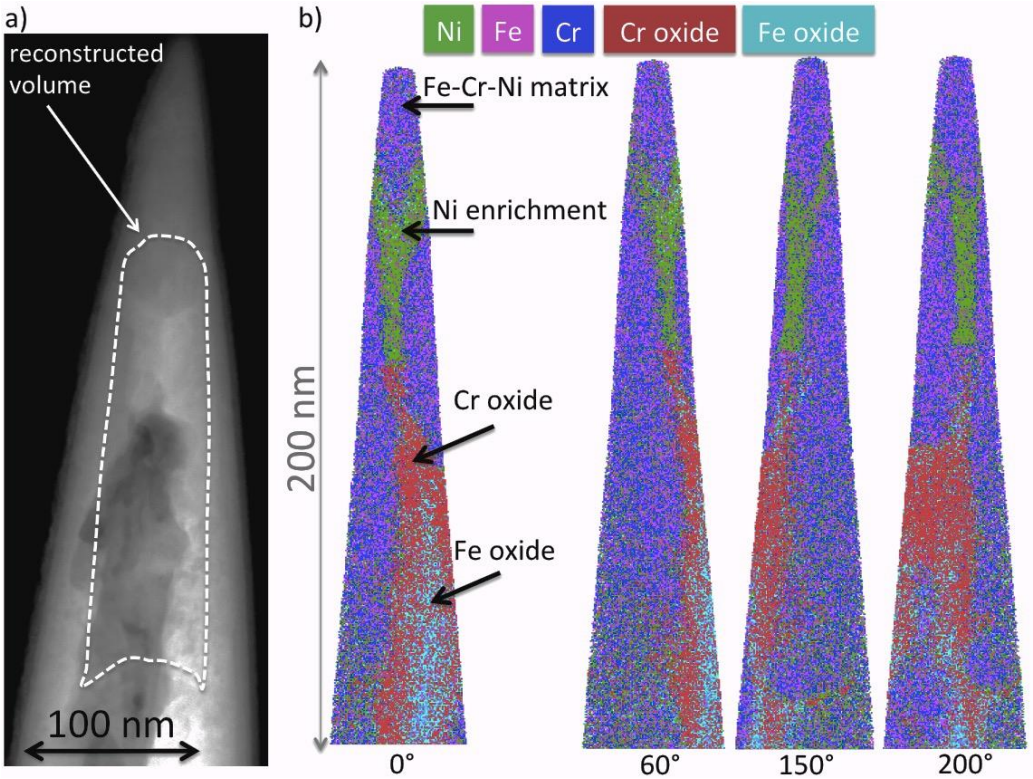

Figure 50. Overview of APT needle 3: a) STEM HAADF image indicating the approximate location of the reconstructed volume; b) atom probe reconstruction viewed at different rotations around the z-axis, highlighting the matrix, Ni-enrichment and Cr- and Fe-rich oxides (Cr oxide: CrO^+ and CrO_2^+ ions, Fe oxide: FeO^+ and FeO_2^+); *Reprinted from Corrosion Science, Vol. 98, Meisnar et al, Atom probe tomography of stress corrosion crack tips in SUS316 stainless steel, pp. 661-671, Copyright (2015), with permission from Elsevier*

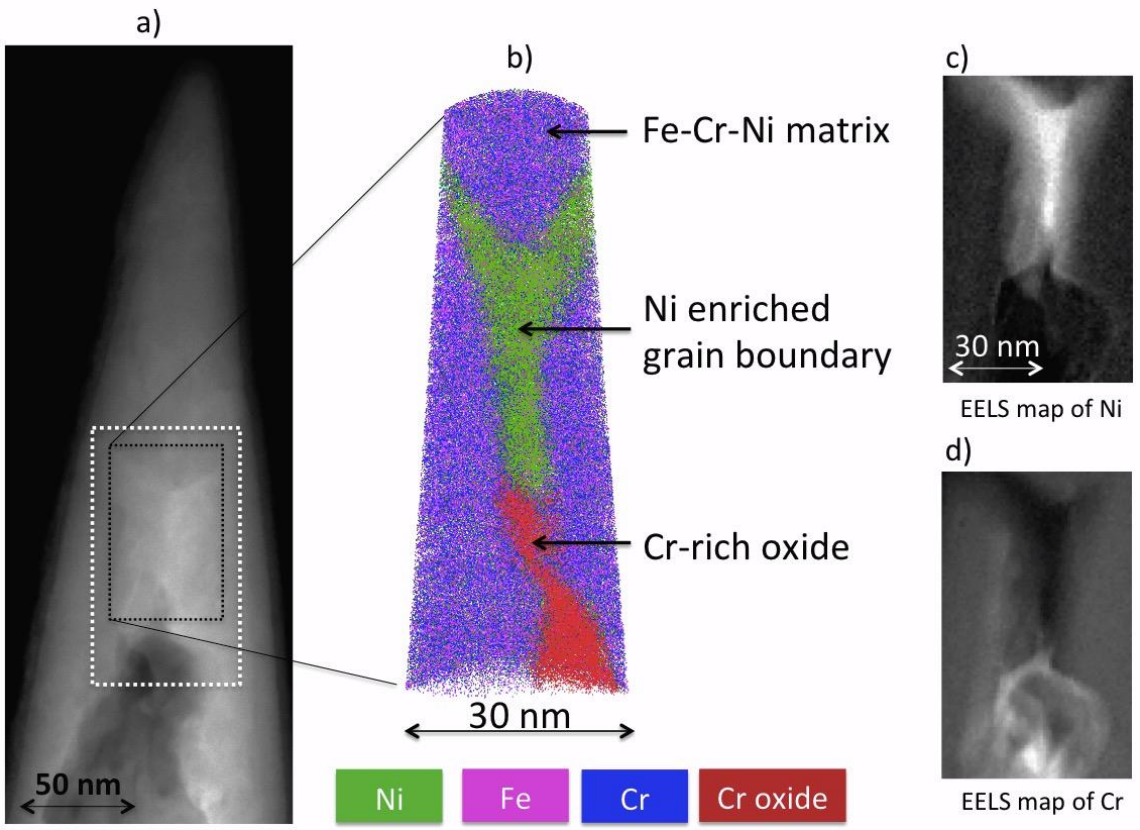

Figure 51. APT needle 3: results overview; a) STEM DF image: location of reconstructed APT volume indicated (black box) and EELS maps (white box) indicated; b) atom probe reconstruction with colour code, locations of matrix, Ni-enriched GB and Cr-rich oxide (including CrO and CrO_2) indicated; c) Ni L and d) Cr L edge EELS maps for comparison; *Reprinted from Corrosion Science, Vol. 98, Meisnar et al, Atom probe tomography of stress corrosion crack tips in SUS316 stainless steel, pp. 661-671, Copyright (2015), with permission from Elsevier*

In order to determine the matrix composition and compare it to the nominal composition of 316INSS listed in Table 1, compositional analysis was conducted in the matrix region above the triple point. With 65.2% Fe, 16.7% Cr, 9.4% Ni, 1.5% Mn and 1.2% Mo, the experimental values agree well with the nominal compositions of 316INSS. Minor elements such as Si, P, C and S were not determined.

The composition of the Ni-rich region was extracted from two different points, indicated in Figure 52a (point 1 near the GB oxide and closer to the crack tip, point 2 near the triple point); the results are listed in Table 5. Both Ni and Cr contents decline with increasing distance from the crack tip and GB oxide. In contrast, the Fe content seems to increase over the same distance.

	Ni	Fe	Cr	Mn	Mo
1 - bottom (Figure 52a)	67.4	24.8	3.5	0.3	1.1
2 - triple point (Figure 52a)	63.0	29.9	2.4	0.1	1.2

Table 5. Composition in Ni-enriched region; all values in at.%; 1 was extracted from the bottom part of the Ni-rich region, close to the grain boundary oxide; 2 was extracted from the triple point; measurement error 2.9%, based on number of ions

In order to illustrate the Ni distribution in the reconstructed volume, only Ni ions are displayed in Figure 52a. To highlight the region of Ni enrichment, an iso-concentration surface with a threshold of 45.7% Ni was created. A line profile acquired across the width of the Ni-enriched GB region (cylinder C in Figure 52a, dimensions: 5.3 nm x 5.3 nm x 23.4 nm) is shown in Figure 52b. With this data, the width of the Ni-rich GB was determined as 6.5 ± 0.5 nm (FWHM measurement). In this region, the Ni concentration rises from its matrix value of ~ 10 % to ~ 65 %. On the contrary, both Fe and Cr concentrations drop to ~ 30 % and ~ 5 %, respectively. According to the line profile, outside of the Ni-rich GB, the Fe, Cr and Ni concentrations match the nominal matrix composition of the alloy (~ 65% Fe, ~16-18% Cr and 10% Ni, measurement error ~ 2%). It should be noted for the discussion in the next chapter, that no Ni depletion was

observed in the line profile at the interface on either side of the Ni-rich region. In addition, there was no indication of any Fe- or Cr-enrichment in this area.

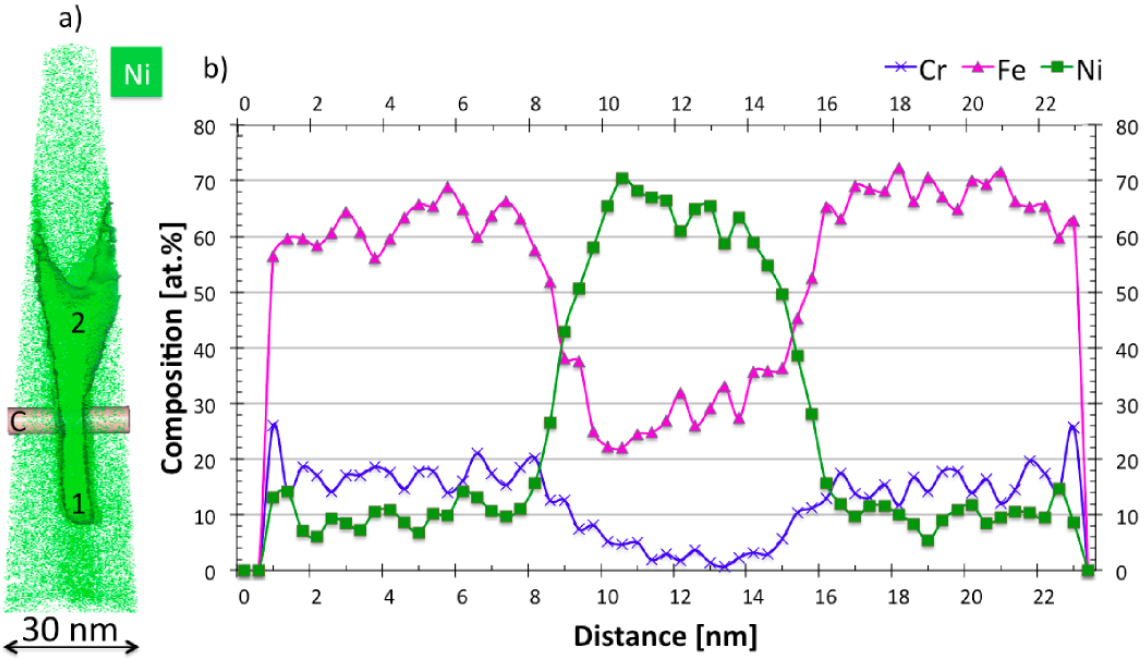

Figure 52. Line profile across Ni enrichment (bin width 0.4 nm); a) APT needle 3, Ni ions (green), area of Ni enrichment enveloped by iso-concentration surface (threshold: 45.7% Ni); C: cylinder for line profile; 1: location of sphere 1 for composition analysis (Table 5); 2: location of sphere 2; b) line profile across Ni enrichment; FWHM of Ni enrichment: 6.5 nm; *Reprinted from Corrosion Science, Vol. 98, Meisnar et al, Atom probe tomography of stress corrosion crack tips in SUS316 stainless steel, pp. 661-671, Copyright (2015), with permission from Elsevier*

In the next step, the Cr-rich GB oxide, starting at the crack tip and reaching as far as the Ni-rich GB region, was investigated further. Figure 53a shows the reconstructed APT needle (for clarity only visualising Fe, Cr, Ni and Cr oxide, i.e. CrO and CrO_2, ions) from different rotation angles, indicating the analysed region with white dashed lines at 0°. Looking at all displayed rotations around the z-axis in Figure 53a, it becomes

clear that the Cr oxide is not uniform throughout the needle and changes its shape significantly from the front to the back of the needle.

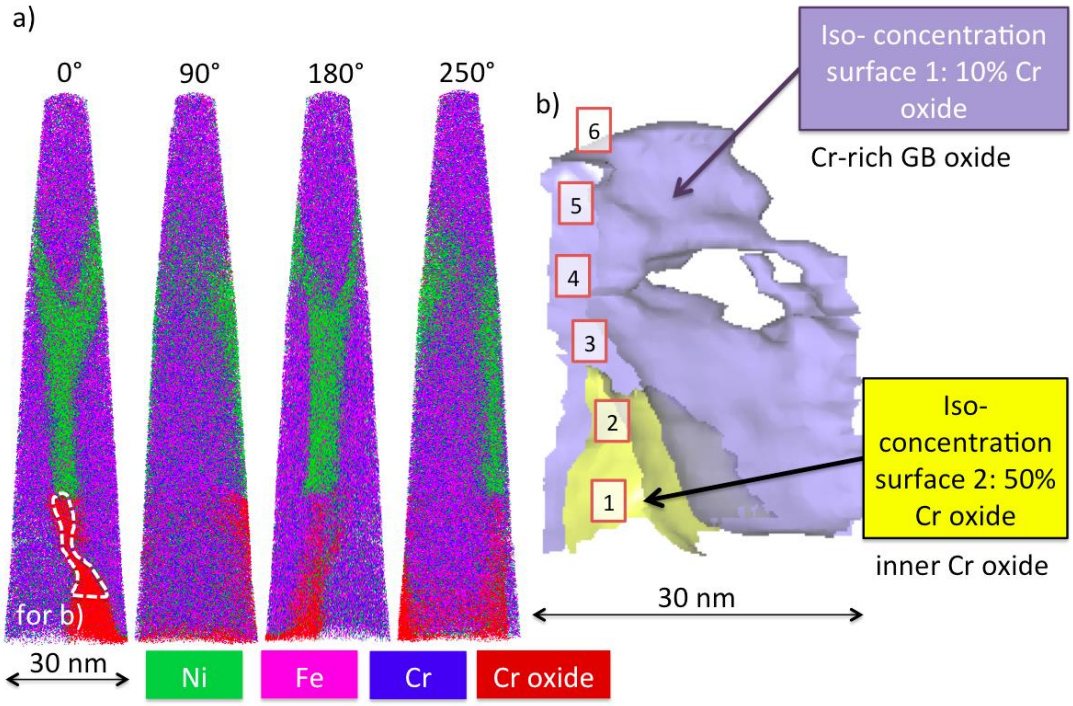

Figure 53. a) Reconstructed volume including Ni enrichment and Cr oxide (including CrO and CrO_2) rotated around z axis; white dashed line indicates location of extract for b); b) plan-view (3D) of Cr oxide: iso-concentration surface 1 envelops regions > 10% Cr oxide, iso-concentration surface 2 envelops regions > 50% Cr oxide; numbers 1 to 6 indicate the locations of composition measurements; *Reprinted from Corrosion Science, Vol. 98, Meisnar et al, Atom probe tomography of stress corrosion crack tips in SUS316 stainless steel, pp. 661-671, Copyright (2015), with permission from Elsevier*

In order to demonstrate the structure of the Cr-rich GB oxide, this region as indicated with white dashed lines in Figure 53a - 0°, is displayed as a close-up 3D side-view in Figure 53b. The application of two different iso-concentration surfaces (1: threshold 10 % Cr oxide, 2: threshold 50 % Cr oxide; Cr oxide... CrO and CrO_2), an easy way in the APT software to illustrate 3D structures, indicates that there are at least two

different types of oxide present. Iso-surface 1 envelops an oxide region containing 10 % or more Cr oxide, whereas iso-surface 2 indicates a volume that contains more than 50 % Cr oxide. In order to identify the oxide structures, the exact composition of the Cr oxide was determined at six different points (Figure 53b, numbers 1-6) with an estimated measurement error of 2.9%. The results are listed in Figure 54.

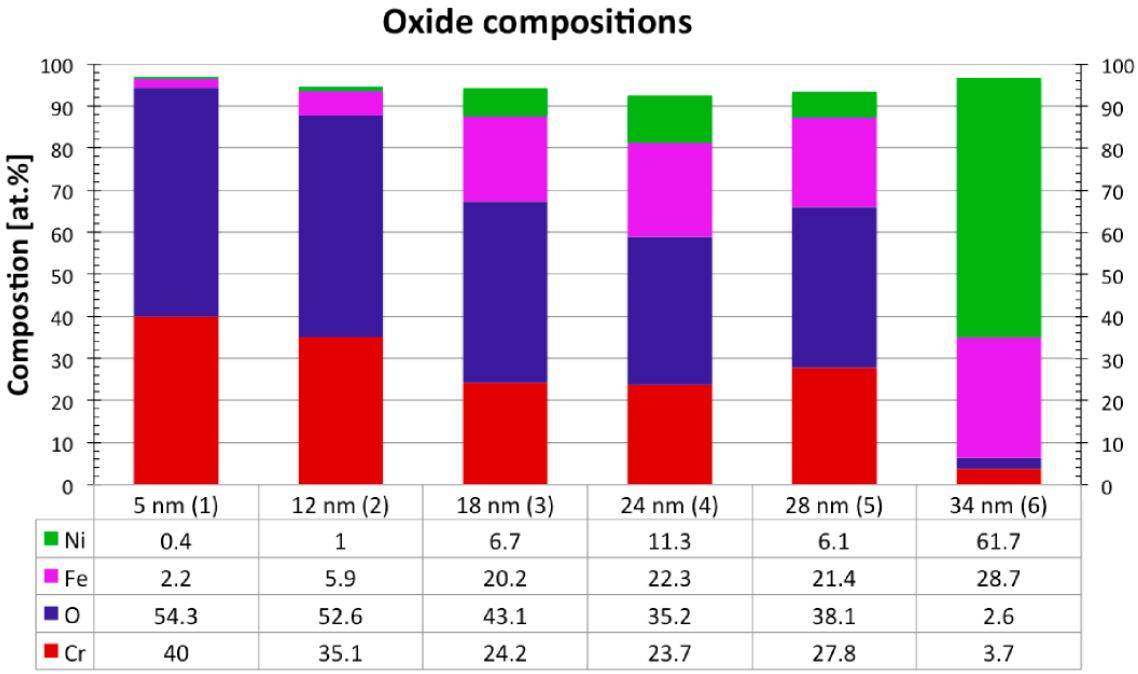

	5 nm (1)	12 nm (2)	18 nm (3)	24 nm (4)	28 nm (5)	34 nm (6)
Ni	0.4	1	6.7	11.3	6.1	61.7
Fe	2.2	5.9	20.2	22.3	21.4	28.7
O	54.3	52.6	43.1	35.2	38.1	2.6
Cr	40	35.1	24.2	23.7	27.8	3.7

Figure 54. Composition measurements (in at. %) from 6 different regions (indicated in Figure 53b) within the Cr-rich oxide and Ni-enrichment; measured distance from crack tip: 1) 5 nm; 2) 12 nm; 3) 18 nm; 4) 24 nm; 5) 28 nm; 6) 34 nm; *Reprinted from Corrosion Science, Vol. 98, Meisnar et al, Atom probe tomography of stress corrosion crack tips in SUS316 stainless steel, pp. 661-671, Copyright (2015), with permission from Elsevier*

The locations of points 1-6 were chosen at nearly-equal distances to each other, with point 1 being the closest to the crack tip and point 6 being the closest to the Ni-rich region and therefore closest to the end of the GB oxide. Figure 54 shows that the O content decreases constantly throughout the GB oxide with increasing distance from the

crack tip. However, it seems that the decline is happening in certain steps: Step 1) point 1 and point 2, ~ 53 % O; Step 2) point 3 to point 5, ~ 40 % O; Step 3) point 6, ~ 2.5 % O. In a similar fashion, the Cr content decreases steadily from point 1 to point 3 (from 40 % to 24.2 % Cr), but remains relatively constant thereafter until it experiences a sudden drop at point 6 to 3.7 % Cr. Both Fe and Ni content start close to 0 % in point 1 and exhibit a sudden surge between points 2 and 3. They remain relatively constant until point 6, where the Ni concentration rises suddenly to 61.7 % and the Fe concentration to 28.7 %.

These results suggest that there may be two different types of Cr oxide present. The inner Cr oxide (discussed in Chapter 1.6.2), usually present ahead of the crack tip, extends ~ 12 nm into the unfractured GB region and consists mainly of O and Cr (points 1 and 2). The stoichiometry in this region suggests an oxide structure of the type Cr_2O_3. Further ahead of the crack tip (points 3 to 5), the intergranular GB oxide changes composition, exhibiting near-equal amounts of Cr and Fe and ~ 40 % O. This indicates a Fe-Cr spinel-type oxide, which has previously been observed along GBs in stainless steels [100].

4.3.3 Discussion

The study of three APT needles with different distances of the crack tip to the apex of the needle showed, that the ideal distance for a successful experiment is between 70 - 150 nm. No data about the crack tip region can be acquired with too far a distance, as the DC voltage limit will be reached before the analysis reaches the region of interest. On

the other hand, the relevant regions might be removed during sample preparation or evaporated too quickly if the distance is too small.

In APT needle 3, the crack tip was located at a suitable distance from the needle apex and therefore, an APT acquisition of the entire crack tip including the GB and Ni enrichment ahead of it was achieved.

As Ni is the noblest element under PWR conditions compared to Fe and Cr, it is inclined to remain metallic when not directly exposed to the environment. Therefore, it diffuses away from any forming oxide structures and as a result, Ni enrichment is often observed in the matrix behind the oxide metal interface and sometimes ahead of crack tips. In this study, a composition profile was acquired across the Ni enriched GB (Figure 52). Despite the high Ni content at the GB, the profile shows no Ni depletion in the adjacent matrix. Similarly, the matrix composition does not account for the Fe and Cr depletion inside the Ni-rich GB by showing any enrichment at the interface region. These observations suggest that the diffusion of metallic species occurs along the GB instead of an inwards or outwards movement through the metal-GB interface. In support of this theory, it is well known that GBs are areas of high local dislocation density and therefore provide fast diffusion paths for the matrix elements to travel to different regions within the material.

Due to the novel method of APT sample preparation, the preliminary study of the crack tip within the APT needle was possible. A key target was to compare the acquired APT data to the ATEM results and it became apparent that each technique has its own advantages and disadvantages. EELS is a widely used analytical technique with resolution limits of less than 1 nm. Nevertheless, the recorded EELS data stem from a

2D projection of, essentially, a 3D volume. This is less of a problem in the case of most TEM foils, where there are usually very few changes along the depth of the sample. Stress corrosion cracks however, include features that may change over the depth of a thin (< 100 nm) TEM lamella. For instance, if the GB is not tilted edge-on, it will appear smeared and slightly broader than it actually is. Another example are features that are so small that they do not extend across the entire depth of the TEM specimen and contributions from the surrounding areas will distort the results. APT on the other hand, is a 3D technique with excellent capabilities, but it involves very complicated sample preparation and highly complex data reconstruction algorithms. Therefore, it has proven very useful to correlate APT results with another high-resolution technique such as ATEM.

It was established via the atom probe data that the GB oxide is not uniform throughout the depth of the sample (Figure 50b). The feature changes both its shape and its composition over this distance. Comparing the EELS data (Figure 49) to the atom probe results (Figure 54), it becomes obvious that there are major compositional differences (EELS experimental error ~ 10%). The EELS data, averaging over the depth of the sample, indicate that the composition of the oxidised GB is 32.0% O, 29.0% Ni, 24.7% Fe, 14.3% Cr. In contrast, the APT data were much more accurate, with a standard error of less than 3%, and showed a separation of the GB oxide into two different oxide phases of different composition (Figure 54). The first oxide phase consists of 55 % O and 40 % Cr, with very small Fe and Ni contributions (Figure 54, points 1 and 2). This stoichiometry matches well with the composition of chromia, or Cr_2O_3. In general, the formation of chromia is very rare in stainless steels under PWR

conditions because there is not enough Cr for it to form. Here, we observed it directly ahead of the crack tip over a distance of < 10 nm. The crack tip is known as a highly stressed region, where the stresses accumulate and diffusion related phenomena are most pronounced. The resulting additional provision of Cr due to higher diffusion in this region might be facilitating the formation of chromia. Due to the small dimensions of this structure, only APT could pick up its existence. These observations might suggest that Cr-rich oxides form more easily in regions where substitutional diffusion is favoured, such as the crack tip with its associated higher applied stresses.

The second oxide phase was found between the chromia phase and the Ni-enriched GB region. This "GB oxide" was determined as Fe-Cr spinel-type oxide (Figure 54, points 3-5), previously observed in stainless steels by Kruska *et al* [100].

Finally, Ni depletion near the crack tip and Ni enrichment ~ 20 nm ahead of it may confirm that the element indeed diffuses through the GB away from the crack tip and any forming oxide structures.

5. The temperature dependence of SCC propagation in stainless steels

The influence of various parameters on the SCC crack propagation process is a recurring theme within this thesis. Chapter 1.6 described how the matrix composition of the alloy, the pre-existing cold work level, as well as the water chemistry can influence the underlying SCC mechanisms. Within the framework of this project, the temperature dependence of the SCC crack growth rate (CGR) in SUS316 stainless steel was investigated. The results and conclusions will be discussed in the next chapters.

5.1 Previous work

Through thorough investigation of the CGR in different stainless steel types over a wide temperature range, Arioka *et al* observed that in cold-worked SUS316 the CGR or SCC penetration depth increases with increasing temperature between 250°C and 330°C [111]. However, it was also established that the CGRs seem inhibited above ~ 330°C and that there is a clear peak in the CGR between 320°C and 340°C [37,206]. Therefore, Arioka *et al* suggested that for non-sensitised SUS316, at least two rate-limiting processes must be involved in the SCC crack propagation process, i.e. thermally activated diffusion and electrochemical reactions on the surface.

According to Arioka's studies, it appears that the relationship between CGR and temperature (T) also depends on the sample's pre-existing cold work level. The lower the cold work level, the lower the temperature at which the peak occurs [38]. Furthermore, the yield strength of SUS316 was found to decrease with increasing T, a very important fact as the CGR itself increases with increasing yield strength [35]. Consequently, it

appears that in addition to diffusion processes and electrochemical reactions, mechanical effects such as plastic deformation and the defect density within the material may be further rate-controlling processes that must also be considered.

5.2 Methodology

There is currently no conclusive justification for the suppression effect on the CGR at higher temperature. The purpose of this thesis is to offer some explanations based on the experimental results acquired. For this purpose, the SUS316 specimens provided by INSS were the focus of this study (more information on the specimens is given in Chapter 2). The four specimens were tested at different temperatures, 320°C, 340°C, 350°C and 360°C, around the peak in the CGR-T diagram. The CGR as a function of T is plotted in Figure 56 (blue line). The objective was to gain an understanding on the changes in the CGR at these temperatures by comparing key SCC features via selected (electron) microscopy methods, i.e. crack path and morphology, elemental distribution, crack tip chemistry, plastic deformation near the crack tip.

In the first stage, all four bulk specimens were cross-sectioned and studied in the optical microscope after colloidal silica polishing. It was observed that the SCC crack paths commence at close proximity to the pre-crack tip and quickly branch off into two separate crack paths, as observed for most specimens extracted in the T-S orientation.

In the next step, the crack lengths were measured in order to establish the CGR (crack length divided by test duration). Historically, the CGR measurement is based on the well-known technique of determining the depth of the SCC crack on the fracture

surface after intentional fracture [35,37], not taking the bifurcation of the crack into account. For this study, however, the crack lengths were obtained from the prepared cross-sections by adding up the lengths of both branches of the SCC crack, as demonstrated in Figure 55. This could be significant for the understanding of applied stresses during testing at each crack tip, since the load is effectively shared between the various active crack tips in the sample.

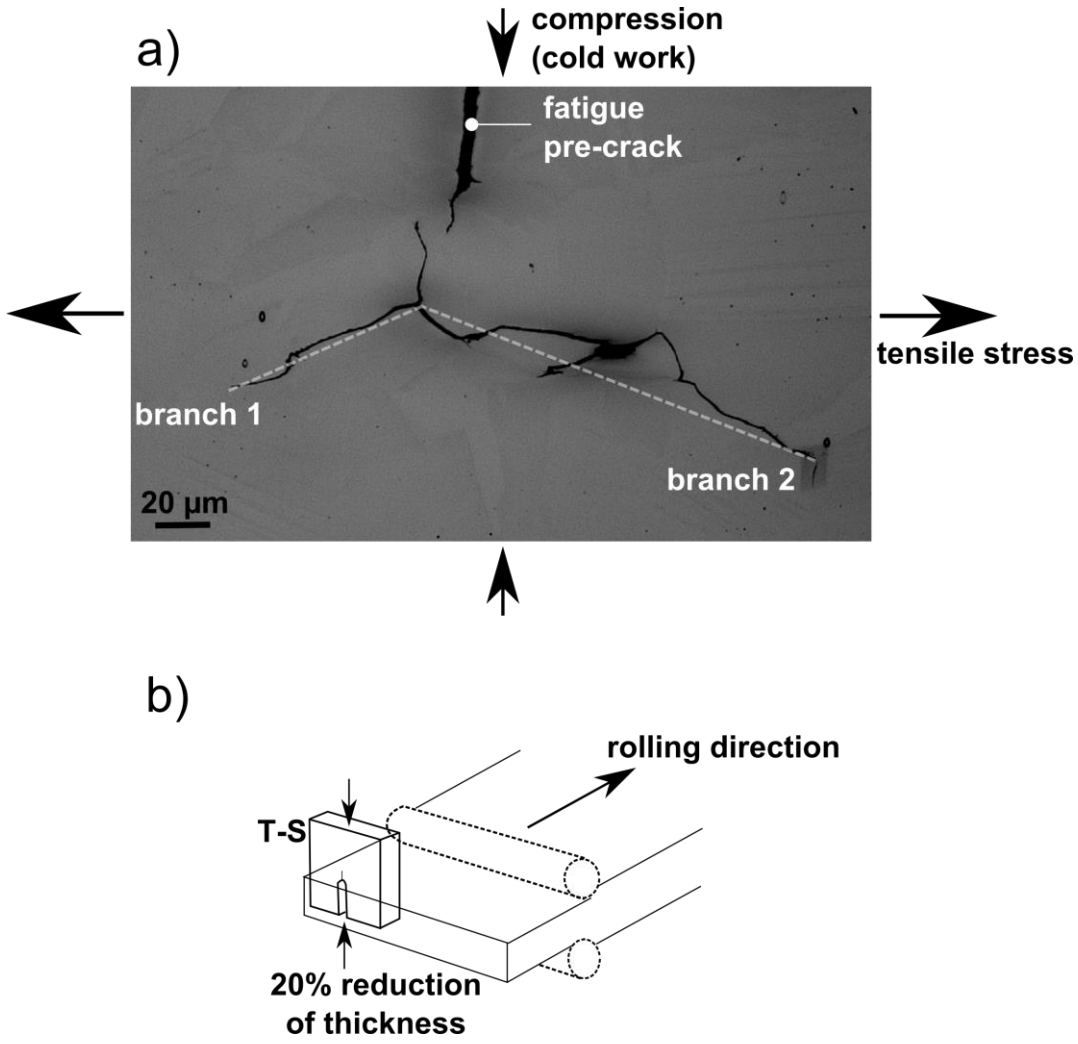

Figure 55. a) Optical micrograph of SCC cross-section in 316INSS O (360°C) sample; pre-crack and SCC crack branches 1 and 2 are indicated as well as cold working and external load direction; b) cold rolling direction for T-S specimen

It has been observed that the crack lengths measured via the two methods are very different for bifurcating cracks and have a significant impact on the calculated CGR. Figure 56 shows that the CGR determined via the historically established fracture-surface-approach (blue line) deviates significantly from this new total-crack-length method (green line), especially at lower temperatures. In addition, Figure 56 reveals the influence of the SCC test temperature on the CGR, which peaks at temperatures between 320°C and 340°C depending on the method used. While the CGR calculated by Arioka *et al* (fracture-surface-method) shows a peak at ~ 340°C, the CGR calculated via the added lengths of both crack branches shows further CGR enhancement at lower temperatures such as 320°C.

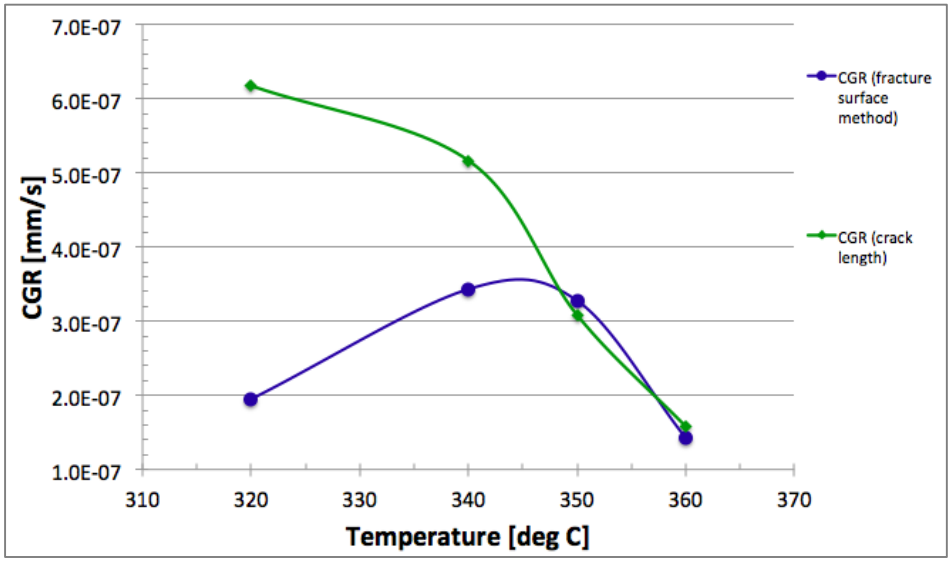

Figure 56. Temperature dependence of SCC CGR as measured via two different methods: fracture-surface-method (blue) has peak at 340°C; crack-length-method (green) grows further with lower temperature until 320°C; CGR measurements based on established crack length divided by SCC test duration

Although no data from samples tested below 320°C have been acquired in this study, the peak in the CGR is expected at 320°C or just below. This assumption is based on the existence of a directly proportional relationship of CGR and T at lower temperatures and the fact that the inhibition of the CGR in austenitic alloys was observed between 320°C and 340°C [37,38].

In order to investigate the relationship between CGR and the SCC test temperature, 15 crack tips were prepared for TEM characterisation from the four 316INSS bulk specimen, (FIB lift-out methodology for the specimen preparation is explained in detail in Chapter 3.4.1). The TEM samples were plasma cleaned for 5 minutes before analysis with a JEOL ARM200F (200 kV) cold-FEG TEM.

Finally, the TEM lamellae were plasma cleaned again and TKD was performed in a Zeiss Merlin SEM on the crack tip region.

5.3 Results

5.3.1 Crack morphology

The study of the crack morphology in the analysed samples includes the examination of the crack lengths, investigation of the crack paths and localisation of all crack tips. This can be achieved via optical microscopy or SEM. In addition, EBSD was used to study crystallographic features along the crack path as well as the localised concentration of plastic deformation in the bulk specimen. Finally, the crack opening mode was determined via TEM imaging.

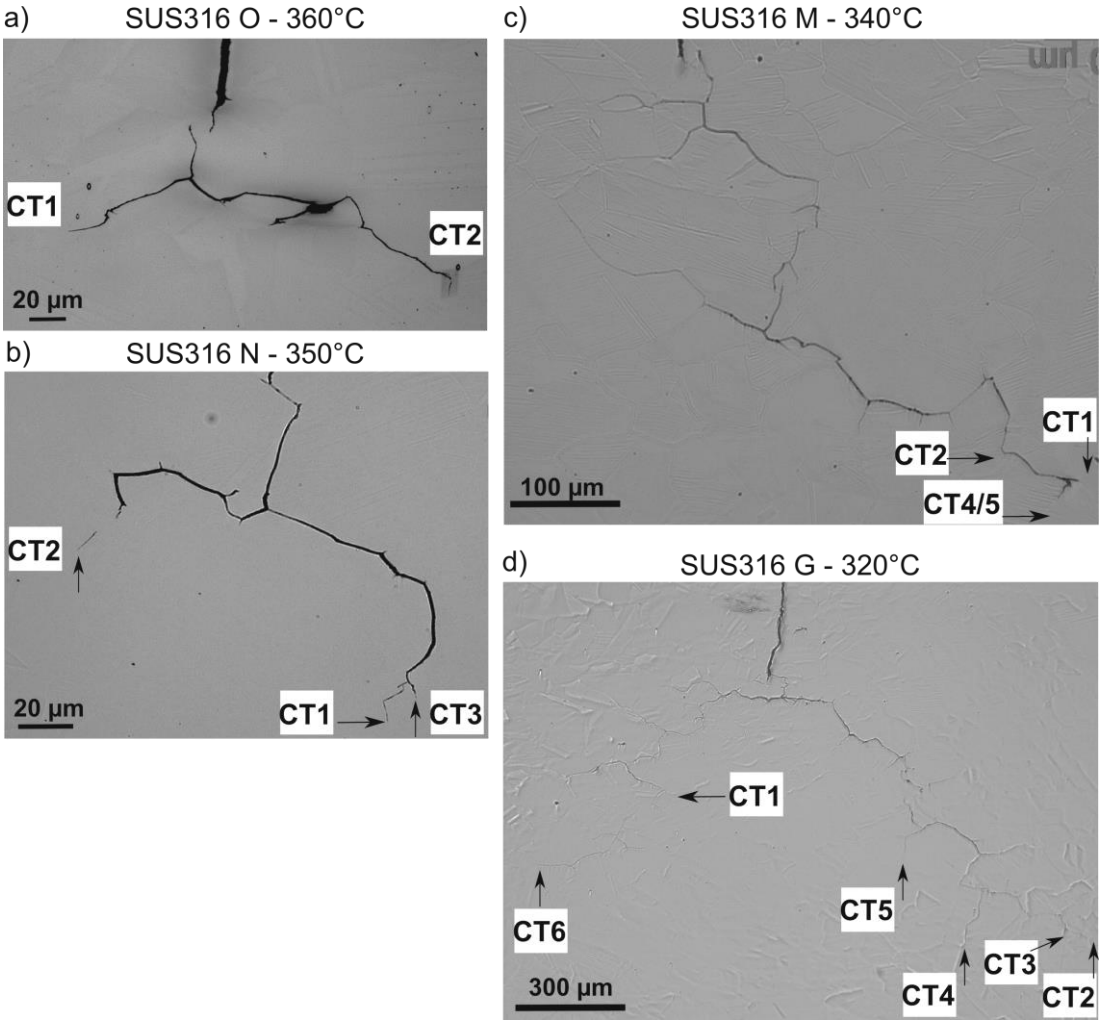

Figure 57. Optical micrographs of all four 316INSS bulk samples: a) O - 360°C; b) N - 350°C; c) M - 340°C; d) G - 320°C; location of crack tip (CT) lift-outs indicated

Sample	Test duration [h]	Total crack length [mm]	CGR [mm/s]e-7	Total number of CTs	No. of CTs lifted out
O - 360°C	720.5	0.41	1.58	2	2
N - 350°C	720.5	0.8	3.08	3	3
M - 340°C	720.5	1.34	5.17	>5	4
G - 320°C	1003.9	2.23	6.17	>10	6

Table 6. 316INSS bulk specimen data: test duration; total length of crack path measured via crack-length-method including both branches; calculated CGR (total crack length divided by test duration); number of SCC crack tips found in sample; number of SCC crack tips lifted out and prepared as TEM lamella

The optical micrographs in Figure 57 show the SCC crack paths in all four 316INSS specimens. The fatigue pre-cracks are all located either just inside or just outside the top edge of the images. The location of all crack tips that were prepared as TEM specimens (in total 15) is indicated. Information on the crack lengths, total number of crack tips and number of TEM lift-outs can be retrieved from Table 6. It can be observed that 316INSS O and N, tested at 360°C and 350°C, respectively, exhibit short total crack lengths, 0.41 mm and 0.8 mm, and only few crack tips. In comparison, 316INSS M and G, tested at 340°C and 320°C, respectively, both exhibit elevated crack lengths and higher crack tip numbers. When normalised by the test duration, the CGR appears as in Figure 56 (green line). It should be noted, that the SCC test for 316INSS G (320°C) was approximately one third longer than the SCC test for the other temperatures, which has been taken into account for the CGR.

Nevertheless, the CGR is still enhanced and almost 5 times higher at 320°C than at 360°C. Furthermore, the number of SCC crack tips increases with decreasing temperature. At 320°C, the total number of located crack tips is more than 5 times higher than at 360°C. It should be noted, that these measurements are only valid for the sample cross-sections currently under review. As SCC cracks are three-dimensional features, the crack length as well as the number of crack tips can vary throughout the depth of the sample. It has been confirmed via the fracture of the SCC specimens by INSS that the maximum crack length can be found halfway through the depth of the bulk specimen. However, as this is true throughout the temperature range in this study, the change in crack length does not have a significant impact on fundamental conclusions of this study.

From the optical micrographs it can also be observed that the crack morphology of 316INSS M (340°C), Figure 57c, deviates from that of the other samples. The crack is relatively asymmetrical and does not branch off into two separate paths as clearly as the other cracks. This could be merely a result of the 3D structure of the SCC crack, i.e. both branches are not visible in the current cross-section, or it might be an indicator of the SCC mechanisms involved. Another possible explanation could be an obstacle in the left crack path in 316INSS M, which resulted in asymmetrical strain distribution and therefore the SCC crack is more pronounced in the other direction.

In the next step, EBSD analysis was performed on the bulk specimens, the results from which are presented in Figure 58 and Figure 59, in the same orientation as the optical micrographs in Figure 57. From the IPF maps it can be observed that the grain size distribution varies slightly depending on the location in the sample. In close proximity to the fatigue pre-crack as well as the SCC crack, the grain size appears to decrease slightly. In addition, the grains seem slightly elongated in horizontal direction, which is most probably due to the direction of the applied cold work. The samples were extracted in T-S direction and therefore cold-rolling was applied in vertical direction, as shown in Figure 58. The external stress (tensile, constant load) was applied perpendicular to the pre-crack. The average MO maps suggest the existence of areas of higher strain concentration in the samples, which seem to be mainly GBs, regions with a high number of DBs as well as some heavily deformed grains. It can be observed in sample 316INSS G (Figure 59c), where a relatively large area was mapped, that regions of higher strain concentration appear everywhere in the analysed region and not solely near the SCC crack.

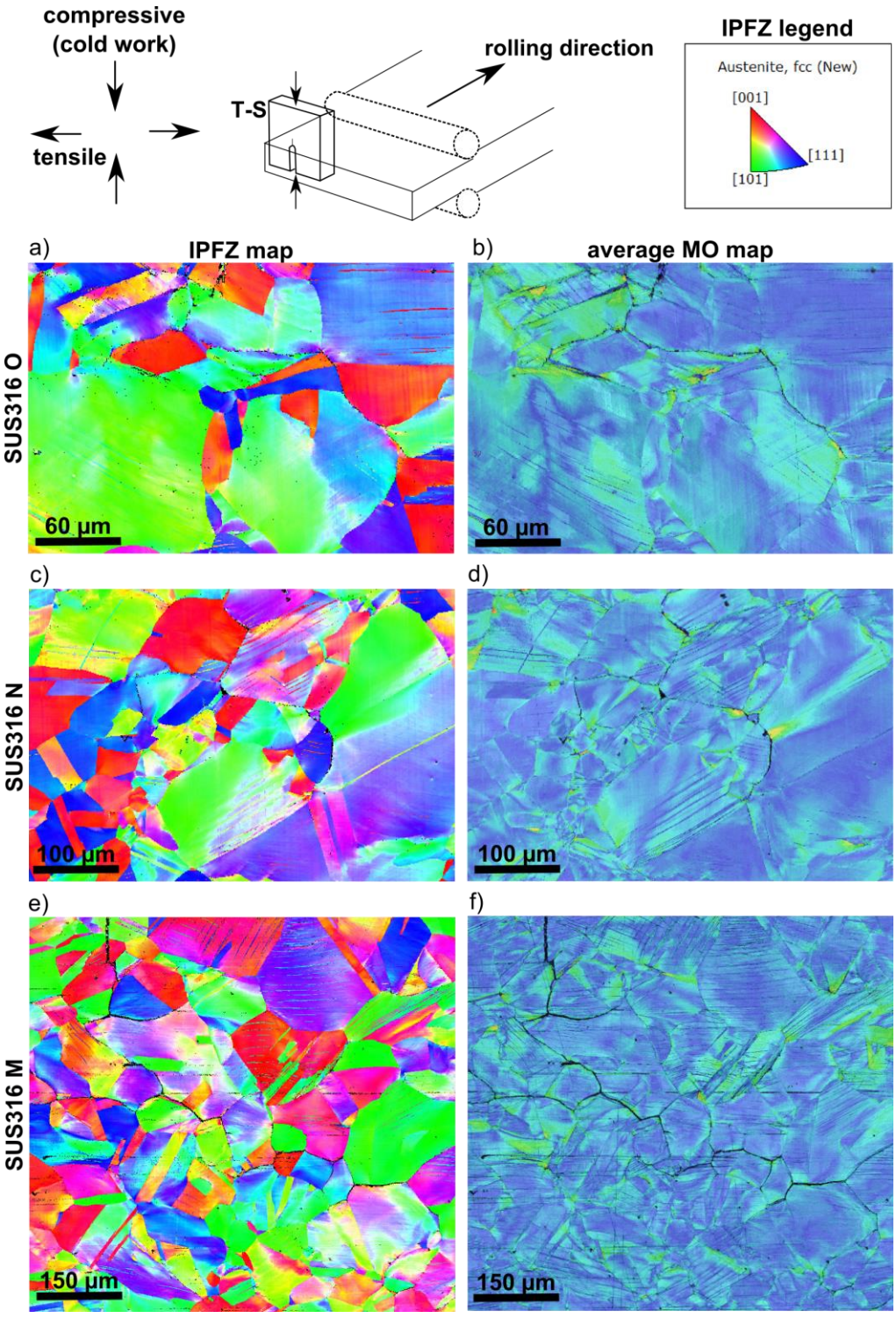

Figure 58. EBSD analysis of samples 316INSS O, N and M; a) IPFZ of 316INSS O (360°C); b) average MO map of 316INSS O (360°C); c) IPFZ of 316INSS N (350°C); d) average MO map of 316INSS N (350°C); e) IPFZ of 316INSS M (340°C); f) average MO map of 316INSS M (340°C); IPF legend and stress (cold-rolling and external load) directions indicated

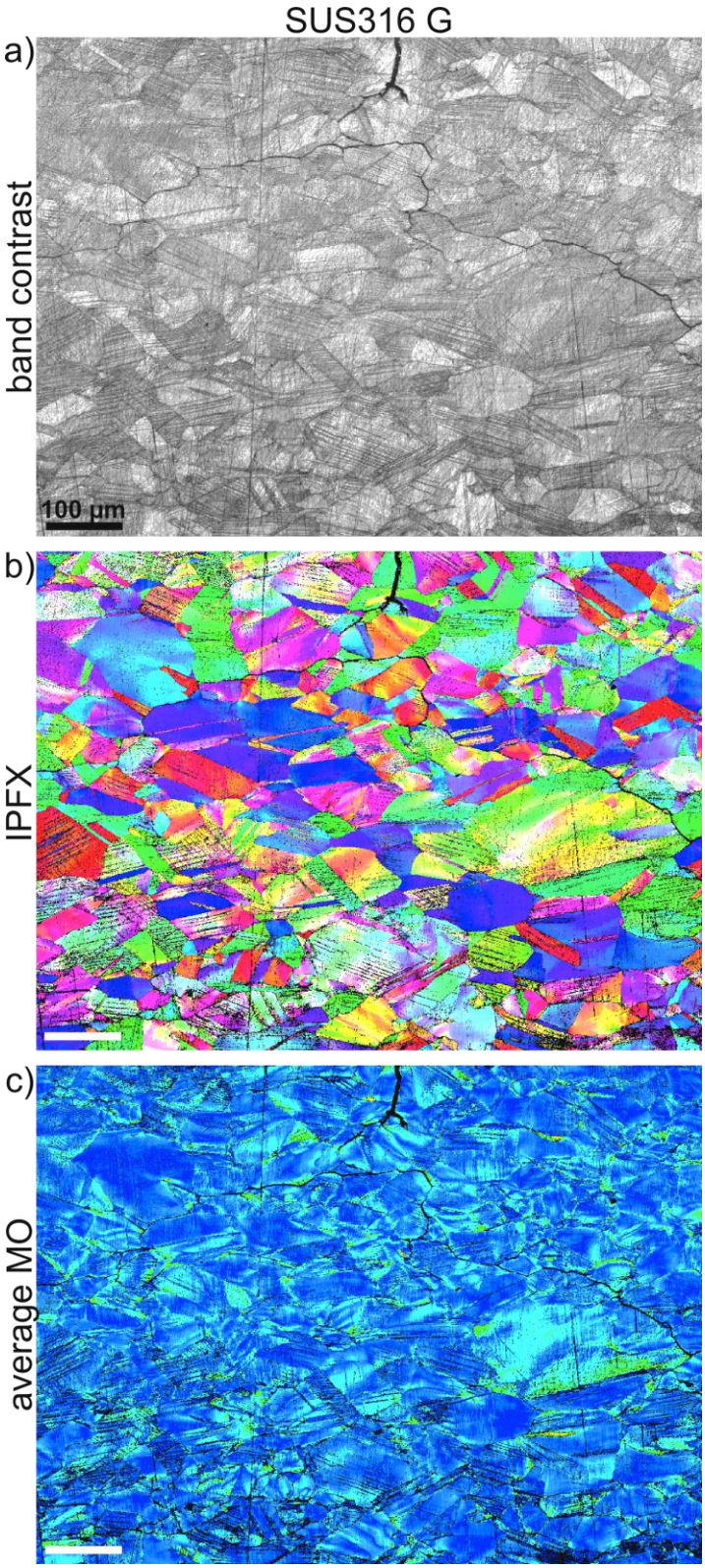

Figure 59. EBSD analysis of 316INSS G (320°C): a) band contrast map; b) IPFX map; c) average MO map

As a final step in the crack morphology study, the SCC crack opening types were investigated based on STEM images of the crack flanks in all 15 samples. In addition, the orientation of the crack tip plane with respect to the external loading direction was determined.

There are two main crack opening mechanisms in fracture mechanics that can also be applied to SCC cracks. The first type is Mode I, also known as cleavage mode, where the force acts on both crack flanks perpendicularly, "tearing" them apart (Figure 60a). The second cracking type, in fracture mechanics called Mode II, is the shear mode (Figure 60b). In this case, the crack flanks undergo parallel shear, detectable by the displacement of certain features along the crack flanks. If there are any steps in the crack opening, these will gape open wider if shear occurred. Although the existence of steps in the crack opening and slip bands might be an indicator of the shear mode, only the analysis of the crack flanks can conclusively confirm which mode was involved. For instance, it is possible that slip occurred at a GB prior to the crack reaching it. In this case, the GB could exhibit steps, which the crack then merely followed without any shear occurring, resulting in step-shaped crack morphology. Furthermore, it has been observed that in some cases, a mixed mode of cleavage and shear is also possible.

The crack opening mode as well as the orientation of the crack tip plane to the external loading direction was determined for all 15 crack tip lift-outs via STEM imaging. This was achieved by observing the general crack morphology, i.e. constant crack width or cleavage-like opening), and features along the crack flanks. The results of this analysis are listed in Table 7.

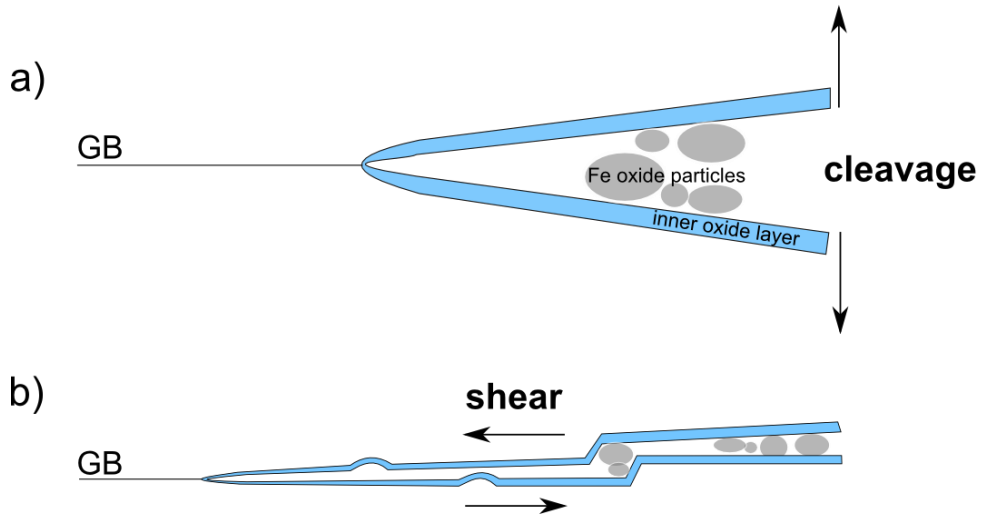

Figure 60. Illustration of different SCC crack opening types: a) cleavage opening; b) shear opening

Sample	T [°C]	CT number	Orientation to load	Crack opening type
316INSS - O	360	1	Parallel	Shear
316INSS - O	360	2	Perpendicular	Cleavage
316INSS - N	350	1	Oblique	Shear
316INSS - N	350	2	Oblique	Shear
316INSS - N	350	3	Oblique	Shear
316INSS - M	340	1	Parallel	Shear
316INSS - M	340	2	Parallel	Mixed mode
316INSS - M	340	4	Perpendicular	Cleavage
316INSS - M	340	5	Parallel	Shear
316INSS - G	320	1	Parallel	Shear
316INSS - G	320	2	Oblique	Cleavage
316INSS - G	320	3	Perpendicular	Cleavage
316INSS - G	320	4	Parallel	Shear
316INSS - G	320	5	Perpendicular	Cleavage
316INSS - G	320	6	Parallel	Shear

Table 7. SCC crack opening type for each crack tip

There are three main crack directions with respect to the external load applied: 1) parallel (crack tip plane is oriented at ~ 0° to the external load); 2) perpendicular (crack tip plane is oriented at ~ 90° to the external load); 3) oblique (crack tip plane is oriented between 10° and 80° to the external load). The results listed in Table 7 are based on the observations made from the STEM images shown in Figure 61, Figure 62, Figure 63 and Figure 64.

The first set of samples for which the crack opening was determined to have occurred in shear mode is shown in Figure 61.

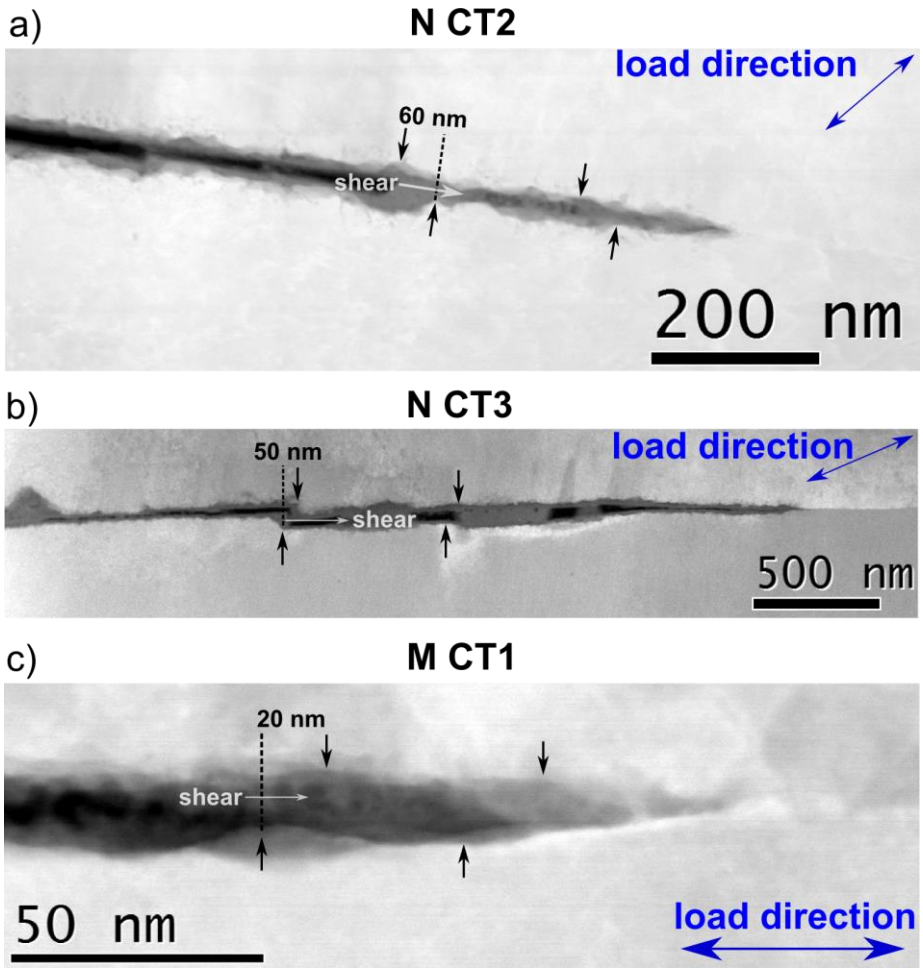

Figure 61. STEM ADF images of samples with shear opening (1): a) N CT2: load direction oblique; b) N CT3: loading direction oblique; c) M CT1: loading direction parallel

The offset of certain features along the crack flanks in cracks N CT2 (Figure 61a), N CT 3 (Figure 61b) and M CT1 (Figure 61c) indicates that shear has occurred. The shear distance in each case is indicated in the images. Another set of cracks that were observed to have opened in shear mode is shown in Figure 62: SCC cracks M CT5 (Figure 62a), G CT1 (Figure 62b), G CT4 (Figure 62c) and G CT6 (Figure 62d). In general, shearing occurred for 9 out of 15 samples, most of which were oriented parallel to the loading direction. Both cracks in O CT1 and N CT1 are not shown in the figures. As N CT1 turned out to be transgranular (shown in Figure 30), it was not included in any further study.

For five of the analysed SCC cracks, cleavage mode was determined as the crack opening mechanism (Figure 63). Cleavage mode was observed mainly for SCC cracks oriented perpendicular to the external loading direction, as can be established from Figure 63a, b, d and e (O CT2, M CT4, G CT3 and G CT5, respectively). In contrast, crack G CT2 in Figure 63c was found to be oriented ~ 60° to the external load direction.

For one SCC crack, both cleavage-like crack opening and displacement of some of the features at the crack flanks were observed. For SCC crack M CT2, in Figure 64, shearing was observed at the crack flanks ~ 600 nm away from the crack tip. At close proximity to the crack tip (~ 200 nm), however, there seems to be no offset of any of the features along the crack flank and the opening appears cleavage-like. Steps were observed both in the crack morphology and in the GB path ahead of the crack tip. This crack was concluded to have opened in a combination of Mode I and Mode II.

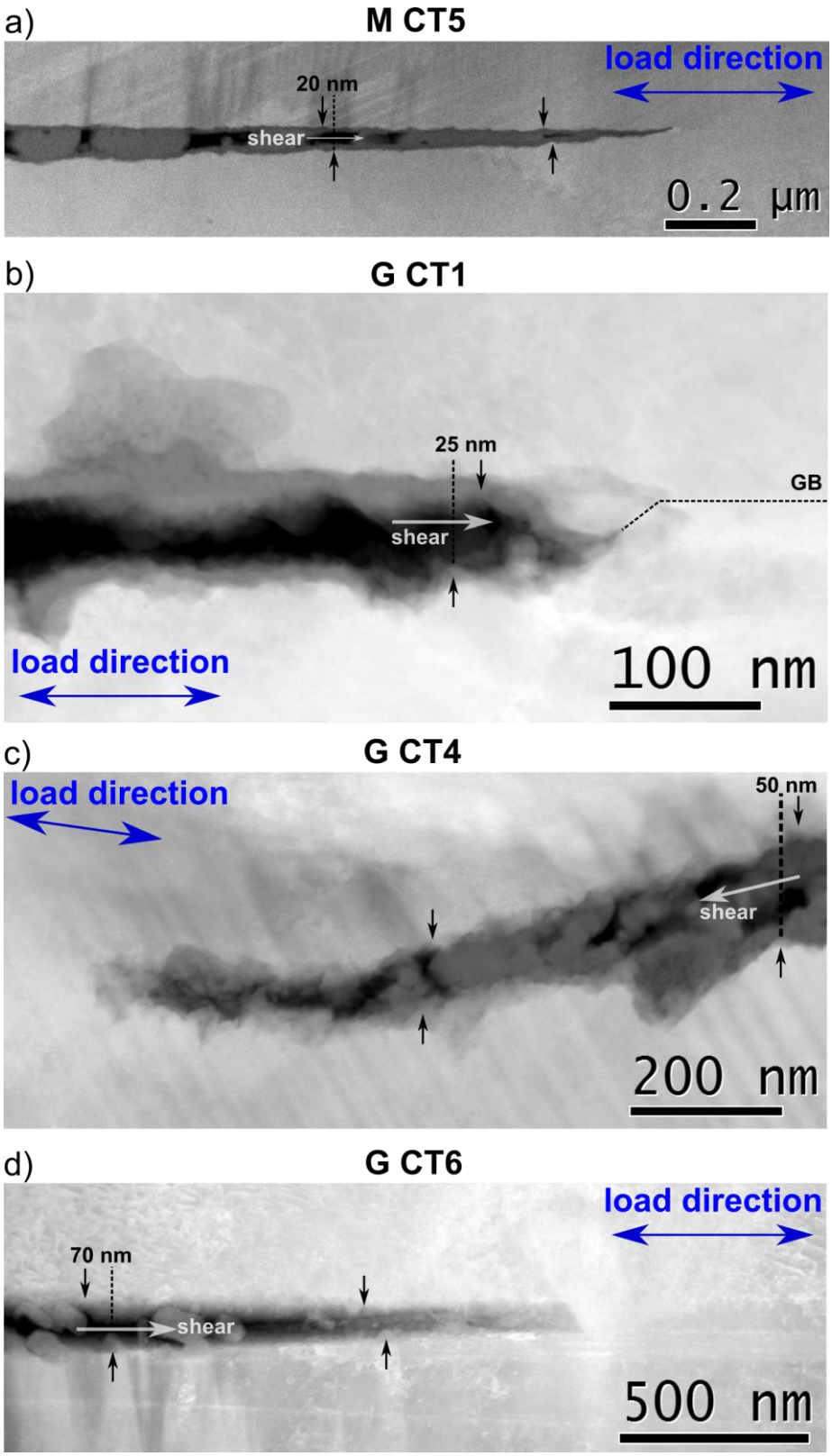

Figure 62. STEM ADF images of samples with shear opening (2): a) M CT5; b) G CT1; c) G CT4; d) C CT6; loading direction parallel in all samples

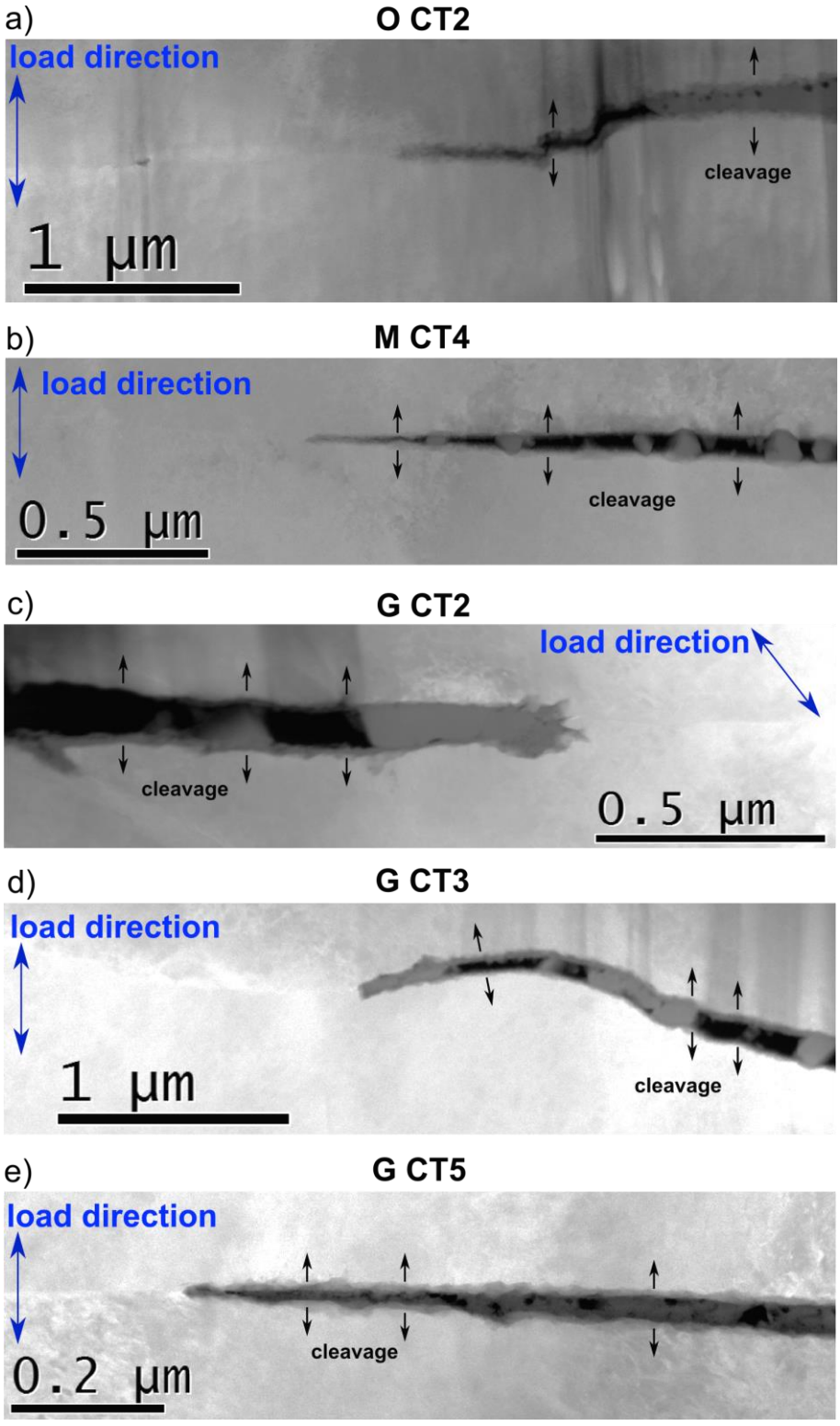

Figure 63. STEM ADF images of SCC crack tips that opened in cleavage mode: a) O CT2; b) M CT4; c) G CT2; d) G CT3; e) G CT5; all loading directions perpendicular except for G CT2, which is oblique

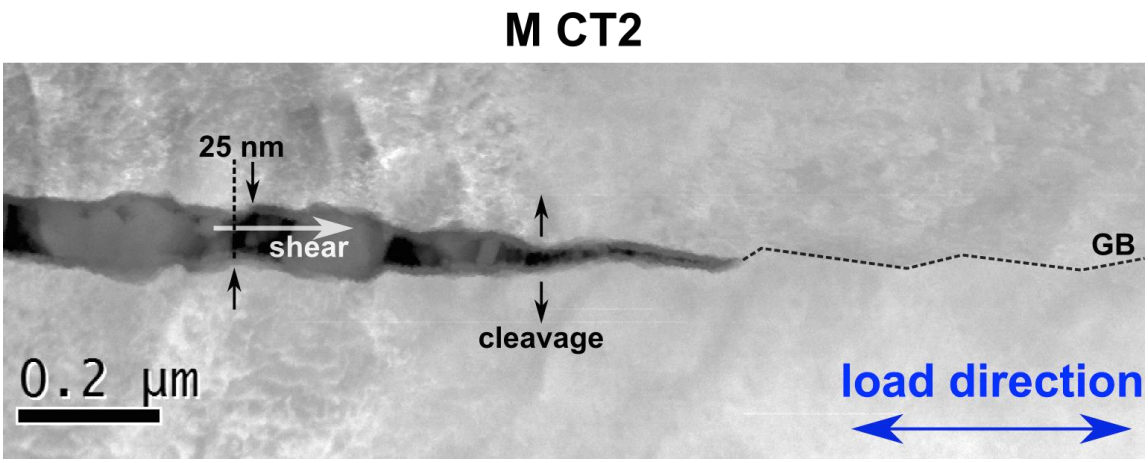

Figure 64. STEM ADF image of SCC crack opening in mixed mode: M CT2, loading direction parallel

5.3.2 Oxide and crack tip chemistry

In this chapter, the results regarding the oxide chemistry in the open crack and near the crack tip as well as the elemental distribution in the crack tip region will be presented. In combination with this data, the crack tip size as well as the existence of Fe oxide particles in the open crack will be used to determine which cracks were active at the end of the SCC test. The formation of oxides near the crack tip and potential differences between the SCC test temperatures was a key topic in this study. A summary of the results of this study is listed in Table 8.

In this thesis, the term "crack tip" refers to the first point of the GB, coming from the un-oxidised side, which is exposed to the environment due to intergranular fracture. In most cases, this is a Cr-rich spinel oxide, which, after fracture, is in contact with the environment. The crack tip opening was determined in each crack at the location where this Cr-rich crack tip oxide is first observed fractured, as illustrated in Figure 65. It was measured from one crack flank to the other. In case of the existence of a Cr-rich oxide

layer on the crack flanks, the crack tip opening was measured from one oxide surface in contact with the environment to the other.

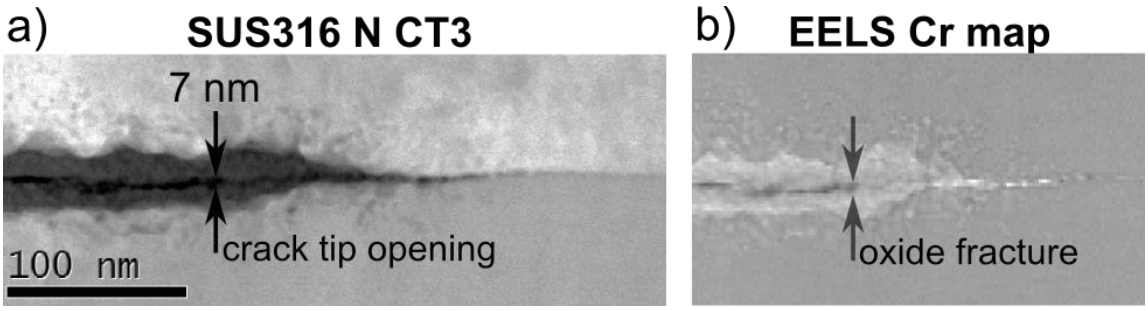

Figure 65. Measurement of crack opening in N CT3: a) STEM ADF image; b) EELS Cr L edge map; the location of oxide fracture was determined in the Cr map and the width of the crack opening at that point was determined in the STEM ADF image

Next, the existence of Fe-rich oxide particles in the crack opening in close proximity (< 200 nm) to the crack tip was established. These oxide particles form in mature cracks due to the precipitation of Fe in the solution (PWR primary water). Their presence in close vicinity to the crack tip indicates that the crack had been arrested for some time before the SCC test was stopped. Hence, there was enough time for Fe oxide particles to precipitate close to the crack tip. The particles in the mature crack are very easy to locate and are large enough, if necessary, to determine their crystal structure via electron diffraction. In Chapter 4.2, the analysis of Fe oxide particles via TKD was mentioned briefly. However, as the dimensions become much smaller closer to the crack tip, EELS analysis had to be conducted in order to determine the composition of the oxides in the crack tip region. The EELS data conducted from all in the framework of this project characterised SCC cracks is presented at the end of this thesis in the Appendix.

Figure 66 shows two SCC cracks (G CT2 and G CT3) with Fe-rich oxide particles in close proximity (< 100 nm) to the crack tip. The Fe oxide particle in sample G CT 2, as presented in Figure 66a, is 350 nm x 80 nm in dimension and located ~ 50 nm from the crack tip. Its measured composition is close to the stoichiometry of Fe_3O_4, magnetite (51% O, 42% Fe, < 4% Cr, < 2% Ni). Similarly, the Fe oxide particle residing close (~ 150 nm) to the crack tip in sample G CT3 was also identified as magnetite with a composition of 57% O, 39% Fe, < 4% Cr, < 2% Ni. This Fe oxide particle, with dimensions of only 170 nm x 30 nm, is considerably smaller than the one in G CT2.

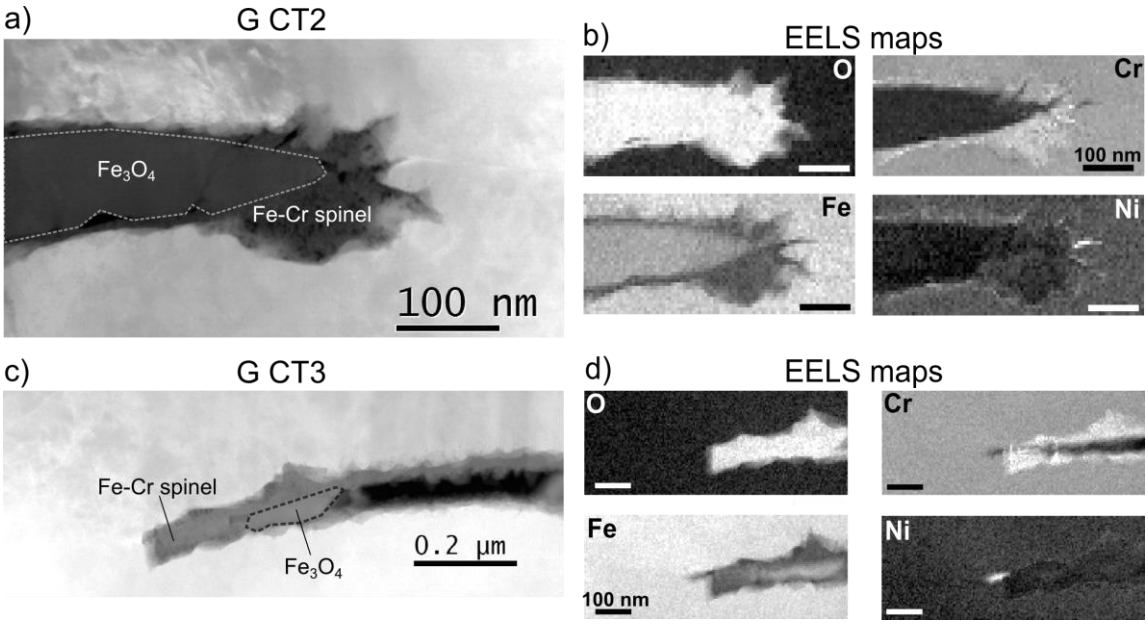

Figure 66. SCC crack tips with Fe oxide (Fe_3O_4, magnetite) in close proximity to crack tip; a) STEM ADF image of G CT2, large Fe_3O_4 particle (350 nm x 80 nm, composition: 51% O, 42% Fe, < 4% Cr, < 2% Ni); b) EELS elemental O K, Cr L, Fe L, Ni L edge maps of G CT2; c) STEM ADF image of G CT3, Fe_3O_4 particle (170 nm x 30 nm, composition: 57% O, 39% Fe, < 4% Cr, < 2% Ni); d) EELS elemental O K, Cr L, Fe L, Ni L edge maps of G CT3; both samples exhibit the same type of crack tip oxide: ~ 52% O, 22% Cr, 20% Fe and 6% Ni (Fe-Cr spinel type oxide)

Both samples exhibit the same type of oxide at their crack tips: the Fe-Cr spinel-type oxide with a composition of ~ 52% O, 22% Cr, 20% Fe and 6% Ni. EELS maps of the analysed regions in samples G CT2 and G CT3 can be observed in Figure 66b and Figure 66d, respectively.

The results in Table 8 indicate that only four out of the remaining 14 samples under examination exhibit Fe-rich oxide particles close to the crack tip. However, this is not surprising as only potentially active crack tips with no Fe oxide present near the crack tip were selected for further TEM studies. With the help of the crack tip opening and the existence of Fe-rich oxide particles near the crack tip, the activity of each crack tip at the end of the SCC test was determined. Due to their large crack tip opening (> 60 nm), combined with the existence of magnetite near the crack tip, cracks O CT1, G CT1, G CT2 and G CT3 were classified as inactive. All other crack tips show signs of activity and were therefore considered active.

Subsequently, both existence and dimension of Ni enrichment at the CT and the crack flanks as well as the oxide chemistry at the CT were determined via the acquired EELS data. Only some EELS elemental maps are shown in the main text of this thesis for illustration purposes. However, the EELS data from all 14 crack tips are shown in the Appendix.

Quantitative line profiles of 10 pixels width were used in order to determine the oxide composition near the crack tip. The elemental Ni maps were used to determine the existence and dimension of Ni enrichment ahead of the crack tip and at the crack flanks. All results are listed in Table 8.

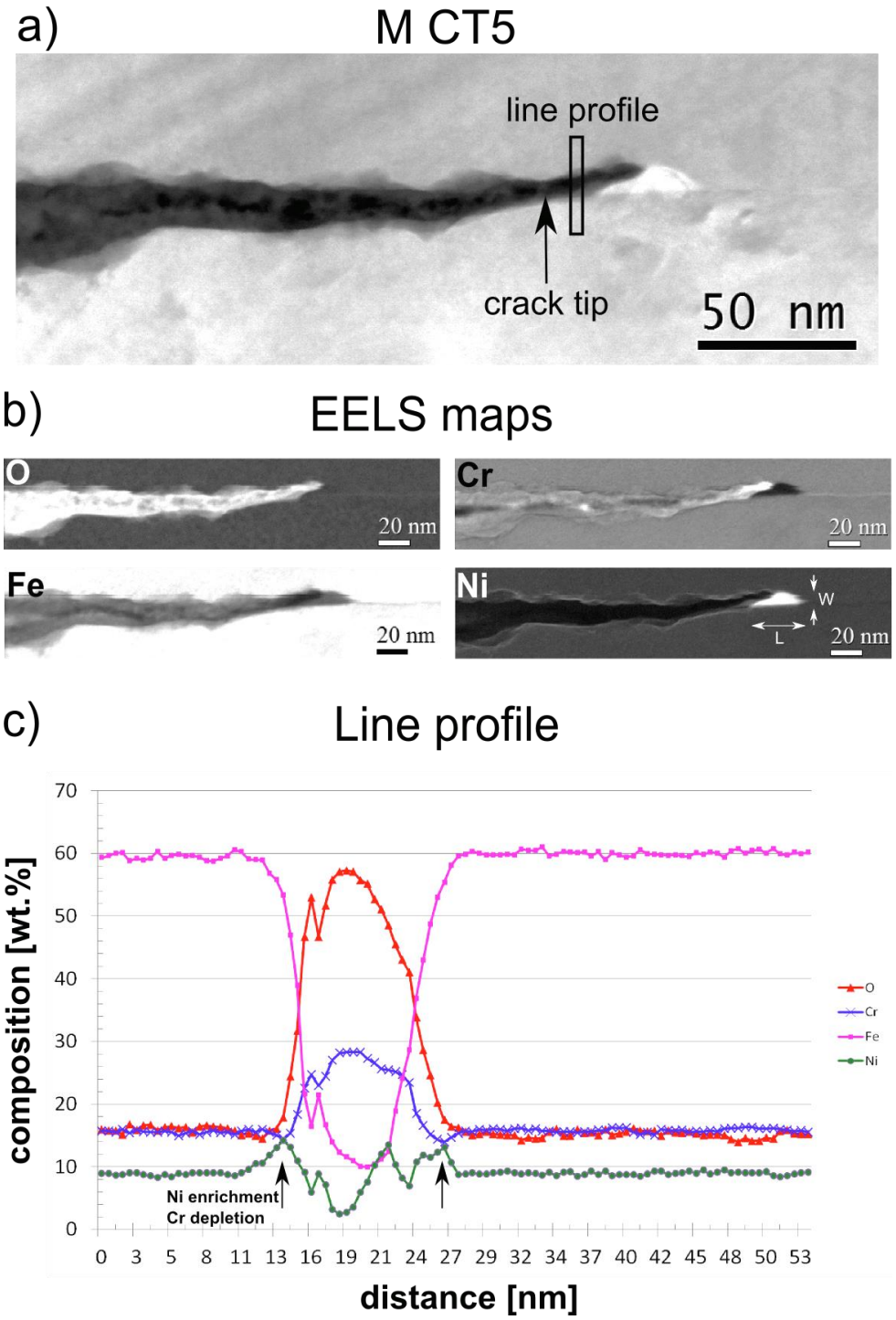

Figure 67. Determination of crack tip and oxide chemistry in 316INSS M CT5; a) STEM ADF image, indicating location of line profile (black box, 10 pixels width) and the crack tip (black arrow); b) EELS elemental O K, Cr L, Fe L and Ni L edge maps, Ni edge map indicates the dimensions of the Ni-rich region ahead of the crack tip (34 nm x 9 nm); c) Line profile across crack tip

The crack tip and oxide chemistry was determined as shown in Figure 67. First, the location of the crack tip was determined, after which a line profile was extracted in the oxidised region just ahead of the crack tip, as indicated in Figure 67a.

The line profile is displayed in Figure 67c and clearly shows the oxidised region ahead of the crack tip between 13 nm and 27 nm distance on the x-axis. The vertical axis shows the compositions in weight-percent (wt.%). While the oxidised region ahead of the crack tip appears to be rich in Cr, it seems depleted in both Fe and Ni. However, at the metal-oxide interface on both sides, there seems to be a zone of Ni-enrichment (width ~ 2 nm) and slight Cr depletion. The averaged composition of the crack tip oxide was determined as: 56% O, 26% Cr, 13% Fe and 5% Ni. Finally, the dimensions of the Ni-enriched region ahead of the crack tip were determined via the EELS elemental Ni map as 34 nm x 9 nm, as shown in Figure 67b. The results from all crack tips are listed in Table 8 and will be discussed further in Chapter 5.4.

Sample	T [°C]	CT no.	CT opening [nm]	Fe oxide	Crack tip oxide [wt.%]				Ni enrichment ahead of CT L x W [nm]	Ni enrichment at crack flanks: width [nm]	State end of SCC test
					O	Cr	Fe	Ni			
316INSS - O	360	1	70	Yes	**40**	**25**	**21**	**14**	200 x 100	-	**Inactive**
316INSS - O	360	2	35	No	**42**	**19**	**33**	**6**	50 x 25	38	**Active**
316INSS - N	350	2	20	No	**55**	**18**	**22**	**2**	40 x 21	7	**Active**
316INSS - N	350	3	7	No	**57**	**24**	**15**	**4**	50 x 6	7	**Active**
316INSS - M	340	1	15	No	**18**	**21**	**50**	**10**	70 x 5	-	**Active**
316INSS - M	340	2	15	No	**20**	**20**	**50**	**10**	10 x 10	5	**Active**
316INSS - M	340	4	16	No	**34**	**19**	**37**	**9**	No	-	**Active**
316INSS - M	340	5	12	No	**56**	**26**	**13**	**5**	34 x 9	2	**Active**
316INSS - G	320	1	60	Yes	**52**	**22**	**19**	**6**	75 x 30	5	**Inactive**
316INSS - G	320	2	100	Yes	**52**	**22**	**20**	**5**	50 x 5	5	**Inactive**
316INSS - G	320	3	70	Yes	**52**	**23**	**19**	**6**	80 x 15	4	**Inactive**
316INSS - G	320	4	50	No	**18**	**18**	**56**	**7**	No	-	**Active**
316INSS - G	320	5	15	No	**43**	**28**	**15**	**14**	85 x 20	5	**Active**
316INSS - G	320	6	70	No	**20**	**19**	**55**	**6**	No	-	**Active**

Table 8. Overview of crack tip and oxide chemistry: size of crack tip opening, existence of outer Fe-rich oxide close to crack tip (< 200 nm), quantitative data on crack tip oxide composition (similar oxide type marked with same colour), Ni enrichment data, final conclusion on the activity of the crack at the end of the SCC test

5.3.3 Grain boundary oxidation and chemistry

It has been established that GB oxidation plays a fundamental role in the IGSCC crack propagation process. In general, the relaxed, unstrained SUS316 stainless steel matrix does not exhibit GB oxidation. However, in case of cold work or external stresses, this phenomenon was found in SS previously near the oxidised surface [100] and ahead of SCC crack tips. An oxidised GB ahead of the SCC crack tip makes the GB more brittle and therefore more prone to fracture. As shown in Chapter 4.3, GB oxidation has been studied in the framework of this project via atom probe tomography. The width of GBs can be just a few nanometers, which is why APT is the ideal technique for this purpose. Furthermore, APT has excellent chemical sensitivity, which can be used for analysing the GB chemistry and segregation of trace elements. However, the sample preparation for APT, described in detail in Chapter 3.4.2, can be very cumbersome and therefore, EELS is often used instead. In this thesis, as lamellae specimen had already been prepared for TEM, EELS was used for analysing the GB chemistry in the 14 SCC crack tip specimens.

The EELS elemental O K edge maps were used to determine the existence of GB oxidation. For this purpose, line profiles (10 pixels width) were extracted perpendicular to the GB ahead of the crack tip. Figure 68 shows the investigation of the GB chemistry in sample N CT3. The EELS O K edge map clearly indicates the existence of GB oxidation. First, the location of the crack tip was determined, as shown in Figure 68b by the EELS Cr L edge map, and then the length of the oxidised portion of the GB was measured, starting at the crack tip, ending where O could no longer be detected. It was

established that the length of the oxidised portion of the GB ahead of the crack tip in N CT3 is ~ 185 nm, as shown in Figure 68a.

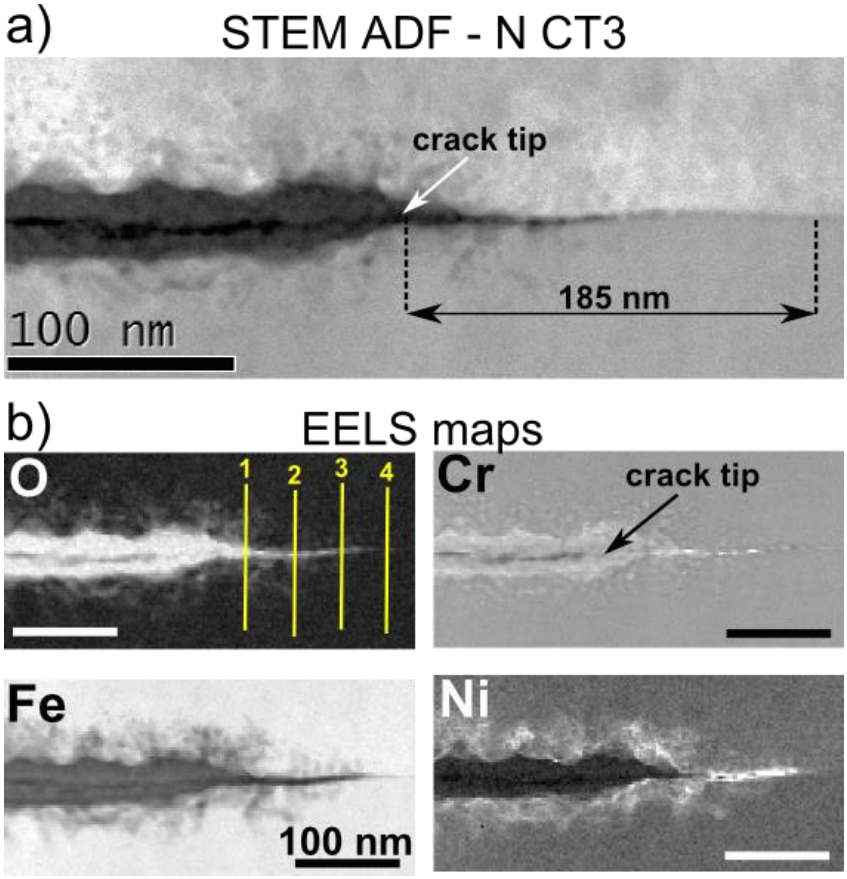

Figure 68. Determination of the GB chemistry in N CT3 via EELS line profiles: a) STEM ADF image, location of crack tip indicated with white arrow, oxidised portion of GB: 185 nm length; b) EELS O K, Cr L, Fe L and Ni L edge maps, indicating the location of 4 line profiles acquired (yellow lines) and the crack tip (black arrow)

Subsequently, a number of line profiles were extracted along the GB in order to measure its composition in different regions. The first line profile, number 1 in Figure 68b, was extracted just ahead of the crack tip and is displayed in Figure 69a. It was determined that the width of the oxidised GB at this point is 15 nm and that the composition (57% O, 24% Cr, 15% Fe, 4% Ni) is very close to the stoichiometry of

$(FeCr_2)O_4$. Three other line profiles (number 2, 3 and 4 in Figure 68b) were extracted further ahead of the crack tip at 65 nm, 104 nm and 155 nm, respectively. It was observed, that the width of the oxidised GB decreased from 15 nm in line profile 1 to 7 nm in profiles 2 (Figure 69b) and 3 (Figure 70a) and finally 4 nm in profile 4 (Figure 70b).

With increasing distance away from the crack tip, the composition of the oxidised GB changes quite significantly. The composition extracted from line profile 2 indicates a Ni- and Cr-rich spinel oxide that is depleted in Fe (42% O, 22 % Cr, 14% Fe, 22% Ni). Further away from the crack tip, line profile 3 as indicated in Figure 68b, this composition changes to 23% O, 19% Cr, 30% Fe, 26% Ni, a Ni-rich oxide with nominal Cr composition and slight Fe depletion. Finally, in the last portion of detectable GB oxidation, line profile 4 ~ 180 nm ahead of the crack tip, the O content decreases to 11%. The Fe, Cr and Ni contents at this point are very close to their nominal matrix values (18 % Cr, 57% Fe, 14% Ni), although slight Ni-enrichment remains.

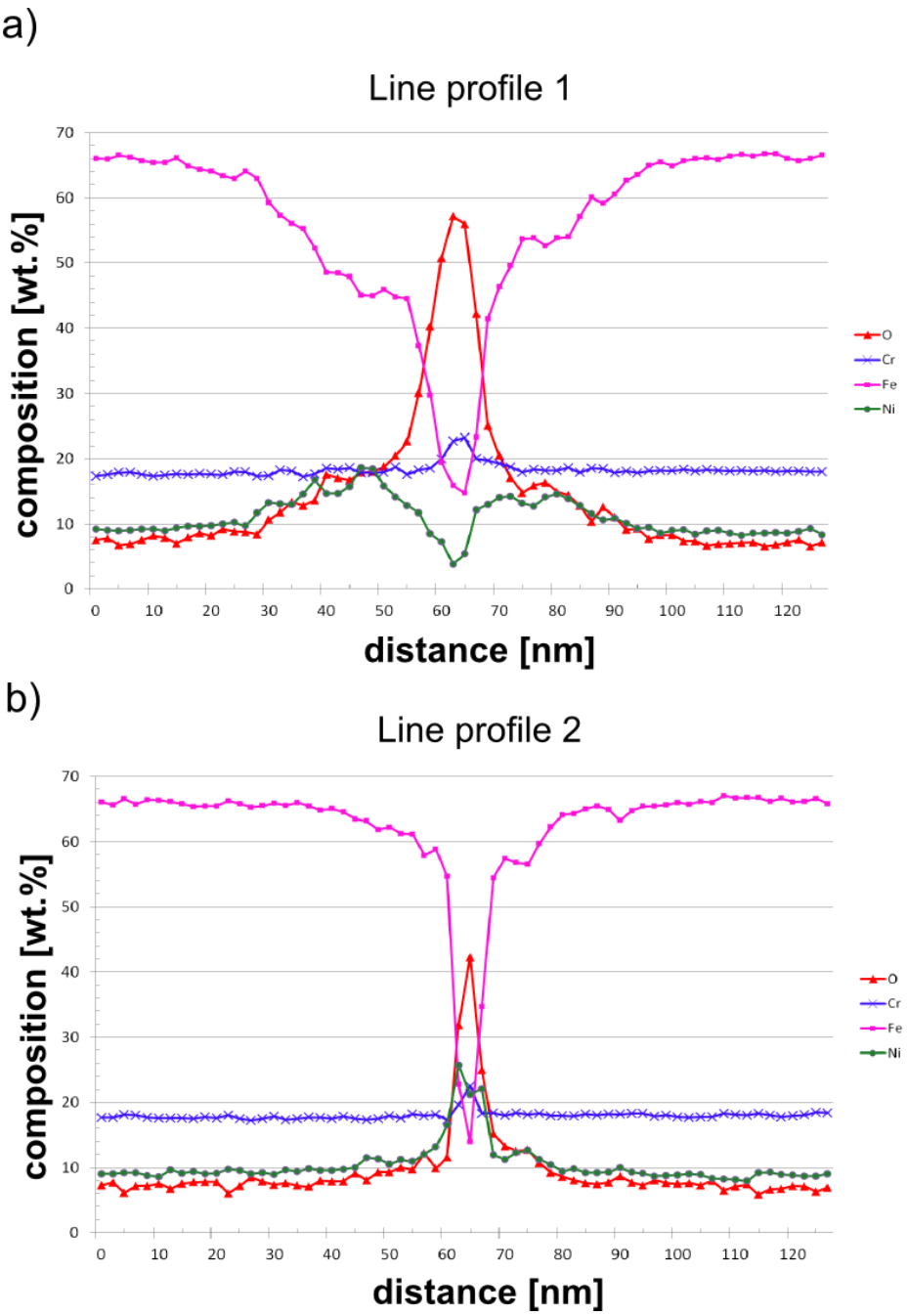

Figure 69. EELS line profiles 1 and 2 from Figure 68b: a) line profile 1, closest to crack tip (FWHM of oxidised GB ~ 15 nm, approx. composition: 57% O, 24% Cr, 15% Fe, 4% Ni); b) line profile 2, in Ni-rich region (FWHM of oxidised GB ~ 7 nm, approx. composition: 42% O, 22 % Cr, 14% Fe, 22% Ni)

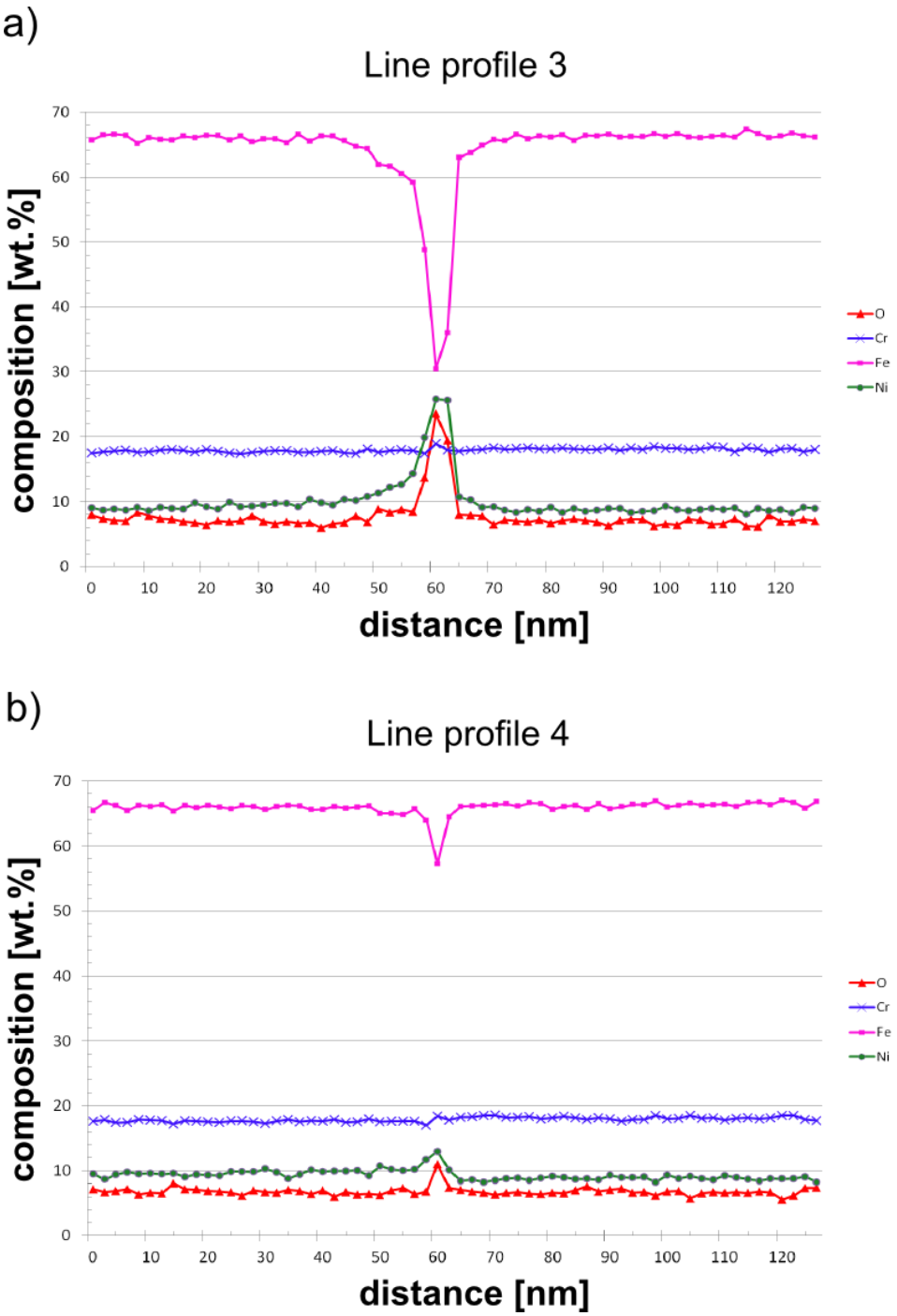

Figure 70. EELS line profiles 3 and 4 from Figure 68b: a) line profile 1, in Ni-rich region (FWHM of oxidised GB ~ 7 nm, approx. composition: 23% O, 19% Cr, 30% Fe, 26% Ni); b) line profile 2 (FWHM of oxidised GB ~ 4 nm, approx. composition: 11% O, 18 % Cr, 57% Fe, 14% Ni)

GB oxidation was also detected in sample M CT2, as shown in Figure 71. The length of the oxidised portion of the grain boundary could not be measured accurately because it extends beyond the acquired EELS maps (Figure 71b and c), but it measures at least 120 nm. The composition of the GB, which was relatively constant throughout its length, was measured via a line profile (location marked yellow in Figure 71c) ~ 120 nm ahead of the crack tip. At this point, the width of the oxidised GB measures 2 nm and the composition is 17% O, 19 % Cr, 55% Fe, 9% Ni, similar to line profile 4 in sample N CT3 (Figure 70b).

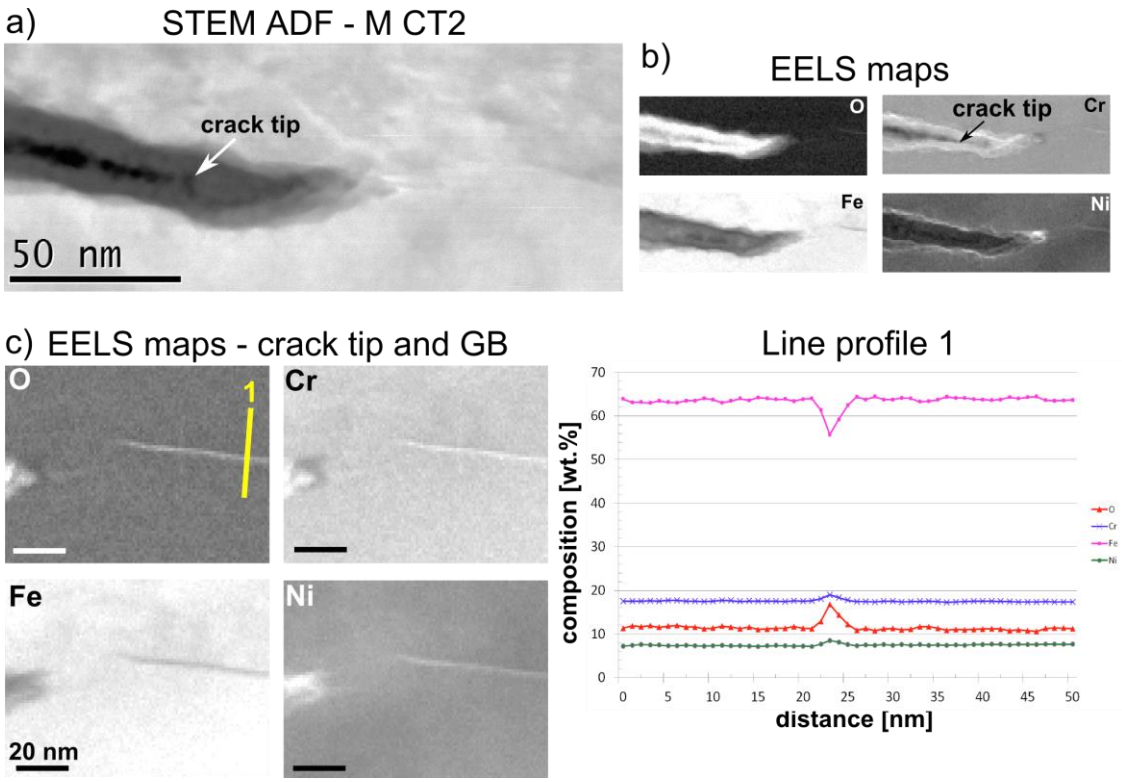

Figure 71. Determination of the GB chemistry via EELS line profiles: a) STEM ADF image, location of crack tip indicated with white arrow; b) EELS O K, Cr L, Fe L and Ni L edge maps, smaller magnification, crack tip (black arrow) location indicated; c) EELS O K, Cr L, Fe L and Ni L edge maps, larger magnification, location of line profile indicated (yellow line); line profile 1: FWHM ~ 2 nm; composition: 17% O, 19 % Cr, 55% Fe, 9% Ni

In general, only 4 (O CT1, N CT3, M CT 2 and M CT5) out of 14 SCC crack tips were found to exhibit detectable GB oxidation. Nevertheless, the GB composition was measured for all samples, as displayed in Table 9.

Sample	T [°C]	CT number	GB oxidation Length [nm]	GB chemistry [wt.%] O	Cr	Fe	Ni
316INSS - O	360	1	-	8.5	15	63	13.5
316INSS - O	360	2	50	**11**	**18**	**57**	**14**
316INSS - N	350	2	-	6	18	60	15
316INSS - N	350	3	185	**13**	**17**	**50**	**19**
316INSS - M	340	1	-	7.5	16	59	17
316INSS - M	340	2	> 120	**17**	**19**	**55**	**9**
316INSS - M	340	4	-	7	18	63	10
316INSS - M	340	5	> 80	**19**	**19**	**54**	**8**
316INSS - G	320	1	-	5	15	60	20
316INSS - G	320	2	-	6	13	50	30
316INSS - G	320	3	-	7.5	14	45	33
316INSS - G	320	4	-	0	18.5	75	6.5
316INSS - G	320	5	-	8.5	18	62	11
316INSS - G	320	6	-	6	19	69	6

Table 9. Grain boundary chemistry in 316INSS: GB oxidation ahead of 4 crack tips (O CT2, N CT3, M CT2 and M CT4) measured in the last oxidised portion of the GB far away from the crack tip; GB chemistry in non-oxidised GBs was measured ahead of the crack tip and inner oxidation front

For the 4 samples with GB oxidation, the GB chemistry was measured well ahead of the crack tip, as shown in samples N CT3 (line profile 4) and M CT2 in order to eliminate potential influences of the crack tip chemistry on the measurement. The GB chemistry in all other samples was measured ahead of the crack tip and the oxidation

front (also known as crack tip oxide and listed in Table 8). It should be noted, that the GB composition measurements might deviate slightly from the true composition due to contributions from the matrix as a consequence of the 2D projection in TEM. Further discussion of GB oxidation will follow in Chapter 5.4.

5.3.4 Oxidation of crack flanks

As the SCC crack propagates further, new metal is exposed to the environment, which is then subject to corrosion attack. Due to the nature of stainless steel, a protective oxide layer forms quickly on all exposed surfaces. It has already been discussed in Chapter 1.6.2 that this oxide consists of a dual layer structure. While the exposed surface oxidises, Fe has been observed to move outwards from the matrix into the solution (PWR primary water), precipitating as crystalline oxide particles in the open crack. In contrast, Ni tends to diffuse away from any forming oxides and accumulates behind the matrix-oxide interface. Chromium is known to move very little during the oxidation process at the crack flanks and therefore, the Cr content is usually relatively constant in this region.

The inward and outward movement of Fe, Ni and O at the crack flanks is subject to the process of diffusion of metallic and non-metallic species in the crystal lattice. While O can diffuse through the matrix via interstitials, the diffusion of Fe and Ni occurs via substitution. For this reason, the diffusion process is highly dependent on the mobility of both vacancies and lattice atoms within the material, which is known to be directly related to temperature.

The influence of the SCC test temperature on the diffusion at the crack flanks was analysed via the acquired STEM images and EELS elemental maps for all samples. Figure 72 shows the ongoing diffusion processes at the crack flanks close to the crack tip in samples O CT2 (360°C) and N CT2 (350°C). Both of these samples were determined as active at the end of the SCC test. The STEM ADF images and EELS Fe and Ni L edge maps of O CT2 are displayed in Figure 72a.

From the EELS maps it is apparent that heavy diffusion of Fe and Ni took place at the crack flanks. The diffusion zone reaches ~ 50 nm into the matrix. Figure 72b shows a similar image for sample N CT2. Oxide fingers reach deeply (~ 60 nm) into the material at the crack flanks. In general, it seems that the oxidised regions are Fe-depleted and Ni-enriched, as indicated by the black and white arrows in the EELS maps in Figure 72b. This is also true for sample N CT3, which was shown in the previous chapter (Figure 68). The EELS maps for N CT3 indicate heavy diffusion at the crack flanks up to 70 nm into the matrix and Fe-depleted oxide fingers protruding into the metal perpendicular to the crack. This continues on in the region ahead of the crack tip where the oxidised GB becomes less than 10 nm thick. In conclusion, heavy diffusion of metallic and non-metallic species took place at the crack flanks in all active high-T samples (360°C and 350°C).

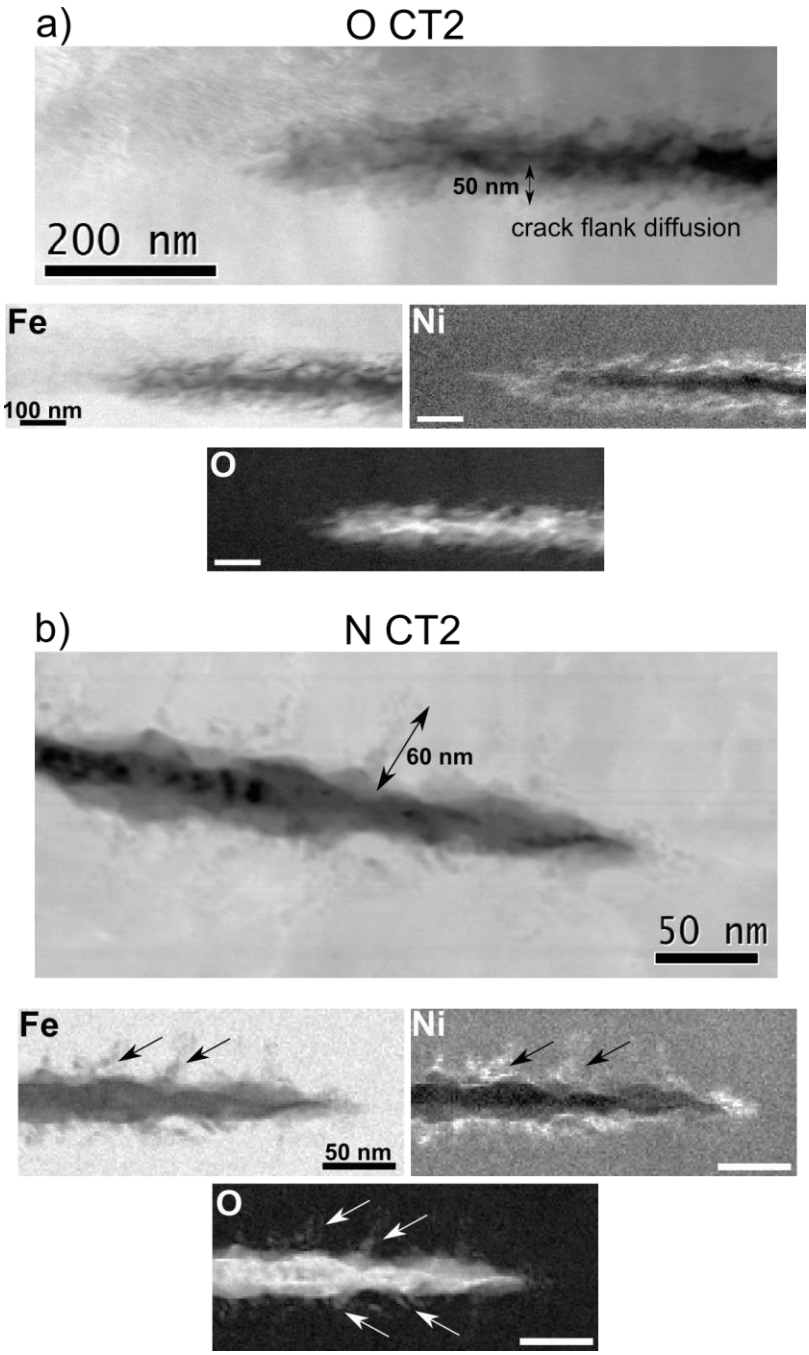

Figure 72. Diffusion processes at crack flanks in O CT2 and N CT2; a) STEM ADF image and EELS elemental O K, Fe and Ni L edge maps of O CT2; zone of diffusion at crack flank ~ 50 nm; b) STEM ADF image and EELS elemental O K, Fe and Ni L edge maps of N CT2; zone of diffusion at crack flank ~ 60 nm; black/white arrows: Fe-depleted oxide fingers protruding into the matrix, Ni-enrichment

In the next step, the crack flanks of the low-T samples (340°C and 320°) were analysed and are presented in Figure 73 and Figure 74, respectively. Figure 73 shows the STEM ADF images and EELS elemental maps of samples M CT1, M CT4 and M CT5 (340°C). These datasets indicate that the depth in which oxidation and diffusion of metallic species at the crack flank occurred is much smaller, ~ 5 nm - 10 nm width, compared to the high-T samples (360°C and 350°C, Figure 72). This is also true for the samples tested at 320°C in Figure 74. Although oxidation of the crack flanks has apparently taken place and very thin Ni enrichment can be found at most crack flanks (Figure 73a and c, Figure 74a), no oxide fingers are protruding into the matrix perpendicular to the crack in any of these samples. This was found for all samples tested at these lower temperatures, i.e. 340°C and 320°C.

In conclusion, it appears that long-range diffusion of metallic and non-metallic species at the crack flanks took place in high-T samples (360°C and 350°C), whereas the oxidation of the crack flanks near the crack tip of low-T samples (340°C and 320°C) is much more localised. The trend of the crack flank oxide thickness depending on the SCC test temperature is illustrated in Figure 75.

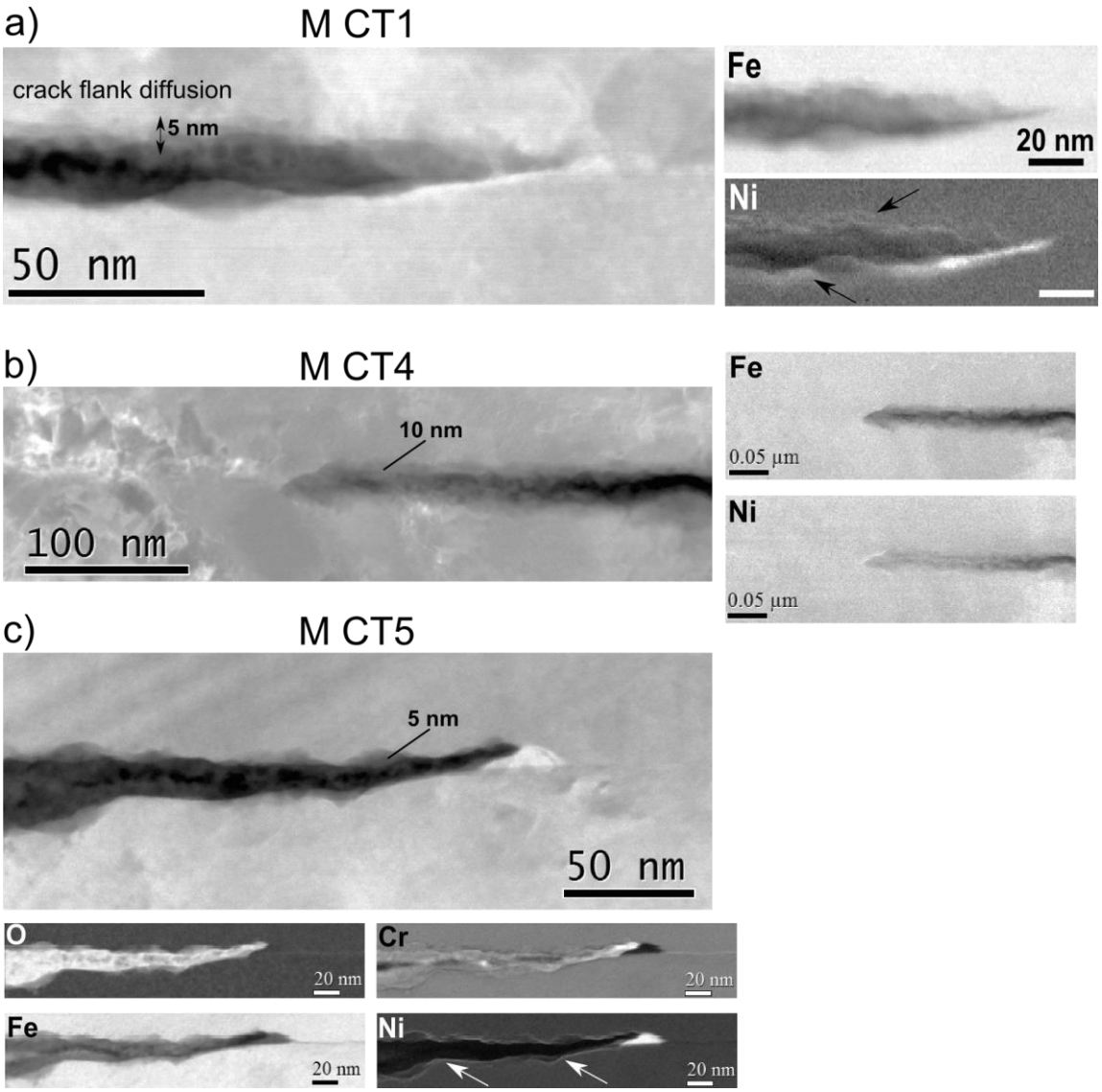

Figure 73. Diffusion processes at crack flanks in M CT1, M CT4 and M CT5; a) STEM ADF image and EELS elemental Fe and Ni L edge maps of M CT1; zone of diffusion at crack flank ~ 5 nm; black arrows: some Ni enrichment at crack flanks; b) STEM ADF image and EELS elemental Fe and Ni L edge maps of M CT4; zone of diffusion at crack flank ~ 10 nm; c) STEM ADF image and EELS elemental O K, Fe, Cr and Ni L edge maps of M CT5; zone of diffusion at crack flank ~ 5 nm; white arrows: thin Ni-enrichment at crack flanks

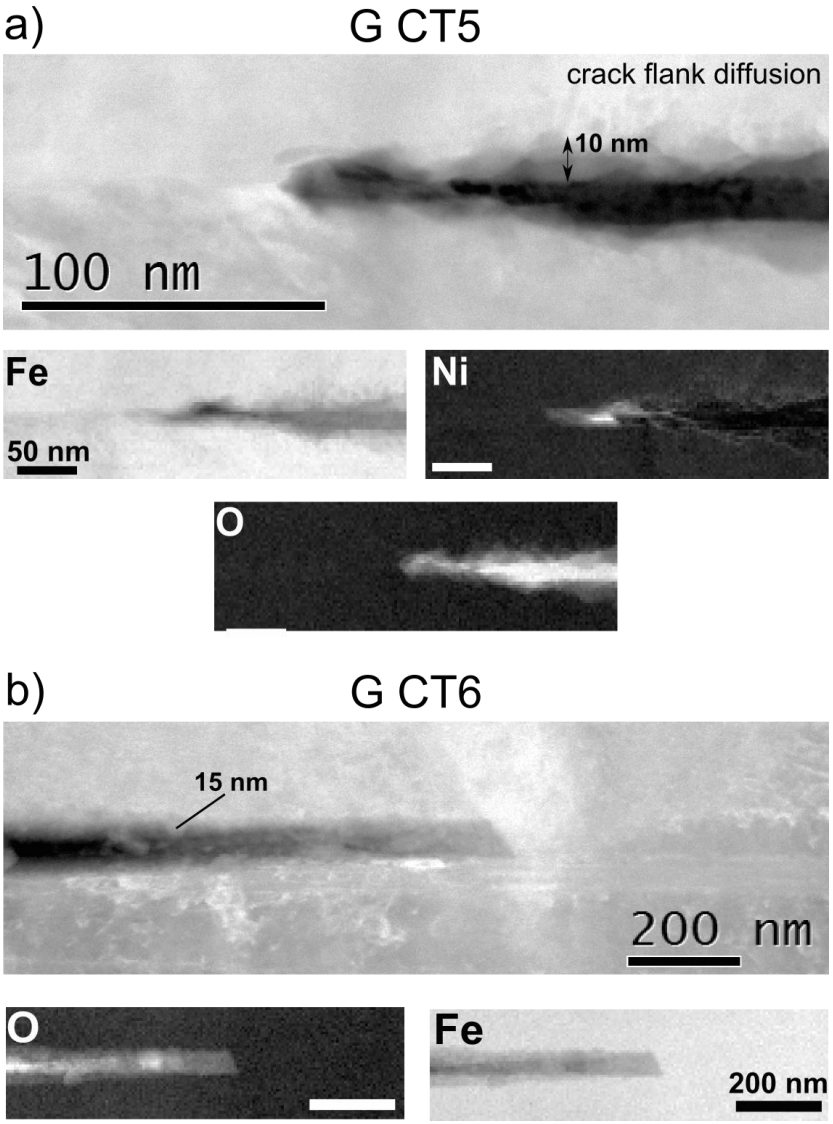

Figure 74. Diffusion processes at crack flanks in G CT5 and G CT6; a) STEM ADF image and EELS elemental O K, Fe and Ni L edge maps of G CT5; zone of diffusion at crack flank ~ 10 nm; b) STEM ADF image and EELS elemental O K, Fe L edge maps of G CT6; zone of diffusion at crack flank ~ 15 nm;

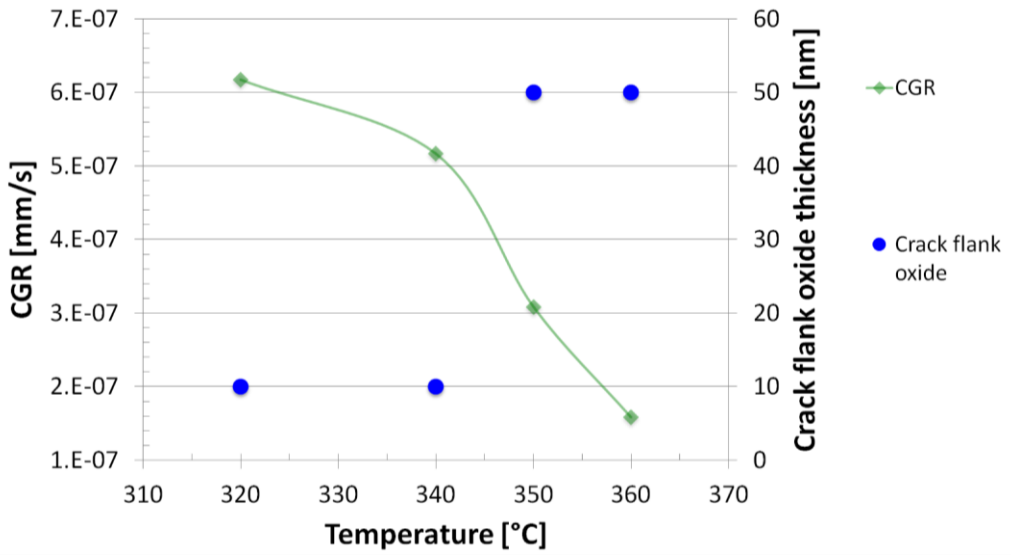

Figure 75. Comparison of crack flank oxide thickness at different temperatures (blue points); T-dependence of CGR (green line)

As a final step in the analysis of the crack flank oxidation, the oxidation width of the crack flanks in the mature crack was measured. The mature crack is the portion of the SCC crack, which was exposed to the environment for some time before the end of the SCC test. A protective oxide layer of certain width formed on its crack flanks and magnetite can often be found inside of it. Figure 76 shows the measurement of the width of the crack flank oxide in samples N CT2, N CT3 and M CT4. The results of all samples are listed in Table 10.

There does not seem to be an obvious correlation of the crack flank oxidation and the SCC test temperature. This is not altogether surprising because it is known that oxidation of exposed surfaces takes place until a protective oxide layer of certain thickness is reached. This thickness mainly depends on the material and the environment. Higher temperatures may lead to higher oxidation rates and quicker formation of the oxide film, but should not have an impact on its width. Although there

does not seem to be a "global" correlation of the oxide width and the test temperature, the highest oxide film widths occur at 360°C (30 - 40 nm). The smallest film width was measured in samples M CT5 and G CT5 (~ 12 nm). The majority of SCC cracks however, has an average oxide film width of ~ 15 - 20 nm at the crack flanks in the mature crack. The results also showed that the oxidation on both crack flanks is rather irregular and only for very few samples both crack flanks oxidised symmetrically.

Sample	T [°C]	CT number	Crack flank oxidation [nm] Grain 1	Grain 2
316INSS - O	360	1	40	40
316INSS - O	360	2	30	35
316INSS - N	350	2	15	15
316INSS - N	350	3	20	15
316INSS - M	340	1	15	15
316INSS - M	340	2	14	13
316INSS - M	340	4	19	15
316INSS - M	340	5	11	12
316INSS - G	320	1	17	16
316INSS - G	320	2	20	15
316INSS - G	320	3	28	20
316INSS - G	320	4	25	17
316INSS - G	320	5	12	12
316INSS - G	320	6	22	25

Table 10. Oxidation at crack flanks in mature crack (> 500 nm away from crack tip)

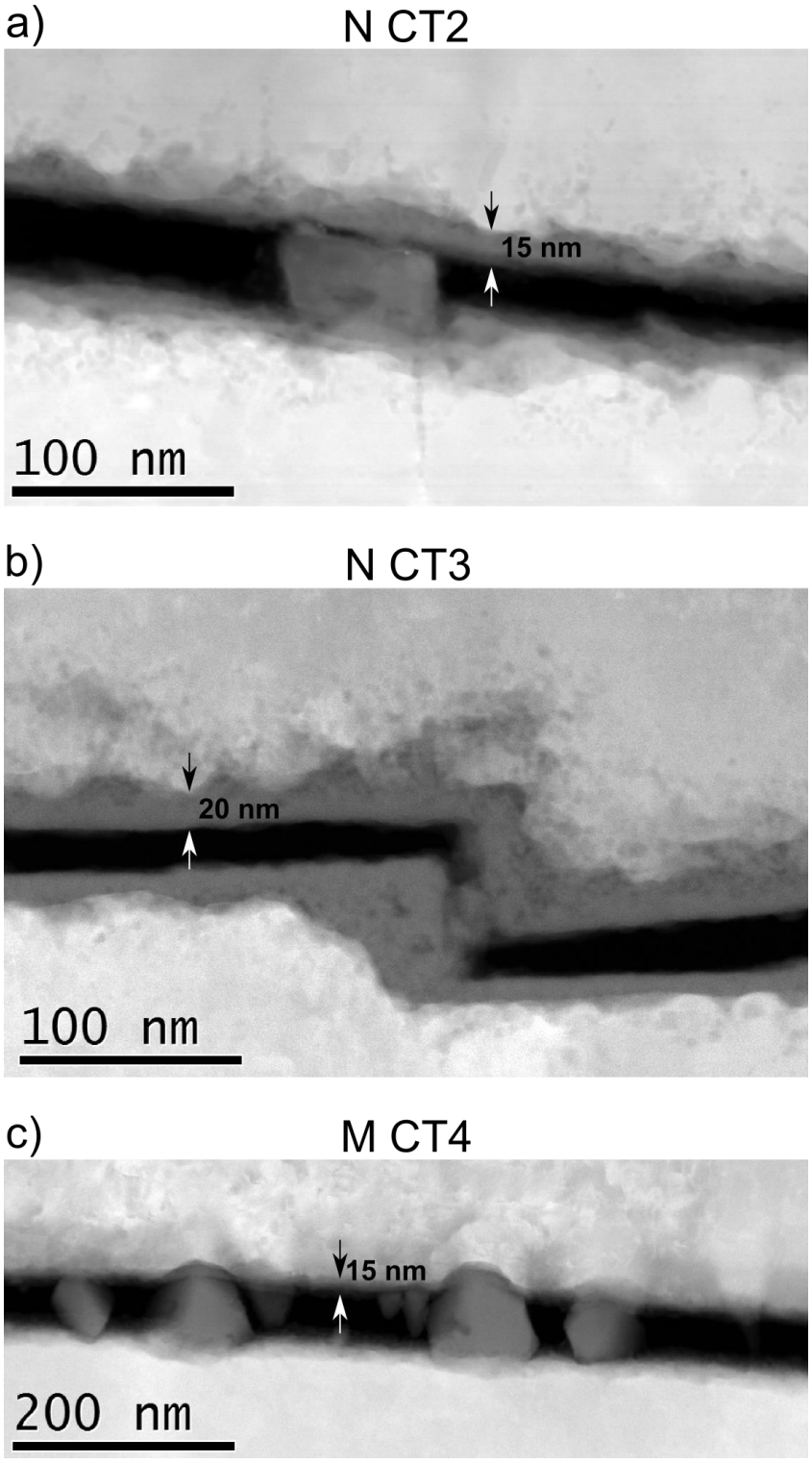

Figure 76. Crack flanks in mature crack (> 500 nm ahead of crack tip): a) STEM ADF N CT2; b) STEM ADF N CT3; c) STEM ADF M CT4; crack flank measurement indicated with black/white arrows

5.3.5 Plastic deformation near crack tip

It has been shown that there is evidence of the involvement of a thermally activated diffusion mechanism in the propagation of SCC. The results in the previous chapter indicate that diffusion at the crack flanks is more pronounced at higher temperatures (360°C and 350°C) than at lower temperatures (340°C and 320°C). This can be explained by the fact that higher diffusion rates at elevated temperatures result in increased oxidation rates at exposed surfaces as well as higher mobility of vacancies and matrix constituents. However, in order to explain the reverse effect in the CGR vs. temperature diagram, shown in Figure 56, there must be another rate-controlling process involved in the SCC crack propagation process.

It has been mentioned that previous studies of Arioka & Terachi *et al* established the influence of mechanical parameters on the CGR in SUS316 [35,37,38]. For instance, the higher the cold work level in SUS316, the higher the CGR. It was also established that the yield strength of SUS316 decreases with increasing temperature. While the yield strength at 320°C is 575 N/mm^2, it declines to 570 N/mm^2 at 360°C [18]. This is because at higher temperatures, dislocations can move more easily through the crystal, enabling the material to deform plastically along slip planes. At lower temperatures, the dislocation mobility is lower and their movement through the crystal is restricted. Therefore, the material is less ductile and fractures at lower stresses than it would at higher temperatures.

While the temperature has an impact on the yield strength of the material, the CGR of SCC in SUS316 increases with increasing yield strength. In 2012, Hallberg *et al* investigated the opening stress in front of crack tips via finite element modeling and

found that the opening stress and crack opening mode do indeed depend on the temperature [207].

In this study, the stress concentration and dislocation density near the crack tip in all 14 TEM specimens was investigated applying the previously described method of measuring plastic deformation near the crack tip via TKD (Chapter 4.2.5). For this purpose the size and extent of the plastic zone at the crack tip was measured for all samples. A summary of the results is listed in Table 11.

Figure 77 shows the measurement of deformation in sample O CT1 (360°C). The crack tip has previously been established to be inactive and no obvious stress concentration around the crack tip can be observed in the average MO map, Figure 77a. In fact, the size of the PZ was determined as 100 nm x 150 nm and its extent as 1.7° ± 0.7° (top grain, Figure 77b) and 2.5°± 1.0° (bottom grain, Figure 77c), which indicates relatively low levels of deformation around the crack tip. However, there seems to be elevated plastic deformation at the grain boundary ~ 2 μm ahead of the crack tip. In this zone of higher dislocation density, slip transfer has taken place, with a number of slip bands intersecting the GB. The results of O CT2, also tested at 360°C, and N CT2 (350°C) were already shown in Chapter 4.2.5, Figure 43 and Figure 42, respectively. Sample N CT3 (350°C), not shown here, exhibited slight FIB damage in one of the grains and therefore only one grain could be examined. Table 11 not only contains information on the size and extent of the PZ, it also includes the average value of the PZ extent, measured across all grains in all samples with the same SCC test temperature.

These average values will be used later to compare the magnitude of plastic deformation at the crack tip in all samples.

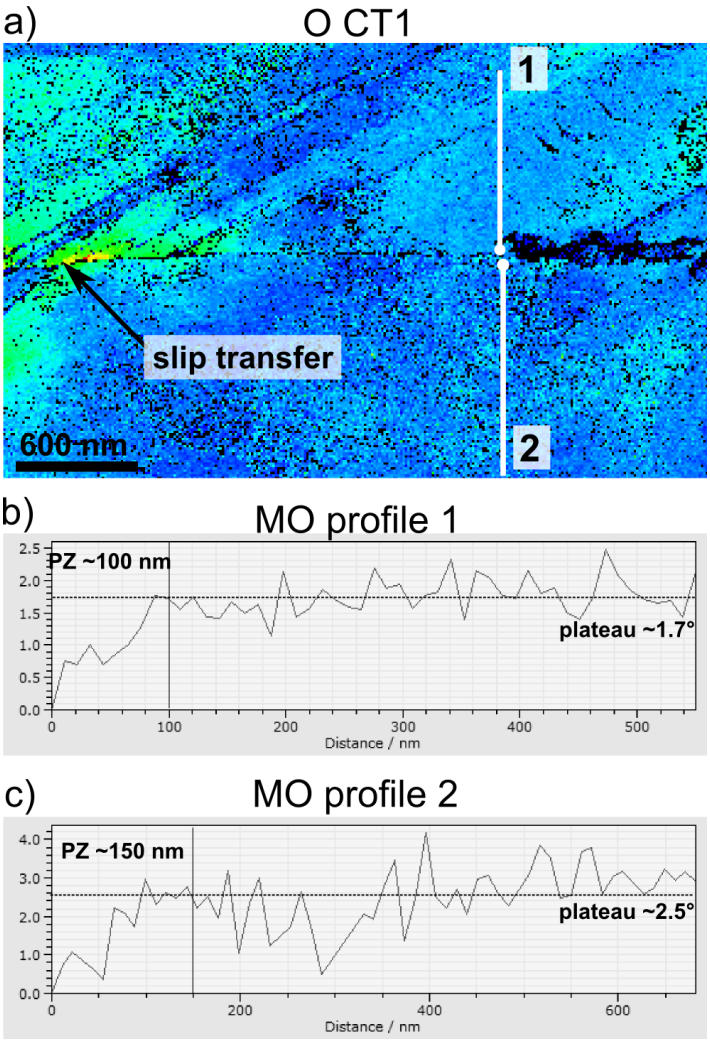

Figure 77. Measurement of PZ size and extent in O CT1 (360°C); a) average MO map indicating location of line profiles 1 and 2 and slip transfer at GB ahead of crack tip; b) MO profile 1 (PZ size: 100 nm; PZ extent: 1.7° ± 0.7°); c) MO profile 2 (PZ size: 150 nm; PZ extent: 2.5°± 1.0°)

While the average MO in samples tested at high temperatures (360°C and 350°C) is relatively low, ~ 2.6° and ~ 3.0°, respectively, Figure 78 and Figure 79 show much higher levels of plastic deformation at the crack tips at lower temperature (340°C and

320°C). Figure 78 for instance, shows high levels of plastic deformation at the crack tip and the crack flanks of sample M CT1. In addition, the existence of a high number of slip bands in the top grain and cross-slip in the bottom grain indicates high dislocation densities in this sample. Both the size and the extent of the PZ around the crack tip are significantly higher (top grain: 320 nm, 9.1° ± 1.5°; bottom grain: 450 nm, 6.0°± 1.7°) than in any of the samples tested at 360°C or 350°C.

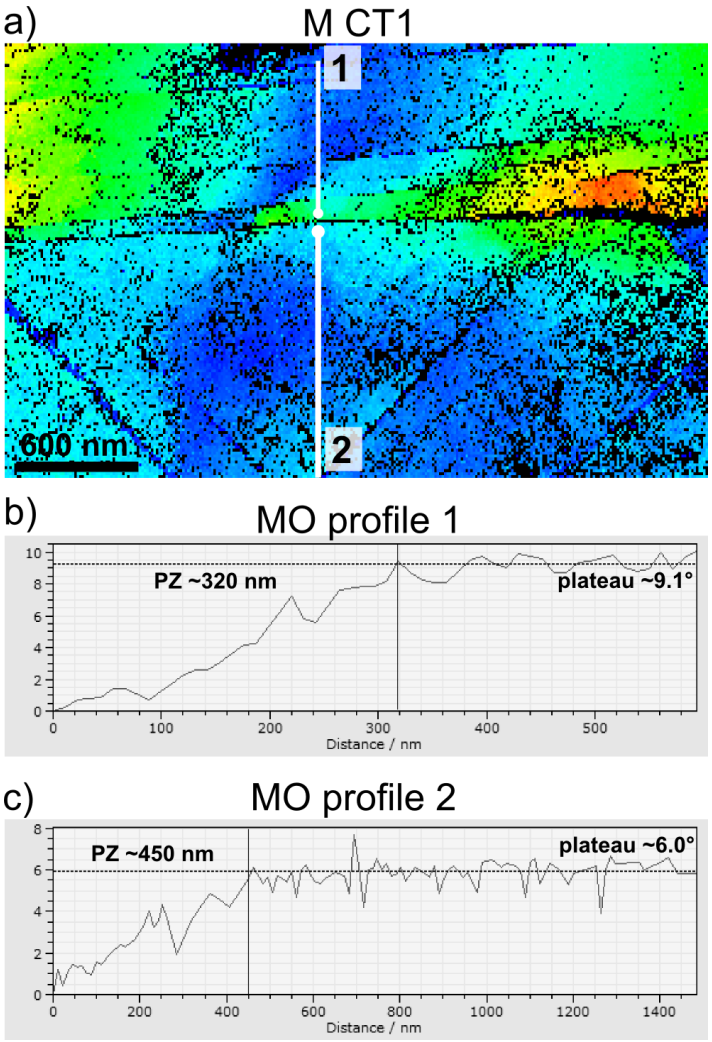

Figure 78. Measurement of PZ size and extent in M CT1 (340°C); a) average MO map indicating location of line profiles 1 and 2; b) MO profile 1 (PZ size: 320 nm; PZ extent: 9.1° ± 1.5°); c) MO profile 2 (PZ size: 450 nm; PZ extent: 6.0°± 1.7°)

Nevertheless, the extent of the PZ in the bottom grain of sample G CT1 in Figure 79 is even higher with 10°. Figure 79a shows both average MO map and STEM ADF image of the same region in G CT1 for comparison; the regions of high plastic deformation around the crack tip are indicated.

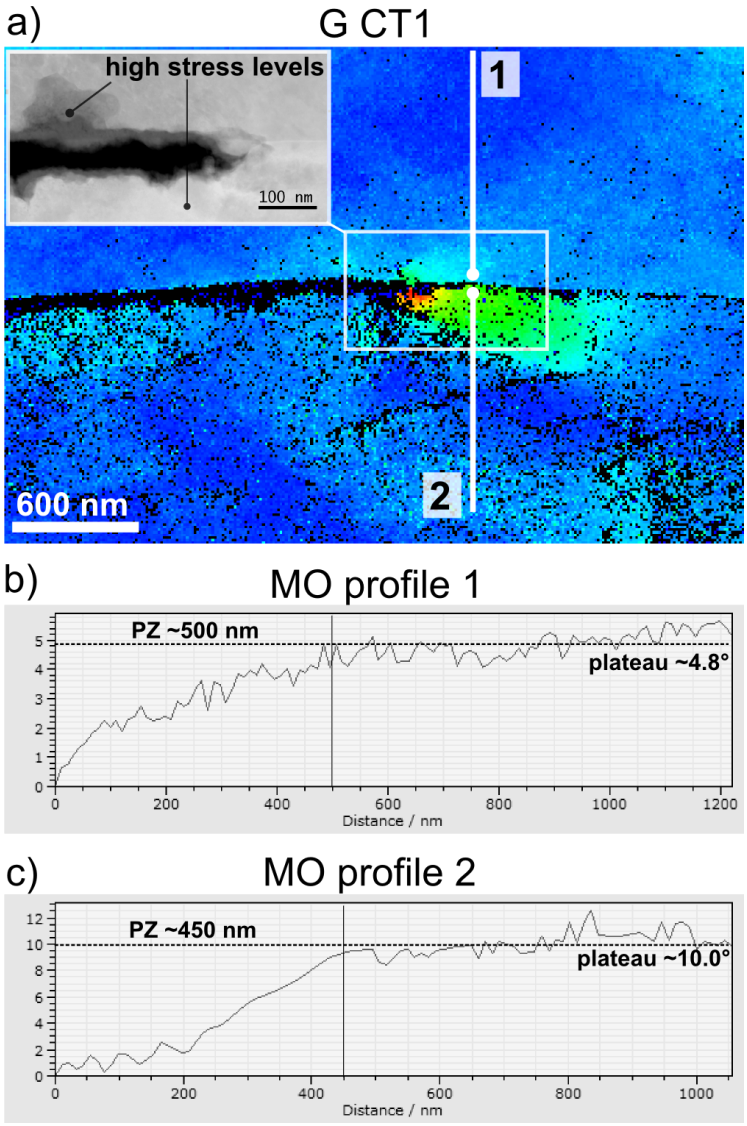

Figure 79. Measurement of PZ size and extent in G CT1 (320°C); a) average MO map indicating location of line profiles 1 and 2; insertion: STEM ADF image of M CT1; b) MO profile 1 (PZ size: 500 nm; PZ extent: 4.8° ± 1.1°); c) MO profile 2 (PZ size: 450 nm; PZ extent: 10.0°± 1.9°)

The average value of the extent of the plastic zone around the crack tip, which is related to the amount of dislocations and plastic deformation in this region, were calculated as well and are listed in Table 11. The size and extent of the PZ in all samples tested at low temperatures (340° and 320°C) suggest that the dislocation density and the strain concentration in the crack tip region is higher in these samples than in those tested at higher temperatures (360°C and 350°C). As a matter of fact, the level of plastic deformation appears to increase steadily with decreasing SCC test temperature.

Sample	T [°C]	CT number	GB MO [°]	PZ size [nm x nm]	Extent of PZ [°]		
					grain 1	grain 2	average
316INSS - O	360	1	28	100 x 150	1.7	2.5	**2.6 ± 1**
316INSS - O	360	2	55	200 x 300	-	3.8	
316INSS - N	350	2	55	200 x 200	2.8	2.0	**3.0 ± 0.9**
316INSS - N	350	3	55	-	4.2	-	
316INSS - M	340	1	42	320 x 450	9.1	6.0	**5.8 ± 1.1**
316INSS - M	340	2	57	600 x 500	5.0	7.0	
316INSS - M	340	4	42	400 x 250	5.5	3	
316INSS - M	340	5	35	150 x 400	6.0	5.0	
316INSS - G	320	1	25	450 x 500	10	4.8	**7.6 ± 1.2**
316INSS - G	320	2	12	100 x 150	4	6	
316INSS - G	320	3	50	50 x 150	3.8	3.5	
316INSS - G	320	4	55	600 x 400	12.5	12	
316INSS - G	320	5	50	400 x 500	8	5	
316INSS - G	320	6	50	400 x 500	15	6	

Table 11. Results of crystallographic and plastic deformation study: GB misorientation; plastic zone size; extent of plastic zone in both grains and average over entire temperature range

In order to relate the level of plastic deformation around the crack tip to the SCC test temperature, the diagram shown in Figure 80 was created. The orange line represents the extent of the PZ (quantities taken from Table 11, average extent of PZ [°]), also known as the level of plastic deformation, and its dependency on the SCC test temperature of the sample. The curve's progression is very similar to the CGR-T curve (green line), which has been included for comparison.

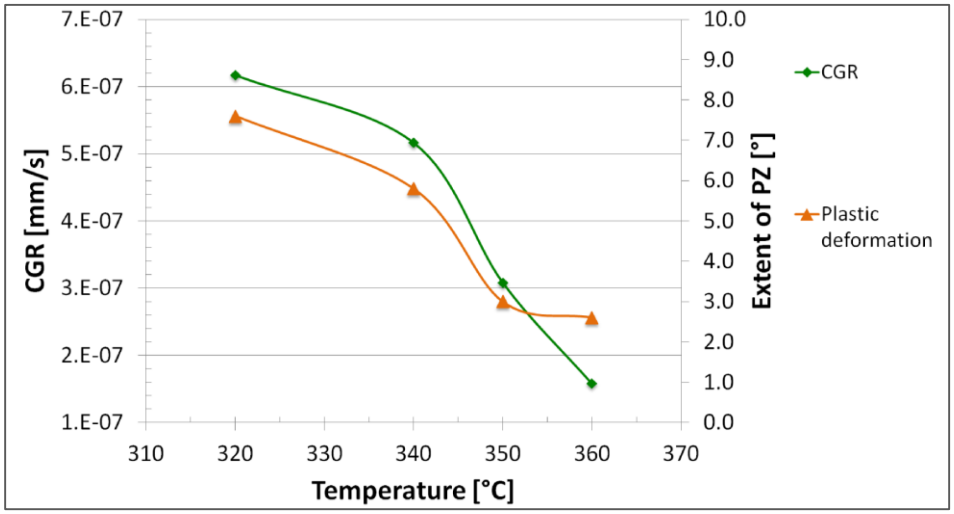

Figure 80. Temperature dependence of the CGR (green line) and the extent of the plastic zone around the crack tip (orange line)

At higher temperature (360°C and 350°C), the level of plastic deformation around the crack tip in the samples is very similar. With decreasing temperature, however, the extent of the plastic zone and therefore also the amount of plastic deformation at the crack tip increases. The highest level of deformation is reached at the lowest temperature analysed, 320°C. The excellent correlation of the progression of the two curves in Figure 80 indicates that mechanical response-based mechanisms are indeed involved in the overall SCC crack propagation process and have a clear impact on its temperature dependence.

5.4 Discussion

The main purpose of the study presented in this chapter is to provide a possible explanation for the temperature dependence of the SCC CGR in SUS316 in the range of 320°C to 360°C, based on the experimental results obtained. The study included optical microscopy, EBSD and TKD as well as analytical TEM. This "multi-scale" approach was selected to ensure that SCC features from all length-scales are taken into account. This section discusses possible mechanisms occurring during SCC crack propagation, based on information on the crack morphology, oxide compositions (outer oxide, inner oxide at the crack flanks and near the crack tip, GB oxidation), the crack tip chemistry and plastic deformation near the crack tip.

5.4.1 General observations

The results from the optical micrographs in Chapter 5.3.1 showed that both the CGR and number of crack tips in the sample tested at 320°C are significantly (up to 5 times) higher than in the sample tested at 360°C (Figure 57). While 316INSS O (360°C) only has two crack tips at the crack front (one on each side of the bifurcated crack), the number of crack tips in 316INSS G (320°C) is at least 10. The difference is that in 316INSS G, the "main" two crack branches each have a high number of bifurcations along their paths and therefore many not fully developed, mostly arrested inactive cracks. Remarkably, the width of the mature cracks along the crack path is very similar in both samples (316INSS O and G) and therefore should not influence the CGR in terms of the entire crack area, as the total crack area would be increased in case of

higher crack width. However, it is questionable why there are so many more crack bifurcations along the crack path in the low-T[§] sample and therefore many more crack tips. One possible reason could be that the threshold stress intensity for fracture of the GBs is smaller at 320°C, leading to their fracture at lower stresses than at higher T (such as 360°C and 350°C). Many of the cracks in the 320°C sample may have developed for some time but were arrested due to an obstacle in their path. As a result, more crack bifurcations and more inactive cracks can be observed. One other potential indication of higher threshold stress intensities at higher T is the existence of a transgranular crack in the 350°C sample (316INSS N, CT 1). Usually, transgranular cracking can occur when the GB strength is high enough so intergranular cracking is impeded. In sample 316INSS G (320°C) no transgranular cracks were found.

Furthermore, near the fatigue pre-crack, when using the same magnification in this area, all four SCC cracks look very similar. It was observed that only further away from the crack tip in the low-T samples (340°C and 320°C), frequent bifurcating of the main crack path occurred. In fact, the EBSD maps in Figure 58 and Figure 59 show that the SCC crack in the low-T sample (320°C), due to its length, encountered a much higher number of GBs, acting as potential crack paths, along its way than SCC cracks in high-T samples (360°C, 350°C). As a consequence, at low T, the number of encounters with a potentially susceptible GB was much higher. This could also explain the higher number of bifurcations and crack tips in 316INSS G and M.

[§] T... temperature

In accordance with data in the literature on SCC samples extracted in T-S orientation, bifurcation close to the fatigue pre-crack was found in all samples, although 316INSS M only developed a short left branch. The two main crack branches were discovered at an angle of ~ 120° to each other in the analysed samples. Branching in T-S specimen is a result of the external load and the extraction of the specimen regarding the rolling direction, as illustrated in Figure 81a. In addition, due to the cold work, many grains appeared slightly elongated in the horizontal direction in the EBSD maps, Figure 58 and Figure 59, which could be the reason for the crack propagation occurring in a net direction of about 60° with respect to the horizontal.

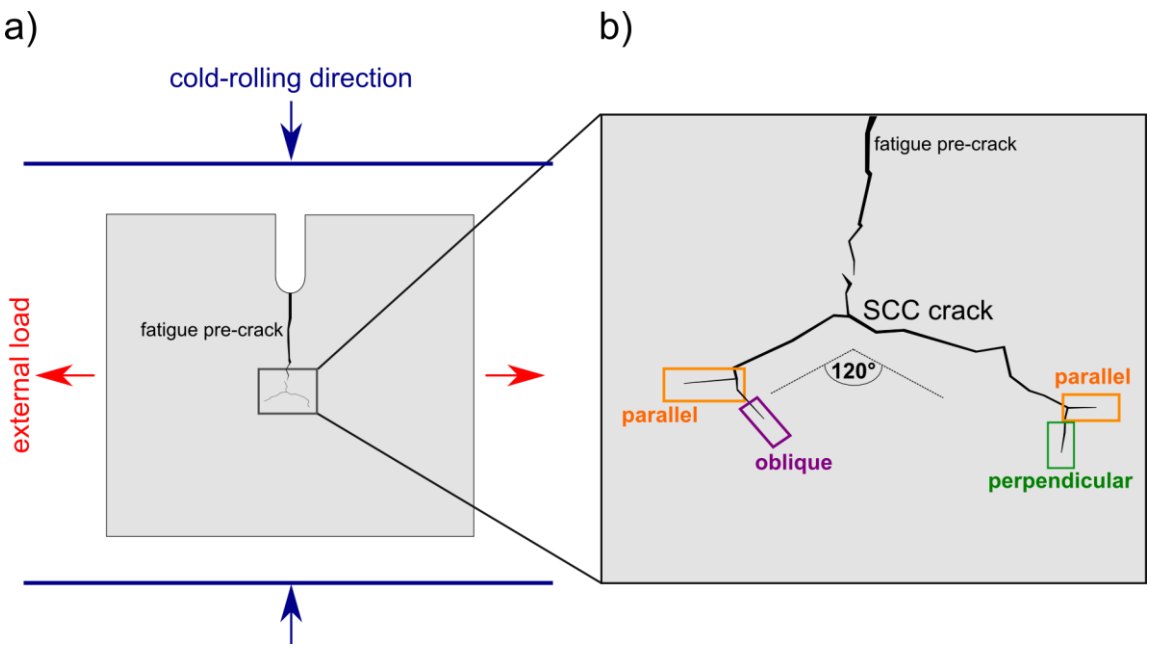

Figure 81. Illustration of SCC specimen extracted in T-S direction: a) notched SCC specimen with fatigue pre-crack; directions of cold-rolling and external load indicated; b) close-up view of SCC crack with bifurcation close to pre-crack; two crack branches at angle of ~ 120° to each other; 3 main crack directions with respect to external load: parallel, perpendicular and oblique

It was established that the majority of the crack tips analysed in this study opened in shear mode. This is especially those cases in which the crack front was oriented parallel to the external loading direction, Figure 81b (orange). Due to the high level of deformation in the samples, many slip systems might have been activated either before or during the SCC crack propagation process. In addition, due to the general inclination of the SCC crack of ~ 60° away from the horizontal and towards the external loading direction, most of the crack tips analysed were oriented parallel or oblique to the external load, as illustrated in Figure 81b (orange and purple). These circumstances could explain the more frequent crack opening in shear mode. In contrast, all cracks oriented perpendicular to the loading direction, i.e. force perpendicular to crack plane, opened in cleavage mode. This is not surprising, as cleavage-like cracking involves the "breaking apart" of the two crack flanks in opposite direction, Figure 60. Moreover, most cracks oriented perpendicular to the loading direction were found in the 340°C and 320°C samples. However, this could be merely a result of the higher number of lift-outs from low-T samples and the absence of such cracks in the high-T samples.

One sample was found to show both signs of shear and cleavage mode, as highlighted in Figure 64. In this sample, the crack path as well as the GB ahead of the crack exhibit a number of steps, coinciding with slip bands in the top grain. Due to the evidence on the crack flanks it was concluded, that in the earlier stages of crack propagation a slip-event must have occurred. Later, the crack opening continued in cleavage mode without any more slip-events until the SCC test was stopped. It should be noted, that if the events had happened the other way around, mainly evidence of shear would have been found. Since the SCC samples are highly deformed, the probability of

a slip event occurring near the crack path is high but it still depends on the crystallographic orientation of the easy-slip planes in the respective grains. In addition, many active slip systems may not be detected due to unfavourable orientation with regard to the extraction of the crack tip from the bulk specimen.

Using data on the existence of Fe oxide particles near the crack opening, the activity of every crack tip at the end of the SCC test was established. Apart from 4 inactive cracks, all other cracks were determined to be still active at the end of the SCC test. This is not surprising, as potentially active crack tips were targeted for lift-out. Three out of four inactive cracks are from sample 316INSS G (320°C), but this might be merely due to the higher total number of lift-outs. As mentioned before, there was also a higher total number of crack tips present in this sample and therefore, the probability of some of them being inactive is potentially higher.

The crack tip opening of the active cracks varied significantly between 7 nm and 70 nm. Interestingly, all crack tip openings from 316INSS M (340°C) were quite similar ~ 15 nm, whereas two out of three active crack tips from 316INSS G (320°C), both of them opening in shear mode, had crack tip openings of > 50 nm. Hence, no obvious correlation between the crack tip opening and the SCC test temperature could be found.

In general, five different types of crack tip oxide were discovered. It should be again mentioned that the crack tip is defined as the most recently fractured portion of the intergranular oxide at the crack front (or the GB). The "crack tip oxide" is defined as the oxidised region, or section of the GB, directly ahead of the crack tip that has not fractured yet, as shown in Figure 65 and Figure 67. The crack tip oxide chemistry

observed in this chapter is listed in Table 8 and shows mainly four different oxide types, although another oxide type was discovered directly ahead of the crack tip in the APT characterisation (Chapter 4.3.2). In summary, the different crack tip oxides are (values in wt. %, measurement error ~ 10%):

1) Chromia (Cr_2O_3): This oxide phase was found in a very localised region directly ahead of the crack tip via APT. Due to its small size and complicated 3D structure, this oxide would have been hard to observe with TEM. In general, chromia does not usually form in SUS316 under PWR primary water conditions due to the lack of available Cr. However, it can form locally in highly deformed regions that are exposed to high stresses, such as SCC crack tips.

2) Fe-Cr spinel-type oxide (Fe ≅ Cr content): This oxide type consists of ~ 57% O and ~ 43% metal, the stoichiometry of M_3O_4 (M... metal). The typical composition found in the analysed samples is ~ 52% O, 22% Cr, 20% Fe and 6% Ni. In this work, this oxide type was mainly found ahead of inactive crack tips filled with magnetite, such as G CT2 and G CT3 (Figure 66). These crack tips were exposed to the environment for a relatively long time before the SCC test was stopped and therefore diffusion processes had enough time to redistribute metallic species such as Fe and Ni. As a result, substantial Ni enrichment was found ahead of the Fe-depleted Fe-Cr spinel oxide.

3) $(FeCr_2)O_4$: This oxide type also consists of ~ 57% O and ~ 43% metal, whereas the metal component is divided between Cr and Fe in a 2:1 ratio. Therefore, the general

composition of this oxide is ~ 57% O, 29% Cr and 14% Fe, with almost no detectable amounts of Ni. It was found ahead of two active crack tips (N CT3 and M CT5) and with slight change in composition, i.e. enriched in Ni and deficient in O, in one other sample (G CT5). In all of these samples, the crack opening was found to be very small (< 15 nm) and a substantial region of Ni enrichment was detected ahead of the oxidation front. This could be a potential reason for the higher Ni content in the crack tip oxide in G CT5, as the composition was measured very close to the Ni enriched region, where EELS might have picked up the enhanced Ni signal. Nevertheless, the formation of $(FeCr_2)O_4$ requires heavy diffusion of Fe in order to achieve significant Fe depletion. Hence, despite the cracks being active, there must have been enough time for the oxide to form and for Fe to diffuse outwards into the PWR primary water solution, while Ni accumulated ahead of the oxidation front. A possible explanation for this could be the existence of a GB oxide ahead of the crack tip. This was actually observed in N CT3 and M CT5. This oxide might have formed ahead of the crack tip along the GB due to the accelerated diffusion of metallic and non-metallic species in this region, without being in direct contact with the environment. With an oxide forming at the GB, Fe and Ni had already started to redistribute in this region, i.e. Fe into the solution towards the crack tip and Ni away from it, before the propagating crack even reached this area. As a result, the oxidation front, i.e. the Fe-depleted $(FeCr_2)O_4$ oxide, the oxidised GB and the Ni-enrichment, might have developed steadily ahead of the constantly propagating SCC crack, as exemplified in Figure 68.

4) 20% O, nominal matrix composition: This oxide type is the closest to nominal matrix composition that has been found ahead of any of the analysed crack tips. It consists of ~ 20% O, >50% Fe, 18-20% Cr and 6-10% Ni. It was exclusively found ahead of (in total 4) active crack tips with little or no Ni enrichment. These crack tips might have fractured very recently and although oxidation had started, little diffusion of metallic species had taken place yet, although there is some degree of Fe depletion. Therefore, the composition is very close to nominal matrix composition. Special attention was paid to crack tips G CT4 and G CT5 with crack tip openings of 50 nm and 70 nm, respectively. No Ni enrichment was detected either ahead of the crack tip or at the crack flanks. Instead of steady crack propagation at constant speed, these cracks might have opened suddenly over a relatively large distance, possibly due to a sudden shear event, as both cracks opened in shear mode, due to large deformations in the material around the crack. As a result, there would have been no time for Ni to accumulate ahead of the crack front or at the crack flanks and most of the Fe still remained in place.

5) Fe spinel oxide: This oxide is very similar to the previous oxide, but with higher O content and lower Fe content. The general composition is ~ 40% O, 33% Fe, 18% Cr and up to 10% Ni. This oxide type was found ahead of two active crack tips (O CT2 and M CT4), which both opened in cleavage mode. It appears that Fe already had time to diffuse away from the crack tip into the solution, while most of the Ni, which is known to diffuse slower than Fe, still remained in place.

Nickel enrichment was found across the entire temperature range in all but three samples (M CT4, G CT4 and G CT6), tested at 340°C and 320°C. In general, the largest Ni-rich regions were found ahead of inactive crack tips, where Ni probably had enough time to accumulate significantly. Ni enrichment ahead of the crack tip was mainly found along the GB, through which it appears to have diffused away from the oxidation front. The build-up of significant Ni-enrichment ahead of inactive crack tips seems to be a further obstacle for the crack to advance. In these samples, the oxidation front appears to be trying to find its way around the Ni-rich region, for instance in samples O CT1 and G CT1, to be found in the Appendix, instead of straight along the GB. As a result, GB migration has occurred in sample O CT1, as described in Chapter 4.2.3 and illustrated in Figure 39.

Detectable levels of grain boundary oxidation were found in four samples (O CT2, N CT3, M CT2 and M CT5), all tested between 340°C and 360°C. In contrast, no obvious GB oxidation was found for any of the samples tested at 320°C. The chemistry of the GB oxide was measured far away from the crack tip in order to minimise the influence of the crack tip chemistry, including potential Fe depletion and Ni enrichment. The average GB oxide was measured to consist of 10-20% O, 17-19% Cr, >50% Fe and 8-20% Ni. In cases where there is Ni-enrichment along the GB, the O content is slightly decreased. It should be pointed out that the background O level in the matrix was measured to be ~ 7.5% due to oxidation of the TEM foil after preparation in air, whereas oxides do not re-oxidise in air and their composition is therefore reliable. Hence, in the matrix, only O contents of > 8% could be reasonably detected. The GB chemistry in all

samples with no GB oxidation was either close to nominal matrix composition or exhibited some Ni enrichment.

Oxidised GBs were shown to be very narrow features of just a few nanometres width and therefore the amount of oxidation is limited. It was also demonstrated that diffusion of metallic species mainly takes place along the GB path instead of through the metal-oxide interface, as no effects of depletion or enrichment were found in the matrix behind the metal-oxide interface. The GB oxide composition in sample N CT3 was measured in four different regions to determine the flux of the matrix constituents through the oxidised GB. It was established that Fe was moving toward the crack tip, whereas Ni must have moved in the opposite direction.

It should be noted, that the EELS measurements of the GB oxide, although relatively reliable, are subject to slight measurement errors due to the influence of the surrounding matrix. More accurate measurements were demonstrated using APT, which is capable of providing accurate compositions of very localised 3D regions (Chapter 4.3).

5.4.2 Elevated diffusion at higher temperature

In Chapter 5.3.4 it was shown that more extensive diffusion of matrix elements and O has taken place at the crack flanks, in close proximity to the crack tip, in all high-T samples, tested at 350°C and 360°C. Oxide fingers of ~ 50 - 60 nm length penetrate the crack flanks, accompanied with Fe depletion and Ni enrichment behind the metal-oxide interface. Therefore, it appears that while the crack flanks oxidised, Fe diffused outwards from the matrix into the PWR primary water solution and Ni moved further

into the matrix away from any forming oxide structures. In contrast, the diffusion processes at the crack flanks in the low-T samples, tested at 340°C and 320°C, seem much less pronounced. The average crack flank oxide width was determined as ~ 5 - 10 nm and no oxide fingers penetrating the crack flanks were detected in the EELS elemental maps. Nevertheless, some (very thin, ~ 5 nm width) Ni enrichment could be detected at some of the crack flanks. These findings suggest that the diffusion at higher T ranges further than at lower T, implicating faster diffusion of metallic and non-metallic species at the crack flanks for the 360°C and 350°C samples.

Thorough investigation of the EELS elemental maps in Figure 72 reveals that some portions of the oxide fingers penetrating the matrix at the crack flanks near the crack tip are slightly enriched in Ni. It has been established, that, in general, Ni is rejected by the forming oxides and therefore diffuses into the matrix. The diffusion of Ni in the SS matrix is substitutional and therefore requires free lattice spaces to inhabit. Since Fe diffused outwards into the PWR primary water solution, the forming oxide structures became Fe depleted and hence, additional free spaces in the lattice were available. According to the detected Ni enrichment near the boundaries of the oxide fingers (or metal oxide interface), it appears that the Ni has utilised the enhanced dislocation density in the oxide to move through that region further into the matrix. Since the diffusion velocity of Ni is slower than that of Fe, it accumulates at the oxide-metal interface of the oxide fingers, which therefore appear slightly Ni-enriched.

The extent of the diffusion process in all samples was measured at the crack flanks in order to minimise the influence of other processes occurring near the crack tip. As mentioned before in this thesis, the GB is a fast-diffusion path for both O and metal

atoms due to its higher dislocation density. However, diffusion processes at the GB close to the crack tip are not only temperature-controlled, they can also be driven by other factors. Elevated strain concentrations around the crack tip, for example, result in higher strain gradients in this region, which can lead to accelerated diffusion of vacancies and interstitial atoms [208]. Therefore, it would have been more challenging to interpret the ongoing diffusion processes near the crack tip, as various factors would have been likely to contribute to the measurement.

Analysis of the width of the crack flank oxides in the mature crack (> 500 nm away from crack tip) yielded less conclusive results. It was found that, in general, all crack flanks were covered with an oxide layer of constant thickness between 10 - 25 nm, although some oxide layers reached up to 40 nm width. However, no correlation between the temperatures could be detected. The thickness of the oxide layer was rarely found to be equal on opposing crack flanks. This might be a result of different crystallographic orientation of the two grains and therefore easier penetration/dissolution of one grain compared to the other. It could be argued, that the observations previously discussed, i.e. deeper oxide penetration at higher T, might also be a consequence of crystallography. However, this is very unlikely due to the significant (constant) difference in oxidation depth (5 - 10 nm for low T and 50 - 60 nm for high T) between the two temperature ranges. It should be noted, that the majority of cracks opened asymmetrically, meaning that, in general, one of the grains was preferentially oxidised. This supports the theory of the impact of crystallographic grain orientation on the oxidation thickness at the crack flanks in the mature crack.

5.4.3 Enhanced mechanical response at lower temperatures

As the sample is exposed to external stresses or internal strain, the material responds with modifications in its microstructure, i.e. slip, dislocations, twinning and DBs. Stainless steels are usually highly ductile and therefore deform plastically under these conditions. Dislocation movement is a very important factor for the plastic deformation of the material and if the mobility of dislocations is impeded, e.g. due to obstacles such as DBs or GBs, the material loses some of its ductility. In this case, it becomes more difficult for the material to compensate for stress and strain via plastic deformation - the material becomes harder.

There are certain areas in the sample, which are prone to the accumulation of lattice defects, resulting in locally higher strain concentrations. In SCC, these areas in the sample are usually mainly the crack tips, but also GBs and DBs. The crack tip is usually a zone of locally higher strain concentration and dislocation density relative to other areas in the sample, also known as the "plastic zone". It has been established, that the size and extent of the plastic zone is crucial for the crack propagation process and depends on the existing strain gradient and the dislocation density in this area. As mentioned previously, high strain gradients also have the effect of attracting additional vacancies and interstitial atoms, enhancing the dislocation density and movement even further.

In this study, the size and extent of the plastic zone have been established via TKD (as shown in Chapter 4.2.5) and the results were correlated with the SCC test temperature. It was found that the extent of the plastic zone, as measured via misorientation plateaus, was higher for the low-T samples than for the high-T samples.

This observation suggests that the dislocation density and therefore the strain concentration around the crack tip is higher at lower T. In addition, in most samples tested at low T (340°C and 320°C) the dislocation density in the entire sample was generally found to be higher (more DBs or slip bands) than in samples tested at high T (350°C and 360°C).

When the average dislocation density in the PZ near the crack tips (in units of misorientation degrees) was plotted against the SCC test temperature in Figure 80, the curve showed very similar progression as the curve illustrating the temperature dependence of the CGR. Therefore, it was concluded that the mechanical response of the material to external stress and internal strain indeed has an effect on the temperature dependence of the CGR. Apparently, the strain concentration around the SCC crack tips has a significant impact on the crack propagation process and appears to be higher for lower temperatures.

In contrast, the measurements of the plastic zone size do not show any conclusive trend, but seem to increase slightly at lower temperatures. In fracture mechanics, the general concept is that higher strain gradients arise from the reduction of the plastic zone size. This is because the same number of dislocations confined to a smaller area results in higher dislocation density. In this study, it was established that the total number of dislocations (the misorientation level) in the plastic zone is generally higher at lower T. Therefore, instead of a reduction of the plastic zone size, the dislocation density increases around the crack tip due to a higher number of lattice defects. These potentially result from dislocation pile-up due to the restricted ductility at lower T.

5.4.4 A possible explanation for the inhibition of the CGR at higher temperature

Based on previous work by Arioka & Terachi *et al* and the study presented in this thesis, it could be established that the SCC CGR in SUS316 stainless steels in PWR primary water increases between temperatures of 250°C and 330°C and declines towards higher temperatures. Therefore, it was proposed that at least two rate-controlling mechanisms have to be involved in the SCC crack propagation process.

Arioka *et al* suggested thermally activated diffusion as the first mechanism, facilitating the growth of the CGR with increasing T due to enhanced oxidation rates. Similarly, through high-resolution analytical STEM, this study demonstrated enhanced oxidation rates at the crack flanks at higher T (350°C and 360°C) compared to lower T (340°C and 320°C). Evidently, thermally activated diffusion is likely to be one of the rate-controlling factors in the SCC crack propagation process. Nevertheless, it was observed that the CGR dropped significantly above 320°C, as shown in this work. Therefore, it appears that, in the respective temperature range, the effect of diffusion was perturbed by another mechanism.

Based on the results in Terachi's study on the impact of mechanical properties on the CGR, the second mechanism suggested in this thesis is the mechanical response to externally applied forces and internal strain. Specifically, at higher T, dislocations move more easily through the crystal lattice and plastic deformation such as slip compensates for most of the applied stresses. At lower T, however, the dislocation mobility is restricted and the material does not deform as easily. This can result in dislocation pile-up and brittle-like fracture at SCC crack tips, although SUS316 is considered a highly ductile material.

It seems possible, that the interaction of increasing oxidation at higher T and brittle-like fracture towards lower T might lead to a maximisation of the CGR. However, within the temperature range in this study, it appears that the effect of mechanical response-based mechanisms is more dominant than thermally activated diffusion, especially at higher T. Potential reasons for this phenomenon and its underlying mechanisms are discussed in the following paragraphs.

Great significance in the crack propagation process has often been attributed to the formation and mobility of vacancies in the crack tip region. While higher diffusion rates at higher T result in increased vacancy generation and movement, higher strain gradients at the crack tip due to locally higher concentration of defects at lower T can have the same or maybe an even more pronounced effect. Figure 82 illustrates a proposed mechanism of how the flux of defects (such as vacancies and interstitial atoms) may have occurred near the crack tip at low T (340°C and 320°C) and high T (350°C and 360°C). An increased flux of dislocations towards the crack tip, mainly through the GB, but potentially also from other regions in the sample, is suggested for SCC crack tips at low T in Figure 82a. The high local dislocation density in the plastic zone, due to lower ductility at lower T, results in a higher strain gradient that attracts more dislocations towards the crack tip, further increasing the dislocation density in the PZ. In addition, the flux of vacancies into the PZ may lead to the formation of voids inside the crack tip (or GB) oxide directly ahead of the crack tip, making this region more brittle and prone to fracture.

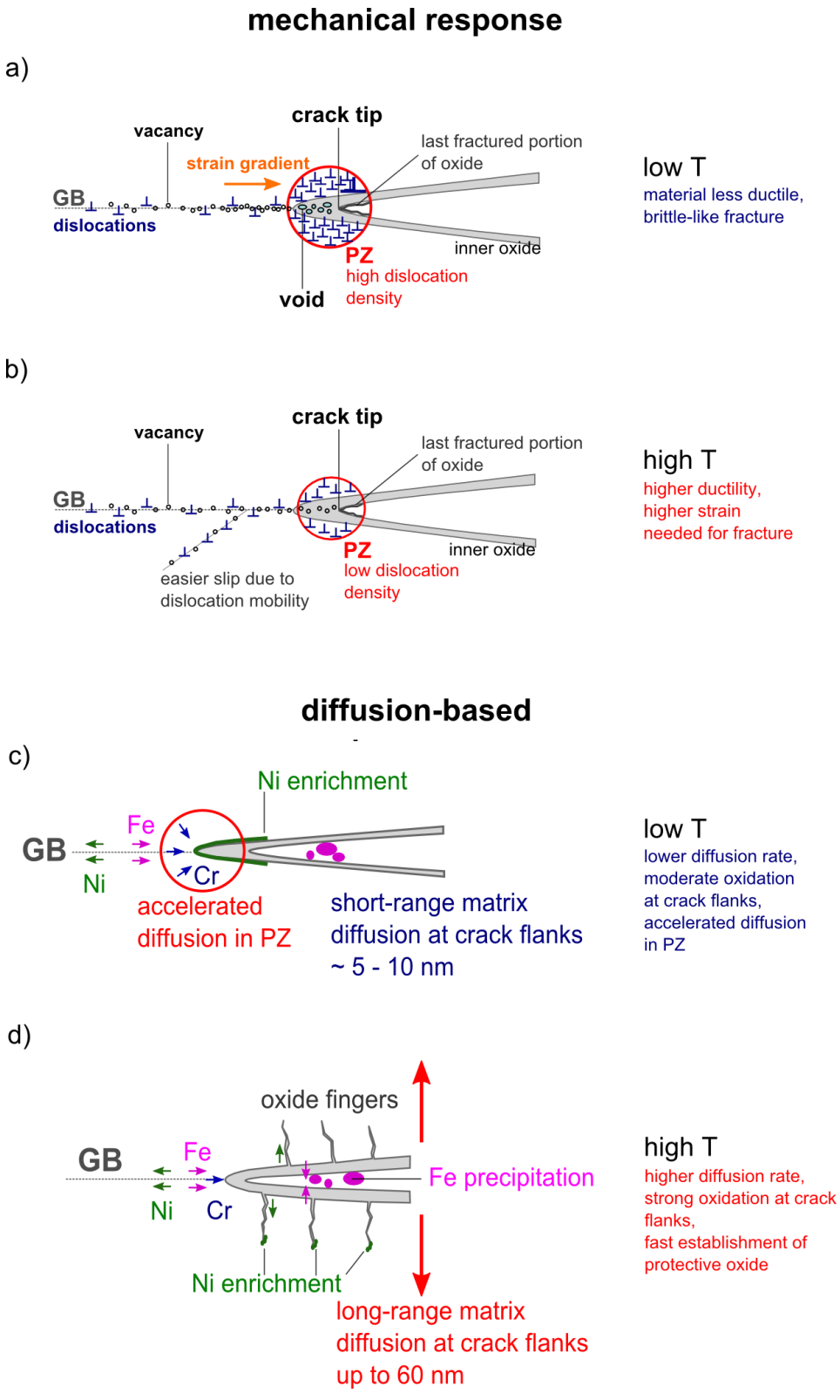

Figure 82. Illustration of possible mechanisms occurring at the crack tip; Mechanical response-based mechanisms: a) low T; b) high T; Diffusion-based mechanisms: c) low T; d) high-T

In contrast, the SCC samples tested at higher T deform more easily via slip due to enhanced dislocation movement through the crystal, as shown in Figure 82b. Therefore, the dislocation density is lower near the crack tip and fewer vacancies accumulate to form voids due to the smaller strain gradient. In general, it is assumed that the material as well as the crack tip region will be more ductile and less prone to fracture at higher T. In addition, diffusion-based phenomena, described in more detail in Chapter 5.4.2, are illustrated in Figure 82c and Figure 82d for low and high temperature, respectively. That both mechanisms are not entirely separable is shown in Figure 82c, where higher defect density in the PZ accelerates the diffusion of metallic and non-metallic species towards the crack tip. Due to that phenomenon, it is believed that Cr could accumulate in high enough quantities to form chromia directly ahead of the crack tip, as observed in Chapter 4.3.2.

In conclusion, the accumulation of vacancies near the crack tip, also known as voids, has often been thought of as a precursor for crack propagation. A high number of voids ahead of the crack tip combined with the more brittle-like behaviour of the material at low T is very likely to result in enhanced CGRs compared to high T. This could be a potential explanation for the reverse effect of the temperature dependence of the CGR in SUS316 above 320°C. Although the peak CGR in this study was found around 320°C, it is known that this peak varies depending on the cold-work level of the material, the material composition as well as the water chemistry.

It should be pointed out, that thermally activated diffusion and mechanical response are only two of many mechanisms potentially involved in SCC crack propagation (as discussed in Chapter 1.5 - Proposed models for SCC). One factor, which

has not yet been studied extensively in the research community, is the adsorption of hydrogen at the crack tip and its influence on the material in this region. It is known that due to the electrochemical processes near the crack tip, including metal dissolution and hydrogen gas generation, hydrogen is both released into the solution but also adsorbed by the material. This could potentially lead to hydrogen embrittlement as well as accelerated diffusion of metallic and non-metallic species in the crack tip region. Therefore, it is conceivable that hydrogen plays an important role in the SCC crack propagation process and also in the temperature dependence of the CGR.

6. Conclusions

The task of material selection for nuclear engineering purposes always entails a compromise between choosing the material with the best possible mechanical properties (strength, ductility, hardness, etc.) and the safest operation (e.g. the lowest possible SCC susceptibility). This search is aggravated by the fact that usually, the "strongest" material is not always the "safest" and that the material's properties can easily change in different environments.

This study showed, that SUS316 is most susceptible to SCC in PWR primary water at ~ 320°C. The reasons for this phenomenon, however, are still under discussion amongst researchers. Within the framework of this thesis, new methods were developed and explored (low-kV EDX in Chapter 4.1, TKD in Chapter 4.2 and APT in Chapter 4.3), with the expectation that they would contribute to our knowledge about the ongoing SCC mechanisms. The utilisation of these novel methods, combined with conventional techniques such as EBSD and analytical TEM, enabled the author to gain further understanding of the ongoing processes occurring in the crack tip region and to offer suggestions based on the experimental results.

6.1 New experimental techniques

These are the new experimental techniques that were developed or utilised successfully for SCC research:

1. **Low-energy EDX**

   This technique was determined to be very useful for the initial analysis of SCC cracks. The spatial resolution of SEM-EDX is increased due to the smaller interaction volume of low-energy X-rays with the bulk specimen. Active or inactive crack tips could be identified and microstructural features, such as oxidised deformation bands, could be easily located. In addition, small regions of Ni enrichment were detected ahead of some crack tips.

2. **Transmission Kikuchi diffraction**

   Due to the use of an electron transparent TEM foil, and therefore reduction of the interaction volume of the electron beam with the sample, the spatial resolution of orientation mapping was significantly increased with TKD. In the framework of this project, TKD was used for determining grain orientations and misorientations within the sample, for localising nanoscale crystallographic features such as GB migration and lattice defects as well as for the quantification of the plastic zone around the crack tip. TKD became a key technique within this work and some of the final conclusions of this thesis are based on it.

3. **Atom probe tomography of SCC crack tips**

   A new method for preparing atom probe needles containing entire SCC crack tips (including open crack, crack tip, GB oxide and Ni enrichment) was developed. With one sample in particular it was shown that APT is able to generate unique data for SCC characterisation, especially in the confined region of the GB oxide directly

ahead of the crack tip. It was determined, that the oxide composition near the crack tip is very close to Cr_2O_3 stoichiometry and changes considerably with increasing distance away from the crack tip. Comparison with EELS data in the same region showed, that the influence of contributions from the surrounding matrix obscure the EELS compositional measurements. It was concluded that APT is an excellent technique for the measurement of very localised compositions, but involves high efforts in sample preparation with a comparatively small success rate.

6.2 Novel insights into SCC crack propagation mechanisms

The mechanisms of SCC crack propagation are a topic of intense research in the SCC community. Within the framework of this project, some insights into the processes involved in SCC crack propagation could be gained.

1. **Influence of external load direction**

   Strong correlation between the direction of the externally applied load with regard to the crack plane and the SCC opening mechanism were found. Most cracks oriented parallel or oblique to the load opened in shear mode, whereas perpendicular cracks mainly opened in cleavage mode. Furthermore, it was established that the majority of all analysed cracks opened in shear mode, potentially a result from the extraction of the sample in T-S orientation.

2. Influence of test temperature on CGR

While a steady increase of the CGR between 250°C and 330°C was reported by Arioka *et al*, it was discovered that the CGR decreases between 320°C and 360°C in SUS316 exposed to PWR primary water. Optical micrograph images showed significantly larger crack lengths at 320°C compared to SCC samples tested at elevated temperature (340°C, 350°C and 360°C). As reported by other researchers, such an inhibition of the CGR towards higher temperatures was also found in samples with different cold work level and composition. Only Alloy 600 does not show the same effect [206].

3. Crack tip and GB oxide chemistries

A number of different types of crack tip oxides were found in this study: an Fe-Cr spinel type oxide, $(FeCr_2)O_4$ and two oxides close to matrix composition but with varying O and Fe contributions. In addition, the APT measurements also indicated that, immediately ahead of the analysed crack tip, a small but detectable phase of Cr_2O_3 is present. The existing oxide types are indicators for the ongoing processes in the crack tip region, allowing the deduction of the state of the crack tip at the end of the SCC test.

Grain boundary oxidation (length up to 120 nm) was found ahead of 4 out of 14 crack tips, mainly towards higher temperatures. The GB oxide chemistry suggests that the GB is being used as a fast-diffusion path for Fe and Ni, towards and away from the crack tip respectively.

4. The effect of thermally activated diffusion

As suggested by Arioka *et al*, the results of this work indicate that thermally activated diffusion indeed acts as a rate-controlling factor in SCC crack propagation. It was found that the oxidation of crack flanks near the crack tip is more pronounced at higher temperatures. It appears that, as predicted, at higher temperatures elevated diffusion rates result in accelerated oxidation rates.

5. The impact of mechanical response and plastic deformation

Mechanical response to external stresses and internal strain was determined as another rate-controlling factor in SCC crack propagation. The dislocation density and therefore strain concentration was found to be significantly increased at low SCC test temperatures compared to high ones. Due to the correlation of the temperature dependence of the CGR and the strain concentration around crack tips, it was concluded that mechanical response-based mechanisms dominate the SCC crack propagation process between 320°C and 360°C.

6. Crack tip mechanisms at low and high temperature

Based on experimental evidence, possible implications of the mechanical response-based mechanisms occurring at the SCC crack tip were proposed. Due to restricted dislocation mobility at lower temperatures, the strain concentration in the PZ around the crack tip is enhanced. As a result, additional dislocations are attracted by the elevated strain gradient into the plastic zone and the crack tip region becomes more

brittle and prone to fracture. This could be a possible explanation for the 5 times higher CGR at 320°C than at 360°C.

7. Future work

Our understanding of the underlying mechanisms of SCC has grown significantly over the past decades, not least because of the steady improvement of experimental techniques such as electron microscopy. However, the multitude of factors potentially involved in the SCC crack propagation process continuously offers new subjects of study. Based on the work conducted in the framework of this thesis, the following topics are proposed as potential future areas of study:

1. **High-resolution strain mapping via TKD**

   The acquisition of accurate quantitative data of the strain distribution in the SCC crack tip samples is necessary. This can potentially be achieved via high-resolution strain mapping using TKD and may lead to more reliable and comparable data on the plastic zone around the crack tip. Computer algorithms such as the ones developed and used by Wilkinson *et al* may be very helpful for the exact determination of the strain concentrations in the SCC crack tip samples [199,209].

2. **Extensive crack tip characterisation via APT**

   The characterisation of SCC crack tips via APT provided additional information on the GB chemistry directly ahead of the crack tip. Although the sample preparation efforts are increased, further studies are recommended in order to investigate the exact oxide compositions at different locations. This could lead to further understanding of the process of oxide formation near the crack tip and inside the GB. A possible routine could involve the preparation of an atom probe needle from

already analysed TEM specimen via STEM and TKD. The already thinned sample could be transferred from the TEM Cu grid to a tomography holder and then thinned from the other two sides. The final needle shape can then be achieved via annular milling as demonstrated in Chapter 3.4.2.

3. The influence of hydrogen in the crack tip region

It has been established that the adsorption of hydrogen can cause hydrogen embrittlement in the crack tip region and may accelerate the SCC crack propagation process. In addition, hydrogen is known to stabilise vacancies, pinning them to certain areas of localised strain concentration. For this reason, high-resolution studies locating adsorbed hydrogen in the crack tip area are necessary. This could potentially help to identify the impact of hydrogen on SCC. However, detecting hydrogen is not trivial as it is extremely volatile and not bound chemically. Due to the small dimensions of TEM and APT samples, hydrogen can escape from the crack tip region during or after the sample preparation process. Nevertheless, hydrogen trapped in vacancies or voids occurring in the crack tip region is weakly bound and may therefore be detected via APT. Conducting the SCC test in heavy water may help to distinguish between hydrogen (deuterium) resulting from electrochemical processes and hydrogen generated during sample preparation or the experiment.

4. Extended study of the temperature dependence of the CGR

The experiments conducted by Arioka and Terachi allow us to understand the impact of factors such as cold work, material composition and water chemistry on the T-

dependence of the CGR. However, their data do not explain the reasons for the influence of temperature on the SCC crack propagation process. Only microstructural studies such as the one shown in Chapter 5 of this thesis can reveal the mechanisms involved. Therefore, more studies, similar to the one conducted in this project, focussing on the impact of parameters such as the alloy composition, cold work level or water chemistry are necessary. Arioka *et al* demonstrated, for instance, that Alloy 600 (Ni-based superalloy) does not show the inhibition of the CGR at higher temperatures as all other alloys in his study (e.g. SUS316, Alloy 690, Alloy 800) [206]. It is therefore recommended to study samples with varying Ni content as an attempt to elucidate this phenomenon.

5. The stress-driven migration of atoms

Further studies are suggested into the mechanism of stress-driven diffusion of atoms to the crack tip and to the crack flanks, as previously established by Rauh and Bullough [210] in 1985. The results of this thesis suggest that the strain concentrations near the crack tip have a significant impact on the local distributions of Fe, Cr and Ni. Specifically the increased Ni enrichment towards higher temperatures and the increased Cr concentration near the crack tip, forming chromia, requires further investigation. The effects of stress and strain on the elemental distribution could potentially be established in the absence of a chemical environment, excluding the effects of corrosion.

8. Appendix

The elemental EELS O K, Fe L, Cr L and Ni L edge maps of all studied 316INSS samples are displayed on the following pages. A STEM image is shown for comparison.

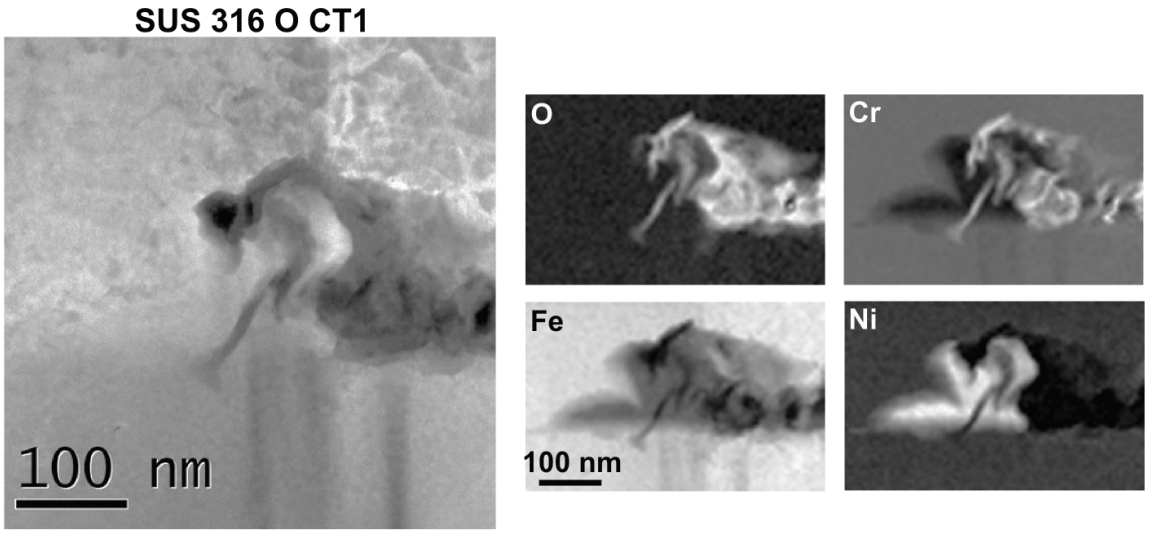

Figure 83. 316INSS O CT1: STEM ADF image (left) and EELS elemental maps (right)

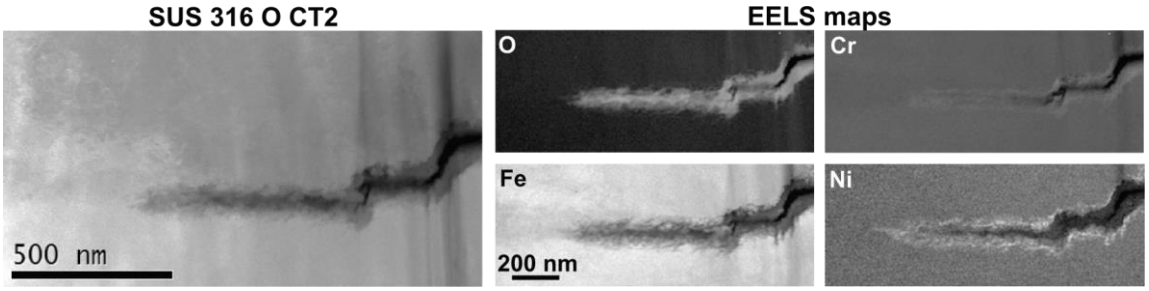

Figure 84. 316INSS O CT2: STEM ADF image (left) and EELS elemental maps (right)

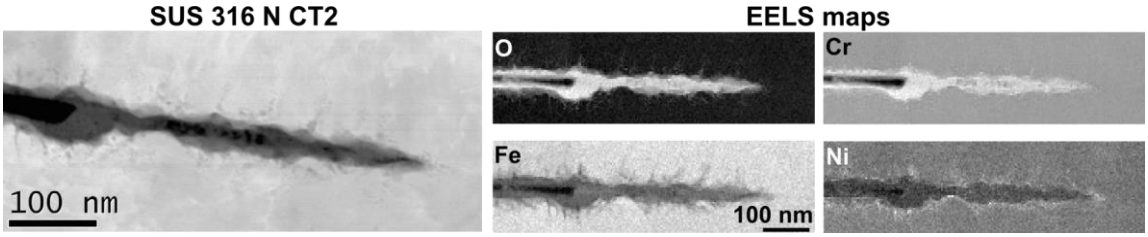

Figure 85. 316INSS N CT2: STEM ADF image (left) and EELS elemental maps (right)

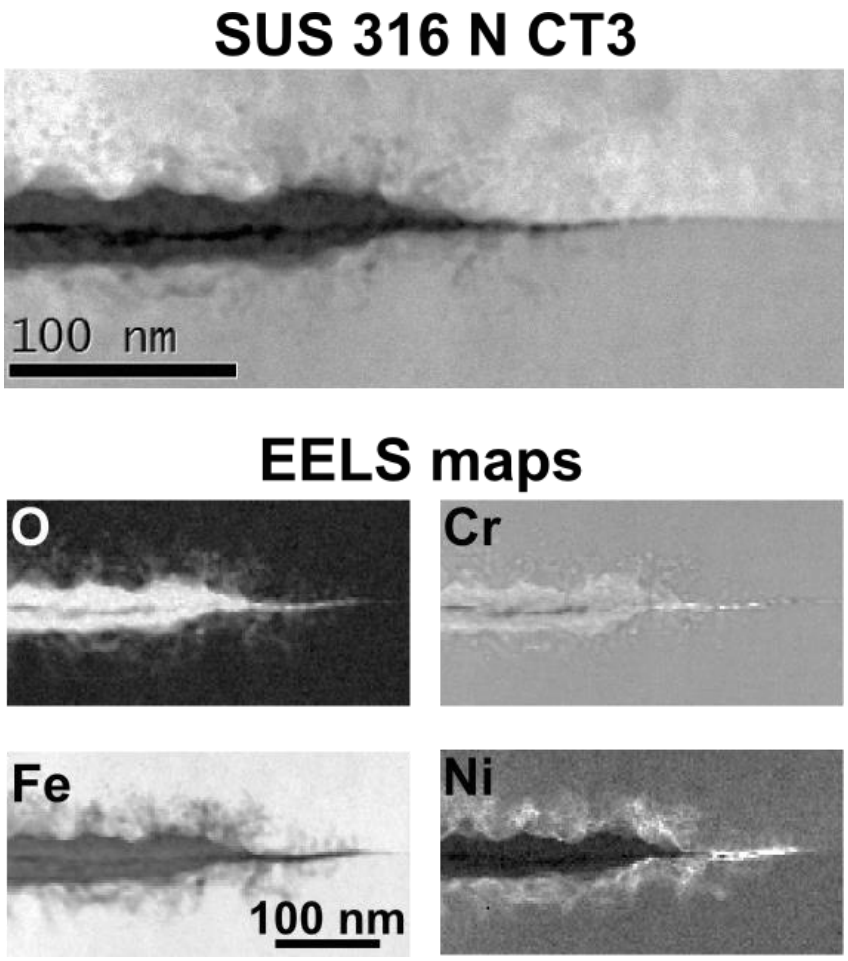

Figure 86. 316INSS N CT3: STEM ADF image (top) and EELS elemental maps (bottom)

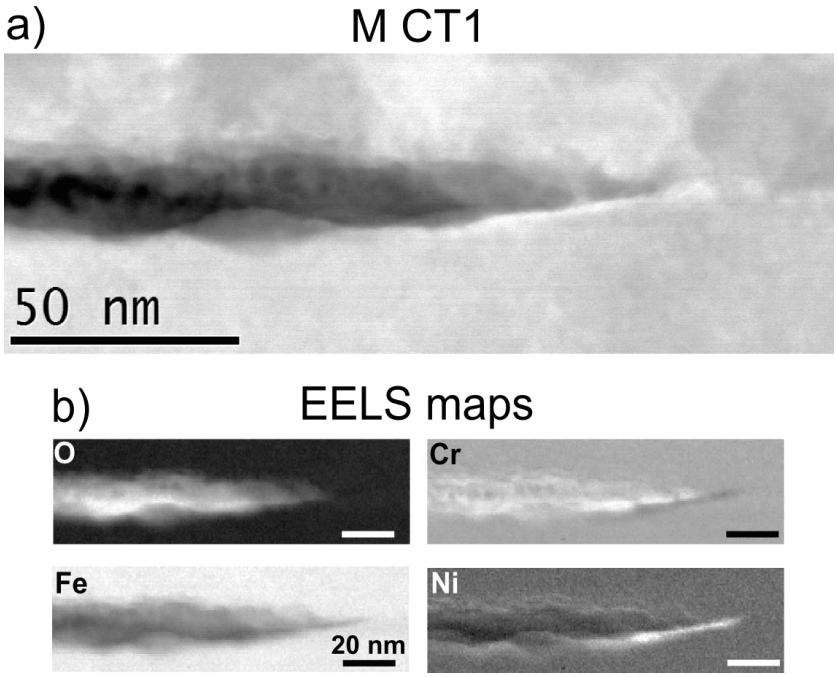

Figure 87. 316INSS M CT1: a) STEM ADF image; b) EELS elemental maps

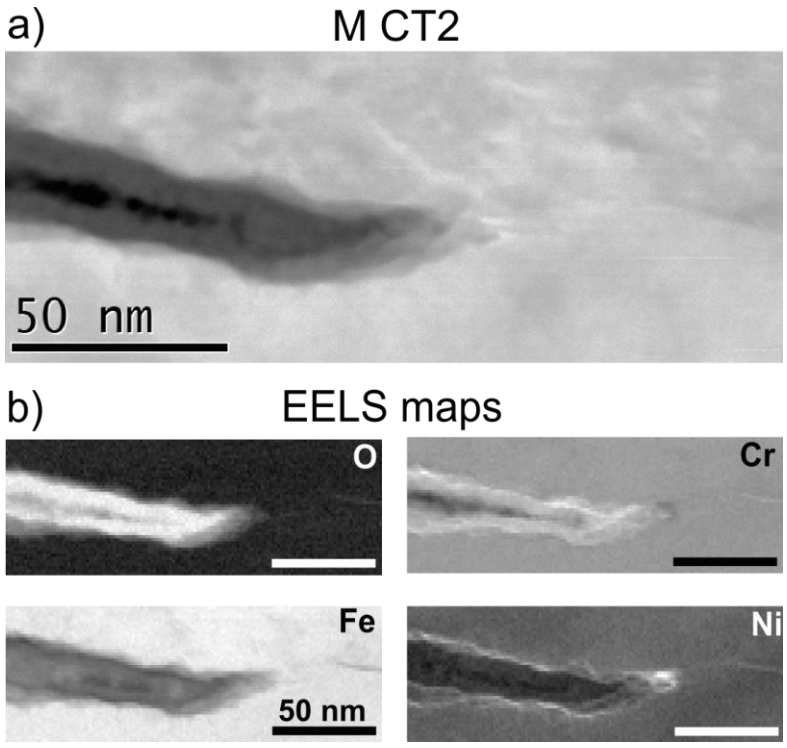

Figure 88. 316INSS M CT2: a) STEM ADF image; b) EELS elemental maps

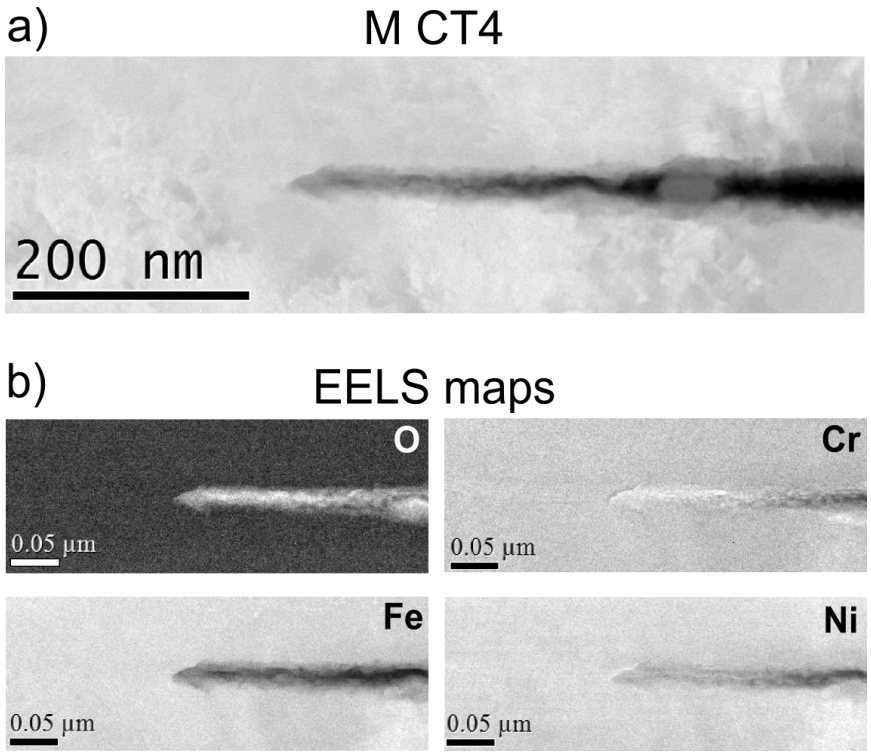

Figure 89. 316INSS M CT4: a) STEM ADF image; b) EELS elemental maps

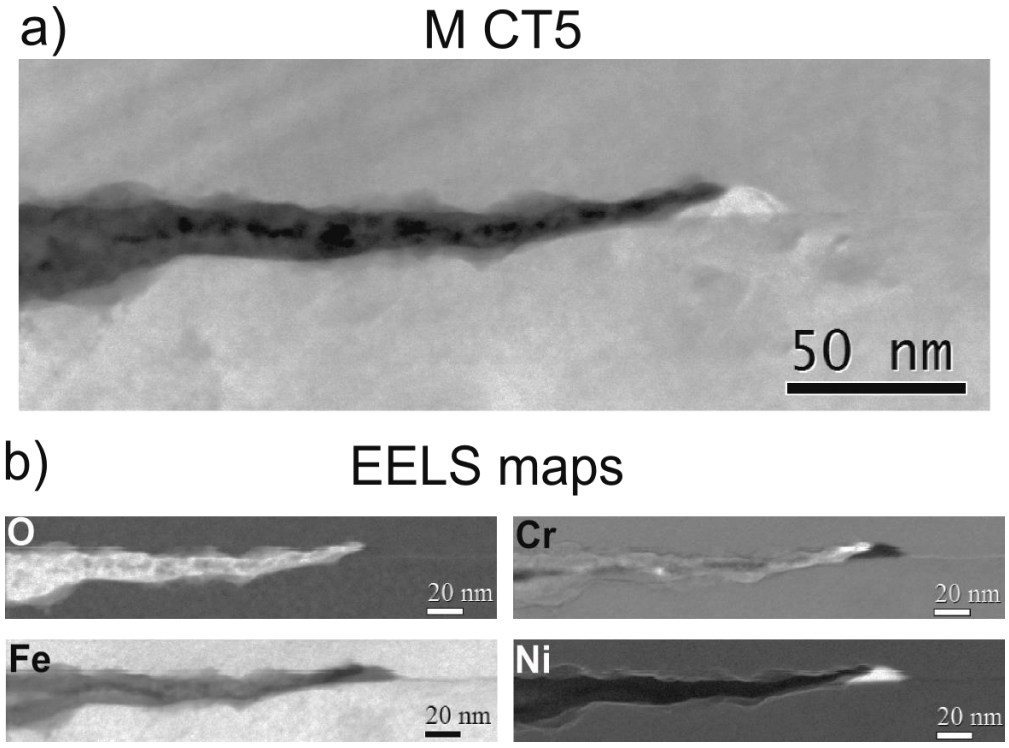

Figure 90. 316INSS M CT5: a) STEM ADF image; b) EELS elemental maps

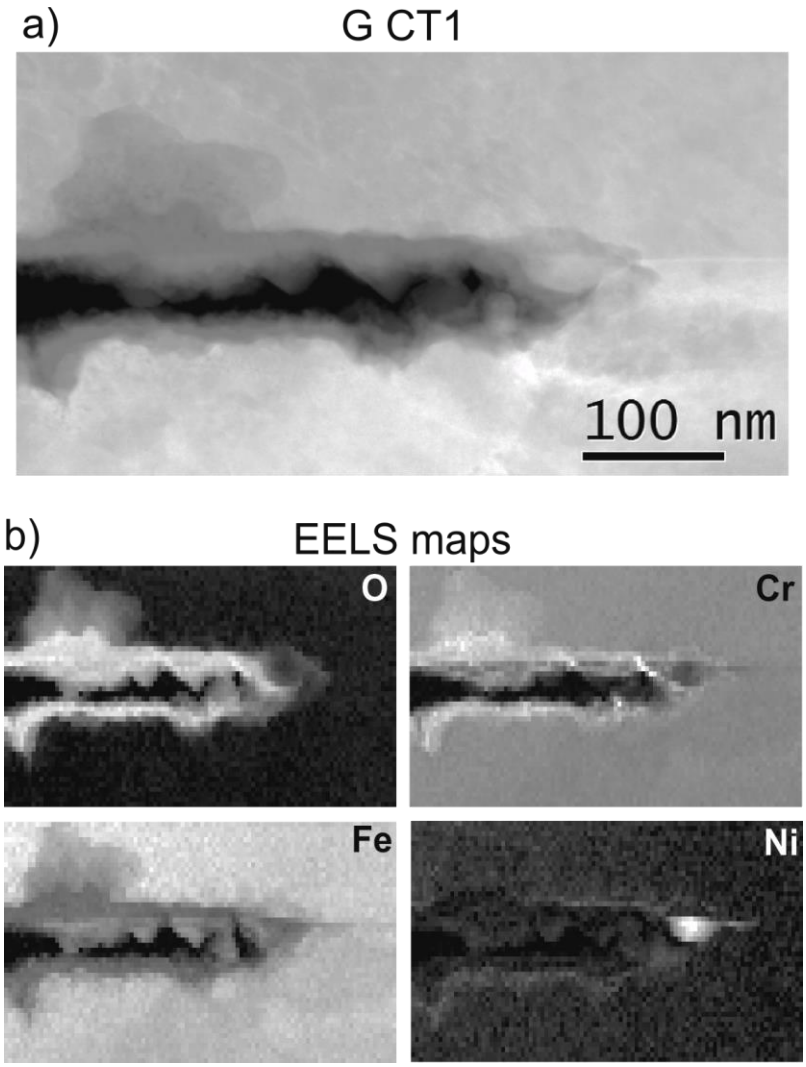

Figure 91. 316INSS G CT1: a) STEM ADF image; b) EELS elemental maps

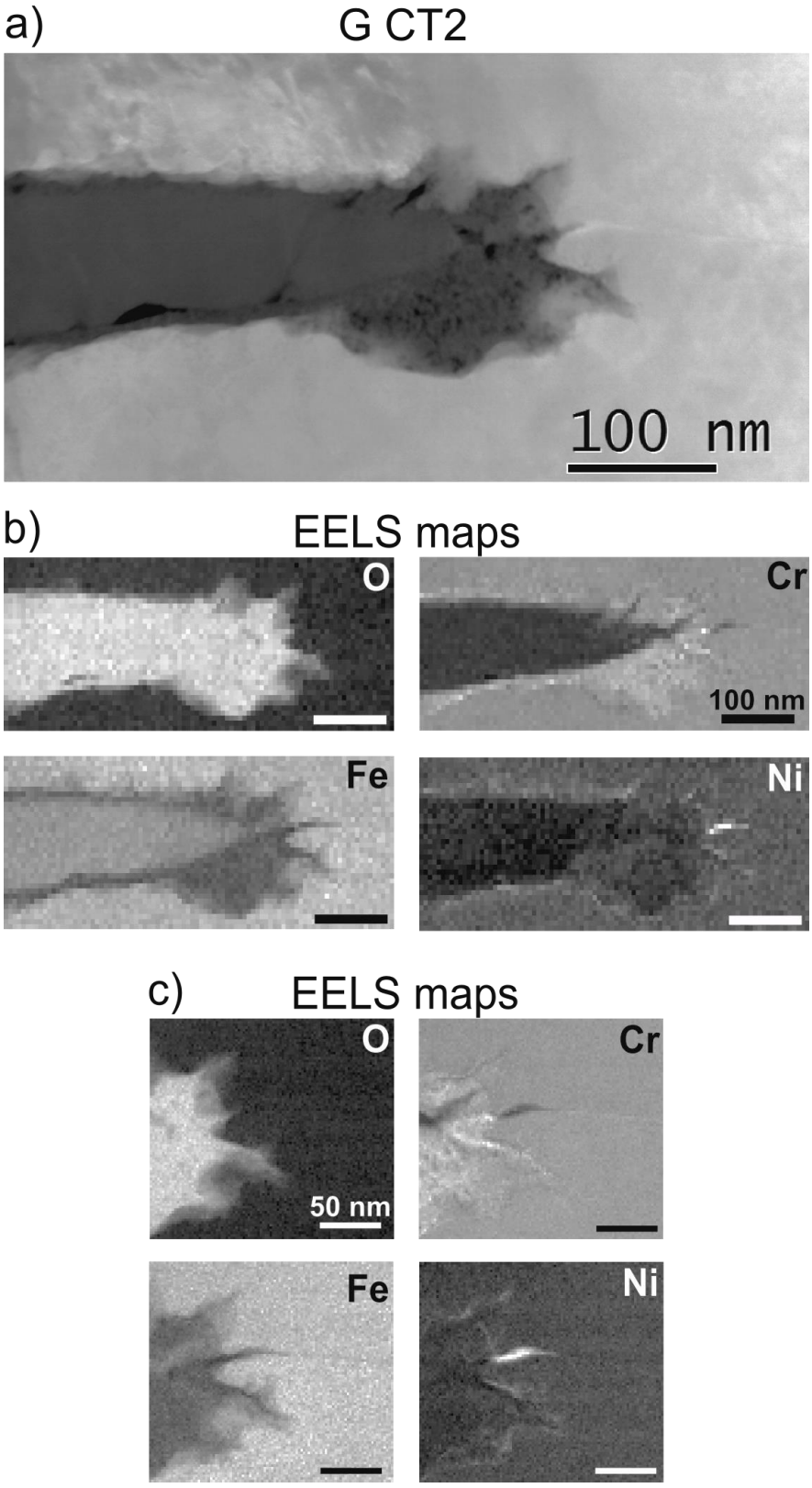

Figure 92. 316INSS G CT2: a) STEM ADF image; b) EELS elemental maps; c) EELS elemental maps (larger magnification)

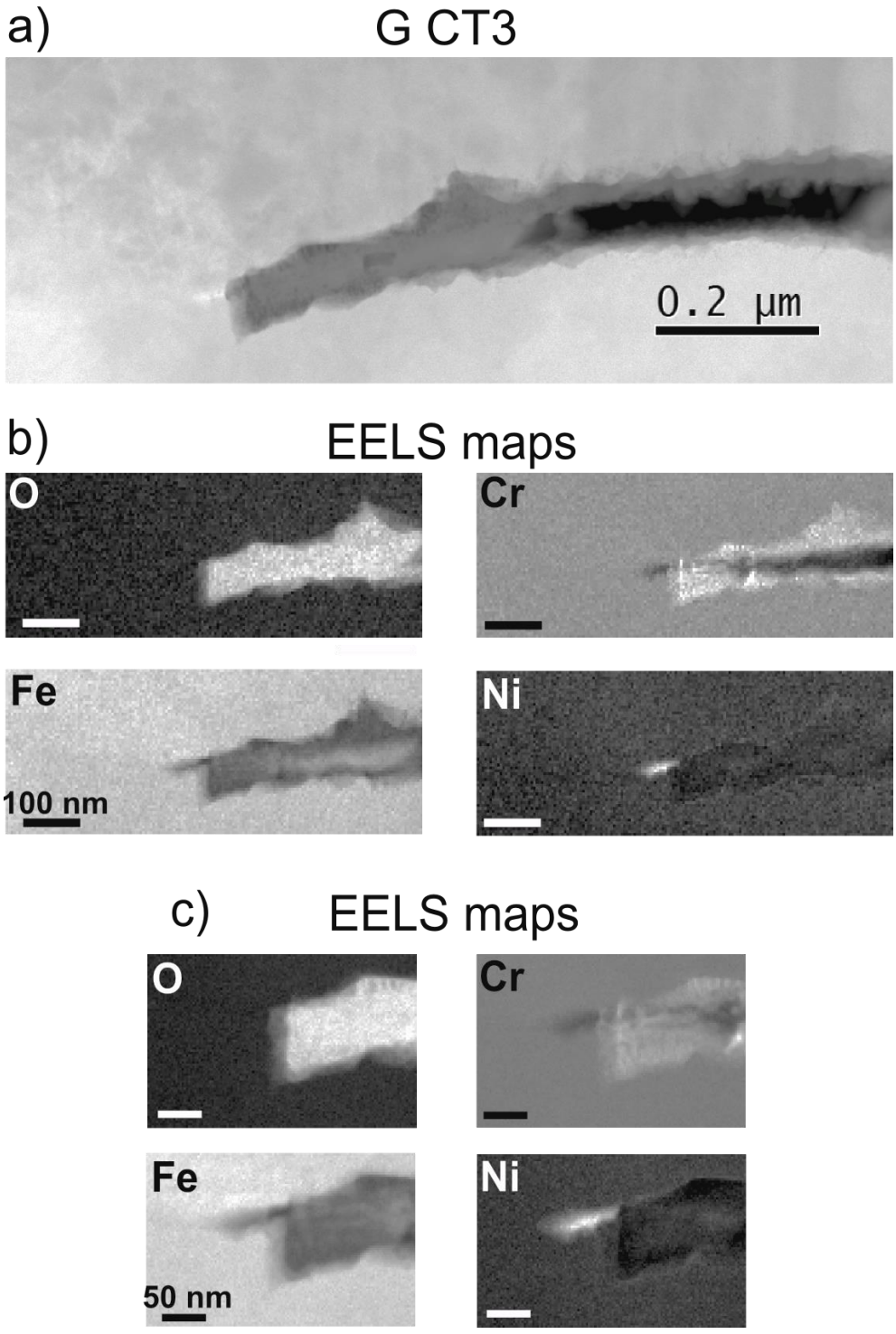

Figure 93. 316INSS G CT3: a) STEM ADF image; b) EELS elemental maps; c) EELS elemental maps (larger magnification)

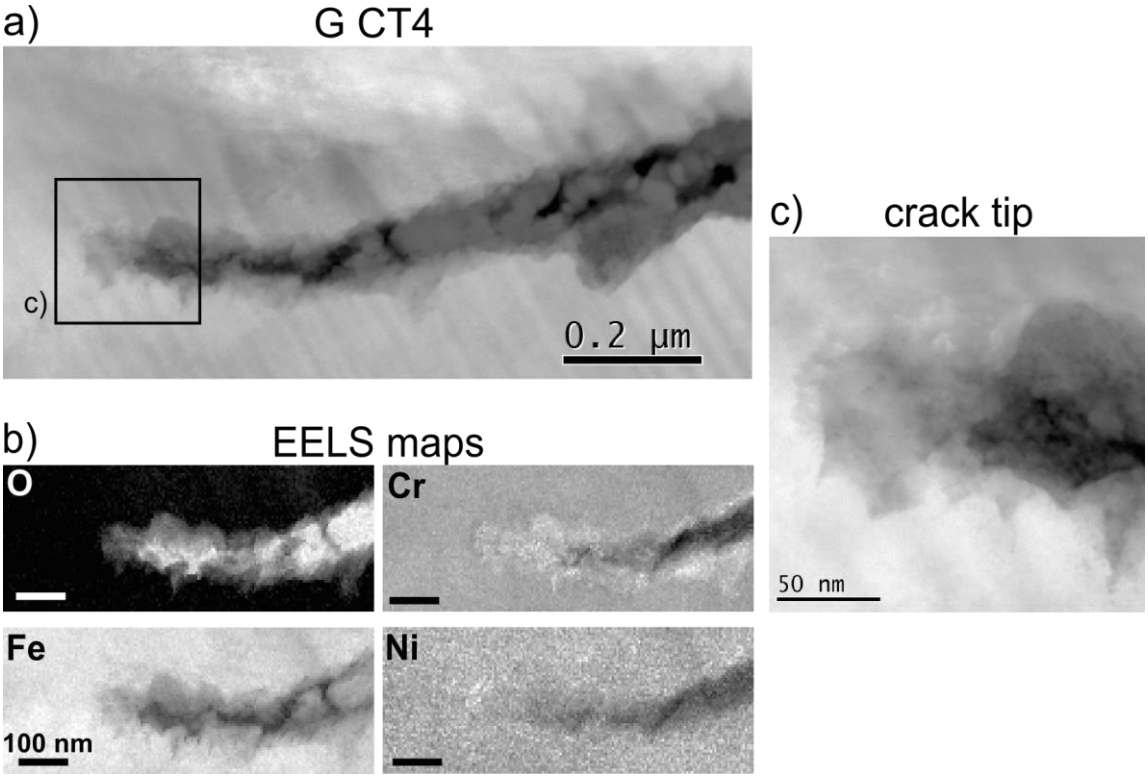

Figure 94. 316INSS G CT4: a) STEM ADF image; b) EELS elemental maps; c) STEM HAADF close-up of crack tip

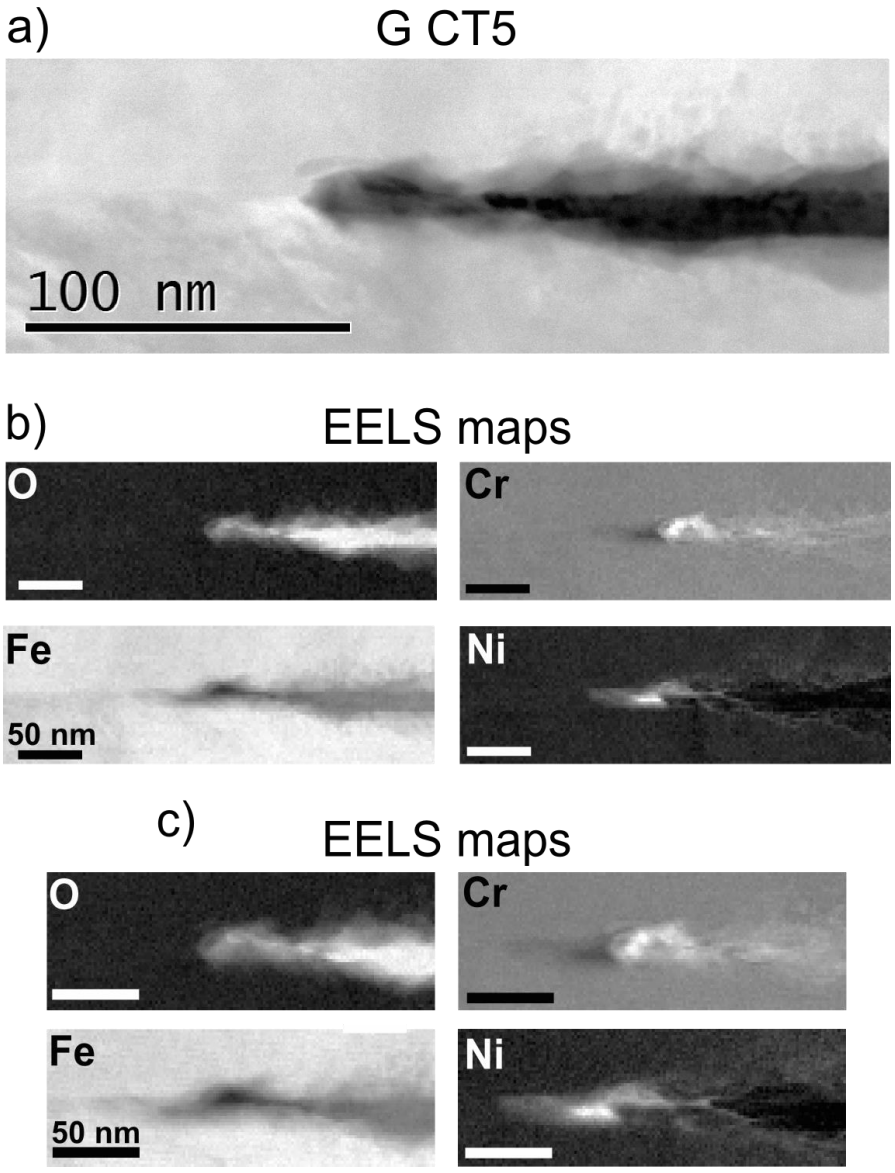

Figure 95. 316INSS G CT5: a) STEM ADF image; b) EELS elemental maps; c) EELS elemental maps (larger magnification)

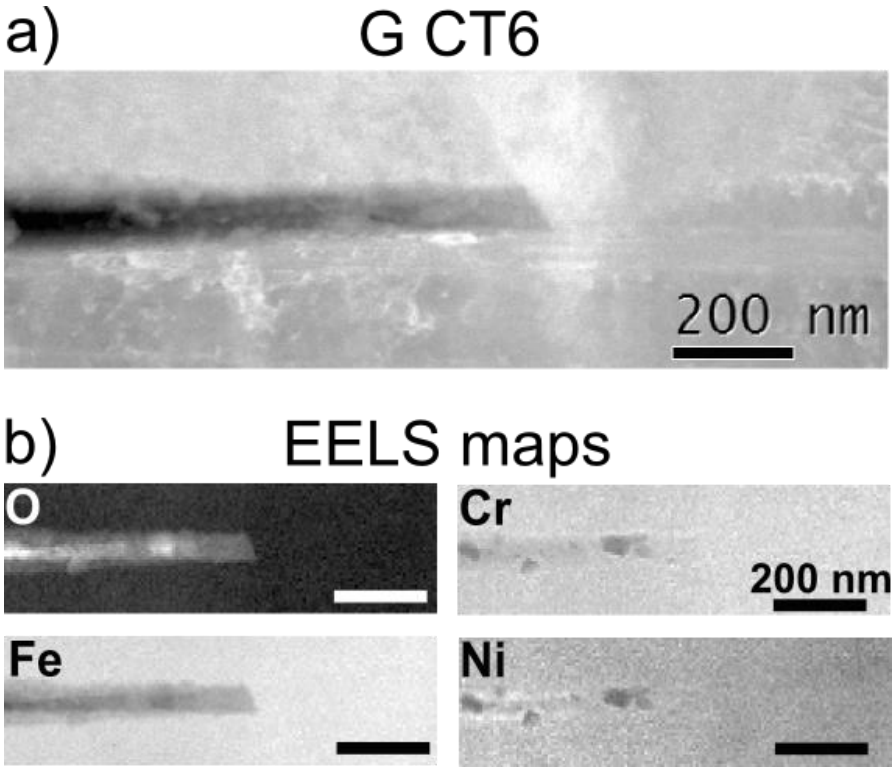

Figure 96. 316INSS G CT6: a) STEM ADF image; b) EELS elemental maps

9. Bibliography

[1] T Allen, J Busby, M Meyer, D Petti. Materials challenges for nuclear systems, Materials Today. 13 (2010) 14-23.

[2] T Shoji, Z Lu, Q Peng, Factors affecting stress corrosion cracking (SCC) and fundamental mechanistic understanding of stainless steels, in: Raja VS, Shoji T (Eds.), Stress Corrosion Cracking: Theory and Practice, 1st ed., Woodhead Publishing, 2011, pp. 245-272.

[3] U.S.NRC, Davis-Besse Reactor Pressure Vessel Head Degradation - Overview, Lessons Learned and NRC Actions Based on Lessons Learned, (2008).

[4] IAEA, Stress Corrosion Cracking in Light Water Reactors: Good Practices and Lessons Learned, IAEA, (2011).

[5] P Roberge, Corrosion Engineering - Principles and Practice, McGraw-Hill, United States, 2008.

[6] W Revie, Uhlig's Corrosion Handbook, 3rd edition ed., Wiley, Canada, 2011.

[7] MJN Pourbaix, CM Rorive-Bouté. Graphical study of metallurgical equilibria, Discuss.Faraday Soc. 4 (1948) 139-154.

[8] P Delahay, M Pourbaix, P Van Rysselberghe. Potential-pH diagrams, J.Chem.Educ. 27 (1950) 683-688.

[9] D Cubicciotti. Potential-pH diagrams for alloy-water systems under LWR conditions, J.Nucl.Mater. 201 (1993) 176-183.

[10] PL Andresen, Basic Elements of Initiation and Propagation of SCC in Water-cooled Nuclear Power Systems, Quantitative Micro-Nano Approach to Predicting SCC of Fe-Cr-Ni Alloys - meeting notes, Toronto, (2013).

[11] RB Rebak, Stress corrosion cracking (SCC) of nickel-based alloys, in: Raja VS, Shoji T (Eds.), Stress Corrosion Cracking: Theory and Practice, 1st ed., Woodhead Publishing, 2011, pp. 273-306.

[12] PL Andresen, FP Ford, Prediction of stress corrosion cracking (SCC) in nuclear power systems, in: Raja VS, Shoji T (Eds.), Stress Corrosion Cracking: Theory and Practice, 1st ed., Woodhead Publishing, 2011, pp. 651-713.

[13] AJ Sedriks, Corrosion of stainless steels, 2nd ed., John Wiley and Sons, New York, 1996.

[14] JF Grubb, T DeBold. Corrosion of wrought stainless steels, ASM Handbook Volume 13B, Corrosion: Materials. (2005).

[15] V Kain, Stress corrosion cracking (SCC) in stainless steels, in: Raja VS, Shoji T (Eds.), Stress Corrosion Cracking: Theory and practice, 1st ed., Woodhead Publishing, 2011, pp. 199-244.

[16] V Kain, RC Prasad, PK De, HS Gadiyar. Corrosion assessment of AISI 304L stainless steel in nitric acid environments – an alternate approach, ASTM Journal of Testing and Evaluation. 23(1) (1995) 50-54.

[17] P Scott. A review of irradiation assisted stress corrosion cracking, J.Nucl.Mater. 211 (1994) 101-122.

[18] TS Byun, N Hashimoto, K Farrell. Temperature dependence of strain hardening and plastic instability behaviors in austenitic stainless steels, Acta Materialia. 52 (2004) 3889-3899.

[19] W Karlsen, G Diego, B Devrient. Localized deformation as a key precursor to initiation of intergranular stress corrosion cracking of austenitic stainless steels employed in nuclear power plants, J.Nucl.Mater. 406 (2010) 138-151.

[20] W Dietzel, P Bala Srinivasan, Testing and evaluation methods for stress corrosion cracking (SCC) in metals, in: Raja VS, Shoji T (Eds.), Stress corrosion cracking: Theory and Practice, 1st ed., Woodhead Publishing, 2011, pp. 133-166.

[21] ASTM, ASTM G47 - 98(2011) Standard Test Method for Determining Susceptibility to Stress-Corrosion Cracking of 2XXX and 7XXX Aluminum Alloy Products, ASTM, (2011).

[22] ISO, ISO 7539-6:2011 - Corrosion of metals and alloys - Stress corrosion testing, ISO, (2011).

[23] NACE, TM0198-2011, Slow Strain Rate Test Method for Screening Corrosion-Resistant Alloys for Stress Corrosion Cracking in Sour Oilfield Service, NACE, (2011).

[24] NACE, TM0177-2005: Laboratory Testing of Metals for Resistance to Sulfide Stress Cracking and Stress Corrosion Cracking in H2S Environments, NACE, (2005).

[25] A Turnbull. Test methods for environment assisted cracking, Br.Corros.J. 27 (1992) 271-289.

[26] AJ Sedriks, Stress corrosion cracking – test methods, NACE - Corrosion Testing Made Easy. (1990).

[27] W Dietzel, K Schwalbe. Monitoring stable crack growth using a combined AC/DC potential drop technique, Z. Materialprüfung/Mats. Testing. 28 (1986) 368-372.

[28] K Strieder, KH Daum, W Dietzel, J Müller-Roos, The use of slow strain rate tests for measuring the velocity of environmentally assisted cracking, Structural Integrity: Experiments - Models - Applications, Proceedings of the 10th European Conference on Fracture, ECF 10, Berlin, K.-H. Schwalbe and C. Berger (Eds.), Deutscher Verband für Materialforschung und -prüfung e.V., (1994) 715-720.

[29] N Winzer, A Atrens, W Dietzel, G Song, KU Kainer. Comparison of the linearly increasing stress test and the constant extension rate test in the evaluation of transgranular stress corrosion cracking of magnesium, Materials Science and Engineering A. 472 (2008) 97-106.

[30] R Staehle, Definition of precursors, incubation, slow growth and propagation of SCC, The SCC initiation workshop, Beaune, France, IJNESE Volume 2, Issue 3 September 2012 PP. 79-87 (2008).

[31] K Arioka, Role of diffusion of vacancy in materials lead to SCC initiation, Quantitative Micro-Nano Approach to Predicting SCC of Fe-Cr-Ni Alloys - meeting notes, Toronto, (2013).

[32] K Arioka, T Miyamoto, T Yamada, T Terachi. Formation of cavities prior to crack initiation and growth on cold-worked carbon steel in high-Temperature Water, Corrosion. 66 (2010) 0150081-01500814.

[33] K Arioka, T Miyamoto, T Yamada, T Terachi, Formation of crack embryos prior to crack growth in high temperature water, 14th International Conference on Environmental Degradation of Materials in Nuclear Power Systems Water Reactors 2009, American Nuclear Society (ANS). 2 (2009) 895-909.

[34] K Arioka, T Miyamoto, T Yamada, T Terachi, Role of cavity formation on crack growth of cold-worked carbon steel, TT 690 and MA 600 in high temperature water, 15th International Conference on Environmental Degradation of Materials in Nuclear Power Systems-Water Reactors 2011, Wiley. 1 (2011) 52-66.

[35] T Terachi, T Yamada, T Miyamoto, K Arioka. SCC growth behaviors of austenitic stainless steels in simulated PWR primary water, J.Nucl.Mater. 426 (2012) 59-70.

[36] K Arioka, T Yamada, T Terachi, T Miyamoto, Temperature, potential and sensitization effects on intergranular crack growth and crack-tip appearance of cold worked 316, 13th International Conference on Environmental Degradation of Materials in Nuclear Power Systems 2007, Canadian Nuclear Society (CNS). 1 (2007) 1-13.

[37] K Arioka, T Yamada, T Terachi, T Miyamoto. Dependence of stress corrosion cracking for cold-worked stainless steel on temperature and potential, and role of diffusion of vacancies at crack tips, Corrosion. 64 (2008) 691-706.

[38] K Arioka, T Yamada, T Miyamoto, T Terachi. Dependence of stress corrosion cracking of Alloy 690 on temperature, cold work, and carbide precipitation - Role of diffusion of vacancies at crack tips, Corrosion. 67 (2011).

[39] RB Mears, RH Brown, EH Dix, A Generalized Theory of Stress Corrosion of Alloys, Symposium on stress corrosion cracking of metals, ASTM. (1944) 323.

[40] HL Logan. Film-rupture mechanism of stress corrosion, Journal of Research of the National Bureau of Standards. 48(2) (1952) 99.

[41] GF Sager, RB Mears, RH Brown, Tests for determining susceptibility to Stress Corrosion Cracking, Symposium on stress corrosion cracking of metals, ASTM, (1944) 255.

[42] JC Scully. Stress corrosion crack propagation: A constant charge criterion, Corros.Sci. 15 (1975) 207-224.

[43] SP Lynch, Mechanistic and fractographic aspects of stress-corrosion cracking (SCC), in: Raja VS, Shoji T (Eds.), Stress Corrosion Cracking: Theory and Practice, 1st ed., Woodhead Publishing, 2011, pp. 1-78.

[44] DA Vermilyea. Theory for the propagation of stress corrosion cracks in metals, J.Electrochem.Soc. 119 (1972) 405-407.

[45] PL Andresen, F Peter Ford. Life prediction by mechanistic modeling and system monitoring of environmental cracking of iron and nickel alloys in aqueous systems, Materials Science and Engineering. 103 (1988) 167-184.

[46] EM Gutman. An inconsistency in "film rupture model" of stress corrosion cracking, Corros.Sci. 49 (2007) 2289-2302.

[47] MM Hall Jr. Critique of the Ford-Andresen film rupture model for aqueous stress corrosion cracking, Corros.Sci. 51 (2009) 1103-1106.

[48] MM Hall Jr. An alternative to the Shoji crack tip strain rate equation, Corros.Sci. 50 (2008) 2902-2905.

[49] Z Lu, T Shoji. Unified interpretation of crack growth rates of Ni-base alloys in LWR environments, J.Pressure Vessel Technol.Trans.ASME. 128 (2006) 318-327.

[50] RC Newman, C Healey. Stability, validity, and sensitivity to input parameters of the slip-dissolution model for stress-corrosion cracking, Corros.Sci. 49 (2007) 4040-4050.

[51] M Vankeerberghen, G Weyns, S Gavrilov, B Martens, J Deconinck. Crack propagation rate modelling for 316SS exposed to PWR-relevant conditions, J.Nucl.Mater. 384 (2009) 274-285.

[52] A Turnbull. Modelling of environment assisted cracking, Corros.Sci. 34 (1993) 921-960.

[53] MM Hall Jr. Film rupture model for aqueous stress corrosion cracking under constant and variable stress intensity factor, Corros.Sci. 51 (2009) 225-233.

[54] J Galvele. A stress corrosion cracking mechanism based on surface mobility, Corros.Sci. 27 (1987) 1-33.

[55] K Sieradzki, FJ Friedersdorf. Notes on the surface mobility mechanism of stress-corrosion cracking, Corros.Sci. 36 (1994) 669-675.

[56] EM Gutman. Notes on the discussion concerning the "surface mobility mechanism" of stress corrosion cracking, Corros.Sci. 45 (2003) 2105-2128.

[57] EM Gutman. An inconsistency in "surface mobility mechanism" of stress corrosion cracking, Corrosion. 61 (2005) 197-200.

[58] JR Galvele. Surface mobility mechanism of stress-corrosion cracking, Corros.Sci. 35 (1993) 419-434.

[59] AR Troiano. The role of hydrogen and other interstitials in the mechanical behavior of metals, Trans ASM. 52 (1960) 54.

[60] CD Beachem. A new model for hydrogen-assisted cracking (hydrogen "embrittlement"), Metallurgical Transactions. 3 (1972) 441-455.

[61] SP Lynch. Environmentally assisted cracking: Overview of evidence for an adsorption-induced localised-slip process, Acta Metallurgica. 36 (1988) 2639-2661.

[62] SP Lynch. Mechanisms and kinetics of environmentally assisted cracking: Current status, issues, and suggestions for further work, Metall Mat Trans A Phys Metall Mat Sci. 44 (2013) 1209-1229.

[63] Ladna B., Birnbaum H.K. A study of hydrogen transport during plastic deformation, Acta Metallurgica. 35 (1987) 1775-1778.

[64] Kimura A., Birnbaum H.K. Hydrogen induced grain boundary fracture in high purity nickel and its alloys-Enhanced hydrogen diffusion along grain boundaries, Acta Metallurgica. 36 (1988) 757-766.

[65] Chu W.Y., Birnbaum H.K. Hydrogen embrittlement of iron-nickel alloys, MTA. 20 (1989) 1475-1482.

[66] Sofronis P., Birnbaum H.K., Hydrogen enhanced localized plasticity: A mechanism for hydrogen related fracture, ASME Aerosp Div Publ AD. 36 (1993) 15-25.

[67] Birnbaum H.K. Hydrogen effects on deformation - Relation between dislocation behavior and the macroscopic stress-strain behavior, Scripta Metallurgica et Materiala. 31 (1994) 149-153.

[68] Birnbaum H.K., Sofronis P. Hydrogen-enhanced localized plasticity - a mechanism for hydrogen-related fracture, Mater.Sci.Eng.A. 176 (1994) 191-202.

[69] Birnbaum H.K., Sofronis P., Hydrogen-dislocation interactions, Proceedings of the 5th International Conference on Hydrogen Effects in Materials. (1996) 15-34.

[70] Ferreira P.J., Robertson I.M., Birnbaum H.K. Hydrogen effects on the interaction between dislocations, Acta Mater. 46 (1998) 1749-1757.

[71] HW Liu. A unified model of environment-assisted cracking, Acta Materialia. 56 (2008) 4339-4348.

[72] SP Lynch. Comments on "A unified model of environment-assisted cracking", Scr.Mater. 61 (2009) 331-334.

[73] PM Scott, M Le Calvar, Some possible mechanisms of intergranular stress corrosion cracking of alloy 600 in PWR primary water, 6th International Conference on Environmental Degradation of Materials in Nuclear Power Systems-Water Reactors, TMS. (1993) 657-667.

[74] RB Rebak, Z Szklarska-Smialowska. The mechanism of stress corrosion cracking of alloy 600 in high temperature water, Corros.Sci. 38 (1996) 971-988.

[75] S Lozano-Perez, M Meisnar, J Dohr, K Kruska, Reviewing the internal oxidation mechanism as a plausible explanation for SCC in PWR primary water, 16th International Conference on Environmental Degradation of Materials in Nuclear Power Systems-Water Reactors, NACE (digital copy). (2013).

[76] SM Bruemmer, LE Thomas, Insights into stress corrosion cracking mechanisms from high-resolution measurements of crack-tip structures and compositions, Materials Research Society Symposium Proceedings. 1264 (2010) 159-170.

[77] MJ Olszta, DK Schreiber, LE Thomas, SM Bruemmer, Penetrative internal oxidation from alloy 690 surfaces and stress corrosion crack walls during exposure to PWR primary water, 15th International Conference on Environmental Degradation of Materials in Nuclear Power Systems-Water Reactors 2011, Wiley. 1 (2011) 317-328.

[78] RC Newman, Stress corrosion cracking, in: Richardson JA (Ed.), Shreir's corrosion, 4th ed., Elsevier, Amsterdam, 2010, pp. 864-901.

[79] RH Jones, Stress corrosion cracking, ASM Metals Handbook, 9th ed., ASM, Metals Park, OH, 1987, pp. 145-163.

[80] EA West, MD McMurtrey, Z Jiao, GS Was. Role of localized deformation in irradiation-assisted stress corrosion cracking initiation, Metall Mat Trans A Phys Metall Mat Sci. 43 (2012) 136-146.

[81] S Lozano-Perez, MR Kilburn, T Yamada, T Terachi, CA English, CRM Grovenor. High-resolution imaging of complex crack chemistry in reactor steels by NanoSIMS, J.Nucl.Mater. 374 (2008) 61-68.

[82] RP Wei, Fracture mechanics: Integration of mechanics, materials science and chemistry, Fracture Mechanics: Integration of Mechanics, Materials Science, and Chemistry. (2010) 1-214.

[83] K Arioka, T Yamada, T Terachi, RW Staehle. Intergranular stress corrosion cracking behavior of austenitic stainless steels in hydrogenated high-temperature water, Corrosion. 62 (2006) 74-83.

[84] T Terachi, K Arioka, Characterization of Oxide Film Behaviors on 316 Stainless Steels in High-Temperature Water - Influence of Hydrogen and Oxygen Considerations for Initiation of SCC, NACE - International Corrosion Conference Series. (2006) 066081-0660810.

[85] T Terachi, K Fujii, K Arioka. Microstructural characterization of SCC crack tip and oxide film for SUS 316 stainless steel in simulated PWR primary water at 320°C, J Nucl Sci Technol. 42 (2005) 225-232.

[86] S Lozano-Perez, JM Titchmarsh. TEM investigations of intergranular stress corrosion cracking in austenitic alloys in PWR environmental conditions, Materials at High Temperatures. 20 (2003) 573-579.

[87] S Lozano-Perez, JM Titchmarsh, ML Jenkins, TEM characterization of stress corrosion cracks in 304SS, Institute of Physics Conference Series, IOP Publishing Ltd., 179 (2004) 233-236.

[88] S Lozano-Perez. Novel characterization of stress corrosion cracks, Journal of Physics: Conference Series, IOP Publishing Ltd., 126 (2008).

[89] S Lozano-Perez, CA English, T Terachi, T Yamada, A multi-scale approach to stress corrosion cracking, International Corrosion Conference Series, NACE (08495). (2008).

[90] S Lozano-Perez, T Yamada, T Terachi, M Schröder, CA English, GDW Smith, et al. Multi-scale characterization of stress corrosion cracking of cold-worked stainless steels and the influence of Cr content, Acta Materialia. 57 (2009) 5361-5381.

[91] M Olszta, D Schreiber, L Thomas, S Bruemmer. High-resolution crack imaging reveals degradation processes in nuclear reactor structural materials, Advanced Materials and Processes. 170 (2012) 17-21.

[92] R Bauch, M Cambini, P Weisgerber, C DeAsmundis, C Plog. Investigations on oxide formed in high-temperature water on austenitic steel, J.Nucl.Mater. 92 (1980) 334-344.

[93] J Robertson. The mechanism of high temperature aqueous corrosion of stainless steels, Corros.Sci. 32 (1991) 443-465.

[94] B Stellwag. The mechanism of oxide film formation on austenitic stainless steels in high temperature water, Corros.Sci. 40 (1998) 337-370.

[95] Z Szklarska-Smialowska, K- Chou, Z Xia. The composition and properties of oxide films on type 304 stainless steel on exposure to lithiated water at 100-350°C, Corros.Sci. 32 (1991) 609-619.

[96] RL Tapping, RD Davidson, E McAlpine, DH Lister. The composition and morphology of oxide films formed on type 304 stainless steel in lithiated high temperature water, Corros.Sci. 26 (1986) 563-576.

[97] Y- Kim. Characterization of the Oxide Film Formed on Type 316 Stainless Steel in 288°C Water in Cyclic Normal and Hydrogen Water Chemistries, Corrosion. 51 (1995).

[98] T Miyazawa, T Terachi, S Uchida, T Satoh, T Tsukada, Y Satoh, et al. Effects of hydrogen peroxide on corrosion of stainless steel, (V) characterization of oxide film with multilateral surface analyses, J Nucl Sci Technol. 43 (2006) 884-895.

[99] P Marcus, Surface Oxide Films, Quantitative Micro-Nano Approach to Predicting SCC of Fe-Cr-Ni Alloys - meeting notes, Toronto, (2013).

[100] K Kruska, S Lozano-Perez, DW Saxey, T Terachi, T Yamada, GDW Smith. Nanoscale characterisation of grain boundary oxidation in cold-worked stainless steels, Corros.Sci. 63 (2012) 225-233.

[101] DK Schreiber, MJ Olszta, DW Saxey, K Kruska, KL Moore, S Lozano-Perez, et al. Examinations of oxidation and sulfidation of grain boundaries in alloy 600 exposed to simulated pressurized water reactor primary water, Microscopy and Microanalysis. 19 (2013) 676-687.

[102] A La Fontaine, H- Yen, PJ Felfer, SP Ringer, JM Cairney. Atom probe study of chromium oxide spinels formed during intergranular corrosion, Scr.Mater. 99 (2015) 1-4.

[103] N Birks, GH Meier, FS Pettit, Introduction to the high temperature oxidation of metals, Second edition, Cambridge University Press, 2009, pp. 1-338.

[104] RW Staehle, Critical analysis of "tight cracks", 13th International Conference on Environmental Degradation of Materials in Nuclear Power Systems 2007, Canadian Nuclear Society (CNS). 3 (2007) 1877-1957.

[105] SM Bruemmer, MJ Olszta, MB Toloczko, LE Thomas, High-resolution characterizations of grain boundary damage and stress corrosion cracks in cold-rolled alloy 690, 15th International Conference on Environmental Degradation of Materials in Nuclear Power Systems-Water Reactors 2011, Wiley. 1 (2011) 288-301.

[106] K Kruska, S Lozano-Perez, DW Saxey, T Terachi, T Yamada, GDW Smith, 3D atom-probe characterization of stress and cold-work in stress corrosion cracking of 304 stainless steel, 15th International Conference on Environmental Degradation of Materials in Nuclear Power Systems-Water Reactors 2011, Wiley. 2 (2011) 891-898.

[107] K Arioka, T Yamada, T Terachi, G Chiba. Influence of carbide precipitation and rolling direction on intergranular stress corrosion cracking of austenitic stainless steels in hydrogenated high-temperature water, Corrosion. 62 (2006) 568-575.

[108] JC Langevoort, T Fransen, PJ Gellings. On the influence of cold work on the oxidation of some stainless steels. Werkst.Korros. 34 (1983) 500-504.

[109] JC Langevoort, T Fransen, PJ Geilings. On the influence of cold work on the oxidation behavior of some austenitic stainless steels: High temperature oxidation, Oxidation Metals. 21 (1984) 271-284.

[110] M Mizouchi, Y Yamazaki, Y Iijima, K Arioka. Low temperature grain boundary diffusion of chromium in SUS316 and 316L stainless steels, Materials Transactions. 45 (2004) 2945-2950.

[111] K Arioka, T Yamada, T Terachi, G Chiba. Cold work and temperature dependence of stress corrosion crack growth of austenitic stainless steels in hydrogenated and oxygenated high-temperature water, Corrosion. 63 (2007) 1114-1123.

[112] S Lozano-Perez, K Kruska, I Iyengar, T Terachi, T Yamada. The role of cold work and applied stress on surface oxidation of 304 stainless steel, Corros.Sci. 56 (2012) 78-85.

[113] RB Rebak, Z Xia, Z Szklarska-Smialowska. Effect of temperature and cold work on the crack growth rate of alloy 600 in primary water, Corrosion. 51 (1995) 689-697.

[114] WC Moshier. Effect of cold work and processing orientation on stress corrosion cracking behavior of alloy 600, Corrosion. 56 (2000) 307-320.

[115] C Guerre, O Raquet, E Herms, S Marie, M Le Calvar, SCC crack growth rate of cold-worked austenitic stainless steels in PWR primary water conditions, 13th International Conference on Environmental Degradation of Materials in Nuclear Power Systems 2007, Canadian Nuclear Society. 1 (2007) 676-699.

[116] Swann P.R. Extrinsic stacking faults in Cu-7.3wt.% Al, Acta Metallurgica. 14 (1966) 76-77.

[117] Swann P.R., Warlimont H. The electron-metallography and crystallography of copper-aluminum martensites, Acta Metallurgica. 11 (1963) 511-527.

[118] Swann P.R. The dislocation distribution near the surface of deformed copper, Acta Metallurgica. 14 (1966) 900-903.

[119] I Karaman, H Sehitoglu, YI Chumlyakov, HJ Maier. The deformation of low-stacking-fault-energy austenitic steels, JOM. 54 (2002) 31-37.

[120] M Hadji, R Badji. Microstructure and mechanical properties of austenitic stainless steels after cold rolling, Journal of Materials Engineering and Performance. 11 (2002) 145-151.

[121] EH Lee, TS Byun, JD Hunn, MH Yoo, K Farrell, LK Mansur. On the origin of deformation microstructures in austenitic stainless steel: Part I - Microstructures, Acta Materialia. 49 (2001) 3269-3276.

[122] V Kain, Corrosion-resistant materials, Functional Materials. (2012) 507-547.

[123] A Kelly, KM Knowles, Crystallography and Crystal Defects: Second Edition, Crystallography and Crystal Defects: Second Edition, Wiley. (2012).

[124] KP Shah, Plastic Deformation and Fracture, practicalmaintenance.net 2014.

[125] KM Knowles, D Holmes, A Bridges, H Scott, Slip geometry: the critical resolved shear stress, www.doitpoms.ac.uk/tlplip/slip, (2014).

[126] SG Chowdhury, S Das, PK De. Cold rolling behaviour and textural evolution in AISI 316L austenitic stainless steel, Acta Materialia. 53 (2005) 3951-3959.

[127] F Scenini, A Sherry. Stress corrosion cracking of sensitized type 304 stainless steel in high-temperature water with anionic impurities contamination, Corrosion. 68 (2012) 1094-1107.

[128] V Tsakiris, DV Edmonds. Martensite and deformation twinning in austenitic steels, Materials Science and Engineering A. 273-275 (1999) 430-436.

[129] Y Li, F Bu, W Kan, H Pan. Deformation-induced martensitic transformation behavior in cold-rolled AISI304 stainless steels, Mater.Manuf.Process. 28 (2013) 256-259.

[130] JC Bavay, Austenitic Stainless Steels, in: Lacombe P, Baroux B, Beranger G (Eds.), Stainless Steels, Les Editions de Physique Ulis, 1993, pp. 551.

[131] Ferreira P.J., Robertson I.M., Birnbaum H.K., Influence of hydrogen on the stacking-fault energy of an austenitic stainless steel, Mater Sci Forum. 207-209 (1996) 93-96.

[132] S Singh, C Altstetter. Effects of hydrogen concentration on slow crack growth in stainless steels, Metallurgical Transactions A. 13 (1982) 1799-1808.

[133] T- Perng, CJ Altstetter. Hydrogen effects in austenitic stainless steels, Materials Science and Engineering: A. 129 (1990) 99-107.

[134] P Tsong-Pyng, CJ Altstetter. Effects of deformation on hydrogen permeation in austenitic stainless steels, Acta Metallurgica. 34 (1986) 1771-1781.

[135] T Perng, M Johnson, CJ Altstetter. Influence of plastic deformation on hydrogen diffusion and permeation in stainless steels, Acta Metallurgica. 37 (1989) 3393-3397.

[136] M Hatano, M Fujinami, K Arai, H Fujii, M Nagumo. Hydrogen embrittlement of austenitic stainless steels revealed by deformation microstructures and strain-induced creation of vacancies, Acta Materialia. 67 (2014) 342-353.

[137] M von Ardenne. Das Raster-Elektronenmikroskop. Theoretische Grundlagen, Zeitschrift für Physik. 109 (1938) 553-572.

[138] J Goldstein, D Newbury, Scanning Electron Microscopy and X-ray microanalysis, 3rd edition ed., Springer, New York, 2003.

[139] CL Collins, J Holland, SR Burgess, PJ Statham, N Rowlands. Accurate quantitative EDS mapping at high count rates with a large area silicon drift detector, Microsc.Microanal. 15 (2009) 230-231.

[140] CL Collins, J Holland, SR Burgess, N Rowlands. X-Max large area SDD detectors - Creating a real impact on nano-science, Microsc.Microanal. 15 (2009) 172-173.

[141] SR Burgess, J Holland, C Collins, S Sharp. X-ray nano-analysis of sub-100nm particles using EDS in conjunction with SEM, Microsc.Microanal. 14 (2008) 1098-1099.

[142] S Burgess, X Li, J Holland. Improving Low Energy Sensitivity of EDS Detectors for SEM – Higher Spatial Resolution X-ray analysis and Detection of Light elements Including Lithium, Microscopy and Micoranalysis. 27 (2013) 8.

[143] P Statham. New Real Time Visualisations for X-ray Mapping Data, Microscopy and Microanalysis. 17 (2011) 886.

[144] D Drouin, AR Couture, D Joly, X Tastet, V Aimez, R Gauvin. CASINO V2.42 - A fast and easy-to-use modeling tool for scanning electron microscopy and microanalysis users, Scanning. 29 (2007) 92-101.

[145] M Meisnar, S Lozano-Perez, M Moody, J Holland. Low-energy EDX - A novel approach to study stress corrosion cracking in SUS304 stainless steel via scanning electron microscopy, Micron. 66 (2014) 16-22.

[146] AJ Schwartz, M Kumar, BL Adams, D Field. Electron Backscatter Diffraction in Materials Science, 2nd ed., Springer. (2009).

[147] D Dingley. Progressive steps in the development of electron backscatter diffraction and orientation imaging microscopy, J.Microsc. 213 (2004) 214-224.

[148] RR Keller, RH Geiss. Transmission EBSD from 10 nm domains in a scanning electron microscope, J.Microsc. 245 (2012) 245-251.

[149] PW Trimby. Orientation mapping of nanostructured materials using transmission Kikuchi diffraction in the scanning electron microscope, Ultramicroscopy. 120 (2012) 16-24.

[150] S Zaefferer. A critical review of orientation microscopy in SEM and TEM, Crystal Research and Technology. 46 (2011) 607-628.

[151] N Brodusch, H Demers, R Gauvin. Nanometres-resolution Kikuchi patterns from materials science specimens with transmission electron forward scatter diffraction in the scanning electron microscope, J.Microsc. 250 (2013) 1-14.

[152] KP Rice, RR Keller, MP Stoykovich. Specimen-thickness effects on transmission Kikuchi patterns in the scanning electron microscope, J.Microsc. 254 (2014) 129-136.

[153] PW Trimby, JM Cairney. Transmission kikuchi diffraction in the scanning electron microscope: Orientation mapping on the nanoscale, Advanced Materials and Processes. 172 (2014) 13-15.

[154] PW Trimby, Y Cao, Z Chen, S Han, KJ Hemker, J Lian, et al. Characterizing deformed ultrafine-grained and nanocrystalline materials using transmission Kikuchi diffraction in a scanning electron microscope, Acta Materialia. 62 (2014) 69-80.

[155] K Babinsky, R De Kloe, H Clemens, S Primig. A novel approach for site-specific atom probe specimen preparation by focused ion beam and transmission electron backscatter diffraction, Ultramicroscopy. 144 (2014) 9-18.

[156] M Meisnar, A Vilalta-Clemente, A Gholinia, M Moody, AJ Wilkinson, N Huin, et al. Using transmission Kikuchi diffraction to study intergranular stress corrosion cracking in type 316 stainless steels, Micron. 75 (2015) 1-10.

[157] RM Langford, YZ Huang, S Lozano-Perez, JM Titchmarsh, AK Petford-Long. Preparation of site specific transmission electron microscopy plan-view specimens using a focused ion beam system, Journal of Vacuum Science and Technology B: Microelectronics and Nanometer Structures. 19 (2001) 755-758.

[158] YZ Huang, S Lozano-Perez, RM Langford, JM Titchmarsh, ML Jenkins. Preparation of transmission electron microscopy cross-section specimens of crack tips using focused ion beam milling, J.Microsc. 207 (2002) 129-136.

[159] JM Cairney, DW Saxey, D McGrouther, SP Ringer. Site-specific specimen preparation for atom probe tomography of grain boundaries, Physica B: Condensed Matter. 394 (2007) 267-269.

[160] MK Miller, KF Russell. Atom probe specimen preparation with a dual beam SEM/FIB miller, Ultramicroscopy. 107 (2007) 761-766.

[161] MK Miller, KF Russell, K Thompson, R Alvis, DJ Larson. Review of atom probe FIB-based specimen preparation methods, Microscopy and Microanalysis. 13 (2007) 428-436.

[162] DW Saxey, JM Cairney, D McGrouther, T Honma, SP Ringer. Atom probe specimen fabrication methods using a dual FIB/SEM, Ultramicroscopy. 107 (2007) 756-760.

[163] K Thompson, D Lawrence, DJ Larson, JD Olson, TF Kelly, B Gorman. In situ site-specific specimen preparation for atom probe tomography, Ultramicroscopy. 107 (2007) 131-139.

[164] S Lozano-Perez. A guide on FIB preparation of samples containing stress corrosion crack tips for TEM and atom-probe analysis, Micron. 39 (2008) 320-328.

[165] P Felfern, SP Ringer, JM Cairney. Shaping the lens of the atom probe: Fabrication of site specific, oriented specimens and application to grain boundary analysis, Ultramicroscopy. 111 (2011) 435-439.

[166] PJ Felfer, T Alam, SP Ringer, JM Cairney. A reproducible method for damage-free site-specific preparation of atom probe tips from interfaces, Microsc.Res.Tech. 75 (2012) 484-491.

[167] J Takahashi, K Kawakami, Y Yamaguchi, M Sugiyama. Development of atom probe specimen preparation techniques for specific regions in steel materials, Ultramicroscopy. 107 (2007) 744-749.

[168] A Eades. Atom probe microanalysis: Principles and appilcations to materials problems, by M.K. Miller and G.D.W. Smith. Materials Research Society, Pittsburgh, 1989, 278 pp, $47.00 (US), $56.00 (foreign), Microsc.Res.Tech. 20 (1992) 217-217.

[169] R Fainchtein, PR Zarriello. A computer-controlled technique for electrochemical STM tip fabrication, Ultramicroscopy. 42–44, Part 2 (1992) 1533-1537.

[170] DJ Larson, DT Foord, AK Petford-Long, TC Anthony, IM Rozdilsky, A Cerezo, et al. Focused ion-beam milling for field-ion specimen preparation: Preliminary investigations, Ultramicroscopy. 75 (1998) 147-159.

[171] DJ Larson, DT Foord, AK Petford-Long, A Cerezo, GDW Smith. Focused ion-beam specimen preparation for atom probe field-ion microscopy characterization of multilayer film structures, Nanotechnology. 10 (1999) 45-50.

[172] DJ Larson, A Cerezo, YQ Ma, TJ Godfrey, PH Clifton, GDW Smith. Sharpening and positioning of regions of interest in atom probe samples using in-situ sputtering, Microscopy and Microanalysis. 9 (2003) 578-579.

[173] D Lawrence, K Thompson, D Larson, B Gorman. Site-specific lift out sample preparation technique for atom probe analysis, Microscopy and Microanalysis. 12 (2006) 1742-1743.

[174] D Lawrence, K Thompson, DJ Larson. Site-specific specimen preparation technique for atom probe analysis of grain boundaries, Microscopy and Microanalysis. 12 (2006) 1740-1741.

[175] R Shivaraman, RM Ulfig, DJ Larson, H Fukuzawa, DC Bell, H Wang, et al. Pre-sharpened microtips: An efficient sample preparation method for atom probe tomography, Microscopy and Microanalysis. 15 (2009) 296-297.

[176] MI Hartshorne, D Isheim, DN Seidman, ML Taheri. Specimen preparation for correlating transmission electron microscopy and atom probe tomography of mesoscale features, Ultramicroscopy. 147 (2014) 25-32.

[177] L Viskari, M Hörnqvist, KL Moore, Y Cao, K Stiller. Intergranular crack tip oxidation in a Ni-base superalloy, Acta Materialia. 61 (2013) 3630-3639.

[178] DB Williams, CB Carter, Transmission Electron Microscopy - A Textbook for Materials Science, Springer, New York, NA, 2009.

[179] WJ Nisbet, GW Lorimer, RC Newman. A transmission electron microscopy study of stress corrosion cracking in stainless steels, Corros.Sci. 35 (1993) 457-469.

[180] Y Nemoto, Y Miwa, M Kikuchi, Y Kaji, T Tsukada, H Tsuji. Development of analytical method and study about microstructure of oxide films on stainless steel, J Nucl Sci Technol. 39 (2002) 996-1001.

[181] LE Thomas, SM Bruemmer, Insights into environmental degradation mechanisms from analytical transmission electron microscopy of SCC cracks, Proceedings of the Ninth International Symposium on Environmental Degradation of Materials in Nuclear Power Systems - Water Reactors, TMS. (1999) 41-47.

[182] MJ Olszta, DK Schreiber, LE Thomas, SM Bruemmer, Electron microscopy characterizations and atom probe tomography of intergranular attack in alloy 600 exposed to PWR primary water, 15th International Conference on Environmental Degradation of Materials in Nuclear Power Systems-Water Reactors 2011, Wiley. 2 (2011) 1422-1435.

[183] P Trebbia, C Mory. EELS elemental mapping with unconventional methods II. Applications to biological specimens, Ultramicroscopy. 34 (1990) 179-203.

[184] P Trebbia, N Bonnet. EELS elemental mapping with unconventional methods I. Theoretical basis: Image analysis with multivariate statistics and entropy concepts, Ultramicroscopy. 34 (1990) 165-178.

[185] S Lozano-Perez, V de Castro Bernal, RJ Nicholls. Achieving sub-nanometre particle mapping with energy-filtered TEM, Ultramicroscopy. 109 (2009) 1217-1228.

[186] B Gault, MP Moody, F De Geuser, A La Fontaine, LT Stephenson, D Haley, et al. Spatial resolution in atom probe tomography, Microscopy and Microanalysis. 16 (2010) 99-110.

[187] A Cerezo, PH Clifton, S Lozano-Perez, P Panayi, G Sha, GDW Smith. Overview: Recent progress in three-dimensional atom probe instruments and applications, Microscopy and Microanalysis. 13 (2007) 408-417.

[188] JH Bunton, JD Olson, DR Lenz, TF Kelly. Advances in pulsed-laser atom probe: Instrument and specimen design for optimum performance, Microscopy and Microanalysis. 13 (2007) 418-427.

[189] B Gault, M Moody, J Cairney, S Ringer, Field Ion Microscopy, Springer New York, 2012, pp. 9-28.

[190] S Lozano-Perez, DW Saxey, EA Marquis, T Terachi, T Yamada. Atom-probe tomography of surface oxides in a 20% cold worked stainless steel tested under PWR primary water conditions, Microscopy and Microanalysis. 15 (2009) 304-305.

[191] TF Kelly, TT Gribb, JD Olson, RL Martens, JD Shepard, SA Wiener, et al. First data from a commercial local electrode atom probe (LEAP), Microscopy and Microanalysis. 10 (2004) 373-383.

[192] S Lozano-Perez, DW Saxey, T Yamada, T Terachi. Atom-probe tomography characterization of the oxidation of stainless steel, Scr.Mater. 62 (2010) 855-858.

[193] K Thompson, B Gorman, DJ Larson, B Van Leer, L Hong. Minimization of Ga induced FIB damage using low energy clean-up, Microscopy and Microanalysis. 12 (2006) 1736-1737.

[194] TF Kelly, DJ Larson. Local electrode atom probes, Mater Charact. 44 (2000) 59-85.

[195] M Meisnar, M Moody, S Lozano-Perez. Atom probe tomography of stress corrosion crack tips in SUS316 stainless steels, Corros.Sci. 98 (2015) 661-671.

[196] SM Bruemmer, MJ Olszta, MB Toloczko, LE Thomas. Linking grain boundary microstructure to stress corrosion cracking of cold-rolled alloy 690 in pressurized water reactor primary water, Corrosion. 69 (2013) 953-963.

[197] S- Baik, MJ Olszta, SM Bruemmer, DN Seidman. Grain-boundary structure and segregation behavior in a nickel-base stainless alloy, Scr.Mater. 66 (2012) 809-812.

[198] SM Bruemmer, MJ Olszta, MB Toloczko, LE Thomas, Linking grain boundary microstructure to stress corrosion cracking of cold rolled alloy 690 in PWR primary, International Corrosion Conference Series 2012, NACE. 7 (2012) 5912-5927.

[199] TB Britton, AJ Wilkinson. High resolution electron backscatter diffraction measurements of elastic strain variations in the presence of larger lattice rotations, Ultramicroscopy. 114 (2012) 82-95.

[200] VY Gertsman, SM Bruemmer. Study of grain boundary character along intergranular stress corrosion crack paths in austenitic alloys, Acta Materialia. 49 (2001) 1589-1598.

[201] S Lozano-Perez, J Dohr, M Meisnar, K Kruska. SCC in PWRs: Learning from a Bottom-Up Approach, Metallurgical and Materials Transactions E. 1 (2014) 194-210.

[202] DK Schreiber, MJ Olszta, SM Bruemmer. Grain boundary depletion and migration during selective oxidation of Cr in a Ni-5Cr binary alloy exposed to high-temperature hydrogenated water, Scr.Mater. 89 (2014) 41-44.

[203] Y Guo, TB Britton, AJ Wilkinson. Slip band-grain boundary interactions in commercial-purity titanium, Acta Materialia. 76 (2014) 1-12.

[204] E Lehockey, Y Lin, O Lepik. Mapping Residual Plastic Strain in Materials Using Electron Backscatter Diffraction, Electron backscatter diffraction in Materials Science, AJ Schwartz, M Kumar and BL Adams (Eds.), Springer, (2000) 247-264.

[205] MMJ Treacy, JM Gibson. The effects of elastic relaxation on transmission electron microscopy studies of thinned composition- modulated materials, Journal of Vacuum Science & Technology B. 4 (1986) 1458-1466.

[206] K Arioka, T Yamada, T Miyamoto, M Aoki. Intergranular stress corrosion cracking growth behavior of Ni-Cr-Fe alloys in pressurized water reactor primary water, Corrosion. 70 (2014) 695-707.

[207] H Hallberg, L Banks-Sills, M Ristinmaa. Crack tip transformation zones in austenitic stainless steel, Eng.Fract.Mech. 79 (2012) 266-280.

[208] V Vitek. A theory of diffusion controlled intergranular creep crack growth, Acta Metallurgica. 26 (1978) 1345-1356.

[209] AJ Wilkinson, G Meaden, DJ Dingley. Mapping strains at the nanoscale using electron back scatter diffraction, Superlattices Microstruct. 45 (2009) 285-294.

[210] H Rauh, R Bullough. Stress-driven migration of point defects to a crack. Proc R Soc London Ser A. 397 (1985) 121-141.